Long-Range Interactions
in
Dilute Granular Systems

Samenstelling promotiecommissie:

prof. dr. F. Eising	Universiteit Twente, voorzitter/secretaris
prof. dr. S. Luding	Universiteit Twente, promotor
prof. dr. ir. H.W.M. Hoeijmakers	Universiteit Twente
prof. dr. D. Lohse	Universiteit Twente
prof. dr. D. Wolf	Universität Duisburg-Essen
prof. dr. A. Schmidt-Ott	Technische Universiteit Delft
prof. dr. D. Rixen	Technische Universiteit Delft

Long-Range Interactions in Dilute Granular Systems
M.-K. Müller

Cover image: by M.-K. Müller

Printed by Gildeprint Drukkerijen, Enschede
Thesis University of Twente, Enschede - With ref. - With summary in Dutch.
ISBN 978-90-365-2625-8

LONG-RANGE INTERACTIONS IN DILUTE GRANULAR SYSTEMS

PROEFSCHRIFT

ter verkrijging van
de graad van doctor aan de Universiteit Twente,
op gezag van de rector magnificus,
prof. dr. W.H.M. Zijm,
volgens besluit van het College voor Promoties
in het openbaar te verdedigen
op vrijdag 8 februari 2008 om 13.15 uur

door

Micha-Klaus Müller

geboren op 3 mei 1972
te Mutlangen, Duitsland

Dit proefschrift is goedgekeurd door de promotor:

prof. dr. S. Luding

Abstract

Homogeneously distributed and ring-shaped dilute granular systems with both short-ranged (contact) and long-ranged interactions are studied, using Molecular Dynamics (MD) methods in three dimensions.

From the technical and algorithmical side, a new algorithm for MD methods is developed that handles long-range forces in a computationally efficient and scientifically accurate way for a certain parameter range. For each particle, the new method is a hierarchy of the known linked cell structure in combination with a multi-pole expansion of the long-range interaction potentials between the particle and groups of particles far away. It is shown that the computational time expense reduces dramatically as compared to the straight-forward direct summation method.

The interplay between dissipation at contact and long-range repulsive/attractive forces in homogeneous dilute particle systems is studied theoretically. The pseudo-Liouville operator formalism, originally introduced for hard-sphere interactions, is modified such that it provides very good results for weakly dissipative systems at low densities. By numerical simulations, the theoretical results are generalized to higher densities, leading to an empirical correction factor depending on the density. In the case of repulsive systems, this leads to good agreement with the simulation results, while dissipative attractive systems, for intermediate densities, surprisingly show nearly the same cooling behavior as systems whithout mutual long-range interactions. As most essential observation, we note that the Hierarchical Linked Cell algorithm provides good results, as long as the thermal energy is higher than the Coulomb/escape energy barrier between two particles.

Ring-shaped dissipative particle systems with long-range attraction forces in a central gravitational potential are studied as an astrophysical example, using the HLC algorithm. It is found that for a given attraction strength, weak dissipation does not support clustering whereas strong dissipation leads to the formation of moonlets. On the other hand, the space and density dependent viscous behaviour of ring shaped particle systems is investigated by solving an approximate Navier-Stokes hydrodynamic set of equations for the density and by comparing its behavior with dynamical simulations. We find that non-gravitating rings show better agreement with theory than self-gravitating rings.

Contents

1 Introduction 5

1.1 Forces in General 6
1.2 Intermolecular Forces 8
1.3 Intergranular Forces 11
    1.3.1 Contact Forces 11
    1.3.2 Long-Range Forces 13
1.4 Organization of the Thesis 14

2 Long-Range Forces 17

2.1 Long-Range Forces in General 17
    2.1.1 Gravitational Forces 18
    2.1.2 Coulomb Forces 18
2.2 Close-by Single Particles 19
2.3 Distant Pseudo Particles 21
2.4 Summary 28

3 Computer Simulation 31

3.1 Molecular Dynamics 31
    3.1.1 Contact Forces 33
    3.1.2 Dissipative Forces 33
3.2 Particle-Particle Methods (PP) 35
3.3 Tree-Based Algorithms 35
    3.3.1 Barnes-Hut 36
    3.3.2 The Fast Multipole Method (FMM) 38
3.4 Grid-Based Algorithms 41
    3.4.1 Particle-Mesh (PM) 41
    3.4.2 Multigrid Techniques 44
3.5 Hybrid Algorithms 46
3.6 The Hierarchical Linked Cell Method (HLC) 47
    3.6.1 The Linked Cell Neighborhood 47
    3.6.2 The Inner Cut-Off Sphere 49
    3.6.3 The Hierarchical Linked Cell Structure 50
    3.6.4 Non-periodic Boundary Conditions 52
    3.6.5 Periodic Boundary Conditions 53
    3.6.6 The Outer Cut-Off Sphere 53

3.6.7 Computational Time 55
3.7 HLC versus PP 57
3.7.1 Bulk Force State 57
3.7.2 Temperature 59
3.7.3 Error Estimation 61
3.8 Summary 63

4 Dilute Homogeneous Particle Systems 65
4.1 Fundamental Properties 65
4.1.1 Granular Temperature 65
4.1.2 Excluded Volume 68
4.1.3 Pair Distribution Function 69
4.2 Systems without Long-Range Interactions 71
4.2.1 Collision Frequency 71
4.2.2 Kinetic Energy and the Homogeneous Cooling State 72
4.2.3 Dissipation Rate 74
4.2.4 Summary 74
4.3 Repulsive Long-Range Interactions 75
4.3.1 Pair Distribution Function 75
4.3.2 Collision Frequency 76
4.3.3 Kinetic Energy 78
4.3.4 Dissipation Rate 79
4.3.5 Many-Body and other Effects 81
4.3.6 Improved Time Evolution of Dynamical Observables . . . 88
4.3.7 Summary for Repulsive Systems 89
4.4 Attractive Long-Range Interactions 90
4.4.1 Pair Distribution Function 90
4.4.2 Collision Frequency 91
4.4.3 Kinetic energy 95
4.4.4 Many-Body and other Effects 100
4.4.5 Improved Time Evolution of Dynamical Observables . . . 102
4.4.6 Cluster Regime 104
4.4.7 Summary for Attractive Systems 105
4.5 Summary 106

5 Ring-Shaped Particle Systems 109
5.1 General Aspects 110
5.1.1 Keplerian Motion 110
5.1.2 Granular Temperature 111
5.1.3 Virial Theorem 112
5.1.4 Optical Depth 113
5.1.5 Kinematic Viscosity 113
5.2 The Model System 114

5.2.1 Forces 114
5.2.2 Adjusting the Time Step 117
5.2.3 HLC versus PP 119
5.2.4 Computational Time 120
5.3 The Deliquescing Particle Ring 121
5.3.1 The Hydrodynamic Equations in 2D 122
5.3.2 Density-independent Kinematic Viscosity 125
5.3.3 Radius and Density dependent Kinematic Viscosity 125
5.3.4 Moments of the Distribution 126
5.4 Non-gravitating Ring Systems 128
5.5 Gravitating Ring Systems 131
5.6 Summary 136

6 Summary 137

7 Concluding Remarks and Outlook 143

A Some Kinetic Theory 145
A.1 The Liouville Operator 145
A.2 The pseudo-Liouville Operator 146
A.3 Ensemble Averages 147
A.4 Collision Frequency 149
A.4.1 ... in the Absence of Long Range Forces 150
A.4.2 ... in the Presence of Repulsive Long Range Forces 151
A.4.3 ... in the Presence of Attractive Long Range Forces 151
A.5 Kinetic Energy 153
A.5.1 ... in the Absence of Long Range Forces 155
A.5.2 ... in the Presence of Repulsive Long Range Forces 155
A.5.3 ... in the Presence of Attractive Long Range Forces 155
A.6 The Dilute Limit 156
A.7 More about the pseudo-Liouville Operator 157
A.8 Effective Particle Radius 159

B Multipole Expansion 161

C Pair Distribution Function 167

References 169

Acknowledgements 179

Curriculum Vitæ 181

1 Introduction

Many-body systems consist of many particles interacting with each other through forces. Depending on the particle size[1], we deal with systems that can be described by a quantum-mechanical approach or by the laws of classical mechanics. In the latter case, particles are macroscopic in size, and an inherent feature of these particles is their capability to dissipate kinetic energy during mechanical contacts.

In this thesis, we will exclusively deal with the simulation of macroscopic dissipative particle systems. These particle systems are commonly referred to as *granular media* and are – from the point of view of modern physics – complex systems far from thermodynamic equilibrium since they do not obey the energy conservation law. Earliest scientific research on granular media was carried out by *C.A. de Coulomb* in the eighteenth century, *G. Hagen* (1852), *O. Reynolds* (1885) and much more recent by *R.A. Bagnold* (1954).

Granular media occur in our daily life in the form of sand at the beach, pharmaceutical pills, pebbles used for constructing streets and buildings, or simply cereals we eat for breakfast. The behavior of granular media under gravity is manifold, and it depends on its packing density whether it behaves like a solid, a liquid [66] or a gas. Granular media with high densities are encountered in industrial sintering where they form extremely rigid solids. In other processes, the knowledge about the flow behavior of a more dilute granular medium such as suspensions or pastes is important. Furthermore, the behavior of a dilute assembly of granules under gravity controls, e.g., landsliding and debris avalanches.

In this thesis, we will mainly deal with dilute granular media, commonly referred to as *granular gases* which are not subject to gravity (or at least subject to a vanishing external net force).

Naturally occurring granular gases are planetary rings in which the gravitational force towards the central planet acting on the particles is balanced by the centrifugal force [11,31,37,87,130]. Vertically shaken or heated containers filled with granules under gravity [29, 83] are another example of granular gases. The *one component plasma* [7, 57] is composed of positive ions with a negatively charged background of free electrons that are smeared out in order to maintain a neutral net charge. These systems can be regarded as the elastic limit of a granular gas

---

[1] The most apparent difference between molecules and macroscopic granules is their size: molecular size ranges between Angstroms (molecular hydrogen) and some hundreds of nanometers (polymeric molecules) whereas the size of granules can be observed between a few microns (fine powders) and dozens of meters (icy rocks in planetary rings).

and represent an important practical example for the simulated elastic systems in this work.

Granular gases [13, 97] are dilute, thermodynamically open, systems for which the mechanical energy is persistently removed by dissipative collisions amongst the granules. In contrast to molecules, macroscopic granules will transfer kinetic energy into their internal structure, where it is irreversibly lost, e.g., it is used for the excitation of rotational and vibrational modes within the particles. Plastic deformation and heating or even fragmentation of the particles can be the consequence. Many collective phenomena due to the dissipative nature of a granular gas are observed, e.g., cluster instability and self-organization [34, 70, 75, 81, 85], deviation from the Maxwell-Boltzmann velocity distribution with constant and velocity-dependent coefficient of restitution [12–14, 114], phase transitions [30, 94] and the formation of vortices [68, 95].

All of the collective phenomena in molecular and granular systems are driven by particle-particle forces of different range. One has to understand the nature of these forces in order to go one step further and investigate the resulting phenomena. In the following, we discuss the fundamentals of classical mechanics and see how forces are regarded nowadays in natural sciences.

1.1 Forces in General

Forces have attracted our attention for centuries via the response of materials or objects that are exposed to them. Since the seventeenth century the nature of forces has been investigated scientifically (*I. Newton*, 1687 [91]; *H. Cavendish*, 1798). *Newton* distinguished between cause and effect of a force action. Every force of any origin that is imposed on a freely moving object will have influence on this object by accelerating it. The response of the object gives information about the magnitude and direction of the acting force.

Effects of forces can be observed in our daily life and the underlying forces can have various origins: a car that drives a curve experiences the centripetal force which is directed towards the center of the curve (and is a consequence of the static friction force (*C.A. de Coulomb*, 1781 [23]) between the tires and the ground) and holds the car on its path.

A dropping stone hits the ground and experiences repulsion otherwise it would penetrate. On the other hand, wind pushes a catboat in forward direction by blowing into the sails. In both cases, repulsion forces due to a quantum-mechanical exclusion principle (*W.E. Pauli*, 1924) are responsible for the momentum transfer between colliding molecules of the stone and the ground and between those of the air and the sails.

Gravitational forces towards the center of the earth pull the stone towards the ground and likewise prevent us from hovering into space and keep us on the

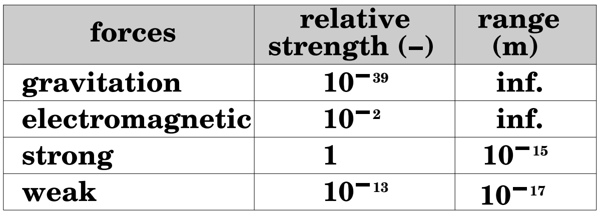

forces	**relative strength (–)**	**range (m)**
gravitation	**10^{-39}**	**inf.**
electromagnetic	**10^{-2}**	**inf.**
strong	**1**	**10^{-15}**
weak	**10^{-13}**	**10^{-17}**

Figure 1.1: All naturally occurring forces can be reduced to the four fundamental forces in physics.

ground. The same force makes the planets orbiting around the sun and allows for such huge cosmological structures like galaxies and clusters of galaxies. The range of the gravitational force is infinite.

Ferrimagnetic materials with permanent magnetic moments like the small magnets that pin shopping lists onto our refrigerators' doors are attracted by materials that contain iron via "magnetic" forces. On the other hand, electrically charged objects experience forces when exposed to electric (*C.A. de Coulomb*, 1785 [24]) and magnetic fields (*J.C. Maxwell*, 1864; *H.A. Lorentz*, 1895). These electromagnetic forces are responsible for, e.g., the occurrence of northern lights in polar regions of the earth and are technically used, e.g., in eddy current-retarders in modern trains for deceleration. Like gravitational forces, electromagnetic forces are of infinite range. In praxis, however, electromagnetic foces will never be of infinite range because of shielding. This leaves the gravitational force as the only force of true infinite range.

Moreover, we perceive the power of chemical binding forces if we break solid materials apart or if we ignite chemical explosives like fireworks New Year's Eve. Chemical binding forces are much weaker than the nuclear binding forces which make the atomic nuclei stable. The nuclear force is used and controlled by today's nuclear power plants and is also responsible for the energy production in the centres of stars like the sun and appears as the most powerful force in nature. In contrast to the gravitational and electromagnetic force, it is very short ranged (*H. Yukawa*, 1935).

So far, we have spoken about a huge variety of forces which seem to be completely different. But they can indeed be reduced to some few fundamental forces[2]. Nowadays, theoretical physicists know four fundamental forces in nature (see Fig. 1.1) which are completely different in origin, range and strength. The gravitational force is the weakest fundamental force in nature. Only because it cannot be screened it appears to us to be strong in everyday life. At very short distances, i.e., in case of molecular bonds between atoms, the electromagnetic forces

---

[2] An introduction to elementary particle physics and to the fundamental forces can be found under *http://www.cern.de.*

name	*van-der-Waals* attractive contribution	range
Keesom force	permanent dipole – permanent dipole	$-p_i^2 p_j^2/(kTr^7)$
Debye force	permanent dipole – induced dipole	$-p_i^2 \alpha_j/r^7$
London force	temporary dipole – temporary dipole	$-\alpha_i \alpha_j I_i I_j/\big((I_i+I_j)r^7\big)$

Table 1.1: $\boldsymbol{p}$ is the permanent dipole moment, α the electronic polarizability and I the ionization (excitation) potential of an electronically polarizable molecule. k, T and r denote the Boltzmann constant, temperature of the system and the separation length between both molecules. The negative sign indicates the attractive nature of these forces – as convention, repulsive forces are positive.

exceed the gravitational forces by many orders of magnitude. Thus, concerning the breaking up and rearranging of chemical bonds during chemical reactions, the gravitational force can be neglected.

Chemical binding forces and all mechanical (repulsive) contact forces seem to be very different in nature but fundamentally they belong to the category of electromagnetic forces. Nuclear forces are the strongest forces and act only over distances comparable with the separation length of the nucleons, thus much shorter than the size of an atomic nucleus. On the other hand, the weak force is responsible for the β-decay of the neutron, with a range much shorter than that of the strong force.

Disregarding gravity as well as weak and strong forces, in the following we will focus on the category of electromagnetic forces which can affect the behavior of matter and its various forms of appearance on any length scale, before we turn to granular forces in subsection 1.3.

1.2 Intermolecular Forces

Intermolecular forces are electromagnetic or – more precisely – electrostatic forces, which determine a variety of phenomena such as the behavior of solids and fluids. The most famous electrostatic force is the conservative Coulomb force, which acts between electrically charged particles as $1/r^s$, where r is the distance between the two particles and s is a power that describes range and magnitude of the potential. The strongest possible forces with $s = 2$, however, only act between charged particles that are point particles (e.g., in ionic crystals) or appear as point particles from far away. In fluids, such as real gases or aqueous solutions, generally $s > 2$. Commonly, the value of s depends on both the spatial charge distribution within the molecules involved in the interaction process and their polarizability. So, the interaction between permanent and induced dipole moments in molecules are the origin of the so-called *van-der-Waals*-forces (vdW) and the range is typically $s = 7$. The corresponding equation of state for imperfect gases (*J.D. van der Waals*, 1873) takes these into account, causing differences with the perfect gas law. An application of the equation of state to biological systems can be found, e.g., in Ref. [129]. In the following we will discuss the origin of these forces and their s-values in more detail.

The interaction force between two polar molecules (with permanent dipoles $\boldsymbol{p}_i$ and $\boldsymbol{p}_j$) is called the *Keesom*-force (*W.H. Keesom*, 1921) and depends on the strength of the dipoles and on the thermal energy kT in the system. At low temperatures, the ability of molecules to orient themselves relative to each other such that they experience attraction is increased. For high temperatures, this ability is limited because the strong random movement of the molcules makes an ordered orientation less likely.

Attraction forces between polar and non-polar molecules are different in power but of the same range as the Keesom-forces. A molecule with a permanent dipole moment, $\boldsymbol{p}_i$, can induce a dipole moment in a non-polar particle with polarizability α_j by displacing its spatial electronic distribution from the positively charged nucleus. This results in an attractive interaction force, referred to as the *Debye*-force (*P.J.W. Debye*, 1912) between permanent and induced dipole moments. This force depends on the permanent dipole moment $\boldsymbol{p}_i$ of the first and the electronic polarizability α_j of the second molecule.

The third possibility of having attractive interactions with range $1/r^7$ stems from the interaction between two temporary dipole moments, i.e., from the interaction between two similar non-polar molecules, each with polarizability α. These forces, e.g., explain the condensation of non-polar gases to liquids such as liquid helium or liquid benzene and are stronger [58] than the forces mentioned above. Quantum-mechanically, the spatial electron charge distribution around the molecule changes rapidly due to the moving electrons and leads to a temporary dipole moment. This induces an instantaneous dipole moment within a nearby non-polar molecule. This leads to a mildly attractive interaction between both molecules. It is obvious that the size of the electron cloud influences the interaction strength and the larger the molecules the stronger is their polarizability and the stronger the attraction. Besides this, also the ionization potential, I, affects the attraction strength. These forces are called *London* dispersion[3] forces (*F.W. London*, 1927). Further investigation of the London dispersion forces was described in Refs. [79, 80].

According to Ref. [32], all these types of forces are combined together to a net vdW-force that corresponds to a $1/r^7$-term. The interaction force between such

---

[3] *London* chose the term “dispersion” because the polarizability and, thus, the interaction force depends on many excitation frequencies (ionization potentials) of the molecule wherein a temporary dipole is induced. If the local oscillating electrical field from the inducing temporary dipole provides these frequencies (primarily located in the near infrared, visible and ultraviolet part of the spectrum) the polarizability will increase strongly.

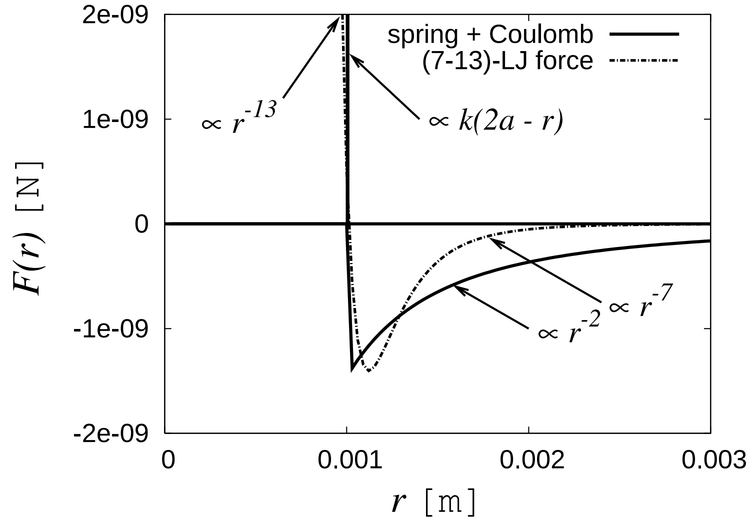

Figure 1.2: Comparing the widely used *Lennard-Jones*-force with a force model (spring + Coulomb force) typically used in this thesis (see section 4). k denotes the spring stiffness and $2a = 0.001$ m (at contact) the separation length of two particles, each with particle radius a, at force equilibrium.

molecules over the whole r-range is expressed by the *Lennard-Jones*-force (*J.E. Lennard-Jones*, 1931 [61, 65]). This force contains the attractive vdW-term for large distances, $1/r^7$, (see Tab. 1.1) and, additionally, the strong repulsive term for short distances, $1/r^{13}$, that takes the quantum-mechanical exclusion principle into account. The *Lennard-Jones*-force ("LJ") is also displayed in Fig. 1.2. With approximately the same global force minimum, the LJ force approaches zero much faster than the Coulomb force with increasing r. This illustrates the different range of different forces we deal with. The very long-range of Coulomb forces are a challenge for numerical simulations as it will be shown in section 3. The vdW-forces are a small part of the huge variety of electrostatic forces that contribute to the common category of attractive *cohesive* and *adhesive*[4] forces. Other attractive electrostatic forces act via *hydrogen bonds* [58,60] which are usually stronger than a typical vdW-bond and are, e.g., responsible for the unusual behavior of water to have a lower density in its solid state than in its liquid state. More examples are *metallic bonds* in metals and the *covalent atomic bonds* which hold together the atoms within all molecules. On the microscopic level, both cohesive and adhesive forces are of the same origin, i.e., they are electrostatic intermolecular forces such as vdW-forces. Adhesive forces act between molecules

---

[4] from Latin: *co* + *haerere* - to cohere, to cleave, to stick together; *ad* + *haerere* - to adhere, to stick, to be attached

of different surfaces or phases (e.g., varnish sticks on the car's surface or the glue holds two pieces of paper together) whereas cohesive forces occur between molecules of the same material. The interplay of both determines the *wetting* behavior of surfaces (see *Lotus effect* which denotes a very weak wettability [17]) and the *capillary* forces in porous media. Cohesion alone, e.g., can explain the *surface tension* of liquid surfaces.

1.3 Intergranular Forces

Analogous to the elastic exclusion forces, which are common for atoms in solids, liquids and gases, as described above, colliding macroscopic particles, such as grains, exert repulsive forces and – in addition – inelastic or *dissipative* forces [25, 98]. These forces reduce the kinetic energy of both particles from its pre-collisional value by a factor which is in theory related to the coefficient of restitution, that describes the material property. Energy loss is the result of the conversion of kinetic energy into internal degrees of freedom of the grains, i.e., into heating and *plastic deformation*, taking place at contact, see section 1.3.1. In contrast, long-range forces are typically conservative – either attractive or repulsive, see section 1.3.2.

1.3.1 Contact Forces

Contact interactions between macroscopic particles are understood as pairwise mechanical forces, neglecting electromagnetic and gravitational (long-range) forces. In the context of the fundamental forces discussed above, mechanical contact and friction forces (atomic friction, *G.A. Tomlinson*, 1929 [123]) are grouped into the category of electromagnetic interactions, since they are due to the electromagnetic forces acting between the atoms of the outermost atomic layers of two bodies in contact. This microscopic point of view, however, is not helpful to describe intergranular forces between macroscopic particles as shown in the following.

The assumption of small deformation, no fragmentation, no significant heating of the particles and the preservation of their spherical shape after many collisions (which is not necessarily the case, see Ref. [15]) leads to simple models for treating mechanical interactions between macroscopic particles, both theoretically and numerically. Some of these *viscoelastic*[5] models are introduced now.

The complicated movement of both particles in their centre-of-mass system is

---

[5] Viscoelasticity means that during the collision particles dissipate kinetic energy (viscous behavior) and after the collision they recover their spherical shape (elastic behavior). The term "elastic" here is not to be confused with the case of elastic simulations in chapter 4 where the coefficient of restitution equals unity.

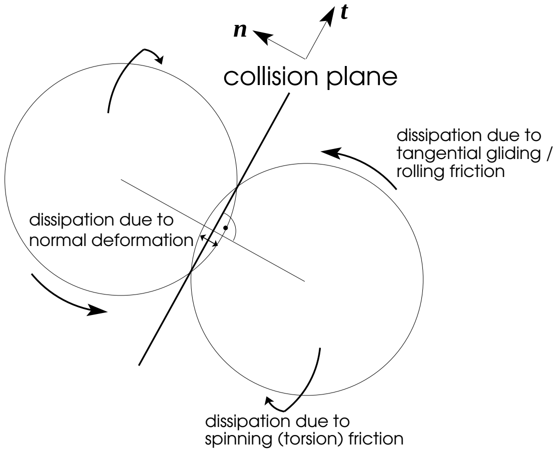

Figure 1.3: Geometry of collision of two spherical particles of identical radius. The collision plane is perpendicular to the center-to-center vector. Sliding, rolling and torsion "friction" is not applied in the simulation of our particle systems in this thesis.

typically simplified by splitting motion into normal $\boldsymbol{n}$ and tangential $\boldsymbol{t}$-direction relative to their collision plane (Fig. 1.3). This leads to the consideration of the coefficients of *normal* and *tangential restitution*. Normal dissipation can result from plastic deformation, and tangential dissipation from Coulomb friction between the particles' rough surfaces.

Two models which represent viscoelastic interactions in normal direction are known as the *linear spring-dashpot* (LSD) and the *non-linear Hertz*-model with various viscous forces. In the former the force varies linearly with the "deformation" in normal direction and in the latter the force behaves non-linearly [13, 50, 69, 98]. Both experiments [11] and theory [14] have shown that the restitution coefficient depends on the normal relative impact velocity, i.e., it was found that it decays with increasing impact velocity. In particular, it is shown [101] that a constant coefficient is indeed inconsistent with the theory of dissipative bodies. An analytical closed form for the velocity dependent normal coefficient of restitution which is based on the well-known *Hertz*-law can be found in Refs. [13, 114]. Many analytical results in continuum mechanics and kinetic theory of granular systems simplify drastically if we assume a constant coefficient of normal restitution. So, many numerical experiments with a constant coefficient using the LSD and Hertz model were performed [34, 76, 82] in order to justify the simplified continuum results[6]. A more realistic model for normal contact forces using the LSD and allowing for plastic deformation of the particles is proposed in Ref. [128] and discussed in Refs. [71–74][7]. In the latter articles, the model also takes into account attractive adhesion forces in normal direction for very close particle encounters into account. The loading (particle penetration) and unloading process (particle releasing) corresponds to a piece-wise linear, hysteretic, adhesive force model in normal direction.

Tangential contact forces act in addition to the normal contact forces if both particles have rough surfaces, see Fig. 1.3. We do not discuss in details of friction forces, instead refer to literature dealing with rough particles and their rotation. The original formulation of Coulomb friction can be found in Refs. [23, 25] and for the tangential friction in simulations, we refer to Refs. [21,25,69,73,109]. Due to the low density of granular gases, the relative motion of the particles and the mean free path (as compared to the particle radius) are high enough in order to expect mainly binary collisions. Since tangential forces are less important in the dilute limit than in the case of dense gases, we use in this thesis only normal dissipation forces by means of the simplest available model, the LSD.

1.3.2 Long-Range Forces

In contrast to tangential forces, in dry dilute granular systems intergranular long-range forces are very important and act in addition to the mechanical short range forces described in the preceding subsection, even when both particles are not in physical contact anymore. In this sense, all the intermolecular forces briefly discussed in section 1.2 are denoted as long-range forces. Intergranular long-range forces are also electromagnetic in nature [8, 22], i.e., they obey the laws of both electrostatic and magnetic interactions. In the following, we focus on electrostatically interacting granular materials only because the occurrence of electrically neutral granular media in nature is the exception rather than the rule due to the fact that collisional electrification (charging) is widely observed. Note that gravitational long-range forces differ from $s = 2$ electrostatic forces in the sign and are applied especially in astrophysics.

Electrostatically charged granular media can be found in many technical processes in industry, e.g., granular pipe flow [131], electro-sorting in waste disposal processing [92], electrophotography in print processes [20, 53], electrostatical synthetics coating [63] and finally electrospraying of pesticides in greenhouses [2, 33, 88]. Electrostatically charged macroscopic solid particles can be obtained by procur-

---

[6] For the sake of simplicity, in this thesis we perform simulations with constant coefficient of restitution only.

[7] In this model, the particle shape remains physically conserved but the repulsive force stops acting **before** both particles detach and leads to the impression that the spheres have plastically deformed.

ring mechanical contacts between them [67, 90] under dry conditions. *Triboelectrification*[8] is mostly applied but its theoretical fundamentals are poorly understood. The electrification (charging) of materials by contact depends, of course, strongly on the material properties, whether we deal with conductors, insulators or semi-conductors. The reason for the strong electrification ability of insulators compared with conductors can be explained by their weak conductivity for electrical charges. In case of insulators, the induced charges cannot flow back that easily from the insulator's surface as compared to a conductor. That is why one can induce charges on an insulator more and more by rubbing (repeatedly contacting) whereas for conductors rubbing will not lead to higher electrostatic charge than a single contact would. Finally, the intensity of the charge transfer depends on the work functions of the materials, their conductivity and the geometrical arrangement of the contact surfaces. For deeper understanding of these material properties we refer to textbooks on solid state physics such as Ref. [62]. In the following, however, we do not consider the process how granular materials are charged, i.e., the charge is supposed to be an inherent and constant property of the particles.

1.4 Organization of the Thesis

In this work we deal with both the numerical and theoretical investigation of long-range potentials in discrete many-body systems. One aim is the development of a new algorithm for a Molecular Dynamics type of method. This algorithm should be able to handle long-range interactions between the particles as accurate and efficient as possible in order to compete with the traditional algorithms available on the scientific "market". The presented algorithm is based on the linked cell neighborhood search, as proposed in Ref. [1], and hierarchically combines linked cells together to superior cells. A multipole expansion of the charge (mass) distribution in the superior cells forms pseudo particles that act on the particle of interest.

Furthermore, we will make an effort to extend the theory on short range forces developed in Ref. [43] (this theory only takes into account mechanical collisions between the particles), for long-range forces. In Ref. [111] a theory for $1/r$ repulsive long-range potentials has already been derived from a phenomenological point of view but as far as we know, a more rigorous theory on both repulsive

---

[8] from Greek: *tribein* - rubbing. There are triboelectric series of materials obtained by contacting synthetics with each other and measuring the polarity after the electrostatic induction process. An arbitrary material of the series will experience negative charging by contacting a material listed above and positive charging by being in contact with a material listed below. The charging effect is stronger the farther both materials are listed from each other.

and attractive long-range forces is lacking. The third part of the thesis describes the application of the theory to the results obtained through the simulation of homogeneous particle systems and the application of the hierarchical linked cell numerical method to ring shaped particle systems.

The organization of the thesis is as follows:

Chapter 2 considers the implementation of the hierarchical linked cell algorithm. By means of examples of particle constellations far away from a test particle, we will conclude in which way it is most efficient to carry out the multipole expansion. This gives us information about the construction of the hierarchical linked cell structure.
Chapter 3 contains an overview of the conventional algorithms for $1/r$ long-range potentials used in many fields of research such as in astrophysics, biophysics or medical sciences. We explain their functionality, advantages and disadvantages and finally introduce the hierarchical linked cell algorithm as implemented.
In *Chapter 4* we will consider the time evolution of rather small dilute dissipative particle systems in presence of both repulsive and attractive $1/r$ long-range interaction potentials. We present a theory for predicting the time evolution of these systems, assuming the systems to be homogeneous. The results of the numerical simulations are compared with the theoretical results. The former results are obtained by the straightforward but highly time-consuming method of direct summation that generates most accurate results. Subsequently, the hierarchical linked cell algorithm will be benchmarked and compared with the direct summation method.
Finally, in *Chapter 5*, the hierarchical linked cell algorithm is applied to the large-scale astrophysical example of a ring-shaped particle system around a central mass involving also the $1/r$ self-gravity potential of the ring particles. Ring-shaped particle systems orbiting around central objects such as planets or stars represent annular flows of granules with different orbiting velocities, depending on the distance from the central object. Here, we focus on the macroscopic kinematic viscosity parameter of a dynamically broadening ring system composed of many particles. How the interplay between dissipative collisions and long-range attractive forces will affect the viscous behavior of such dynamical annular flows, will be illustrated by a few examples.
After summary and concluding remarks in *Chapters 6* and *7*, the appendices provide the basic mathematical framework needed to derive the theoretical results used.

2 Long-Range Forces

In this chapter, long-range forces are introduced for particle pairs and then discussed, especially for particles, which can be grouped to so-called distant pseudo particles. A multipole expansion of the masses (charges) is discussed by means of simple particle test constellations. Finally, we introduce the physics of a simple two particle collision in the presence of a mutual long-range potential.

2.1 Long-Range Forces in General

Two particle long-range potentials have the general form:

$$\phi_{ij}(r_{ij}) = -kc_ic_j\frac{1}{r_{ij}^s} \quad , \tag{2.1}$$

where $s \geq 1$. Main subject of this thesis is long-range interactions with $s = 1$. This corresponds to the (most challenging) longest possible range occurring in nature and appears between charge and mass monopoles. Other naturally occurring examples are molecule interactions with $s = 3$ and can be found between dipole molecules that interact with a permanent dipole moment. Moreover, there are also dipoles that are induced by other dipoles and the interaction law then corresponds to $s = 6$. This interaction is also referred to as the mildly attractive *van der Waals*–law.

In Eq. (2.1), particles i and j influence each other over a distance $r_{ij} = |\boldsymbol{r}_i - \boldsymbol{r}_j|$, where $\boldsymbol{r}_{ij}$ is directed from particle j towards particle i, with the resulting force

$$\boldsymbol{F}_i = -\nabla\phi_{ij} \quad . \tag{2.2}$$

Therefore, $\boldsymbol{F}_{ij}$ is “conservative”, because $\nabla \times \boldsymbol{F}_{ij} = \nabla \times \nabla\phi_{ij} = \boldsymbol{0}$. This means, that the work done for moving a particle between two points is independent of the path it is moved along but depends on its starting and ending points only[1]. A particle j that starts travelling from infinity, $r_{ij}^{(0)} = +\infty$, and approaches a particle i up to the new distance $r_{ij}^{(1)}$ has done some work against the potential, which corresponds to a potential difference $\phi_{ij}(r_{ij}^{(1)}) - \phi_{ij}(r_{ij}^{(0)})$. Defining that the

---

[1] In contrast, dissipative forces do depend on the length of the path, e.g., frictional forces accumulate more work the longer the path along which they act.

potential at infinite distances vanishes, i.e., $\phi_{ij}(r_{ij}^{(0)} = +\infty) = 0$, the potential difference leads us then to Eq. (2.1). Inserting Eq. (2.1) in Eq. (2.2) gives the long-range force acting on particle i

$$\boldsymbol{F}_i(r_{ij}) = -skc_ic_j\frac{\boldsymbol{r}_{ij}}{r_{ij}^{s+2}} \quad . \tag{2.3}$$

All vectors with two indices in this thesis will be directed to the particle indicated by the first index, so that the *action=reaction*-rule, i.e., $\boldsymbol{F}_{ij} = -\boldsymbol{F}_{ji}$ and thus momentum conservation is guaranteed. k is a constant that distinguishes the following two cases.

2.1.1 Gravitational Forces

For the force in Eq. (2.3) the particle quantities c_i and c_j are important. In the case of gravitation ($s = 1$), we deal with masses, so $c_ic_j = m_im_j > 0$. Furthermore, the constant k has to be specified: according to our convention, $k = G = 6.67 \cdot 10^{-11}$ $\mathrm{m^3s^{-2}kg^{-1}} > 0$ leads to the fact that masses attract each other gravitationally. G denotes the gravitational constant and was originally experimentally found and introduced in Ref. [91]. Thus, Eq. (2.3) takes the known form

$$\boldsymbol{F}_i(r_{ij}) = -G\frac{m_im_j}{r_{ij}^3}\boldsymbol{r}_{ij} \tag{2.4}$$

and is called the *Newton* law; it describes situations where masses influence each other. If one of the mass, say m_i, is much smaller than m_j, m_j is assumed to be immobile and the force acting on m_i is $\boldsymbol{F}_i = -m_i\boldsymbol{g}$. Here is $\boldsymbol{g} = Gm_j\boldsymbol{r}_{ij}/r_{ij}^3$, the gravitational acceleration towards the center of the mass m_j.

2.1.2 Coulomb Forces

In Electrodynamics, the charges of the particles are the relevant quantity, i.e., $c_ic_j = q_iq_j$. Equally charged particles, $q_iq_j > 0$, repel each other while unequally charged particles, $q_iq_j < 0$, attract each other. It was experimentally shown that $k = -1/(4\pi\varepsilon_0) = -8.99 \cdot 10^9$ $\mathrm{m^3s^{-2}kg(As)^{-2}} < 0$. Thus, Eq. (2.3) takes the form

$$\boldsymbol{F}_i(r_{ij}) = \frac{1}{4\pi\epsilon_0}\frac{q_iq_j}{r_{ij}^3}\boldsymbol{r}_{ij} \tag{2.5}$$

and is called the *Coulomb* law in honour of its discoverer, see Ref. [24]. ε_0 denotes the permittivity in vacuum.

Both the *Newton* and the *Coulomb* laws are fundamental natural laws in physics describing completely different natural phenomena while differing mathematically in the sign of k only. By our convention, attractive potentials ($k > 0$), Eq. (2.1), are always negative, repulsive potentials ($k < 0$) are positive.

2.2 Close-by Single Particles

As we will see in section 3.6.2, close-by particles are defined to be inside the inner cut-off sphere around the particle of interest (*poi*) and contribute separately to the total force that acts on the *poi*.

The collision dynamics of two approaching (single) particles i and j with charges or masses $c_i \neq c_j$, reduced mass, $m_{\mathrm{red}} = m_i m_j/(m_i + m_j)$, and radii $a_i \neq a_j$ can fully be described in a plane so that polar coordinates can be used. The energy conservation law reads then

$$\frac{1}{2} m_{\mathrm{red}} \Big(v_n^2 + v_\varphi^2 \Big) - \frac{k c_i c_j}{r_{ij}} = \frac{1}{2} m_{\mathrm{red}} \Big({v'}_n^2 + {v'}_\varphi^2 \Big) - \frac{k c_i c_j}{r'_{ij}} \quad . \tag{2.6}$$

The unprimed quantities are those a long time before the collision (if both particles are infinitely far away from each other) and the primed quantities are those at the time when the particles collide. Then, it is $r_{ij} \to \infty$, $v_\varphi \approx 0$ and $r'_{ij} = a_i + a_j$, $v'_n = 0$, $v'_\varphi = 0$. We obtain for the normal relative velocity

$$v_{n,cr} = \left(\frac{2 k c_i c_j}{m_{\mathrm{red}} (a_i + a_j)} \right)^{1/2} \quad , \tag{2.7}$$

which we can consider as a critical normal relative velocity. For the case of two particles with a repulsive potential, the *velocity barrier*, $v_{n,cr} = v_{n,b}$, is the lower limit for the particles' relative approach velocity in order just to have a collision. Inversely, for the case of two particles with an attractive potential, we have the *escape velocity*, $v_{v,cr} = v_{n,e}$, which is the upper limit for the particles' relative separation velocity in order just to collide. Both conditions make only sense if the condition for the maximum impact parameter, $b_{\max}$, is fulfilled as well. Two particles without long-range interactions will collide, irrespective how large their approaching velocity, v_n, is as long as their impact parameter, b, is below the maximum impact parameter $b_{\max} = a_i + a_j$, see Fig. 2.1 (a). The potential dependent maximum impact parameter, derived from the conservation laws of energy and angular momentum [51, 99], reads

$$\frac{b}{a_i + a_j} \quad \leq \quad \frac{b_{\max}}{a_i + a_j} = \left(1 + \frac{k c_i c_j / (a_i + a_j)}{\frac{1}{2} m_{\mathrm{red}} v_{ij}^2} \right)^{1/2} = \left(1 - \frac{E'_{\mathrm{pot}}}{E_{\mathrm{kin}}} \right)^{1/2} \quad . \tag{2.8}$$

In presence of long-range repulsive interactions, the potential energy at contact, E'_{pot}, equals the potential barrier, E_b, two approaching repulsive particles have to overcome in order to collide. The impact parameter will be reduced, see Fig. 2.1 (b). In presence of attractive interactions, $E'_{\mathrm{pot}} = E_e < 0$, it will be extended, see Fig. 2.1 (c), because the particles attract each other and the probability for a collision is increased. E_e denotes the escape energy barrier, two particles have to

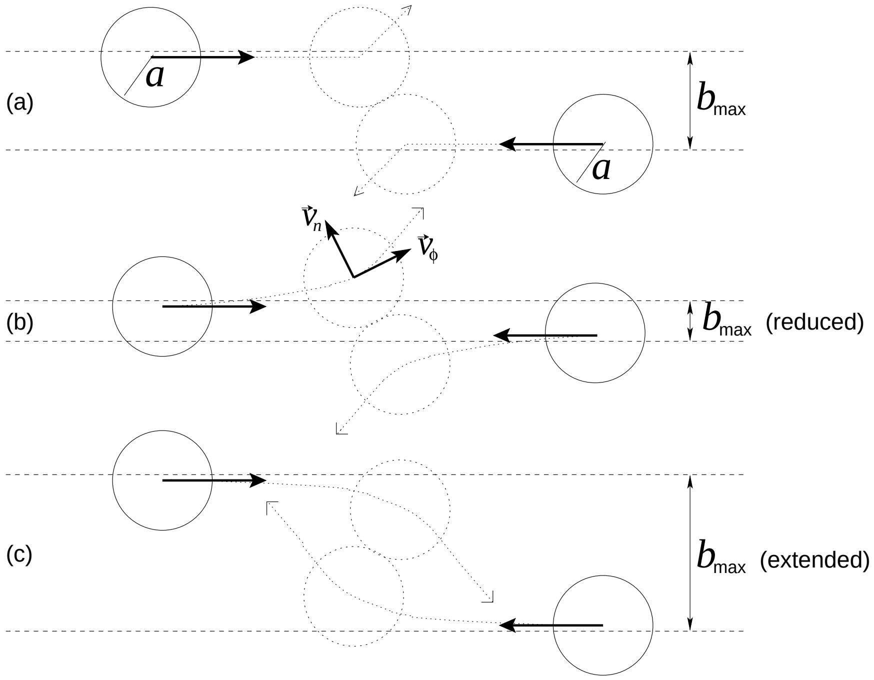

Figure 2.1: The initial impact parameter, b, has to be less than the maximum allowable impact parameter, $b_{\max}$, for which a collision just can occur. For repulsive particles, $b_{\max}$ is reduced (b), for attractive particles, $b_{\max}$ is extended (c) compared with the case without long-range forces (a). $b_{\max}$ is defined by Eq. (2.8).

overcome in order not to collide. In case of attractive particles (long-range forces are gravitational forces due to the presence of masses), we have for mono-disperse particle systems ($m_i = m_j = m$ and $a_i = a_j = a$)

$$k > 0 : \qquad v_{n,e} = \left(\frac{2|k|m}{a}\right)^{1/2} \qquad \text{and} \qquad \frac{b_{\max}}{2a} = \left(1 + \frac{2km}{av_{ij}^2}\right)^{1/2} . \tag{2.9}$$

In case of repulsive forces (long-range forces are electrostatical due to homogeneously charged particles), we have for mono-disperse and mono-charged particle systems ($q_i = q_j = q$)

$$k < 0 : \qquad v_{n,b} = \left(\frac{2|k|q^2}{ma}\right)^{1/2} \qquad \text{and} \qquad \frac{b_{\max}}{2a} = \left(1 + \frac{2kq^2}{mav_{ij}^2}\right)^{1/2} . \tag{2.10}$$

In this thesis, we use the following notations: the energy barrier for repulsive particles is denoted by $E_b = \frac{1}{4}mv_{n,b}^2 = |kc_ic_j|/(2a)$ and the escape energy for attractive particles is denoted by $E_e = \frac{1}{4}mv_{n,e}^2 = |kc_ic_j|/(2a)$. Note, that E_b and

E_e denote the same potential energy of both particles at contact, $r_{ij} = 2a$. In the numerical simulations in chapter 4, the $1/r$-long range potentials are either fully attractive or repulsive. For convenience, we use in both cases the same nomenclature as for attractive masses. In particular, in our numerical simulations we use Eq. (2.9) and set

$$k = -c_e G \ , \qquad \text{where } c_e < 0$$

for attractive forces, and use Eq. (2.10) and set

$$k = -c_b G \ , \qquad \text{where } c_b > 0$$

for repulsive forces. A very important quantity which gives information about when a charged many-body system is dominated by its Coulomb forces or by its thermal energy is the *coupling parameter* and represents the ratio of the two-particle Coulomb potential and the system's actual thermal kinetic energy, $E_b/mT_g(t)$ and $E_e/mT_g(t)$, respectively. m denotes the mass of the particles in a mono-disperse system and $T_g(t)$ the actual granular temperature, we will introduce later in chapter 4. High ratios describe a gas where the long-range forces are prominent whereas low ratios represent gases which are dominated by kinetic energy due to random motion of the particles and where the coupling of long-range forces to the system is rather weak. In the thesis, the coupling parameter or its reciprocal value is referred to as the *order parameter*.

2.3 Distant Pseudo Particles

Our model system has N particles. If we consider $N-1$ particles distributed around a selected *poi* i, all particles will contribute separately to the total force on i and we can write the total long-range interaction laws as

$$\begin{aligned} \phi_{ij}\Big(\{r_{ij}\}\Big) &= -kc_i \sum_j^{N-1} \frac{c_j}{r_{ij}} \quad , \text{ and} \\ \boldsymbol{F}_i\Big(\{r_{ij}\}\Big) &= -kc_i \sum_j^{N-1} c_j \frac{\boldsymbol{r}_{ij}}{r_{ij}^3} \quad , \end{aligned} \tag{2.11}$$

where $\{r_{ij}\}$ is the set of $N-1$ distances. Let us consider now a subset of n_α particles such that all the distances, $\boldsymbol{r}_{j\alpha}$, between the particles j within this ensemble α and an arbitrary point $\boldsymbol{P}^\alpha$ close to the ensemble are much smaller than the distance, $\boldsymbol{r}_{i\alpha}$, between particle i and $\boldsymbol{P}^\alpha$, see Fig. 2.2 (a).

The main idea here is grouping many particles together to a pseudo particle α, where only its distance to the *poi* has to be computed, but not anymore the

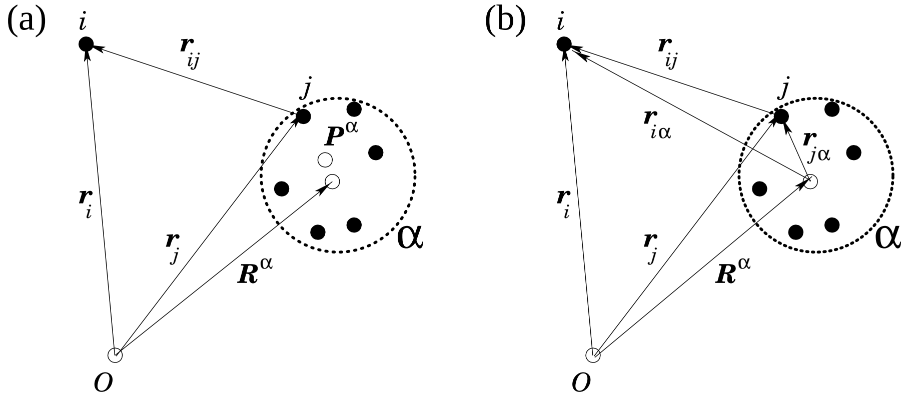

Figure 2.2: A typical situation in a system of discrete particles. O is the origin of the cartesian coordinate system, $\boldsymbol{P}^\alpha$ is a point close (or inside) the particle ensemble α (dotted circle) and $\boldsymbol{R}^\alpha$ denotes the geometrical center of α. As a reference point with distance $\boldsymbol{r}_{i\alpha}$ from i we can either use $\boldsymbol{P}^\alpha \neq \boldsymbol{R}^\alpha$ (a) or $\boldsymbol{P}^\alpha = \boldsymbol{R}^\alpha$ (b).

distances between the *poi* and all ensemble particles separately.
The inverse distance $1/r_{ij} = 1/|\boldsymbol{r}_{i\alpha} - \boldsymbol{r}_{j\alpha}|$ (for all $j \in \alpha$) in Eq. (2.11) can be expanded in a Taylor series which includes force contributions with different range, i.e., different powers of $1/r_{i\alpha}$

$$\begin{aligned}\phi_{i\alpha} &= \phi_{i\alpha}^{(M)} + \phi_{i\alpha}^{(D)} + \phi_{i\alpha}^{(Q)} + \phi_{i\alpha}^{(O)} + \ldots \\ \boldsymbol{F}_{i\alpha} &= \boldsymbol{F}_{i\alpha}^{(M)} + \boldsymbol{F}_{i\alpha}^{(D)} + \boldsymbol{F}_{i\alpha}^{(Q)} + \boldsymbol{F}_{i\alpha}^{(O)} + \ldots \qquad (2.12)\end{aligned}$$

as found in many textbooks, e.g., Refs. [59, 108]. Generally, the power series (2.12) are called “multipole expansions” of the long-range potential and force, respectively, and their terms are referred to as monopole (M), dipole (D), quadrupole (Q), octupole (O) terms, etc. For convenience and for our purpose, one can shift $\boldsymbol{P}^\alpha$ into the geometrical center of α, Fig. 2.2 (b), in order to simplify some of the equations below. Then, $r_{i\alpha} = |\boldsymbol{r}_i - \boldsymbol{R}^\alpha|$, where the geometrical center of α is defined by

$$\boldsymbol{R}^\alpha = \frac{1}{\sum_j^{n_\alpha} |c_j|} \sum_j^{n_\alpha} |c_j| \boldsymbol{r}_j \quad , \qquad (2.13)$$

which is independent of the signs of the $\{c_j\}$.
For a better illustration of the individual contributions from Eq. (2.12) at a particle of interest, in Fig. 2.3 different cases of a charge distribution “far” away from the *poi* are shown and will be discussed in the following. Configurations with equally charged particles represent spatially dispersed monopoles, cases (1) and (4), whereas those with unequally charged particles are spatially dispersed dipoles or multi-poles, cases (2), (3), and (5), where the centers of charge of the

positively and negatively charged particles are separated from each other. For these examples, we place $\boldsymbol{P}^\alpha$ both at the center of charge, $\boldsymbol{R}^\alpha$, and at the position of a member of α (shaded particle in Fig. 2.3), in order to study the influence of the position of $\boldsymbol{P}^\alpha$ on the force computations as well. The force multipole computation of Eq. (2.12) reads

$$\begin{aligned}
\boldsymbol{F}_{i\alpha}^{(M)} &= - \quad kc_i \frac{\boldsymbol{r}_{i\alpha}}{r_{i\alpha}^3} \sum_j^{n_\alpha} c_j \quad , \\
\boldsymbol{F}_{i\alpha}^{(D)} &= - \quad kc_i \left\{ \frac{3\boldsymbol{r}_{i\alpha}(\boldsymbol{r}_{i\alpha} \cdot \boldsymbol{p}^\alpha)}{r_{i\alpha}^5} - \frac{\boldsymbol{p}^\alpha}{r_{i\alpha}^3} \right\} \\
&= - \quad kc_i \frac{3\boldsymbol{r}_{i\alpha}}{r_{i\alpha}^5} \left(x_{i\alpha} \sum_j^{n_\alpha} c_j x_{j\alpha} + y_{i\alpha} \sum_j^{n_\alpha} c_j y_{j\alpha} + z_{i\alpha} \sum_j^{n_\alpha} c_j z_{j\alpha} \right) \\
&\quad + \quad kc_i \frac{1}{r_{i\alpha}^3} \sum_j^{n_\alpha} c_j \boldsymbol{r}_{j\alpha} \quad , \\
\boldsymbol{F}_{i\alpha}^{(Q)} &= - \quad kc_i \left\{ \frac{15\boldsymbol{r}_{i\alpha}\{\boldsymbol{r}_{i\alpha} \cdot (\mathbb{Q}^\alpha \cdot \boldsymbol{r}_{i\alpha})\}}{2r_{i\alpha}^7} - \frac{3\mathbb{Q}^\alpha \cdot \boldsymbol{r}_{i\alpha}}{r_{i\alpha}^5} - \frac{3\boldsymbol{r}_{i\alpha}\mathrm{Tr}\{\mathbb{Q}^\alpha\}}{2r_{i\alpha}^5} \right\} \\
&= - \quad kc_i \frac{15\boldsymbol{r}_{i\alpha}}{2r_{i\alpha}^7} \Bigg(x_{i\alpha}^2 \sum_j^{n_\alpha} c_j x_{j\alpha}^2 + y_{i\alpha}^2 \sum_j^{n_\alpha} c_j y_{j\alpha}^2 + z_{i\alpha}^2 \sum_j^{n_\alpha} c_j z_{j\alpha}^2 \\
&\qquad\qquad + 2x_{i\alpha}y_{i\alpha} \sum_j^{n_\alpha} c_j x_{j\alpha} y_{j\alpha} + 2x_{i\alpha}z_{i\alpha} \sum_j^{n_\alpha} c_j x_{j\alpha} z_{j\alpha} \\
&\qquad\qquad + 2y_{i\alpha}z_{i\alpha} \sum_j^{n_\alpha} c_j y_{j\alpha} z_{j\alpha} \Bigg) \\
&\quad + \quad kc_i \frac{3}{r_{i\alpha}^5} \left(x_{i\alpha} \sum_j^{n_\alpha} c_j x_{j\alpha} \boldsymbol{r}_{j\alpha} + y_{i\alpha} \sum_j^{n_\alpha} c_j y_{j\alpha} \boldsymbol{r}_{j\alpha} + z_{i\alpha} \sum_j^{n_\alpha} c_j z_{j\alpha} \boldsymbol{r}_{j\alpha} \right) \\
&\quad + \quad kc_i \frac{3\boldsymbol{r}_{i\alpha}}{2r_{i\alpha}^5} \left(\sum_j^{n_\alpha} c_j x_{j\alpha}^2 + \sum_j^{n_\alpha} c_j y_{j\alpha}^2 + \sum_j^{n_\alpha} c_j z_{j\alpha}^2 \right) \quad ,
\end{aligned} \tag{2.14}$$

and contains the dipole moment, $\boldsymbol{p}^\alpha$, and the quadrupole moments of α that are combined in the quadrupole tensor, $\mathbb{Q}^\alpha$. Eq. (2.14) is derived in appendix B in detail. For the computation we do not use octupole and higher order terms. The dipole moment is a vector sum and reads

$$\boldsymbol{p}^\alpha := \sum_j^{n_\alpha} c_j \boldsymbol{r}_{j\alpha} \quad .$$

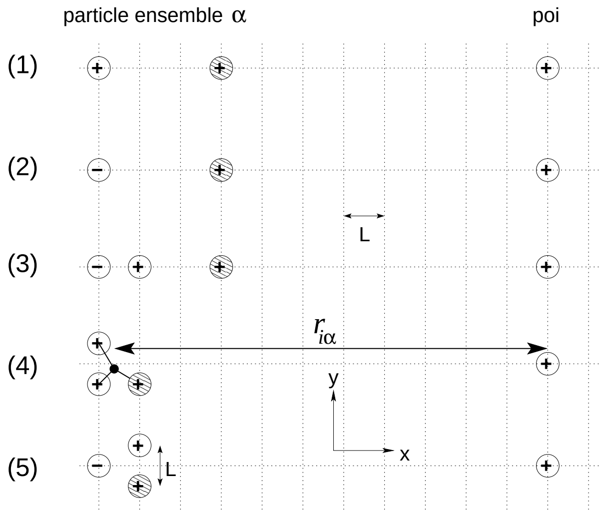

Figure 2.3: Different 2D charge configurations on the left represent different particle ensembles α far away from the particle of interest on the right. Table 2.1 shows the corresponding force contributions to the total force acting on the *poi*. The shaded particles give $\boldsymbol{P}^\alpha$ (case B) while the black dot indicates $\boldsymbol{R}^\alpha$ (case A).

It depends on the charge-weighted separation length of the centers of negative and positive charges. As soon as we deal with differently charged particles within α, we have to take care of non-vanishing dipole contributions. If the separation length is zero $\boldsymbol{p}^\alpha$ vanishes as well. According to our convention, the vector of the dipole moment is always directed towards the positive charges. The next higher order term is the quadrupole contribution of α which is represented by a set of elementary sums

$$\{q^\alpha_{ab}\} = \sum_j^{n_\alpha} c_j a_{j\alpha} b_{j\alpha} \quad ,$$

where $a_{j\alpha}, b_{j\alpha} \in (x_{j\alpha}, y_{j\alpha}, z_{j\alpha})$. There are nine possible combinations of $a_{j\alpha}$ and $b_{j\alpha}$ which are used in literature to be combined to the symmetric quadrupole tensor $\mathbb{Q}^\alpha$ of rank 2 with six independent entries $\{q^\alpha_{ab}\}$. The expression $\mathrm{Tr}\{\mathbb{Q}^\alpha\} = q^\alpha_{xx} + q^\alpha_{yy} + q^\alpha_{zz}$ denotes the trace of the tensor $\mathbb{Q}^\alpha$.

Examples (Special Cases)

For the sake of simplicity, we deal with $|c_i| = |c_j| = 1$ and $k = -1$ for computing the different force contributions in 2D where all particles are arranged in a plane, see Fig. 2.3. In table 2.1 the results are compared to the force, $\boldsymbol{F}_{ij}$, obtained

	$\boldsymbol{F}_i$ ($\times 10^{-3}$)	$\boldsymbol{F}_{i\alpha}$ ($\times 10^{-3}$)	Error	$\boldsymbol{F}_{i\alpha}^{(M)}$ ($\times 10^{-3}$)	$\boldsymbol{F}_{i\alpha}^{(D)}$ ($\times 10^{-3}$)	$\boldsymbol{F}_{i\alpha}^{(Q)}$ ($\times 10^{-3}$)
case A: $P^\alpha(x,y)$ is situated in the center of charges of α, $k=-1$, $\|c_i\| = \|c_j\| = 1$, $n_\alpha = 2, 3$						
(1)	(23.89, 0)	(23.82, 0)	0.3 %	(22.16, 0)	(0, 0)	(1.657, 0)
(2)	(7.361, 0)	(6.998, 0)	4.9 %	(0, 0)	(6.998, 0)	($0^{(*)}$, 0)
(3)	(17.36, 0)	(16.99, 0)	2.1 %	(10.70, 0)	(5.904, 0)	(0.382, 0)
(4)	(26.44, 0.498)	(26.43, 0.490)	1.6 %	(26.36, 0.412)	(0, 0)	(0.072, 0.078)
(5)	(11.66, 0)	(11.66, 0)	0.0 %	(9.365, 0)	(2.417, 0)	(-0.124, 0)
case B: $P^\alpha(x,y)$ is situated in the center of the shaded particle (within α), $k=-1$, $\|c_i\| = \|c_j\| = 1$, $n_\alpha = 2, 3$						
(1)	(23.89, 0)	(26.12, 0)	9.3 %	(31.25, 0)	(-11.72, 0)	(6.592, 0)
(2)	(7.361, 0)	(5.127, 0)	30.3 %	(0, 0)	(11.72, 0)	(-6.592, 0)
(3)	(17.36, 0)	(15.87, 0)	8.6 %	(15.63, 0)	(3.906, 0)	(-3.662, 0)
(4)	(26.44, 0.498)	(26.45, 0.539)	8.2 %	(29.89, 1.494)	(-3.821, -1.287)	(0.386, 0.332)
(5)	(11.66, 0)	(11.65, -0.041)	-	(9.962, 0.498)	(2.060, -0.345)	(-0.377, -0.194)

$^{(*)}$ quadrupole force contribution vanishes because of $q^\alpha_{xx} = 0$, according to Eq. (2.14)

Table 2.1: Forces calculated for the charge configurations displayed in Fig. 2.3, where $\boldsymbol{P}^\alpha$ coincides with $\boldsymbol{R}^\alpha$ (case A) and where $\boldsymbol{P}^\alpha$ is shifted to the center of the shaded particle (case B). Column 2 shows the results of direct summation, Eq. (2.11), column 3 the results of the multipole expansion, Eq. (2.14), and columns 5 to 7 the results of the monopole, dipole and quadrupole force terms separately. Column 4 gives the percentage of difference between column 2 and 3.

by direct summation, see Eq. (2.11). Let us pick out the one-dimensional case (3) and follow the computation of the multipole contribution to the force: the center of charge has the same y-component ($y = 3$) as the particles j. That is why all elementary sums vanish that include y-components. According to Fig. 2.3, assume

$$\begin{array}{ll} c_i = +1\ ,\ \boldsymbol{r}_i = \begin{pmatrix}1\\3\end{pmatrix} & c_{j=1} = -1,\ \boldsymbol{r}_{j=1} = \begin{pmatrix}-10\\3\end{pmatrix} \\ c_{j=2} = +1,\ \boldsymbol{r}_{j=2} = \begin{pmatrix}-7\\3\end{pmatrix} & c_{j=3} = +1,\ \boldsymbol{r}_{j=3} = \begin{pmatrix}-9\\3\end{pmatrix}\ , \end{array}$$

where the length is measured in units of L. Thus, $\boldsymbol{R}^\alpha = (-8.67,\ 3)$ and $\boldsymbol{r}_{i\alpha} = \boldsymbol{r}_i - \boldsymbol{R}^\alpha = (9.67,\ 0)$. Moreover, the vectors $\boldsymbol{r}_{(j=1)\alpha} = (-1.33,\ 0)$, $\boldsymbol{r}_{(j=2)\alpha} = (1.67,\ 0)$ and $\boldsymbol{r}_{(j=3)\alpha} = (-0.33,\ 0)$ are directed to the particles j and contain the information of their spatial distribution around $\boldsymbol{R}^\alpha$. The dipole and quadrupole moments of this charge configuration are

$$\boldsymbol{p}^\alpha = \begin{pmatrix}p_x^\alpha\\p_y^\alpha\end{pmatrix} = \begin{pmatrix}2.67\\0\end{pmatrix} \qquad \text{and} \qquad \mathbb{Q}^\alpha = \begin{pmatrix} q_{xx}^\alpha & q_{xy}^\alpha \\ q_{xy}^\alpha & q_{yy}^\alpha \end{pmatrix} = \begin{pmatrix} 1.1289 & 0 \\ 0 & 0 \end{pmatrix}\ .$$

The force contributions up to the quadrupole term for case (A3) are

$$\begin{aligned} \boldsymbol{F}_{i\alpha}^{(M)} &= -\quad kc_i \frac{\boldsymbol{r}_{i\alpha}}{r_{i\alpha}^3} \sum_j^{n_\alpha} c_j \approx (10.7 \times 10^{-3},\ 0)\ , \\ \boldsymbol{F}_{i\alpha}^{(D)} &= -\quad kc_i \frac{3\boldsymbol{r}_{i\alpha}}{r_{i\alpha}^5} x_{i\alpha} \sum_j^{n_\alpha} c_j x_{j\alpha} + kc_i \frac{1}{r_{i\alpha}^3} \sum_j^{n_\alpha} c_j \boldsymbol{r}_{j\alpha} \approx (5.9 \times 10^{-3},\ 0)\ , \\ \boldsymbol{F}_{i\alpha}^{(Q)} &= -\quad kc_i \frac{15\boldsymbol{r}_{i\alpha}}{2r_{i\alpha}^7} x_{i\alpha}^2 \sum_j^{n_\alpha} c_j x_{j\alpha}^2 + kc_i \frac{3}{r_{i\alpha}^5} x_{i\alpha} \sum_j^{n_\alpha} c_j x_{j\alpha} \boldsymbol{r}_{j\alpha} + kc_i \frac{3\boldsymbol{r}_{i\alpha}}{2r_{i\alpha}^5} \sum_j^{n_\alpha} c_j x_{j\alpha}^2 \\ &\approx \quad (0.38 \times 10^{-3},\ 0)\ . \end{aligned}$$

The sum of these contributions is $\boldsymbol{F}_{i\alpha} \approx (16.99 \times 10^{-3},\ 0)$ as we can read off from the table. Some general rules regarding a multipole expansion can be concluded from the table:

- **(i)** If the net-charge is zero, $\sum_j^{n_\alpha} c_j = 0$, then the monopole term vanishes, $\boldsymbol{F}_{i\alpha}^{(M)} = \boldsymbol{0}$, see cases (A2) and (B2)
- **(ii)** If all particles have the same sign *and* magnitude of the charges, the dipole term vanishes, $\boldsymbol{p}^\alpha = \boldsymbol{F}_{i\alpha}^{(D)} = \boldsymbol{0}$, provided $\boldsymbol{P}^\alpha = \boldsymbol{R}^\alpha$, see cases (A1) and (A4)
- **(iii)** If $\boldsymbol{R}^\alpha$ lies in a plane with all particles j (all cases except (A4), (B4) and (B5)) the out-of-plane components in the elementary sums vanish

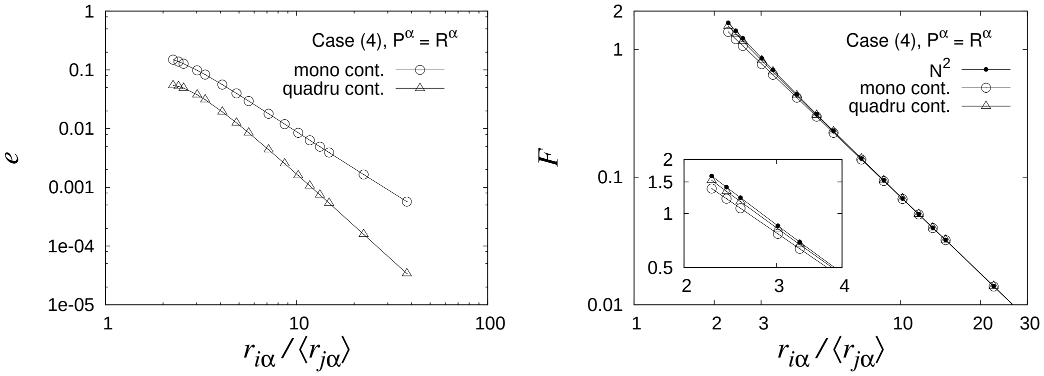

Figure 2.4: (Left) The error, e, shows the difference of the multipole contribution from the PP method and is plotted against the distance between the *poi* and the center of charge (mass) of the particle configuration (4) of Fig. 2.3. (Right) Log-log plot of the force, computed by direct summation (solid circles), by the monopole contribution only (open circles) and by the quadrupole contribution (triangles).

If the total charge vanishes, $\sum_j^{n_\alpha} c_j = 0$, the monopole contribution does as well (i). A typical example is the so-called *ion-(permanent) dipole* interaction[2] which is represented by the dominating dipole term in Eq. (2.14), i.e., force indeed goes with $\propto 1/r_{i\alpha}^3$ because $\boldsymbol{p}^\alpha$ in the numerator remains constant. This case corresponds to $s = 2$ in Eqs. (2.1) and (2.3).

Furthermore (ii), mono-charged particle distributions (all particles are either negatively or positively charged) will lead to a vanishing dipole contribution if $\boldsymbol{P}^\alpha$ is in the center of charge. Because then $\sum c_j \boldsymbol{r}_{j\alpha} = \sum c_j(\boldsymbol{r}_j - \boldsymbol{R}^\alpha) = \sum c_j \boldsymbol{r}_j - \sum c_j(\frac{1}{\sum |c_j|} \sum |c_j| \boldsymbol{r}_j) = \boldsymbol{0}$ (the sums consider all n_α particles in the pseudo particle α).

According to case (iii), the out-of-plane components of the dipole and quadrupole terms vanish if also the position of the *poi* is located within this plane.

Case (4) in Fig. 2.3 corresponds to the systems we simulate in chapter 4: all particles have the same c_j, are either repelling or attracting each other with the same mutual long-range force. For increasing distance between the *poi* and the pseudo particle, we expect the error of the multipole force contribution decreasing. In the left panel of Fig. 2.4, corresponding to the case (4), we have plotted the relative error, $e = \big||\boldsymbol{F}_{ij}| - |\boldsymbol{F}_{i\alpha}|\big|/|\boldsymbol{F}_{ij}|$, against the distance ratio, $r_{i\alpha}/\langle r_{j\alpha}\rangle$. For the case that the quadrupole force contribution is included in the force calculation,

---

[2] In literature [58], the potential of a spatially fixed permanent molecular dipole of two unequal charges $q_1 = q_2 = q_j$ with separation length l at the position of a point charge i obtained by direct summation is $\phi_{ij} = -kq_iq_jl\cos(\theta)/r_{i\alpha}^2 = -kq_iq_j\boldsymbol{l}\boldsymbol{r}_{i\alpha}/r_{i\alpha}^3 = -kq_i\boldsymbol{p}^\alpha\boldsymbol{r}_{i\alpha}/r_{i\alpha}^3$. This corresponds (case (A2) in table 2.1) to the dipole contribution, $\phi_{i\alpha}^{(D)}$, of the multipole expansion in Appendix B. Here, it is $\phi_{i\alpha}^{(D)} \neq 0$ and $\phi_{i\alpha}^{(M)} = \phi_{i\alpha}^{(Q)} = \phi_{i\alpha}^{(O)} = ... = 0$ because we have no charges with equal sign. θ is the angle between the vectors $\boldsymbol{l}$ and $\boldsymbol{r}_{i\alpha}$.

e drops stronger than for the case when it is excluded. As expected, multipoles including quadrupoles show a smaller error than if we neglect the quadrupole contribution. For small distances, e is large in both cases which results in a significant deviation of the force calculation from the direct summation method, see the inset of the right panel of Fig. 2.4. This is to be expected because at small distances the condition for the multipole expansion, $r_{i\alpha} \gg r_{j\alpha}$, is not fulfilled anymore. For the case $r_{i\alpha} \gg \langle r_{j\alpha} \rangle$, the monopole contribution is sufficient for the force calculation because e is in both cases small enough in order to represent the correct force. Note, that the case $r_{i\alpha} \gg \langle r_{j\alpha} \rangle$ also represents the possibility of a small spatially dispersed multipole at moderate distances $r_{i\alpha}$.

2.4 Summary

In this section we discussed long-range potentials and forces in general. We focussed on the longest ranged $1/r$ potential in nature, like the attractive gravitational force between large-scale mass points and the electrostatic forces between small-scale Coulomb charges. The computation of these forces can be carried out either by pair-wise summation or, alternatively, by a multipole expansion of the mass (charge) distribution.

The former one we approached with a detailed discussion of a two-particle collision in presence of long-range forces: for repulsive potentials, the relative approaching velocity of two particles has to exceed a minimum value, $v_{n,b}$, in order to overcome the repulsive barrier at contact. For attractive potentials, the relative separation velocity of two particles has to be smaller than a maximum critical value, $v_{n,e}$, in order to move back and to collide:

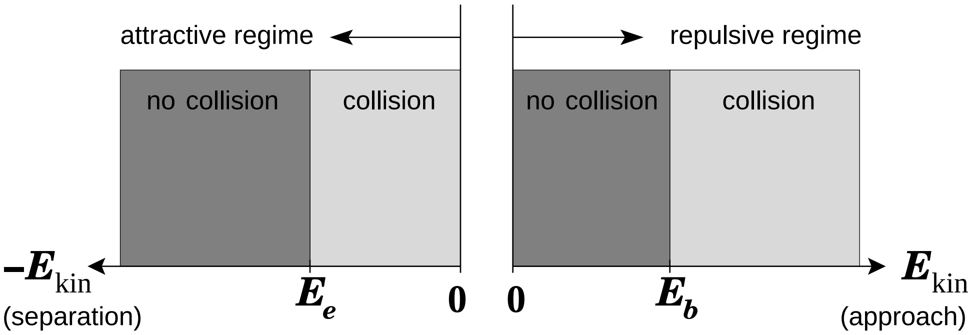

In the case of a multipole expansion, particles are grouped together and act as a huge pseudo particle on a single particle far away. This can be done if $r_{i\alpha} \gg r_{j\alpha}$, where $r_{i\alpha}$ denotes the distance of a particle i from a point close to the pseudo particle α, and $r_{j\alpha}$ are the distances of the particles inside the pseudo particle to the same point. As long as this condition is satisfied, the error in the computation of the force exerted by a pseudo particle on a particle of interest (and vice versa) is small. Therefore, an error estimation was carried out for some test pseudo particles with different $r_{i\alpha}$ and $r_{j\alpha}$. For large distance ratios, $r_{i\alpha}/\left\langle r_{j\alpha}\right\rangle$, (where $\left\langle r_{j\alpha}\right\rangle$ is the mean distance of the particles j from their center of mass) the error becomes smaller and also the influence of the quadrupole contribution in comparison to the monopole contribution becomes much less prominent. In this case, the charge (mass) distribution will act on the *poi* as a monopole. For small distances, both the $r_{j\alpha}$ and the error become important. Furthermore, in case of mono-charged particles it is sufficient to compute the monopole and quadrupole terms only if we set the point close to the pseudo particle into the center of charge (mass) of the pseudo particle. Then the dipole contributions vanish and the implementation will be less complex.

3 Computer Simulation

In this thesis we strictly divide forces into "short" and "long" range interactions because in computer simulations a "mechanical contact" is well-defined as we will see in Sec. 3.1.1. In this sense, short-range forces are active if a mechanical contact occurs. On the other hand, long-range forces are always active, even when there is no mechanical contact. To summarize, we define a force between two particles to be long-ranged if it is also active if there is no physical contact of the particles. Accordingly, we define a force to be short-ranged if it is only active during the duration of the mechanical contact.

Generally, due to the fact that most forces are defined by the distance between two particles, we have to compute the distances between all particles and *all* others. This turns out to be highly inefficient regarding the computational time spent in computer simulations. For short-range forces, a way to speed up the computation is to select only those particles which are close to the particle of interest (*poi*). These particles will obviously represent the near neighborhood around the *poi* and all other particles can be neglected. A problem arises if we want to compute permanently acting (long-range) forces between the *poi* and those particles which are outside of this near neighborhood. Then, we have to consider all other particles regardless of their distances to the *poi*.

A way out of this dilemma will be shown in the following sections (from section 3.3 on) which present a review of the common modeling techniques for long-range forces that reduce the number of distance computations without loosing too much accuracy. There are different ways to reduce the number of distance computations, which will be the main distinguishing feature of these techniques. Finally in section 3.6, we will introduce a new algorithm for long-range forces, the so-called Hierarchical Linked Cell algorithm, which is – on the technical and algorithmical side – the heart of this thesis. However, we start with describing in more detail the particle-particle method (see section 3.2), that will be bypassed by these techniques. Next, however, we will introduce to the Molecular Dynamics (MD) simulation method, in which all of these techniques can be implemented.

3.1 Molecular Dynamics

The force acting on a particle of interest is the most important quantity to be computed in a Molecular Dynamics (MD) environment as we will illustrate in the following. MD simulations were originally designed for the simulation of the motion of molecules as an approach for the understanding of N-body systems. The simulation provides the advantage to make any physical quantity "measurable" at any time such as the kinetic energy or potential energy or even the number of collisions per time unit. Such "measurements" can indeed hardly be performed in real experiments where the experimentalist is limited to the extraction of a few quantities only. Especially the way how MD works, i.e., the complete knowledge of the trajectory of any particle at any time, provides the knowledge of the dynamical situation of a certain particle in the system which is not possible at all for a real experiment that deals with a number of discrete molecules of the order of Avogadro's number.

In MD simulations, the position and velocity vector of each particle, $\boldsymbol{r}_i(t)$ and $\boldsymbol{v}_i(t)$, is calculated. With the additional knowledge of the particle mass, $m_i = (4/3)\pi\rho a_i^3$, and radius, a_i, we are able to solve *Newton*'s equations of motion for each particle i [1,21,44,54], i.e.,

$$\frac{\mathrm{d}^2\boldsymbol{r}_i(t)}{\mathrm{d}t^2} = \frac{\boldsymbol{F}_i(t)}{m} \quad . \tag{3.1}$$

Note, that in the simulations throughout this thesis we deal with mono-disperse particles of the same species ($m_i = m$, $a_i = a$). ρ is the material density of a particle and $\boldsymbol{F}_i(t)$ denotes all forces acting on particle i at time $t > 0$.

In MD simulations, t is discretized in narrow time windows (time steps), denoted by Δt which is taken constant here, and equation (3.1) will be integrated numerically by different solvers [1,102,105]. In our MD code we use *Verlet*'s algorithm [127] which is derived from a Taylor series of the position vector, $\boldsymbol{r}_i$, up to the second order. The resulting algorithm that integrates the equation of motion for particle i reads

$$\boldsymbol{r}_i(t+\Delta t) = 2\boldsymbol{r}_i(t) - \boldsymbol{r}_i(t-\Delta t) + \frac{\mathrm{d}^2\boldsymbol{r}_i(t)}{\mathrm{d}t^2}\Delta t^2 \quad , \tag{3.2}$$

where we use Eq. (3.1) for the second time derivative of $\boldsymbol{r}_i$. Simultaneously, we also compute the actual velocity of the particle,

$$\frac{\mathrm{d}\boldsymbol{r}_i(t)}{\mathrm{d}t} = \frac{1}{2\Delta t}\Big(\boldsymbol{r}_i(t+\Delta t) - \boldsymbol{r}_i(t-\Delta t)\Big) \quad , \tag{3.3}$$

which we use for the computation of the total kinetic energy of the system. t denotes the current time, $t + \Delta t$ is denoted by the time of the next and $t - \Delta t$ the time of the previous time step. Advanced algorithms for solving *Newton*'s equation of motion, e.g., solving the problem with means of multiple time steps, are presented in [41]. As we can see from Eq. (3.2), the knowledge of the position of particle i during the previous time step, of its current position and of the total currently acting forces on i is necessary for computing the position at the

new time. Knowing the new position, it is also possible to compute the current velocity of particle i, see Eq. (3.3).
In the following, we will discuss the forces that can act on the particles and we define to be short-range forces.

3.1.1 Contact Forces

Contact potentials between a particle i and a particle j are only active if the condition for contact is fulfilled. How do we define a "mechanical" contact between two particles in our computer simulation? While carrying out Eq. (3.1) in each time step, it can happen that the distance between the two particles is smaller than $2a$. I.e., we will detect a contact when the inequality

$$\delta(t) = 2a - \boldsymbol{r}_{ij}(t) \cdot \boldsymbol{n}_{ij}(t) > 0 \tag{3.4}$$

for mono-disperse particles is fulfilled. Here, $\boldsymbol{r}_{ij} = \boldsymbol{r}_i - \boldsymbol{r}_j$ is the distance vector and $\boldsymbol{n}_{ij} = (\boldsymbol{r}_i - \boldsymbol{r}_j)/|\boldsymbol{r}_i - \boldsymbol{r}_j|$ is the unit vector, which are directed towards i. If the inequality is fulfilled, the (positive) penetration depth (overlap), δ, is then related to a repulsive interaction force between two granules which depends linearly on δ. The model we use in our simulations corresponds to *Hooke*'s law and reads

$$\boldsymbol{F}_i^{\mathrm{coll}}(t) = k\delta(t)\boldsymbol{n}_{ij}(t) \tag{3.5}$$

in case of two particles in mechanical contact. k works as the spring constant and is proportional to the particle's material's modulus of elasticity. Note, that $\boldsymbol{n}_{ij}$ is perpendicular to the collision plane (see Fig. 1.3). The spring potential of Eq. (3.5) is $(1/2)k\delta(t)^2$ and the dynamics of the overlap corresponds to a spring like behavior. More details on this spring model describing a mechanical contact can be found in the next subsection and in [69, 109].
Real contact forces between macroscopic particles are not only composed of repulsive forces normal to the collision plane but also of forces tangential to the collision plane, such as friction forces. So, they have to be added to Eq. (3.5) in order to complete the collision force. In our simulations of dilute granular media we focus on in chapter 4, collisions do play a minor role because they do not occur very frequently as compared to the case of dense granular systems. So, we will not consider tangential forces throughout the whole thesis, neither do we consider the dynamics such as rotation of the particles that result from tangential forces.

3.1.2 Dissipative Forces

Similar to the repulsive contact forces, also dissipative contact forces only occur when two particles collide mechanically. Dissipative forces between granules make the dynamical behavior of granular gases different from that of molecular gases. Dissipative forces will extend the spring model in section 3.1.1 by the term

$$\begin{aligned}\boldsymbol{F}_i^{\mathrm{diss}}(t) &= -\gamma\big[\boldsymbol{v}_{ij}(t)\cdot\boldsymbol{n}_{ij}(t)\big]\boldsymbol{n}_{ij}(t) \\ &= \gamma\,\frac{\mathrm{d}\delta(t)}{\mathrm{d}t}\,\boldsymbol{n}_{ij} \end{aligned} \tag{3.6}$$

and diminish the repulsive forces. $\boldsymbol{v}_{ij}(t) = \boldsymbol{v}_i(t) - \boldsymbol{v}_j(t)$ denotes the relative velocity between both particles i and j. γ is a proportionality coefficient that is of empirical origin and has to be chosen such that the desired dissipation is obtained. With this dissipative force term and the spring term of Eq. (3.5), the dynamics of the overlap, δ, behaves like a damped oscillation that can be described by

$$\frac{\mathrm{d}^2\delta(t)}{\mathrm{d}t^2} + 2\mu\,\frac{\mathrm{d}\delta(t)}{\mathrm{d}t} + \omega_0^2\delta(t) = 0 \quad . \tag{3.7}$$

with eigen frequency, $\omega_0 = \sqrt{2k/m}$, of the undamped oscillator and a viscous term, $\mu = \gamma/m$. Hence, the damped frequency is $\omega = \sqrt{\omega_0^2 - \mu^2}$ and the contact duration reads

$$t_c = \frac{\pi}{\omega} \quad , \tag{3.8}$$

which is half of the total time period of the (damped) oscillation. As soon as the particles dissipate kinetic energy during their collision, the oscillation will be damped and the solutions of Eq. (3.7) read

$$\begin{aligned}\delta(t) &= \frac{\dot{\delta}(0)}{\omega}\,\exp(-\mu t)\,\sin(\omega t) \\ \dot{\delta}(t) &= \frac{\dot{\delta}(0)}{\omega}\,\exp(-\mu t)\big[-\mu\,\sin(\omega t) + \omega\,\cos(\omega t)\big] \quad . \end{aligned} \tag{3.9}$$

$\dot{\delta}(0)$ denotes the relative velocity of both particles at the beginning of the contact. The collision model described by the ordinary differential equation Eq. (3.7) is in literature referred to as the *linear spring-dashpot* model [69, 109]. For real particles, the dissipated kinetic energy will be transformed into deformation and heat within the colliding particles. In our simulations we do not allow for (elastic or plastic) deformation and possible fragmentation and simply remove dissipated kinetic energy from the system.

In simulations, large $\boldsymbol{v}_{ij}$ and γ can make the total contact force negative such that attractive short-range forces do occur. To avoid this unphysical situation, we therefore set in our MD code

$$\boldsymbol{F}_i(t) = \begin{cases} \big[k\delta(t) - \gamma\big(\boldsymbol{v}_{ij}(t)\cdot\boldsymbol{n}_{ij}(t)\big)\big]\boldsymbol{n}_{ij}(t), & \text{for } |\boldsymbol{F}_i^{\mathrm{coll}}(t)| > |\boldsymbol{F}_i^{\mathrm{diss}}(t)| \\ \boldsymbol{0}, & \text{for } |\boldsymbol{F}_i^{\mathrm{coll}}(t)| < |\boldsymbol{F}_i^{\mathrm{diss}}(t)| \end{cases} \quad . \tag{3.10}$$

One can quantify the dissipative character of a particle-particle collision by means of the so-called coefficient of restitution, r. It is defined as the ratio of the post (at time $t = t_c$) and the pre-collisional (at time $t = 0$) velocities in normal direction between two particles:

$$r = -\frac{\boldsymbol{v}_{ij}^{(n)}(t_c)}{\boldsymbol{v}_{ij}^{(n)}(0)} = -\frac{\dot{\delta}(t_c)}{\dot{\delta}(0)} \overset{(3.9)}{=} \exp\Big(-\frac{\pi\mu}{\omega}\Big) \quad \in \quad [0,1] \;\; , \tag{3.11}$$

where r approaches zero when the collision is highly inelastic and equals unity when the collision is completely elastic. Note, that $\boldsymbol{v}_{ij}^{(n)}(0) = -\boldsymbol{v}_{ij}^{(n)}(t_c)$. So, a simulation with $r = 1$ is referred to as an "elastic" simulation and does not lose any kinetic energy during its time evolution. Elastic N-body systems correspond to molecular gases, i.e., in particular, they exhibit a *Maxwell-Boltzmann*-distribution of the particles' velocities.

In the following, we will focus on the way how forces between molecules can be treated in computer simulations, that are much farther ranging than contact and dissipative forces.

3.2 Particle-Particle Methods (PP)

PP methods most straightforwardly calculate long-range forces. Actually, they perform a pair-wise (or direct) summation of all N particles in the system in order to obtain the forces from all other particles acting on the *poi*. For this, two loops have to be performed. The result will be $N(N-1)/2 \propto N^2$ force calculations. For large N, this is an extraordinary large effort, the CPU (central processor unit) has to spend in order to do all necessary calculations: i.e., we have for the particle-particle method

$$t_{\mathrm{CPU}} \propto \mathcal{O}(N^2) \;\; .$$

Many algorithms that compute long-range forces still use the PP method, but only for a subset $M \ll N$. This subset of particles represents the near neighborhood of the *poi* and is chosen such that the time expense will be $\mathcal{O}(MN)$, for more details see section 3.6.1. The rest of the particles will commonly be treated by tree or grid-based algorithms (see next sections) which reduce the computational complexity significantly. The PP method – even though prohibitively expensive for large N – will be used to provide reference data for small N, to which the new algorithm will be compared to.

3.3 Tree-Based Algorithms

Tree-based algorithms generally subdivide the simulation volume into hierarchically structured spatial regions wherein groups of particles are considered as

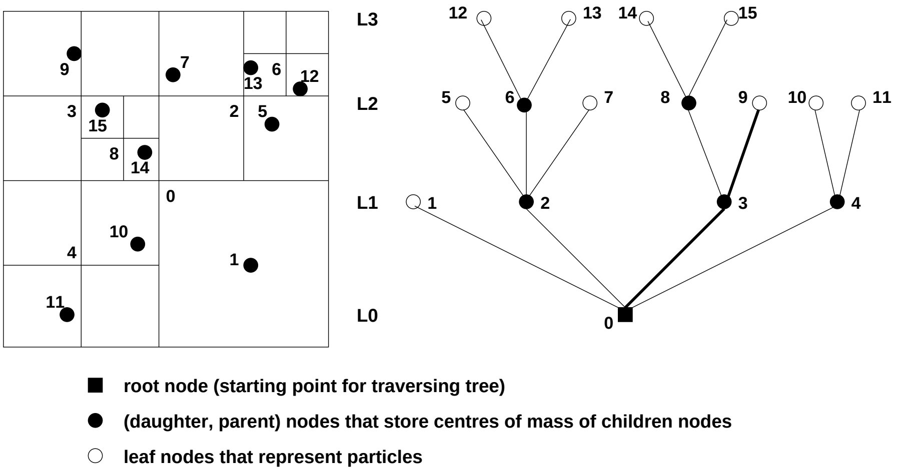

Figure 3.1: A quad tree in 2D with 10 particles. (Left) The simulation volume (root node) is split up into daughter nodes. The higher the particle density the higher is the cell density. (Right) The quad tree, according to Barnes and Hut [6], with its root node, daughter (parent) and leaf nodes. The thick solid lines from root to, e.g., leaf node number 9 make up a twig in the tree.

pseudo particles in order to reduce the number of distance calculations. A hierarchical structure of regions in space can show self-similarity over some hierarchical levels, i.e., large spatial regions (large pseudo particles) are made up of a certain number of smaller spatial regions (smaller pseudo particles) of the same geometry. In the following we will describe the two most common and efficient methods for long-range forces which are in a way based on a hierarchical (tree-like) split up of the simulation volume.

3.3.1 Barnes-Hut

A very common tree algorithm is the Barnes-Hut algorithm, as it was first described in [6] and successfully used in [4], and a multi pole expansion of the particles' masses (charges). The Barnes-Hut method finally assigns in 3D each particle one cubic cell, i.e., in regions where the particle density is high, the cell density will be high as well and the cells' sizes are small.

Practically, in a first step, a cubic “root node” is generated enclosing all particles. Then, the first particle is taken and sorted into the root node. As soon as a second particle is sorted in, the root node will be split up into eight equally sized “daughter nodes”. Then, the next particle will be inserted in one of the daughter nodes and it will be asked whether this daughter node now contains more particles. If so, the daughter node will be divided into eight equally sized daughter nodes in turn and it now has become a "parent node". If not, the daughter node will not be divided into eight sub cells. This procedure goes on until the last particle has been sorted in. Daughter nodes can thus be parent nodes (for the next lower hierarchy level) at the same time. After inserting all particles there could be cells left that contain only one particle and so are called "leaf nodes". They represent the ends of their twigs. Nodes without any particle are not considered in the tree. This structure is called an octtree (a quadtree in 2D and a binary tree in 1D) or Barnes-Hut tree. A 2D example is displayed in Fig. 3.1.

After all particles are inserted, the Barnes-Hut tree can be used to compute the total mass (charge) and the centre of mass (charge) for all nodes in the tree including leaf and daughter (parent) nodes. This is done by beginning with the leafs and ending with the root node. The single particles within the leaf nodes contribute to the total mass (charge) of their parent nodes. Traversing the tree now in the opposite direction, as it was done while constructing the tree, has the advantage in using the already available information of the daughter nodes for obtaining information for their parent nodes.

Given this, the tree code comes to the most crucial part: how to reduce the number of operations for the calculations of the long-range force that acts on each particle. For each particle residing in a parent node of a certain level, the tree code looks for neighboring parent nodes of the same level and calculates the ratios

$$\Theta_{\mathrm{node}} = \frac{r}{L_{\mathrm{node}}} \quad , \tag{3.12}$$

where r is the distance from the *poi* to the center of mass (charge) of the neighboring parent node currently being investigated. L_{node} denotes a measure for the size of the parent node which could be the space diagonal of the cubic node. Thus, each parent node will have its own Θ_{node} and be compared to a pre-defined Θ_{cr}-parameter. If $\Theta_{\mathrm{node}} > \Theta_{\mathrm{cr}}$ the parent node will be far enough away from the *poi* in order to combine all particles in it as a pseudo particle that interacts with the *poi*. If $\Theta_{\mathrm{node}} < \Theta_{\mathrm{cr}}$ the parent node will be too close to use it as a pseudo particle and so its eight daughter nodes will be considered for calculating Eq. (3.12) and it has to be decided again whether they are far or close. As long as $\Theta_{\mathrm{node}} < \Theta_{\mathrm{cr}}$, this procedure will be repeated for this parent node until we have a leaf and finally the force of this single particle will act on the *poi* directly. The Θ-criterion is obviously used for reducing the number of distance calculations for the *poi* and has a similar meaning as the ratio $r_{i\alpha}/\left\langle r_{j\alpha}\right\rangle$ we used for the error estimation for the multipole expansion in Fig. 2.4. This procedure is done for each particle for all nodes of the same level except for those nodes of the same twig where the *poi* belongs to: in Fig. 3.1 (right) for the particle in leaf node 9, node 3 is not allowed to be considered, but the nodes 8, 14 and 15 are because they belong to different twigs. If node 3 would be considered for the force calculation

as well the particle in node 9 would face itself because node 3 contains already information about the particle in node 9.
The choice of the parameter Θ_{cr} determines how strong the tree code is used as a direct summation code. The larger Θ_{cr} the farther the nodes must be in order to be used as pseudo particles. Due to the limitations of the simulation volume, the criterion for considering pseudo particles cannot be fulfilled anymore for arbitrary large Θ_{cr} and so, too large Θ_{cr} makes the tree code operating as a N^2 method.
Now we can think about the real computation of the forces on the *poi*. They are generally split up into three contributions:

- single particles that just collide or are about to collide with the *poi* within the next time steps will act on the *poi* via short-range (contact) forces; this collision administration can be done together with the treatment of nearby particles in the above context
- the long-range force contribution of nearby particles is a superposition of contributions by single particles; the distances between the *poi* and these particles are used
- the long-range force contribution of faraway pseudo particles can be computed using a multipole expansion of the masses (charges) of all particles within the nodes (see appendix B).

The total computational time for constructing a Barnes-Hut octtree is governed by the time cost for subdividing the root cell into daughter cells until in every daughter cell there is exactly one particle, and is of $\mathcal{O}\big(N\log N\big)$ [96]. The time for calculating the force on one particle due to all pseudo particles determined by the criterion (3.12) is of $\mathcal{O}\big(\log N\big)$ [49] and, for N particles, we have again $\mathcal{O}\big(N\log N\big)$. Altogether, for a Barnes-Hut tree, we therefore obtain a computational complexity of

$$t_{\text{CPU}} \propto \mathcal{O}\big(N\log N\big) \quad .$$

Remarkably, a Barnes-Hut tree shows this time expense even if it deals with a highly inhomogeneous problem. Because in regions with high particle densities the octtree exhibits a finer structure with more twigs and leafs than in low-density regions.

3.3.2 The Fast Multipole Method (FMM)

In common with the Barnes-Hut algorithm, the FMM subdivides the d dimensional simulation volume hierarchically into parent and daughter cells. The number of the smallest cells will roughly be of the order of the total number of particles, i.e., $N \propto (2^d)^R$ cells. R is the maximum refinement level corresponding

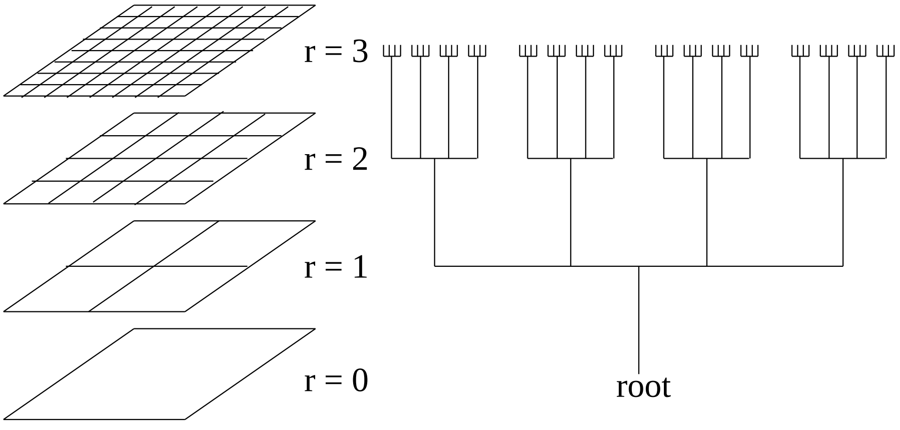

Figure 3.2: (left) The refinement levels r of a 2D simulation volume. The highest refinement level $r = 3$ contains 64 multipole expansions about their geometrical centres which make up hierarchically the multipole expansions of the lower levels $r = 2, 1, 0$ according to a tree (right). Every vertical line in the tree corresponds to one multipole expansion.

to the highest hierarchy of the tree with the finest cells. Furthermore, the FMM tree does show a homogeneous distribution of cells all over the simulation volume. This means, we only have in average one particle per cell. In Fig. 3.2, $d = 2$, $R = 3$, and r is the refinement level.

In contrast to the Barnes-Hut method, we start to calculate the multipole expansions for each cell at the highest refinement level R to the geometrical center of the cell and not to the center of mass (charge) of the particles within the cell. The same is performed for the next lower refinement level $R - 1$ by shifting the already in R obtained multipole expansions from the daughter cells to the centre of their parent cells in $R - 1$ (multipole-to-multipole transformations). This is done successively for all refinement levels until we reach $r = 0$ and finally obtain one multipole expansion relative to the centre of the parent root cell. After this descending in the tree we ascend in turn and will distinguish between near neighbor cells (near field contribution) and so-called “well-separated” cells (far field contribution). Well-separated cells do not share any face, edge or point with our cell of interest. Their multipole expansions contribute via a local Taylor series expansion to the cell of interest (multipole-to-local transformations). Then, the local expansion of the cell of interest will be decomposed to its daughter cells by shifting (local-to-local transformations). So, all these daughter cells of level, e.g., $r = 3$, “feel” later only the influence of cells in $r = 2$ which are well-separated from their parent cells. But they do not feel the influence of some well-separated daughter cells in the same level. These “missing” well-seperated daughter cells will later contribute separately via a local-to-local transformation to the daughter cell of interest. Due to the fact that there are no well-separated cells at refinement levels $r < 2$, see Fig. 3.2, we start ascending the tree from $r = 2$ and perform all these transformations for all cells in all refinement levels up to $r = R$. Finally, at $r = R$, the local expansions from the cells to the individual particle locations inside the cells have to be performed and from this the potentials and forces acting on the particles can be computed. Additionally, at highest refinement level R, the near field contributions come from direct summation between the *poi* inside a daughter cell and single particles within the neighboring cells and the same cell. The FMM was first introduced by [39, 40] wherein the authors make use of the concept of grouping particles together to pseudo particles via multipole expansions and of the concept of a hierarchical construction of cells, according to Barnes and Hut. Here, the total complexity of the FMM is reported to be

$$t_{\mathrm{CPU}} \propto \mathcal{O}(N) \quad ,$$

if the number of cells at $r = R$ is really similar to the number of particles. This would not be true for inhomogeneous systems and, thus, the high efficiency of the FMM method only leads to an advantage for homogeneous systems. The computational complexity depends also on the number of refinement levels R and on the accuracy of the multipole expansions performed in each cell of each hierarchy [113]. If we keep R small then there are more particles in a cell on average and the FMM acts more as a direct summation method. On the other hand, a small maximum refinement level reduces strongly the number of multipole expansions to be performed. A comparison between the time expense of the FMM and Barnes-Hut trees and direct summations in 2D and 3D is given in [96]. Note, that in 2D the multipole and local Taylor series expansions and their up and downward passing through the tree are performed completely different from the 3D case. The computation of the potential is in 2D proportional to $\log|\boldsymbol{r}_{ij}|$ which requires the calculation of the multipole expansions and their transformations by means of the complex plane [40, 96] and in 3D it is proportional to $1/|\boldsymbol{r}_{ij}|$ where they can be computed by means of spherical harmonics [38, 96, 113].

Due to their strong capability to handle inhomogeneous many-body systems, hierarchical tree codes were first developed in the context of astrophysics where the gravitational problems require a treatment of high density gradients and complicated structures such as the evolution of galaxies and colliding galaxies, see [5] and references therein. In contrast, grid-based methods (see next Section 3.4) require a more or less homogeneous distribution of particles in order to run highly efficient because in many cases there is only a homogeneous distribution of grid nodes available. Another problem in astrophysics, where tree codes are used is the evolution of globular star clusters [55], which are very old and nearly spherical star systems in dynamical equilibrium orbiting around the nuclei of galaxies.

3.4 Grid-Based Algorithms

In addition to the discretization of time which most particle simulation techniques have in common, grid-based algorithms also discretize space in order to obtain far field contributions at the *poi*. The near-field contribution can additionally be provided by direct particle-particle summation within a properly defined neighborhood around the *poi*. For the far field contribution, space is divided into a homogeneous distribution of nodes which contain the spatial information about nearby particles. The way of computing the field at the grid points which acts at the *poi* reduces the time expense significantly and is the distinguishing feature of the two grid-based methods described in the following.

3.4.1 Particle-Mesh (PM)

The PM method allows for computing the far-field force contribution also in a much faster way than direct summation methods. It makes use of a spatial grid on which, e.g., *Poisson*'s equation $\boldsymbol{\nabla}^2\phi(\boldsymbol{r}) = \varrho(\boldsymbol{r})$, is solved by means of the *Fast Fourier Transform.* In Fig. 3.3, we sketch how to consider the far-field contribution.

Given a set of particles (a), we introduce an appropriate grid (b) to the simulation volume and assign the particles' charges (masses) to the grid nodes by certain interpolation methods such as the "nearest grid point" or "cloud in cell" (CIC) method. The latter is most popular [52] for such kind of problems. In d dimensions the CIC method interpolates the charge (mass) of one particle to the 2^d nearest grid nodes. This is done by smearing out the particle's charge (mass) to a cloud with the same volume and shape of a cell. This cloud (with its centre at the particle's position) then overlaps with the cells around our 2^d grid nodes differently, corresponding to the distances between the particle and its nearest grid nodes. From this, e.g., the farthest grid node will belong to the smallest charge (mass) fraction of the cloud. This gives a suitable distribution of the particle's charge (mass) to each of the nodes. The fraction will then be added to the node. This assignment has to be done for all particles and finally gives us the total charge (mass) density, $\varrho(\boldsymbol{r})$, via a difference equation which represents the discretized Poisson equation with grid spacing $(\Delta x, \Delta y, \Delta z)$,

$$\begin{aligned} & \frac{\phi_{i+1,j,k} - 2\phi_{i,j,k} + \phi_{i-1,j,k}}{(\Delta x)^2} \\ + & \frac{\phi_{i,j+1,k} - 2\phi_{i,j,k} + \phi_{i,j-1,k}}{(\Delta y)^2} \\ + & \frac{\phi_{i,j,k+1} - 2\phi_{i,j,k} + \phi_{i,j,k-1}}{(\Delta z)^2} = \varrho(\boldsymbol{r}) \ , \end{aligned} \tag{3.13}$$

defined now on the grid nodes and not anymore at the particles' locations. The field, $\phi_{i,j,k}$, corresponds to the potential at the grid points denoted by the triple $\{i, j, k\}$.
In order to solve Poisson equation without integration (which would result in a too high computational complexity), PM uses means of Fourier series ("discrete Fourier transforms", DFT). To be more precise, PM uses the *Fast Fourier Transforms* (FFT) to solve because DFT scales with $\mathcal{O}(N^2)$ while FFT is faster in doing the transformations. Let us briefly describe how DFT works to solve the difference equation (3.13) at the grid nodes (c) because FFT method is quite similar.
The solution of Poisson's difference equation consists of transforming the left and the right-hand side of Eq. (3.13) into a Fourier series and of considering the number of nodes N_n as the number of samples taken for the Fourier transformation. E.g., in x-direction we then have $x = 2\pi n_x/N_{n,x}$ and $n_x = 1...N_{n,x}$ samples. For an arbitrary quantity $q(x, y, z) = q(\boldsymbol{r})$ the Fourier transform is generally written as

$$q(\boldsymbol{r}) \quad \overset{DFT}{\rightarrow} \quad \tilde{q}(\boldsymbol{K}) = \frac{1}{N} \sum_{n_x=0}^{N_{n,x}-1} \sum_{n_y=0}^{N_{n,y}-1} \sum_{n_z=0}^{N_{n,z}-1} q(\boldsymbol{r}) \exp(-i\boldsymbol{K} \cdot \boldsymbol{r})$$

$$q(\boldsymbol{r} + \Delta\boldsymbol{r}) \quad \overset{DFT}{\rightarrow} \quad \tilde{q}(\boldsymbol{K} + \Delta\boldsymbol{K}) = \frac{1}{N} \sum_{n_x=0}^{N_{n,x}-1} \sum_{n_y=0}^{N_{n,y}-1} \sum_{n_z=0}^{N_{n,z}-1} q(\boldsymbol{r}) \exp\big(-i\boldsymbol{K} \cdot (\boldsymbol{r} + \Delta\boldsymbol{r})\big) \ .$$

$q(\boldsymbol{r})$ represents the quantities $\varrho(\boldsymbol{r})$ and $\phi_{i,j,k} = \phi(\boldsymbol{r})$ in the space domain which is transformed to $\tilde{q}(\boldsymbol{K})$ that represents the quantities $\tilde{\varrho}(\boldsymbol{K})$ and $\tilde{\phi}(\boldsymbol{K})$ in the wave number domain. $\boldsymbol{K}$ denotes the vector of the wave number. Carrying out these transformations, one obtains for Poisson's integral equation a simple algebraic equation in the wave number domain, $(i\boldsymbol{K})^2\tilde{\phi}(\boldsymbol{K}) = \tilde{\varrho}(\boldsymbol{K})$. This is the key issue that makes PM with FFT faster than $\mathcal{O}(N^2)$. From this equation we obtain the potential in the wave number domain which can be transformed back to the potential in the space domain we are actually interested in. This backward transformation is the inverse Fourier transform and represents a single step such as the forward transformation. Once having obtained the potential at the grid nodes, we solve the electrical (gravitational) field, according to $\boldsymbol{E} = -\nabla\phi$ and $\boldsymbol{g} = -\nabla\phi$, respectively. In order to interpolate back the potential values to the particles' locations (d) we can also use the CIC method as we used for assigning the particles' charges (masses) to the mesh nodes. After doing this, the forces acting on a particle i are to be computed via $\boldsymbol{F} = q_i\boldsymbol{E}$ and $\boldsymbol{F} = m_i\boldsymbol{g}$, respectively. After considering the other forces as well (e.g., near-field contribution, volume force), the particles can now finally be moved by integration of the equations of motion.
FFT was used in [19], amongst others, and is based on the splitting of the number of samples (grid nodes) into two partial Fourier series with an odd and an

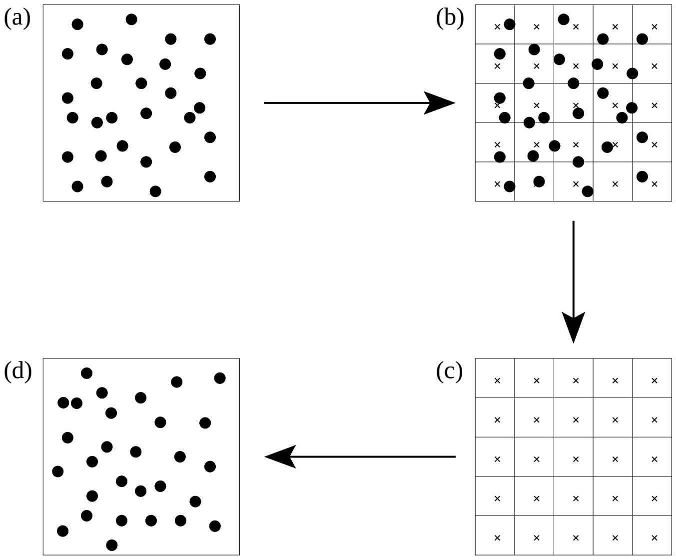

Figure 3.3: A 2D scheme to compute the far-field forces acting on a single particle according to PM: (a) simulation volume with particles. (b) discretize the space by construction of a grid with cells. Grid nodes are represented by the cell centres (crosses). Assign particles' charges (masses) to the grid nodes. (c) solve *Poisson*'s equation on the grid nodes and get the potential field there. (d) interpolate the field to the original locations of the particles and compute the resulting force acting on them.

even number of samples. Its improvement in time expense is based on avoiding the multiple computation of cancelling terms, which have to be computed by DFT. The PM method was proposed by [26] and applied to various astrophysical problems. Together with FFT it reduces the computational complexity to

$$t_{\mathrm{CPU}} \propto \mathcal{O}\big(N_n \mathrm{log} N_n\big) \quad .$$

Note, that in many applications of the particle mesh method the number of grid nodes is proportional to the number of particles, i.e., $N_n \propto N$. A comparison between tree methods and particle mesh methods (including FFT) concerning computational expense and accuracy was presented in [64]. It was found that generally PM methods are not very efficient for inhomogeneous particle systems because in most simulations the spatial nodes are homogeneously distributed. For inhomogeneous problems, tree codes are more advantageous.

3.4.2 Multigrid Techniques

Multigrid techniques make use of several spatial grids (at least two) with different mesh sizes that cover the simulation volume [125]. They are highly efficient in solving elliptical (e.g., *Laplace*, *Poisson*) and parabolic (e.g., *Diffusion*) partial differential equations by approximating the real solution successively. A brief introduction to these techniques is given in [133].
The grid nodes that cover the simulation volume are considered as the space points where the solution of the partial differential equation is iteratively determined. The problem can be represented by a system of linear algebraic equations, i.e., by a matrix equation, for which the error of the solution vector is an expansion into a *Fourier* series. The error will be smoothed by each iteration, differently strong on grids with different mesh sizes. The idea of the multigrid technique is to reduce the number of iterations and, thus, to speed up the algorithm by introducing coarser grids because larger wave-length error components can be smoothed there faster than on grids with smaller mesh size.
The following scheme sketches the multigrid procedure, using two grids of mesh size h and $2h$, respectively:

`(A) convert the PDE into a discrete difference equation on a fine grid with mesh size` h
↓
`(B) guess an initial solution for the resulting system of linear equations and smooth it`
↓
`(C) compute the residual on the fine grid`
↓
`(D) compute the residual on the coarse grid (restriction) with mesh size` $2h$
↓
`(E) solve residual equation on the coarse grid and get the correction`
↓
`(F) interpolate the correction to the fine grid (prolongation) and smooth it`
↓
`(G) add the coarse grid correction to the fine grid solution and repeat if necessary`

Generally, (A) by discretizing *Poisson*'s equation $\boldsymbol{\nabla}^2\phi(\boldsymbol{r}) = \varrho(\boldsymbol{r})$ on a grid with mesh size h we obtain a difference equation as in the case of PM, see Eq. (3.13), where the spacing on a three dimensional cubic grid now is $h = \Delta x = \Delta y = \Delta z$ and the triple $\{i, j, k\}$ denotes the node of interest on the grid. Each node delivers one difference equation resulting in a system of N_n (number of nodes) linear equations, represented by $\mathcal{A}\boldsymbol{\phi} = \boldsymbol{\varrho}$, with $\mathcal{A}$ a matrix with elements $\{a_{p,q}\}$, where $p, q = 1, ..., N_n$, and $\boldsymbol{\varrho}$ the values of the source term at each node. Here, the coefficients $\phi_{i,j,k}$ are combined into a vector, $\boldsymbol{\phi}$, with N_n elements $\{\phi_p\}$. The number of coefficients of each equation depends on how many neighboring nodes around the $\phi_p(x, y, z)$ we take into account for the discretization.
Now, (B) we have to guess an initial solution vector, $\boldsymbol{\phi}^{(m=0)}$, and solve for all the

nodes of interest in the current iteration step m

$$\phi_p^{(m+1)} = \frac{1}{a_{p,p}}\left(\varrho_p - \sum_{q=1}^{p-1} a_{p,q}\phi_q^{(m+1)} - \sum_{q=p+1}^{n} a_{p,q}\phi_q^{(m)}\right) \quad ,$$

where $m+1$ is the next iteration. The solution is computed not only by the values $\phi_p^{(m)}$ in the current iteration step but also by those $\phi_p^{(m+1)}$ computed up to $q = p-1$ in the new iteration step. This iterative procedure is called *Gauss-Seidel* and is stopped if the error, $|\phi_p^{(m+1)} - \phi_p^{(m)}|$, is smaller than a pre-defined limit. This finally provides us the smoothed solution $\{\tilde{\phi}_p\}$. The procedure smoothes the high frequency modes of the error on a grid with spacing h more efficient than the low frequency modes.

The difference between the exact but unknown solution and the obtained smoothed solution, $\boldsymbol{\zeta} = \boldsymbol{\phi} - \tilde{\boldsymbol{\phi}}$ (i.e., the correction), has to be put into the matrix equation $\mathcal{A}\boldsymbol{\zeta} = \boldsymbol{\varrho} - \mathcal{A}\tilde{\boldsymbol{\phi}} = \boldsymbol{r}$ and is to be solved (C). $\boldsymbol{r}$ is the *residual* and considered now as the new source term.

The residual has now (D) to be interpolated on the coarser grid with mesh size $2h$ (*Restriction*) and (E) solved there in order to smooth the solution (i.e., the lower frequency components of the solution on the finer mesh). The point why to introduce a second but coarser grid is that error modes with low frequency on the fine grid will be those with high frequency on the coarse grid: they can be smoothed on the fine grid with mesh size h slower than on the coarse grid. Introducing coarser grids for smoothing low frequency error modes makes the multigrid procedure so fast. If there are still lower frequency modes, we have to introduce another grid with mesh size $> 2h$ in order to reduce them there again more efficiently, etc. The restriction operator maps the residual $\boldsymbol{r}$ on the fine grid to the coarse grid. By using an optimal multigrid procedure, a computational time expense of $t_{\mathrm{CPU}} \propto \mathcal{O}(N_n)$ can be achieved, where N_n is the number of grid nodes (i.e., the number of unknowns in the difference equation).

After smoothing the correction $\boldsymbol{\zeta}$ on the coarse grid (F) we have to interpolate it back to the next finer grid – again using an operator (*Prolongation*) – and smooth the prolongated $\boldsymbol{\zeta}$ there by some iterations (again with *Gauss-Seidel*). This has to be done for each prolongation step.

Attaining finally again the correction on the finest grid by this procedure (G), we have to add the correction to the initial guess, $\tilde{\boldsymbol{\phi}}^{\mathrm{new}} = \tilde{\boldsymbol{\phi}} + \boldsymbol{\zeta}$, and smooth it again thereafter. If necessary, use the new solution and start at (C). The steps (A) to (G) are referred to as the *V-cycle* of a Multigrid procedure, see Fig. 3.4.

Finally, the number of iterations on the finest grid done for smoothing the solution error is mainly responsible for the time spent by the multigrid algorithm. So, an optimal multigrid algorithm will not spend significantly more time in finding solutions on the nodes than it will thereafter do for the computation of the forces on all N particles. Thus, the computational complexity will mainly depend

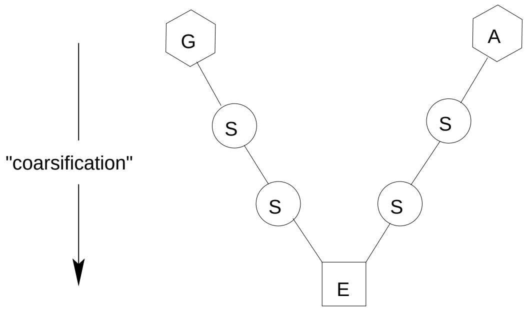

Figure 3.4: *V-circle* of a 4-grid procedure. “G” denotes the starting point of the multigrid procedure. Descending “\” and ascending lines “/” correspond to restriction and prolongation operations, respectively, each with subsequent smoothing “S”. An exact solution is computed on the coarsest grid, “E”. “A” means that after descending back to the finest grid we have to add the correction to the fine-grid solution.

linearly on the number of particles

$$t_{\text{CPU}} \propto \mathcal{O}(N) \quad . \tag{3.14}$$

For molecular simulations, the long-range forces acting on a *poi* will be also split up into the far-field contribution (done by multigrid techniques) and the near-field contribution (done by the PP methods). The use of a multigrid technique in combination with discrete particle systems is described in [122].

3.5 Hybrid Algorithms

Combining some of the above algorithms together can lead to optimum reduction of the CPU time for performing the long-range forces between all N particles. For special physical, astrophysical or biophysical problems very often PP methods are combined with either tree or grid-based algorithms in order to treat the forces in the near neighborhood of a particle accurately. The far-field contributions can then be obtained by tree, PM or multigrid without loosing too much accuracy. As an example, the combination of PP and PM is quite common and referred to as the PPPM (or P^3M) algorithm.

Other hybrid algorithms even combine tree codes with particle mesh codes in order to obtain TreePM algorithms [3, 132, 134] and can also use adaptive time steps [9]. This can be done for cosmological simulations for which the neighborhood of one particle is not treated by PP but by a (modified) tree that takes the strong clustering of particles due to gravitational instabilities into account.

In addition, for larger distances, for which weaker density gradients occur, the PM method is applied. Using a modified TreePM, a spectacular simulation was performed in 2004, the so-called “Millennium Simulation” [120], which dealt with about $2160^3 = 10.0776$ billion discrete particles in order to simulate the evolution of the universe from very early time, i.e., $z = 127$ [1], to the present. The particles simulated do not represent the visible amount of matter in the universe but represent the cold dark matter (CDM) which is thought to have strongest influence on the structural evolution of the universe. Nowadays, one assumes that 80 % of total mass in the universe consists of dark matter whereas the rest we can observe by our eyes and optical telescopes.

3.6 The Hierarchical Linked Cell Method (HLC)

In this section we will introduce a new algorithm that uses the pseudo particle concept described in section 2.3. However, the discrimination between pseudo-particles and nearby single particles proceeds differently since we use the linked cell neighborhood search (see next section 3.6.1) in a hierarchical structure. The combination of both the hierarchical linked cell structure and the pseudo-particle concept for treating long-range forces is new to the best of our knowledge and is expected to present a technique that is competitive to the ones discussed in the preceding sections.

3.6.1 The Linked Cell Neighborhood

In extended particle systems not every particle has to be checked for collision with all other particles. If neighboring particles are too far from our particle of interest (in the following denoted again as the *poi*) it will be redundant to check them for contact with the *poi* because they will anyway not collide during the following time steps. That is why we define a close neighborhood with neighboring particles which are checked for collision only because these particles will most probably collide with the *poi* during one of the following time steps. Defining an average number M of neighboring particles within such a neighborhood, we will deal with a number of operations which is less expensive than $\mathcal{O}(N^2)$, namely $\mathcal{O}(NM)$ or

$$t_{\mathrm{CPU}} \propto \mathcal{O}(N) \tag{3.15}$$

---

[1] The *redshift*, z, is a measure for cosmological distances. The farther galaxies are away from earth the faster they will move away from us. Due to the Doppler effect, their spectral lines will be shifted to longer (redder) wave lengths than it would be for closer galaxies. If z takes large values the galaxy will be very distant and we will observe it as it was in the very past. $z = 127$ corresponds to a distance of about 14 billion light years (close to the “birth” of the universe) but was never observed in galaxies’ spectra.

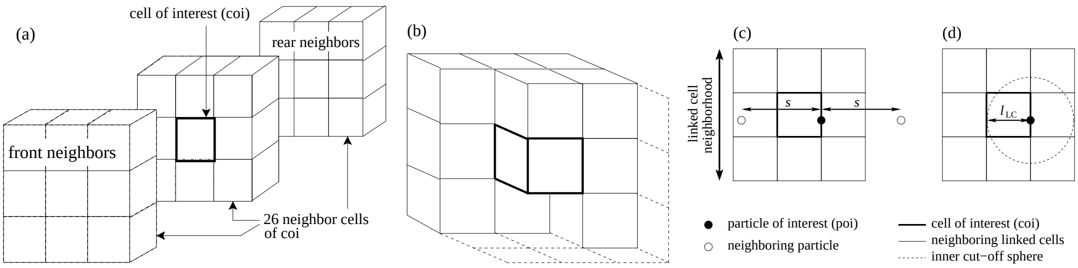

Figure 3.5: (a) A three dimensional linked cell neighborhood, including the cell of interest and its 26 adjacent neighbor cells (front and rear cells are shifted apart from the other cells). (b) Only 13 (of 26) neighboring linked cells are to be considered due to the successive counting through the linked cells. (c) The particles outside (square) the linked cell neighborhood do not interact with the *poi* whereas the particles inside (circle) do – although both are equally distanced with separation length s. This leads to an asymmetry in force computation. (d) The introduction of an inner cut-off sphere around the *poi* avoids these asymmetries because equally distanced neighboring particles inside the inner cut-off sphere will always interact with the *poi*. Here, the largest possible radius is shown.

because for every particle in the system the neighborhood has to be analyzed. For, say, $N = 500$ particles we actually have to perform $N(N-1)/2 \approx 125,000$ computations whereas for this proposed neighborhood method and a typical number $M = 15$ of neighboring particles it will be reduced to $NM \approx 7,500$ calculations. This is a significant reduction of operations that has to performed. The question is now, how to define a near neighborhood of M neighboring particles?
In our hierachical linked cell code the simulation volume is divided into so-called linked cells and by defining only the 26 adjacent cells around the cell of interest (in the following denoted as *coi*) as the “linked cell neighborhood” which is illustrated in Fig. 3.5 (a). Only the M particles therein are checked for collision during the current time step whereas the rest will be ignored. Moreover, due to the fact that we successively consider all cells in the system once as the *coi* and construct for each of them the whole linked cell neighborhood, it is redundant to consider all 26 adjacent neighbor cells. Effectively, we only consider 13 well selected adjacent cells besides the *coi* as it is shown as an example in Fig. 3.5 (b). This can be done because the 13 “missing” neighboring cells will consider the current *coi* as one of their 13 neighboring linked cells if it is their turn to be *coi*. Then, we have considered all particles with all others once inside the linked cell neighborhood around the *coi*. In [89] we compared the efficiency of the method of linked cells with other competitive neighborhood search algorithms such as the

verlet list and the *linked linear list.* In [1] and [98] the linked cell method and others are described very well and their possible computational implementation is briefly sketched.

Technically, all M particles are combined in a linked list which is connected to these neighboring cells. All particles that will enter the linked cell neighborhood during the simulation will be stored in this linked list, others that leave will be released from the list. That means, the list is a dynamical list with changing size (changing M) as a function of time. This necessitates a periodic update of the list. We will be on the safe side if we sort the particles into the list during each time step because the neighborhood will change in each time step. But doing this is a waste of time and we can do the update each z time steps if we make sure that during the time interval $[t, t + z\Delta t]$ the linked cell neighborhood will not change drastically, e.g., that new particles from outside cannot enter the neighborhood and even overlap with the *poi* without being detected. We have to determine the time interval between two updates such that those particles with highest velocities will not manage to enter the linked cell neighborhood from outside *and* collide with the *poi* during this time. Consequently, the update itself must be done more often the faster particles move. So, in the code we determine a critical length, $(l_{\mathrm{LC}} - 2a)/8$ (where l_{LC} is the size of a linked cell and a is the particle radius), that represents the minimal distance two particles have to pass in order to cross one linked cell and collide. The maximum distance the fastest particle would move during a time step is determined via $v_{\max}\Delta t$, where $v_{\max}$ is the maximum velocity in the system measured during Δt. If the sum of maximum distances (accumulated over z time steps) exceeds the critical minimum length the update will have to be done and, thus, we make sure that all particles will be detected that are about to collide during $[t, t + \Delta t]$.

3.6.2 The Inner Cut-Off Sphere

Like the simulation algorithms described in the preceding sections, also the Hierarchical Linked Cell structure (which we will introduce in section 3.6.3), must distinguish between near and far-field contributions. As already mentioned in Sec. 3.6.1, we can use the linked cell neighborhood, i.e., the 3^d cubically arranged linked cells (in dimension d), in order to allow for the computation of the near-field contribution. All the particles in the linked cell neighborhood are combined in a linked list which allows us to compute all their distances to the *poi* directly in order to check them for collision with the *poi*. Simultaneously, we can also use this linked cell neighborhood for the computation of the long-range potential between all neighbors and the *poi* and all neighbors amongst each other. This will lead to the near-field contribution to the total force acting at the *poi*.

However, due to the cubical shape of the linked cell neighborhood, the situation can occur in which a pair of particles interacts via long-range forces but a third particle with exactly the same distance to the *poi* is just located outside the linked cell neighborhood and experiences no long-range interaction at all. This situation is illustrated in Fig. 3.5 (c) and provides an asymmetry in the force calculation. We can avoid this asymmetry by introducing a so-called inner cut-off sphere, Fig. 3.5 (d), where the *poi* is situated at the centre. So, only those particles of the linked list that are located within this sphere provide the near-field contribution. On the one hand, the radius $r_{\rm ico}$ of the sphere must be as large as possible and consider as many particles of the linked list as possible in order to provide highest accuracy in the near-field force calculation. On the other hand, it is technically not possible to construct a sphere that reaches over the limitations of the linked cell neighborhood. So, we have to ensure that $r_{\rm ico}$ is such small that it never reaches over the limitations whenever the *poi* is situated in the *coi*. We can fulfil this condition if we choose for the radius the smallest linked cell size. For cubical linked cells it is $r_{\rm ico} = l_{\rm LC}$.

3.6.3 The Hierarchical Linked Cell Structure

The hierarchical linked cell code (in the following abbreviated by HLC) actually belongs to the group of tree-based algorithms. The reduction of N^2 is mainly achieved by treating particle ensembles as pseudo particles in a hierarchical way. The lowest hierarchy level, h=1, contains 3^d basic cells (linked cells) that are those cells which share a face, edge or vertex with the cell that contains the *poi*. 3^d linked cells or (h=0)-cells make up one (h=1)-cell which in turn – together with 3^d-1 other adjacent (h=1)-cells – is again part of one (h=2)-cell. Moreover, 3^d (h=2)-cells make up one (h=3)-cell. h is also the indication for the hierarchy level we are currently interested in. We can continue this hierarchical structure up to the maximum hierarchy level $h = H_{\rm max}$, obtaining larger and more distant cells for higher hierarchies. A (h-1)-cell in each hierarchy level h represents one pseudo particle and is characterized by the total mass (charge) and the centre of mass (charge) of all (h-2) pseudo particles within this cell. This is shown in Fig. 3.6. So, we are combining 3^d pseudo particles of level h to one pseudo particle of level h+1. In case of PP methods the number of particles will increase steadily if we move away from the *poi*. In contrast, in case of HLC we face always the same number ($= 3^d - 1 = 26$) of pseudo particles if we move away from the *poi*. Moving away here means that we ascend the hierarchy structure to higher hierarchy levels. For the HLC structure, this gives us a smaller number N that leads to a reasonable reduction of the computational complexity. The full force contribution on a particle i reads

$$\boldsymbol{F}_i \approx \underbrace{\sum_{j=1}^{M_{\rm ico}-1} \boldsymbol{F}_{ij}}_{\rm near-field} + \underbrace{\sum_{h=1}^{H_{\rm max}} \sum_{\alpha=1}^{3^d-1} \left(\boldsymbol{F}_{i\alpha}^{(M)(h)} + \boldsymbol{F}_{i\alpha}^{(D)(h)} + \boldsymbol{F}_{i\alpha}^{(Q)(h)} \right)}_{\rm far\ field} \quad , \tag{3.16}$$

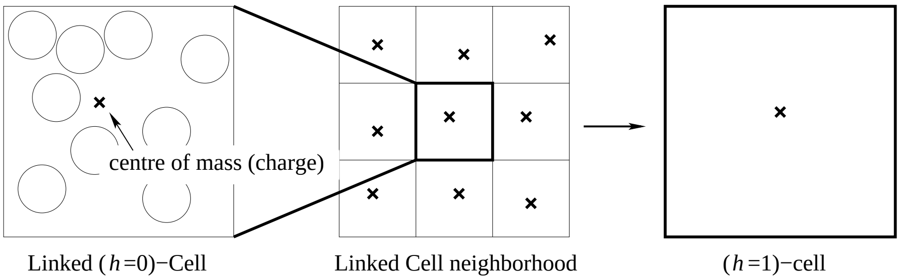

Figure 3.6: The total masses (charges) and centres of mass (charge) of particles within 3^d adjacent and cubically arranged linked cells are combined to the total mass (charge) and centre of mass (charge) of one (h=1)-cell. Likewise for the next higher hierarchy, 3^d (h=1)-cells are grouped together to one (h=2)-cell.

where M_{ico} is a subset of the M particles of the linked cell neighborhood situated within the inner cut-off sphere. The double sum considers the force contribution of the $3^d - 1 = 26$ pseudo particles in $H_{\max}$ hierarchies.

The following information summarizes the key data of the HLC structure in general.

hierarchy level h:	$1 \leq h \leq H_{\max} \quad \wedge \quad h, H_{\max} \in \mathbb{N}$
number of (h-1)-cells:	3^d
number of linked cells in one direction/within (h-1)-cell:	3^h / $3^{d(h-1)}$
number of fringe cells in one direction at one side (see Sec. 3.6.4):	$(3^{H_{\max}}$-1)/2

In order to express the reduction in computational time expense in terms of N, let us think about the number of time consuming computations to be performed for one particle in order to calculate the far-field force contribution with means of the HLC structure. If we build up the hierarchy until h=$H_{\max}$ we will consider (3^d-1)$H_{\max}$ pseudo particles that interact with the *poi*. For a given maximum hierarchy level $H_{\max}$ there are $n_{\text{LC}}^d = 3^{dH_{\max}}$ linked cells that make up the simulation volume. Since the number of particles increases linearly with enlarging the simulation volume we also can write $N \propto n_{\text{LC}}^d = 3^{dH_{\max}}$. From this, we see that $H_{\max} \propto \log_3 N$ and both the number of pseudo particles that act on the *poi* and the number of computations scale like $\mathcal{O}(\log_3 N)$. Therefore, the time expense for all N particles can be considered as

$$t_{\text{CPU}} \propto \mathcal{O}\big(N \log_3 N\big) \quad .$$

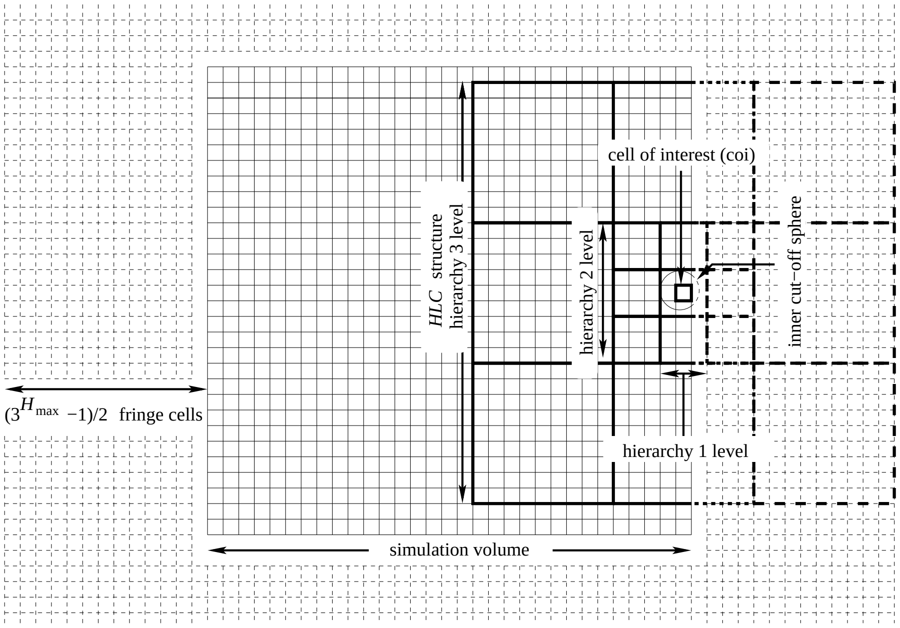

Figure 3.7: A 2D example of the Hierarchical Linked Cell structure in presence of non-periodic boundaries. The structure is built up to the hierarchy-($H_{\max}$=3)-level. A hierarchy-h-level contains 3^d (h-1)-cells. The simulation volume is plotted with solid lines whereas fringe cells are drawn by thin dashed lines.

3.6.4 Non-periodic Boundary Conditions

As in most of the previously introduced methods for the simulation of particle systems with long-range forces, it is also important to specify the boundaries. In our HLC code it is possible to switch between non-periodic and periodic boundaries. If we deal with non-periodic boundaries we automatically activate rigid walls that limit the simulation volume and elastically reflect particles bouncing at the walls. While we use periodic boundaries in one part of this thesis where we deal with homogeneous particle systems, in the other part we study ring shaped particle aggregates (chapter 5) that require non-periodic boundaries.

Usually, there are areas within the simulation volume which are not covered by the HLC structure that is built up around the *poi*. Non-periodic boundaries do not consider the influence of particle ensembles on the *poi* that are located in those areas. Due to the fact that the HLC structure is simply cut off if it reaches over the boundaries of the simulation volume, a situation can occur in which at least half of the simulation volume is not covered by the structure. This is the case if the *poi* is somewhere close to a boundary as is displayed in Fig. 3.7. The cell of interest containing the *poi* is here positioned directly at the boundaries.

In the half space of the right hand side of the *coi*, all hierarchy levels are truncated by the boundaries and one can imagine them to be arranged outside of the simulation volume which is indicated by dashed lines.
The way of grouping (h-1)-cells together to h-cells leads to the necessity of fringe cells located beyond the boundaries of the simulation volume. For the outermost *coi* we have to add ($3^{H_{\max}}$-1)/2 fringe cells in order to be able to consider the hierarchy cells up to the $H_{\max}$-level around the *coi* in the familiar way. This means, that we generally have to distinguish between two cases before constructing the HLC structure: either a ($H_{\max}$-1)-cell has to be constructed completely inside or partly (or even completely) outside the simulation volume.
Since (h-1)-fringe-cells do not contain particles, they will not contribute to both the total mass (charge) and centre of mass (charge) of the larger h-fringe-cell. Generally, the introduction of fringe cells is always required if we do not deal with periodic boundaries.

3.6.5 Periodic Boundary Conditions

Here we briefly show how the HLC structure looks like in the presence of periodic boundary conditions. Periodic boundaries make the (spatially limited) simulation volume infinitely large by mirroring particles in a particular way. A *poi* very close to the boundaries of the simulation volume feels a lack of neighbor particles in comparison with the situation when it is in the middle of the system (in the bulk) where neighbor particles are supposed to be everywhere. Periodic boundary conditions fill up the neighborhood outside the simulation volume by particles from the opposite side by shifting them exactly by the length L. This is illustrated in Fig. 3.8 and is done there for the centres of mass (charge) of cells of any hierarchy. Finally, every particle has its own hierarchical structure which can reach over the boundaries of the simulation volume and contains there particles as well, in contrast to the case of non-periodic boundary conditions for which the fringe cells remain empty.

3.6.6 The Outer Cut-Off Sphere

A simulation algorithm that takes pair-wise particle interactions (section 3.2) in a periodic simulation box into account has to consider all N particles within the box once in a time step. If we deal with periodic boundary conditions we have to introduce a cut-off radius r_{oco} around the *poi*, where only particles with $r_{ij} < r_{\mathrm{oco}}$ are considered. Otherwise, without the introduction of a outer cut-off, neighboring particles can be considered twice for the computation of the forces. The diameter of the cut-off sphere (see larger circle in Fig. 3.8) must therefore be $2r_{\mathrm{oco}} = L_{\min}$, i.e., the size of the shortest edge of the simulation volume, $L_{\min}$,

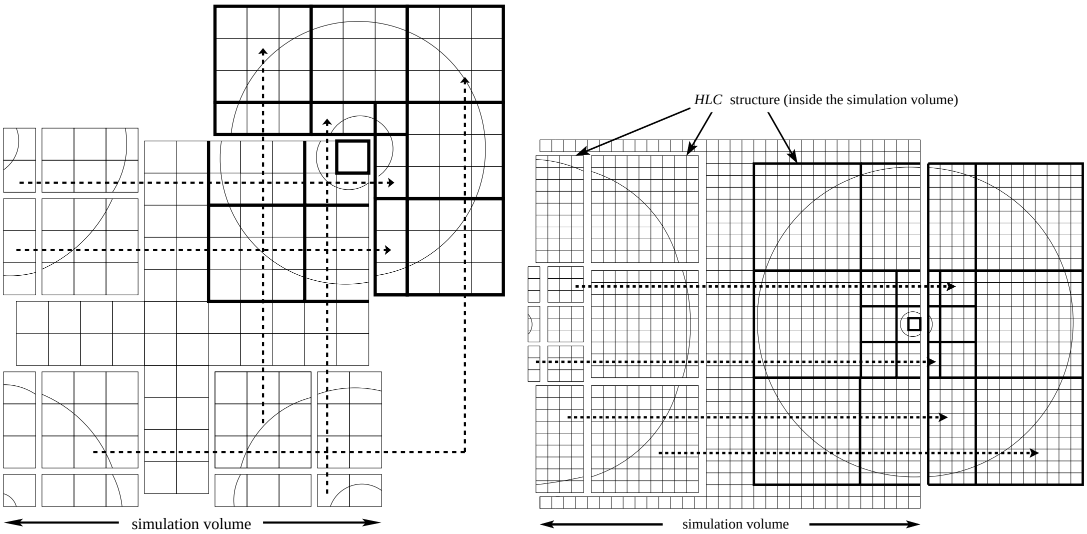

Figure 3.8: (Left) System with $H_{\max} = 2$ in 2D. The HLC structure outside the simulation volume is constructed by shifting corresponding (h=0) and (h=1)-cells from inside the simulation volume (separated from the other cells) towards the correct locations. Dashed straight lines (arrows) have the length L of the simulation volume. (Right) The same as left but a system with $H_{\max} = 3$ in 2D and periodic boundaries are shown only in one direction.

due to symmetry reasons[2]. Thus, the potential at $r_{ij} = r_{\text{oco}}$ has to be truncated and we can use for the long-range potential over the whole r_{ij}-range

$$\phi_{ij}\Big(\{r_{ij}\}\Big) = \begin{cases} -k\sum_{j=1}^{N-1} \frac{c_i c_j}{|\boldsymbol{r}_{ij}|} & \text{for } |\boldsymbol{r}_{ij}| < r_{\text{oco}} \\ 0 & \text{for } |\boldsymbol{r}_{ij}| \geq r_{\text{oco}} \end{cases} . \tag{3.17}$$

So, ϕ_{ij} represents a superposition of the force contributions of almost N particles.

Supposing now the presence of pseudo-particles in the sense of the HLC algorithm, the interaction sphere will cut through the largest (h=$H_{\max}$-1)-cells of the HLC structure, compare Fig. 3.8. From the single particle's point of view we therefore have to decrease the influence of a pseudo particle on the *poi* because all those particles that are situated outside of r_{oco} but belong to the pseudo particle are supposed to be neglected. Due to the fact that we cannot cut the pseudo particles of the highest hierarchy level into pieces as we wish to do, we thus

---

[2] The potential is a central potential which decays radially according to Eq. (2.11). If we deal with non-cubic linked cells the simulation volume will not be cubic as well. Therefore, $2r_{\text{oco}}$ must be as large as $L_{\min}$ in order to keep the outer cut-off sphere within the simulation volume as a whole and, so, to sustain sphericity of the potential.

decided to introduce a multiplicative weighting function for both the potential and the force calculation, that takes the non-consideration of the particles into account that are located outside the sphere. The weight function is constructed such that the force contribution of the pseudo particle α sensitively depends on the location of its center of mass (charge), $\boldsymbol{r}_{i\alpha}$, relative to $r_{\rm oco}$. If $|\boldsymbol{r}_{i\alpha}| = r_{\rm oco}$ the pseudo particle contributes to the force as if it would contain only 50 % of the total number of single particles that it originally contains. If $|\boldsymbol{r}_{i\alpha}| < r_{\rm oco}$ or $|\boldsymbol{r}_{i\alpha}| > r_{\rm oco}$ its contribution is clearly above 50 % and clearly below 50 % of its original contribution, respectively.

We studied the influence of a weight function having these properties and, unfortunately, we finally did not see any improvement in the time evolution of the systems. We will therefore not go into more details concerning the weight function. But we will keep in mind that – from that point of view – the HLC and the direct summation method in section 3.7 are not really comparable because the N^2 method in fact neglects some particles whereas the HLC code considers *all* in the form of ($H_{\rm max}$-1)-pseudo particles, provided that the HLC structure covers all N particles in the system.

3.6.7 Computational Time

As we have already estimated in section 3.6.3, the time spent by the HLC algorithm for computing the force contributions of the pseudo particles scales with N like $\mathcal{O}(N\log_3 N)$. In this section we will prove this estimation.

In the left panel of Fig. 3.9 we have plotted the processor time against the number of particles for constant volume fraction. As expected, the direct summation method (squares) scales like $\mathcal{O}(N^2)$ (upper dashed line). In comparison, the HLC code using both $H_{\rm max} = 2$ (triangles) and $H_{\rm max} = 3$ (upside down triangles) scales like $\mathcal{O}(N\log_3 N)$ over the whole N-range. For small N, the construction of the HLC structure (see Fig. 3.7 for wall boundaries and Fig. 3.8 for periodic boundaries) consumes relatively a lot of time dissembling the strong N-dependence of the computational complexity. This gives a higher time consumption as expected which becomes less and less dominant for increasing N, until the N-dependence turns into a (N^2)-scaling because of the increasing number of particles per cell (see the numbers close to each triangle in the figure). E.g., the largest system for which we have used $H_{\rm max} = 2$ even shows an averaged number of 69.5 particles per cell. It is clear that if a linked cell contains too many particles the algorithm becomes inefficient. This is why we have to switch to the next higher hierarchy for rather small particle numbers N. In the panel we see that we apply $H_{\rm max} = 3$ for $N \gtrsim$ 10,000 and, thenceforward, $t_{\rm CPU}$ indeed scales exactly with $\mathcal{O}(N\log_3 N)$ with increasing particle number. To summarize, for a given particle number N, we have to choose the appropriate $H_{\rm max}$ in order to keep the computational time

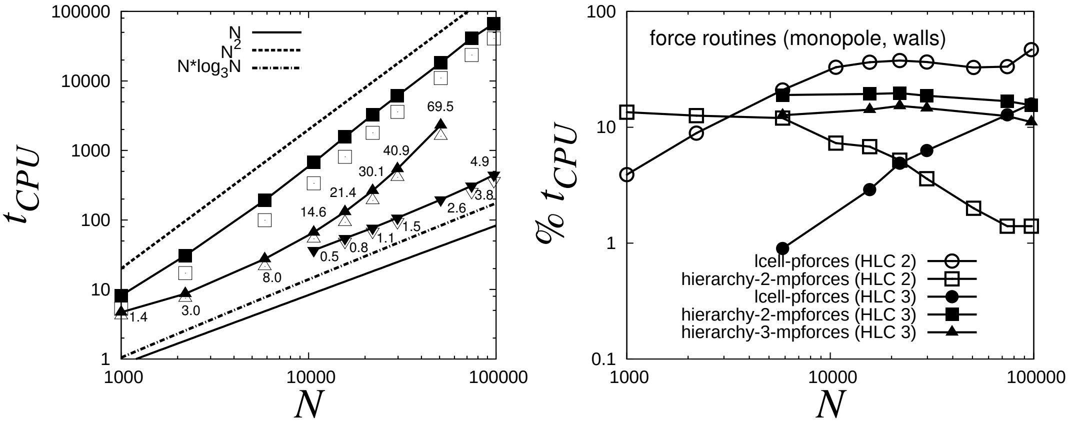

Figure 3.9: Benchmark[3] for homogeneous systems including a mutual $1/r$-long-range potential using the Hierarchical Linked Cell algorithm. (Left) Total CPU time, t_{CPU} (in CPU-seconds), taken for 100 time steps plotted against the particle number N. Solid symbols correspond to periodic, open symbols to wall boundaries. Squares denote results from direct summation, triangles denote HLC with $H_{\max} = 2$, upside-down triangles denote HLC with $H_{\max} = 3$. The given numbers correspond to the number of particles per linked cell for a given N and hierarchy level. (Right) The computational time of some important force-subroutines of the HLC in percent of the total CPU time plotted as function of N in case of wall boundaries.

expense as low as possible. In the right panel of Fig. 3.9, we have plotted the time expense of some subroutines of the HLC algorithm against N in percentage of the total time, t_{CPU}. Open symbols correspond to simulations where we used $H_{\max} = 2$, black symbols to simulations where we used $H_{\max} = 3$. The subroutine `lcell_pforces()` (circles) includes both the pair-wise summation of particles within the inner cut-off sphere and the particle-(pseudo particle) interactions of all hierarchies up to $H_{\max}$. The routines `hierarchy_2_mpforces()` (squares) and `hierarchy_3_mpforces()` (triangles) exclusively compute the force contributions in the hierarchy levels 2 and 3, respectively, and their percental CPU time decrease with increasing N. The decrease implies an increase of the percental complexity of another force routine. This will be the pair-wise summation in `lcell_pforces()` which makes it increasing (circles) with N. Because increasing N (i.e., increasing the size of the simulation volume) and keeping $H_{\max}$ constant means an increasing linked cell size. This increases the radius of the inner cut-off sphere, r_{ico}, wherein more particles will be treated pair-wise. The result will be an increase of `lcell_pforces()` in percentage of t_{CPU}, as shown

---

[3] The benchmark was performed on an Intel(R) Xeon(TM) processor with a 3.06 GHz CPU and 512 Mb RAM.

in the panel. All other routines not considered here (e.g., such as the ones that construct the HLC structure taking into account periodic or wall boundaries) contribute much less to the percental computational complexity, i.e., they consume a constant amount of time, independent of N.

3.7 HLC versus PP

In this section we evaluate the results of the HLC code as we have introduced in the last chapter. A way to do this, is to compare the results with those of a code that has implemented the pair-wise summation of the forces, as discussed in section 3.2. The implementation of the pair-wise treatment of the particles is straightforward and provides the most accurate results. However, accurate results by direct summation are obtained at the expense of computational time, see section 3.6.7.
In the following, we will present the fast $N \log N$ HLC algorithm in comparison with the accurate N^2 algorithm. In this sense, we will check the inter-particle forces and the time evolution of the temperature in a cooling granular gas with $r < 1$.

3.7.1 Bulk Force State

In this section we investigate how the long-range inter-particle forces act. We expect a behavior according to Eqs. (2.1) and (2.3). We perform a simulation with $N = 4913$ and periodic boundary conditions. For the simulation we use both the N^2 method and the HLC algorithm. We let the system evolve in 9,995 time steps and extract the force state of the bulk material from a snapshot thereafter. Furthermore, we shift the force at the point $r = r_{\text{oco}}$ such that it vanishes at the outer cut-off radius, r_{oco} (see section 3.6.6), i.e., for the potential and the force we obtain

$$\begin{aligned} \phi^{\text{shifted}}(r) &= \phi(r)\Big(1 - \frac{r}{r_{\text{oco}}}\Big)^2 \\ |\boldsymbol{F}^{\text{shifted}}(r)| &= -\frac{\mathrm{d}\phi(r)}{\mathrm{d}r} + \left(\frac{\mathrm{d}\phi(r)}{\mathrm{d}r}\right)_{r=r_{\text{oco}}} . \end{aligned} \tag{3.18}$$

In the left panel of Fig. 3.10 we show the repulsive long-range force between two particles in a double linear plot as a function of the separation distance. The solid curve corresponds to Eq. (2.3), the dashed line to the shifted force, see

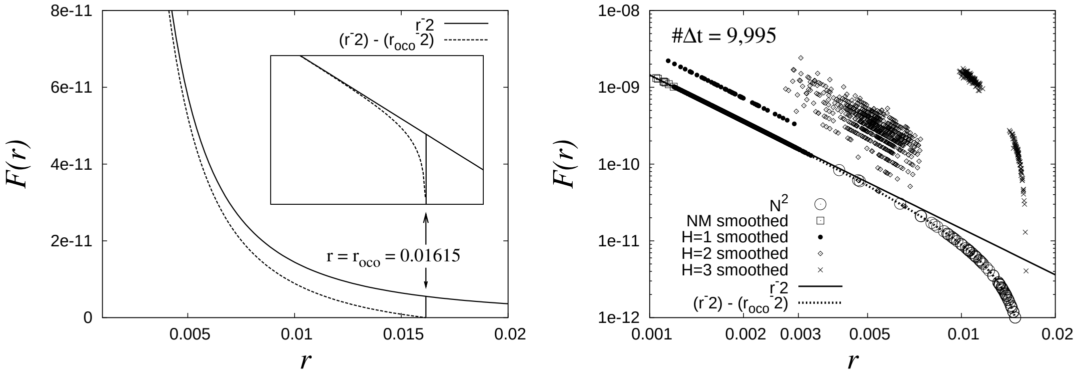

Figure 3.10: Force as a function of the inter particle distance. (Left) Eq. (2.3) (solid line) and Eq. (3.18) (dashed line). (Right) Data from both the N^2 (large open circles) and the HLC algorithm (other symbols). Single particle force contributions provide data coinciding with the dashed line, pseudo particle force contributions are stronger and lie above. Simulation specifications: $N = 4913$, $\nu = 0.076$, $c_b = +2{\cdot}10^7$, $r = 0.85$, $H_{\max} = 3$, $r_{\text{oco}} = 0.01615$. Data extracted from a snapshot taken after 9,995 time steps.

Eq. (3.18)[4]. The inset shows the same but in a double logarithmic plot. The right panel shows the results of the HLC code and the N^2 algorithm in a double logarithmic plot as well: in presence of a shifted potential, all those particles and pseudo particles that are close to the cut-off, $r_{\text{oco}} = 0.01615$, act with a repulsive force, $F(r)$, on the *poi* that drops to zero. Single particle force contributions lie on the dashed line. Pseudo particle force contributions lie above because they have a stronger influence on the *poi* due to the fact that they are composed of many single particles. The single particle contributions within the inner cut-off sphere (open squares) lie on the line as expected. The force contributions of the 26 pseudo particles in first hierarchy (solid circles) both lie on the line and on a line above. This means, that the pseudo particles consist of one and two single particles, respectively. The pseudo particles in second hierarchy show force contributions (open diamonds) that are even stronger, i.e., the pseudo particles consist of more than two single particles. Their contributions seem to be "quantized" which only reveals that the number of single particles within a pseudo particle is also "quantized". In the maximum hierarchy level ($H_{\max} = 3$), the force contributions (crosses) are strongest and show omitted distance domains while dropping to zero. This is due to the geometry of the HLC structure containing the cubic pseudo particles where distances between the pseudo particle and the *poi* simply cannot

---

[4] By computer simulations, we found that there is no significant difference in the time evolution of a repulsive N-body system whether the mutual potential is shifted or not. Thus, we will use in section 3.7.2 a non-shifted force and potential.

be covered. If we divide the force contribution of each pseudo particle by the number of single particles it contains, all the data will collapse onto the dashed line. We have verified this but not shown here. The collapse leads us to the conclusion that the HLC code provides correctly computed forces between the HLC pseudo particles and single particles in presence of periodic boundaries.

3.7.2 Temperature

In this section we evaluate how well the results of the HLC code coincide with those of the direct summation method. Like every model that claims a vast agreement with "reality" (here represented by the N^2 method), also the HLC code will not provide full agreement.

The simulation specifications are as follows: we do not consider a cut-off sphere for the HLC code as discussed in section 3.6.6, nor do we consider a shifted potential for both the HLC and the N^2 code as expressed by Eq. (3.18) and use periodic boundary conditions. For the purpose of evaluation, we anticipate some results from chapter 4 and will refer to this chapter as soon as we need more information.

We will evaluate the quality of the results of the HLC code by focussing on the time evolution of the thermal energy of a dissipative system with both repulsive and attractive long-range forces. Figs. 3.11 and 3.12 show the double logarithmic plot of the decaying thermal energy, $mT_g(t)$, in units of the present long-range potential at contact, E_b or E_e (see Sec. 2.2), plotted against time, t, for different densities, ν. In the repulsive case, Fig. 3.11, we clearly see that the HLC results significantly deviate from the results obtained by the N^2 method as soon as the thermal energy drops noticeably below E_b. The horizontal line indicates the order parameter, $mT_g(t)/E_b$, as being unity. So, we can rely on the results of the HLC code as long as $mT_g(t) \gtrsim E_b$. Surprisingly, for high densities ($\nu = 0.152$, bottom panels), the limit line of confidence can be shifted towards lower values than $mT_g(t)/E_b = 1$.

Moreover, the HLC code can distinguish between two ways of force calculation:

Monopole Force Contribution Only. We truncate the Taylor series expansion of Eq. (2.12) at the dipole term, $\phi_{i\alpha}^{(D)}$ and $\boldsymbol{F}_{i\alpha}^{(D)}$, respectively. The dipole contribution itself vanishes because we implemented the force contributions such that it is $\boldsymbol{P}^\alpha = \boldsymbol{R}^\alpha$ (cf. Fig. 2.2 and appendix B). So, in Fig. 3.11, we present the monopole force contribution only by solid squares ("HLC (H2) m").

Monopole & Quadrupole Force Contribution. In this case, we truncate the Taylor series expansion of Eq. (2.12) at the quadrupole term, $\phi_{i\alpha}^{(Q)}$ and $\boldsymbol{F}_{i\alpha}^{(Q)}$, respectively. I.e., for the simulations in Fig. 3.11, both the monopole and the quadrupole term contribute to the force computation ("HLC (H2) m+q").

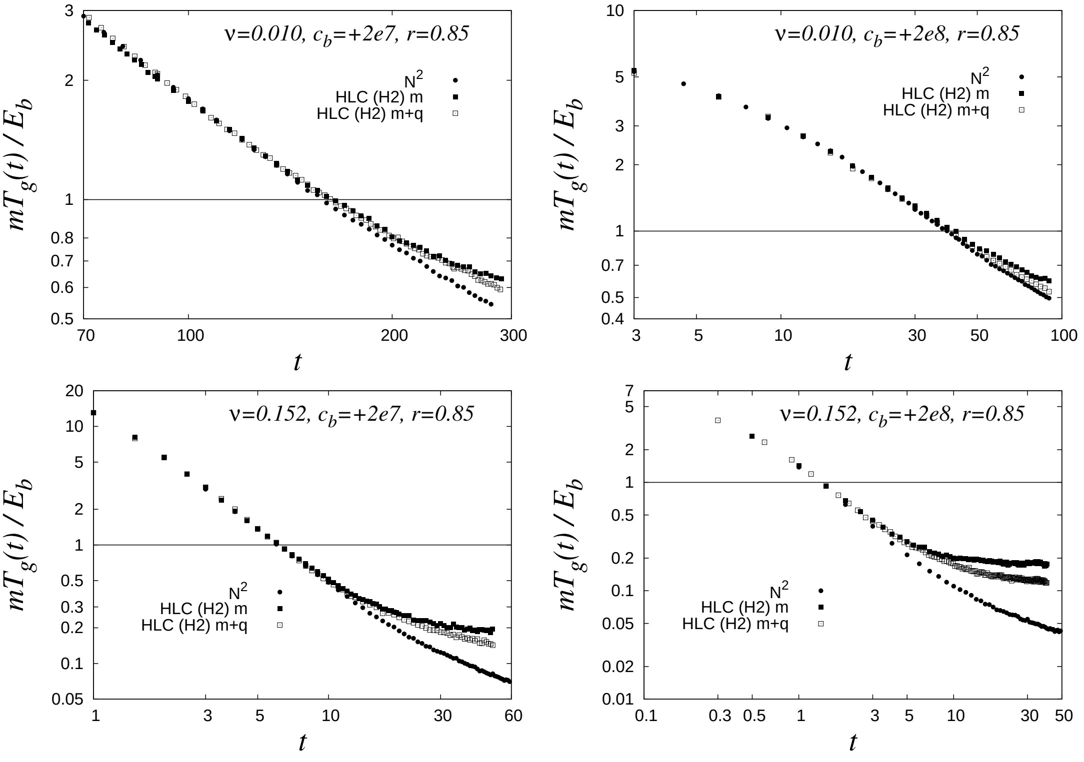

Figure 3.11: The repulsive case: comparing the HLC algorithm ("HLC") with the standard particle-particle method ("N^2", solid circles). HLC with monopole contribution only ("m", solid squares) and additionally with quadrupole contribution ("m+q", open squares). From top to the bottom: densities 0.010 and 0.152. (Left) For the repulsion strength $c_b = +2 \cdot 10^7$. (Right) For the repulsion strength $c_b = +2 \cdot 10^8$.

From Fig. 3.11 we see, that the results provided by direct summation are supposed to be most accurate, and the order parameter has decreased strongest for a given time if we look at the domain where $mT_g(t)/E_b < 1$. So, the results of the HLC code show a less strong decaying order parameter, resulting in a weaker cooling behavior, whatever multipole contribution we applied. In the repulsive case, the HLC code appears to provide a *weaker* long-range potential. As expected, the code including both the monopole and quadrupole computation (open squares) provides results that are closer to those of the N^2 code than the HLC code without quadrupole contributions.

The same "improvement" we see for the attractive case[5] in Fig. 3.12. In contrast

---

[5] In attractive dissipative particle systems, the kinetic energy decays until the system becomes strongly inhomogeneous (for this, we refer to section 4.4) and the transition is indicated by a sudden increase of the kinetic energy.

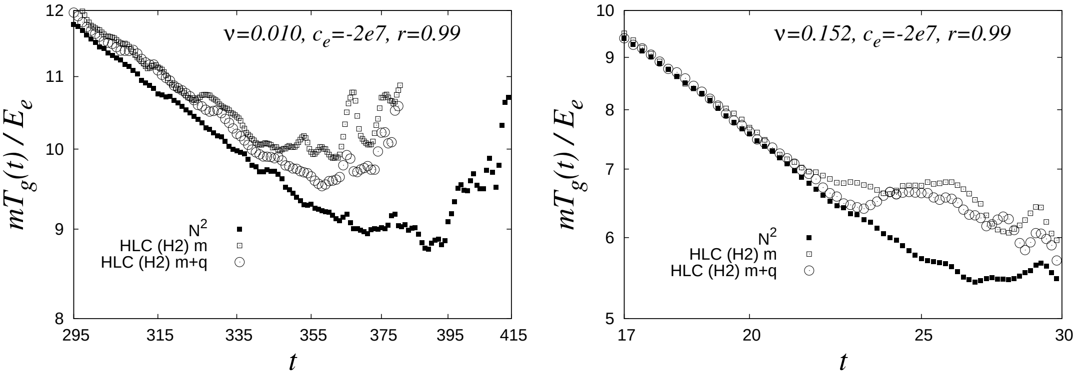

Figure 3.12: The attractive case: comparing the HLC algorithm ("HLC") with the standard particle-particle method ("N^2", solid squares). HLC with monopole contribution only ("m", open squares) and additionally with quadrupole contribution ("m+q", open circles). (Left) For the density 0.010. (Right) For the density 0.152.

to the direct summation method, the HLC code shows an earlier increase of the order parameter, indicating an earlier transition from the homogeneous to the inhomogeneous regime.

In contrast to the repulsive case, for the attractive case, the HLC structure provides a *stronger* mutual potential that makes the transition regime setting in earlier in time. Furthermore, just like in the repulsive case, the HLC code including both mono and quadrupole terms provides a little "improvement" of the results, i.e., the rapid increase of the order parameter is slightly delayed (open circles) towards the N^2 results as compared to using the monopole contribution only (open squares), see both panels of Fig. 3.12. Thus, the implementation of the quadrupole contribution provides improved results, as expected.

3.7.3 Error Estimation

In this subsection we will estimate the error of the force calculation made by the HLC code due to the geometrical arrangement of the pseudo particles. We will use the geometrical specifications of a typical simulation of $N = 1000$ particles as performed in the preceding sections. The length of the simulation volume is $L/l_{\mathrm{LC}} = 9$ and we choose a density of $\nu = 0.152$.

We assume that the distance ratio, $r_{i\alpha}/\left\langle r_{j\alpha}\right\rangle$, is almost independent on the number and spatial distribution of the particles. In particular, the error, e, is only dependent on the distance ratio but not dependent on the choice of c_b and m. This means, particle constellations with a differently strong long-range force contribution on the *poi*, but with the same distance ratio, will give the same error

	hierarchy 1		hierarchy 2	
direction	$r_{i\alpha}/l_{\mathrm{LC}}$	$\langle r_{j\alpha}\rangle/l_{\mathrm{LC}}$	$\langle r_{i\alpha}\rangle/l_{\mathrm{LC}}$	$\langle r_{j\alpha}\rangle/l_{\mathrm{LC}}$
(1 0 0)	1.0...1.5	0.16	2.5...3.5	0.5
(1 0 1)	1.0...2.1	0.24	3.5...4.9	0.7
(1 1 1)	1.0...2.6	0.29	4.3...6.1	0.9
$r_{i\alpha}/\langle r_{j\alpha}\rangle$	6.7		5.9	
	"m"	"m+q"	"m"	"m+q"
e	0.022	0.006	0.028	0.008

Table 3.1: Typical distances, $r_{i\alpha}$, between a pseudo particle α and the *poi* i, and between the particles in α and α's center of mass (charge), $r_{j\alpha}$, in units of a linked cell size, l_{LC}, in different direction of α from i. Different directions provide different distances, which we consider for the computation of $r_{i\alpha}/\langle r_{j\alpha}\rangle$. e is the error of the force computation by the HLC code as compared to the N^2 method for both the monopole contribution excluding the quadrupole term ("m") and including it ("m+q").

for the monopole and quadrupole contributions. So, although the particle constellation we used for the error estimation of the test particle configuration (see case (4) in Fig. 2.3) is different from that in a typical simulation, we can confer the error estimation in the left panel of Fig. 2.4 on the HLC results. From table 3.1 we can determine the typical distance ratios, $r_{i\alpha}/\langle r_{j\alpha}\rangle$, for hierarchy 1 and 2 of a HLC simulation. Conferring these distance ratios on the left panel of Fig. 2.4, we can extract the error made by the force computation for hierarchy 1 and 2 both including and excluding the quadrupole terms. The resulting e is given in the last line of the table. For calculating the distance ratio, we take the mean distance obtained by the three possible arrangements of the cubic pseudo particle relative to the particle of interest: along the edge of the cell of interest in (1 0 0) direction, along the face diagonals of the *coi* in (1 0 1) direction and along the space diagonals of the *coi* in (1 1 1) direction. The direction notation corresponds to the notation according to Miller's indices that are commonly used in solid state physics. We see that hierarchy 2 can contribute a larger error than hierarchy 1 although the corresponding pseudo particles are farther away from the *poi*. As we can see, in the worst case, errors of the order of 3 % in the monopole force contribution of hierarchy 2 can occur and might lead to the deviations between the results, seen in Figs. 3.11 and 3.12, as soon as the particles' long-range potential becomes strong as compared to the actual system's thermal energy.

3.8 Summary

An intuitive approach for calculating long-range forces is to compute for all particles the interaction force with all others. This requires a direct summation of the forces of all particles acting on a *poi*. But this requires a computational complexity of $\mathcal{O}(N^2)$ which is not acceptable for large particle numbers N. Therefore many techniques have been invented that scale down the computational time to $\mathcal{O}(N\log N)$ or even to $\mathcal{O}(N)$. These techniques can be divided into two main categories:
(i) where distant particles are grouped together to pseudo particles in a tree-like hierarchy and then act on each particle, and (ii) where all particles are smeared out over the whole simulation volume and their potential is evaluated on a grid. Once obtained all the forces acting on each particle by either method (i) or (ii), a Molecular Dynamics environment will be able to integrate *Newton*'s equations of motion by means of an adequate integration scheme such as *Verlet*'s algorithm in our case.
Another algorithm that provides the long-range forces on the particles is the Hierarchical Linked Cell algorihm (HLC) we incorporated into an MD environment. The HLC is based on the linked cell structure which is a standard neighborhood search algorithm. The reduction in computational time is achieved by considering the particles in linked cells as pseudo particles and by combining them hierarchically up to larger pseudo particles. Cells of different hierarchies represent differently large pseudo particles at different distances to a *poi*.
The computational time required for the HLC code was found to be $\mathcal{O}(N\log_3 N)$ theoretically and numerically for homogeneous systems. As an example, a typical simulation time of 9,000,000 time steps, performed by an N^2 simulation with $N = 5832$ particles, takes approximately 235 days wall-clock time on an Intel single processor with a 3 GHz CPU. Using $H_{\max} = 2$, it will take about 166 days and with $H_{\max} = 3$ about 26 days, employing the HLC method. The results of the HLC code agree with those of the direct summation code for the repulsive case as long as the condition $mT_g(t) \gtrsim E_b$ is fulfilled. As soon as the thermal energy of the system drops significantly below the mutual repulsive potential at contact, the HLC code leads to weaker cooling, see Fig. 3.11. This observation is independent of the potential strength and density of the system. The same we found for the attractive case but not for such low temperatures. To summarize: for the same $mT_g(t)$, HLC provides better results for smaller E_b (E_e). Finally, the additional use of quadrupole terms for the force computation shows little improvement in both the attractive and the repulsive case.

4 Dilute Homogeneous Particle Systems

In this chapter we will focus on dilute homogeneous particle systems with both long-range repulsion and attraction forces and investigate the interplay between dissipation and long-range forces. In order to obtain accurate results from the simulations, we make use of the straight-forward direct summation method, where each particle interacts with all other particles. This, of course, limits us to small particle numbers.

4.1 Fundamental Properties

In the following subsections, fundamental facts and properties which are important for the description of granular gases such as “granular temperature” and “pair distribution function” are defined and explained in order to be prepared for the subsequent investigation of dilute granular media: in section 4.2 granular gases without long-range forces are introduced as reference. Repulsive and attractive long-range forces are discussed in sections 4.3 and 4.4, respectively, and are compared with the reference results of section 4.2. The summary in 4.5 provides a brief overview of the results of this chapter.

4.1.1 Granular Temperature

The average kinetic energy per particle in a homogeneous poly-disperse particulate system with N discrete particles with masses m_i and velocities $\boldsymbol{v}_i(t)$ is

$$\overline{e}_{\mathrm{kin}}(t) = \frac{E_{\mathrm{kin}}(t)}{N} = \frac{1}{N}\left(\frac{1}{2}\sum_i^N m_i \boldsymbol{v}_i^2(t)\right) \quad , \tag{4.1}$$

where $E_{\mathrm{kin}}(t)$ is the total kinetic energy of the system. The velocities are time dependent due to dissipative collisions. The motion of the particles consists of a macroscopic flow of all particles and their velocity fluctuations that superpose the (bulk) flow. These fluctuations can be understood as a random movement of the particles, similar to the random motion of pollen grains suspended in water[1].

---

[1] The random motion is commonly denoted as “Brownian motion”. In Ref. [27] the random movement of pollen grains is due to their interactions with the randomly moving molecules of the liquid.

The fluctuating velocity is described by the variance $\sigma_v^2(t)$ of the distribution of the particles' velocities around their mean $\langle \boldsymbol{v}(t)\rangle = (1/N)\sum_i^N \boldsymbol{v}_i(t)$:

$$\sigma_v^2(t) := \frac{1}{f\,\langle m\rangle}\sum_i^N \frac{m_i}{N}\Big(\langle \boldsymbol{v}(t)\rangle - \boldsymbol{v}_i(t)\Big)^2 = \frac{1}{f}\Big(\langle \boldsymbol{v}^2(t)\rangle - \langle \boldsymbol{v}(t)\rangle^2\Big)\ , \tag{4.2}$$

where $\langle m\rangle = \sum_i^N m_i/N$ is the average mass of a particle and $\sigma_v(t)$ is the standard deviation of the distribution of the velocities. $f = 3$ is the number of degrees of freedom in the case of only translational motion of the particles in three dimensions. In this thesis we will use the definition of the so-called granular temperature, $T_g(t) := \sigma_v^2(t)$. If there is no macroscopic (average) flow of the particles in the gas, i.e., $\langle \boldsymbol{v}(t)\rangle^2 \ll \langle \boldsymbol{v}^2(t)\rangle$ as assumed in this chapter, the granular temperature of the particles simplifies to

$$\begin{aligned} T_{\mathrm{g}}(t) &\approx \frac{\langle \boldsymbol{v}^2(t)\rangle}{3} \\ &= \frac{1}{3\,\langle m\rangle}\sum_i^N \frac{m_i}{N}\boldsymbol{v}_i^2(t) \\ &\overset{(4.1)}{=} \frac{2}{3\,\langle m\rangle}\frac{E_{\mathrm{kin}}(t)}{N}\ . \end{aligned} \tag{4.3}$$

If we compare the granular temperature of the particles with its counterpart from Thermodynamics, $T(t) = 2E_{\mathrm{kin}}(t)/(3Nk_B)$, we realize that the Boltzmann constant k_B is in our context equivalent to the average particle mass $\langle m\rangle$ and the units change from degrees Kelvin for $T(t)$ to units of a squared velocity for $T_g(t)$. $T_g(t)$ will be used in the following for mono-disperse particles with uniform masses m and radii a.

Per se, granular gases are systems with inelastically colliding bodies. However, granular systems with very weak inelasticity exhibit molecular gas like behavior and collisions will hardly support any loss of kinetic energy. The *equipartition theorem* of standard Thermodynamics does hold and breaks down for stronger dissipative granular gases [47,48]. So, the velocity distribution in elastic granular systems also can simply be obtained by replacing the Boltzmann constant k_B within the *Maxwell-Boltzmann* distribution function by the granule mass m,

$$\rho(\{\boldsymbol{v}\}) = \left(\frac{1}{2\pi T_g(\infty)}\right)^{3/2}\exp\left(-\frac{\boldsymbol{v}^2}{2T_g(\infty)}\right)\ , \tag{4.4}$$

if we assume the gas to be in thermal equilibrium at $t \to \infty$. Eq. (4.4) is the phase space distribution function of appendix A.3 integrated over all particle positions. In order to obtain the number fraction $\mathrm{d}N(v)$ of particles within the

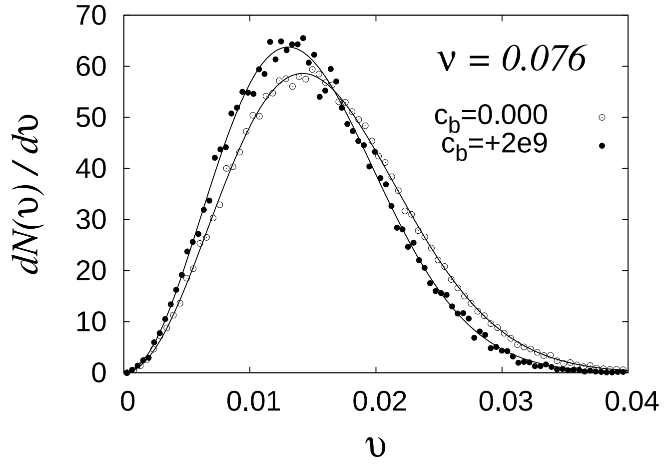

Figure 4.1: The Maxwell-Boltzmann velocity distribution function of an elastic granular gas with volume fraction, $\nu = 0.076$, at equilibrium state ($t \to \infty$) for the case without repulsion ($c_b = 0$) and with repulsion intensity ($c_b = +2 \cdot 10^9$).

velocity interval $[v, v + \mathrm{d}v]$ we simply set (in three dimensions[2]) for the number of particles within a spherical shell in the velocity space

$$\mathrm{d}N(v) = 4\pi v^2 \rho(\{\boldsymbol{v}\})\ \mathrm{d}v \quad . \tag{4.5}$$

$\mathrm{d}N(v)/\mathrm{d}v$ is the well-known Maxwellian number probability distribution function in three dimensions for the whole velocity range the particles in the gas cover. As soon as inelastic collisions between the particles take place, the concept of equipartition of kinetic energy breaks down and the velocity distribution is not Maxwellian anymore. An approach for the velocity distribution function for dissipative many-body systems is introduced in and uses a Sonine polynomials expansion of $\rho(\{\boldsymbol{v}\})$ [13, 30].

Moreover, as shown in many textbooks, the Maxwell velocity distribution is the same for any interaction potential, including long-range interactions we focus on here. Fig. 4.1 shows the Maxwell-Boltzmann velocity distribution according to Eqs. (4.4) and (4.5) for long-range repulsive forces ($c_b = +2 \cdot 10^9$) and without ($c_b = 0$). The velocity distributions are fitted (solid lines), and in the case of $c_b = 0$ we obtain $mT_g(\infty) \approx 1.05 \cdot 10^{-10}$ (where $m = 1.0472 \cdot 10^{-6}$) and for the standard deviation of the velocities $\sigma_v(\infty) \approx 3.9 \cdot 10^{-3}$. In case of $c_b = +2 \cdot 10^9$ we have $mT_g(\infty) \approx 8.9 \cdot 10^{-11}$ and $\sigma_v(\infty) \approx 3.6 \cdot 10^{-3}$.

---

[2] In one dimension ($f = 1$) we obtain the number fraction $2\pi\rho(\{v\})\mathrm{d}v$ and the power $3/2$ in Eq. (4.4) becomes $1/2$. Note, that the standard deviation for $f = 1$ is $\sigma_v(\infty) = \sqrt{T_g(\infty)}$ and for $f = 3$, we have $\sigma_v(\infty) = \frac{1}{\sqrt{3}}\sqrt{3 - 8/\pi}\sqrt{T_g(\infty)} \approx 0.39\sqrt{T_g(\infty)}$.

The fact that a repulsive system is cooler than systems without long-range forces depends on the preparation of the initial configuration, i.e., which initial temperature we will give to the system.

4.1.2 Excluded Volume

For defining a granular temperature, the consideration of particles as point masses is sufficient. In real granular gases, however, particles have a finite volume and the correct measurement of observables, such as the collision frequency, requires the consideration of the particle size. Contrary to point masses, for a given volume fraction

$$\nu = \frac{N}{V}\frac{4}{3}\pi a^3 \quad ,$$

where V is the simulation volume. particles with uniform radius $a > 0$ have less space available for moving due to their mutual exclusion caused by their physical dimension. The higher the volume fraction the stronger particles interact with each other. The effect of restricting the particles' free space for motion is referred to as the *effect of excluded volume.*

The equation of state of an ideal (granular) gas expresses the relation between the state quantities of the gas such as pressure and density and has to be modified due to the excluded volume effect. Particles will be considered as hard spheres that cannot penetrate each other, which leads to the definition of the hard sphere potential,

$$\phi(r_{ij}) = \begin{cases} +\infty & \text{for } |\boldsymbol{r}_{ij}| \leq 2a \\ 0 & \text{for } |\boldsymbol{r}_{ij}| > 2a \end{cases} \quad , \tag{4.6}$$

where we assume mono-disperse particles with uniform radius a. This will lead to an increased pressure (and increased collision frequency) as compared to the case we would consider for a granular gas composed of point masses (with zero diameter). The equation of state for a granular gas can then be expanded in ascending powers of ν and it is found

$$\begin{aligned} \frac{pV}{(3/2)NmT_g} &= 1 + 4\nu + 10\nu^2 + 18.36\nu^3 + 28.2\nu^4 + 39.5\nu^5 + \ ... \\ &\approx 1 + 4\nu\frac{1-\nu/2}{(1-\nu)^3} \quad , \end{aligned} \tag{4.7}$$

which is referred to as the *virial expansion* of the equation of state [16,45,46,103]. The right-hand-side of Eq. (4.7) contains the *pair distribution function* at contact, $r_{ij} = 2a$,

$$g(2a) = \frac{1-\nu/2}{(1-\nu)^3} \tag{4.8}$$

(see section 4.1.3). The hard sphere potential is defined by only one parameter a and so is the right-hand-side of Eq. (4.7). For hard spheres including two-particle long-range interactions, the right-hand-side of Eq. (4.7) will have additional parameters that define the new interaction potential. Especially for Coulomb interactions, the equation of state turnes out to be a non-analytic function of density [104]. Eq. (4.8) takes into account the increased probability to find a neigboring particle at $r_{ij} = 2a$. Repulsive Coulomb forces will lead to a decreased probability whereas attractive Coulomb forces will additionally lead to an increased probability. In section 4.3.1 we show that $g(2a)$ has then to be completed by an exponential factor which considers the modified probabilities.
For very dilute gases, $a \to 0$ and $\nu \to 0$ (decreasing ν can be achieved by decreasing a while keeping N and V constant), Eq. (4.7) becomes the equation for the ideal granular gas, $pV = \frac{3}{2}NmT_g(t) = E_{\text{kin}}(t)$.

4.1.3 Pair Distribution Function

The *pair distribution function* or reduced one-particle distribution function at contact (→ appendix A.3), $g(2a)$, enters the equation of state Eq. (4.7). $g(r_{ij})$ provides information about how the neighborhood of a reference particle i is structured, i.e., counts the number ΔN of neighboring particles j depending on the radial distance r_{ij}. Then the number of particles in a spherical shell around i with volume $4\pi r_{ij}^2 \Delta r_{ij}$ is

$$\Delta N = 4\pi r_{ij}^2 \Delta r_{ij} n^*(r_{ij}) \quad , \tag{4.9}$$

where Δr_{ij} is the width of the shell and

$$n^*(r_{ij}) = n g(r_{ij}) \tag{4.10}$$

is the local number density (at distance r_{ij} from i). Eq. (4.9) provides information about how the distances between all pairs of particles are distributed in the system [45, 58, 98] and we have in the continuous case

$$g(r_{ij}) = \frac{n^*}{n} = \frac{1}{4\pi r_{ij}^2 n} \frac{\mathrm{d}N(r_{ij})}{\mathrm{d}r_{ij}} \quad . \tag{4.11}$$

If the pair distances are equally distributed (case of an ideal gas, $g(r_{ij}) = 1$), we can set $n^* \to n$ if the system is assumed to be homogeneous, i.e., if we assume $n = N/V$ as the number density of the bulk material. From the reference particle's point of view we then will find for each distance the same number of neighboring particles. If the particles do not move independently from each other, i.e., if they interact via collisions and even via long-range repulsive or attractive forces, $g(r_{ij})$ will be different from unity which corresponds to different particle

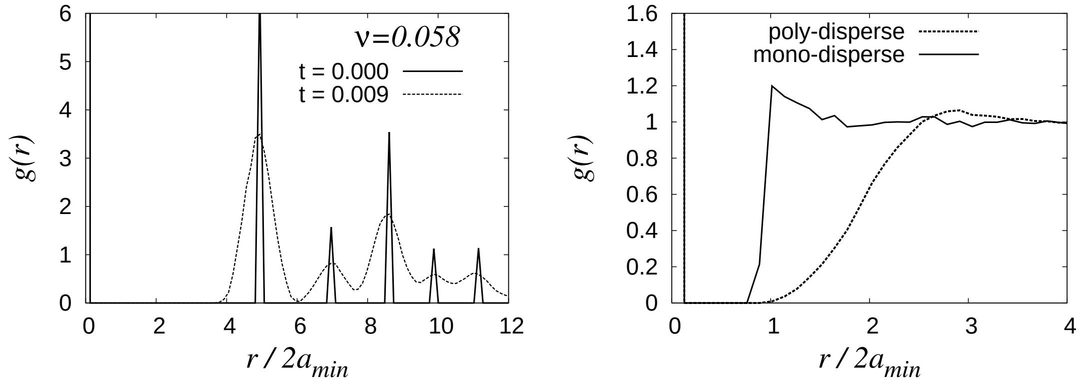

Figure 4.2: (Left) A *hcp*-packing of $N = 8000$ particles at the very beginning of the simulation, $t = 0$ (solid line), and after a short time, $t = 0.009$ (dashed line). (Right) A random packing of a mono-dispersed (solid line) and poly-dispersed (dashed line) particle system with $N = 1000$. The vertical line on the left indicates the fact that the particle of interest is detected by itself.

number densities in the shells. Two-particle interactions of any kind will cause $g(r_{ij})$ to deviate from unity and are considered as *correlations* between the particles. This means that interactions are dependent on particles' locations and the assumption of *molecular chaos*[3] breaks down.

In Fig. 4.2 the pair distribution function is plotted against the inter-particle distance r_{ij} in units of the minimum diameter $2a_{\text{min}}$ for a crystalline (left) and a random poly-disperse arrangement (right) of particles with rather low density. In the initial crystalline case which is a hexagonal closest packing (*hcp*) with lattice spacings of 10 a_{min} in x, y-direction and 14.14 a_{min} in z-direction, $g(r_{ij})$ shows well defined peaks that correspond to high densities at the distance of the nearest, second-nearest, third-nearest, etc. neighbors. In-between there are geometrically excluded regions where the density is zero and no particle can be found.

If we melt the crystal, particles leave their original locations due to their initial random velocity components and come therefore closer to each other. This leads to a significant broadening of the peaks as displayed by the dashed line in the left panel of Fig. 4.2. After much longer time, a random arrangement is found. Equilibriated systems including collisions but no long-range forces (Fig. 4.2, right) show at $r_{ij} \approx 2a_{\text{min}}$ correlated behavior (due to collisions and excluded volume)

---

[3] Molecular chaos denotes the assumption that particles' locations have no influence on the particles' velocities and, thus, on collisions. Then, the reduced two-particle distribution function can be factorized such that the factors depend on the locations and velocities separately, $\rho(\boldsymbol{r}_{ij}, \boldsymbol{v}_i, \boldsymbol{v}_j, t) = \rho(\boldsymbol{r}_{ij})\rho(\boldsymbol{v}_i, t)\rho(\boldsymbol{v}_j, t)$. Usually we introduce the pair distribution function as $\rho(\boldsymbol{r}_{ij}) = g(\boldsymbol{r}_{ij})$. Moreover, $g(\boldsymbol{r}_{ij})$ is the reduced one-particle distribution function $g(r_{ij})$ (see appendix A.3) because the pair distances depend effectively only on the scalar quantity r_{ij}.

whereas at large pair distances $g(r_{ij})$ becomes unity because particles have no (collisional) influence at all on each other. In comparison with mono-disperse particles, for poly-disperse particles with radii $a \in [a_{\min}, 3a_{\min}]$ the slope at the beginning is less strong because the reference particle will "see" contacting particles not only at $r_{ij} = 2a_{\min}$ but also up to the distance $r_{ij} = 6a_{\min}$. This gives a monotone increase of the probability to find a particle between $2a_{\min}$ and $6a_{\min}$. The influence of long-range forces on the distribution function will be discussed in section 4.3.1 in more detail.

4.2 Systems without Long-Range Interactions

The understanding of properties such as temperature and the pair distribution function makes the discussion of the time evolution of quantities such as the rate of dissipated kinetic energy in homogeneous systems easier. As a reference, we first discuss the time evolution of systems without mutual long-range interaction potentials in order to compare the influence of long-range interactions in the next chapters. Furthermore, this is a first check of the code regarding the treatment of collisions only in discrete particle systems with periodic boundary conditions (see section 3.6.5), for which analytical solutions are known [43].

4.2.1 Collision Frequency

The collision frequency or collision rate is defined as the number of collisions per unit time and per particle. Assuming Gaussian velocity distributions, the collision frequency of the homogeneous cooling state is the Enskog collision frequency and reads, according to Eq. (A.17),

$$f_E^0(t) = 16na^2\sqrt{\pi}g(2a)T_g^{1/2}(t) \quad , \tag{4.12}$$

where the Enskog correction factor, $g(2a)$, is applied in order to take also finite densities ν into account. This applies also for the kinetic energy, for which we have shown in Fig. 4.4 the difference between *Haff*'s theory including Enskog's correction (solid lines) and *Haff*'s theory excluding the correction (dashed lines, indicated by "$g(2a) = 1$"). $f_E^0(t)$ expresses the number of collisions *one* particle will have during a unit time. The superscript "0" denotes the case that no long-range forces are considered. We will show in section 4.2.2 that the coefficient of normal restitution, r, enters Eq. (4.12) via the granular temperature, $T_g(t)$.

From the simulations, $f^0(t)$ can be computed by recording the total number of (binary) collisions that appear in our system until the time t of observation. Then there were $2C(t)$ particles involved in these binary collisions. For obtaining the mean number of particle collisions per particle counted within the time interval

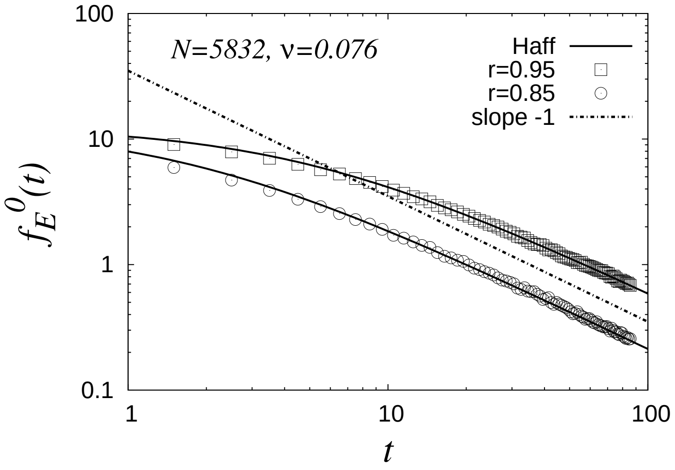

Figure 4.3: A homogeneous system without long-range particle interactions with $N = 5832$. Collision frequency, $f_E^0(t)$, obtained from Eq. (4.13) (symbols) compared with Enskog theory, Eq. (4.15) (solid lines, denoted as "Haff").

$0...t$, we still need to divide this expression by N, obtaining $(2/N)C(t)$. With the time derivation of $C(t)$ we get the number of single particle collisions for a particle per unit time, i.e., the "measured" collision frequency,

$$f^0(t) = \frac{2}{N}\frac{\mathrm{d}C(t)}{\mathrm{d}t} \quad . \tag{4.13}$$

Fig. 4.3 shows the double logarithmic plot of the collision frequency per time and particle as it is calculated from Eq. (4.13) using the results of the simulations. Note the small discretization error from Eq. (4.13) for short times for which the time intervals are rather large.
Anyway, in the following we set $f_E^0(t) \equiv f^0(t)$ and $f_E(t) \equiv f(t)$ because simulation results ("measurements") agree quite well with Enskog's theory.

4.2.2 Kinetic Energy and the Homogeneous Cooling State

Assume (besides fluctuations) a homogeneous density. If the energy density persistently decreases everywhere in the system at the same rate, we will speak about *homogeneous cooling* as we focus on in more detail in appendix A.5. The ordinary differential equation for the energy dissipation rate we derived there, Eq. (A.26), can be solved analytically and its solution is denoted as *Haff*'s law,

$$E_{\text{kin}}(t) = \frac{E_{\text{kin}}(0)}{\left(1 + \frac{1}{2}f_E^0(0)(1-r^2)t\right)^2} \quad , \tag{4.14}$$

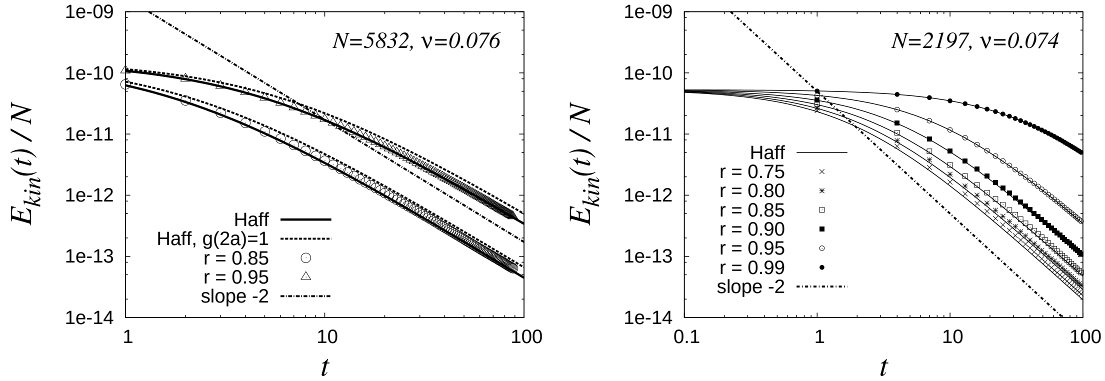

Figure 4.4: (Left) Kinetic energy per particle plotted against time according to Eq. (4.14), with (solid lines) and without (dashed lines) correction factor, $g(2a)$. (Right) Kinetic energy per particle plotted versus time for different coefficients of normal restitution, r. Symbols are simulation data, solid lines correspond to Eq. (4.14).

which describes the decay with time of the kinetic energy of *homogeneous* dissipative granular gases. For large times, we have a decay proportional to $1/t^2$. With Eqs. (4.3) and (4.14) we obtain also the time dependence of the collision frequency from Eq. (4.12):

$$f_E^0(t) = \frac{f_E^0(0)}{1 + \frac{1}{2} f_E^0(0)(1 - r^2)t} \ , \tag{4.15}$$

where $f_E^0(0)$ is the initial collision frequency at $t = 0$. We have already seen the time behavior of $f_E^0(t)$ in Fig. 4.3. Fig. 4.4 shows simulation data and the theoretical prediction for the time behavior of $E_{\text{kin}}(t)$ in a double logarithmic plot. In the left panel we see the improvement of the prediction, see Eqs. (4.14) and (4.12), by considering the pair distribution function at contact, $g(2a)$, (solid lines) compared with the case in which we set $g(2a) = 1$ (dashed lines). If the energy decay can be described by Eq. (4.14) we deal with a regime which features the successive decay of kinetic energy due to dissipative collisions which is referred to as the homogeneous regime or the homogeneous cooling state (in the following abbreviated by HCS, see, e.g., [70]). The right panel shows the double logarithmic plot for different values of the parameter r. Independently from r and from N, all the simulations show an energy decay with $1/t^2$ for large times, and the stronger the dissipation the worse the theoretical prediction of Eq. (4.14).

Deviation from the Homogeneous Regime (Clustering)

The small deviations of the energy decay from the analytical prediction in the right panel of Fig. 4.4, clearly seen for, e.g., $r = 0.75$, stems from weak cluster formation which is caused by strong dissipation. The cluster growth will lead to a strongly inhomogeneous regime in which many clusters are formed - not shown in our simulations. According to [84, 85], in this cluster regime, the evolution of kinetic energy will not behave anymore like $\propto 1/t^2$ but will rather proceed as $\propto 1/t$ (also not shown here). The collision frequency will then decay weaker than $\propto 1/t$. Much later, the cluster-growth regime will pass into the saturation regime where only one final cluster has formed. Here, the decay of kinetic energy and collision frequency will again be the same as for the HCS regime [84]. Furthermore, a cluster growth-regime is also observed for dissipative systems that are governed by long-range attractive forces, see section 4.4.

4.2.3 Dissipation Rate

The energy dissipation rate is defined as the amount of dissipated kinetic energy due to dissipative collisions per time period. From Eqs. (A.23) and (A.26) we define

$$I^0(t) := 3V\gamma(t) = \frac{\partial E_{\mathrm{kin}}(t)}{\partial t} = -\frac{N}{2} f_E^0(t)(1-r^2) m T_g(t) \tag{4.16}$$

as the dissipation rate for granular gases without long-range forces. In contrast to the collision frequency and the kinetic energy, which change their behavior with time, the dissipation rate decays always with $\propto T_g^{3/2}(t)$. For a certain temperature, $mT_g(t)$, there will be a larger loss of kinetic energy for stronger dissipation, as we can see in Fig. 4.5. Here, the dissipation rate is extracted from the simulation by computing the time derivative of the decaying kinetic energy, according to Eq. (4.16).

4.2.4 Summary

Dissipative, homogeneous granular gases show an ongoing decay of their total kinetic energy due to dissipative binary collisions between the particles. The pair correlation function at contact, $g(2a)$, takes particles with finite size into account and provides better agreement between theory and simulation. For large times, the decay follows $\propto 1/t^2$ whereas the collision frequency, $f_E^0(t)$, decreases like $\propto 1/t$ in time. As long as this is valid, the corresponding state of the system is referred to as the homogeneous cooling state and can be described by *Haff*'s law (4.14) and (4.15). Slight deviations from homogeneity, especially for cases of strong dissipation (small r), lead to deviations of simulation data from *Haff*'s law.

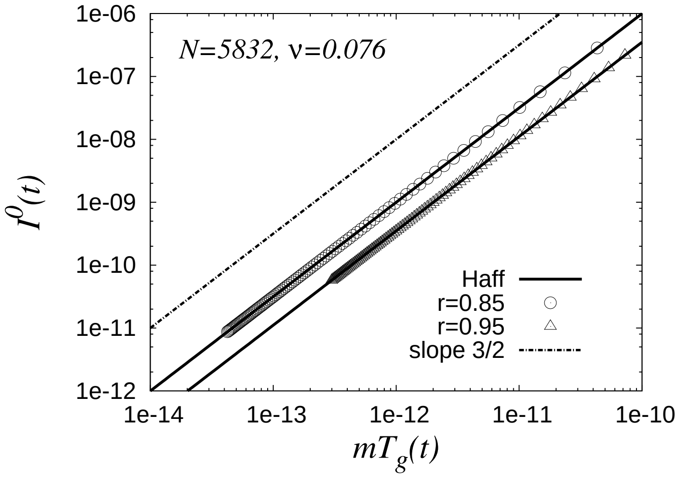

Figure 4.5: Dissipation rate plotted against $mT_g(t)$ for two different r extracted from the same set of data as we already used in the left panel of Fig. 4.4. Early times correspond to top-right, later times to bottom-left.

4.3 Repulsive Long-Range Interactions

In the following, long-range forces in homogeneous dissipative systems will be discussed. Since we already have discussed the difference between the results of the HLC algorithm and the results of the direct particle-particle method in section 3.7.2, we now apply the direct pair-wise treatment as a reference, in order to get most accurate results.

4.3.1 Pair Distribution Function

In this section we investigate the influence of repulsive long-range forces on the internal structure of the particle bulk. We will deal with elastic particle systems in order to circumvent a possible influence of dissipative effects on the results.

In the presence of long-range forces, the pair distribution function at contact, as introduced in section 4.1.3, will be different from the case for which no long-range forces are active. For strong repulsive forces, we will observe effective volume exclusion that ranges much farther than $r_{ij} = 2a$, i.e., a pair of particles will repel each other even if its separation distance is some particle diameters. Such as for the case of physical contacts, also for long-range interactions, particles are spatially correlated. In Fig. 4.6 we have plotted $g(r_{ij})$ against the pair distance in units of the diameter, $2a$, for differently strong repulsive forces. As expected, the larger c_b the stronger the two particles repel each other. This results in a decreasing $g(2a)$ for increasing c_b and a shift of the peak of $g(r_{ij})$ towards larger

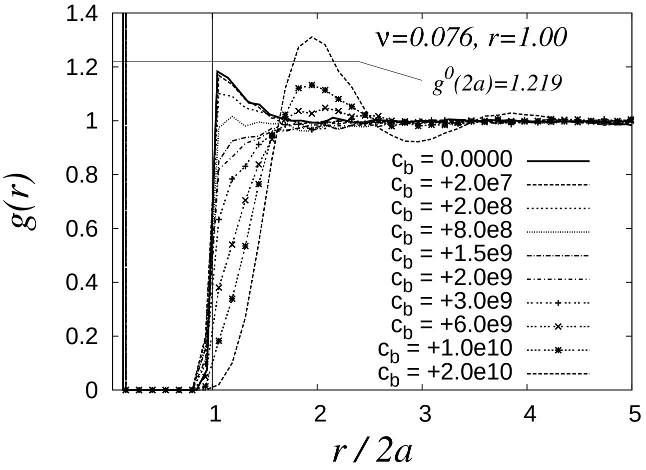

Figure 4.6: The pair distribution function, $g(r_{ij})$, is plotted against the pair distance, r_{ij}, scaled by the particle's diameter, $2a$, for different repulsion strengths, c_b. Density is fixed, $\nu = 0.076$, and the results are taken during thermal equilibrium for particle systems with $N = 1000$.

distances which is equivalent to longer ranged correlations. The value of $g(r_{ij})$ at $r_{ij} = 2a$ without long-range interactions is analytically given by Eq. (4.8) and the point of intersection between the horizontal line at $g(2a) \approx 1.219$ and the vertical line at $r_{ij} = 2a = 0.001$ represents its nominal value. The figure shows that the peak for $c_b = 0$ does not reach its nominal value because it is shifted slightly from the point $r_{ij}/2a = 1$ to the right. In appendix C we will briefly comment on the present data analysis and see that the peak at $r_{ij} = 2a$ will indeed be predicted by Eq. (4.8).

4.3.2 Collision Frequency

According to *Haff*'s law, the collision frequency will behave like $f_E^0(t) \propto T_g(t)^{1/2}$ for granular gases without mutual long-range interactions. As derived by means of the pseudo-Liouville operator formalism in appendix A, Eq. (A.18), for repulsive granular gases we obtain for the collision frequency

$$f_E(t) = f_E^0(t) \exp\left(- \frac{E_b}{mT_g(t)} \right) \quad , \tag{4.17}$$

where E_b denotes the corresponding two-particle energy barrier at contact and is defined in section 2.2. For $r = 1$, $f_E^0(t)$ keeps its initial equilibrium value for all

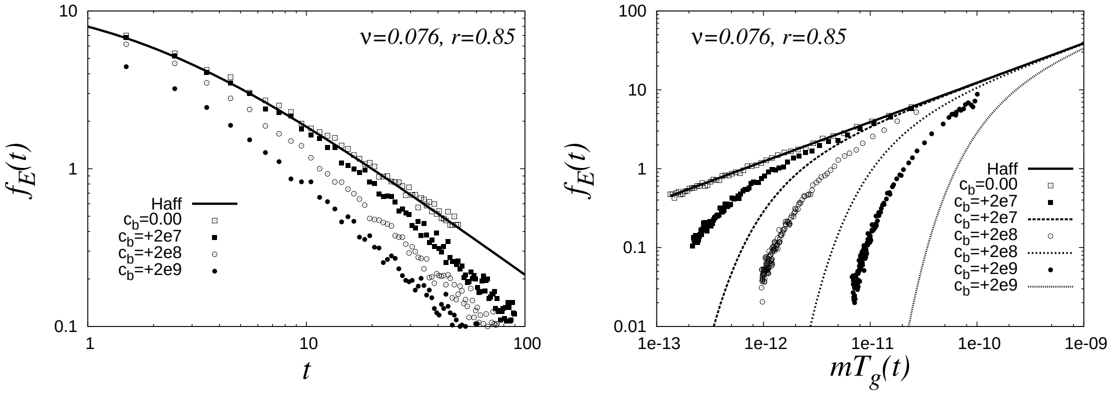

Figure 4.7: Collision frequency, $f_E(t)$, plotted as a function of time (left) and as a function of thermal energy, $mT_g(t)$, (right). Stronger repulsive long-ranged potentials lead to a stronger (faster) decrease of $f_E(t)$ (simulation data = symbols, two-particle theory = lines).

times[4]. For a fixed E_b, the collision rate remains constant and for increasing repulsion, $f_E(t)$ decreases due to the fact that stronger repulsion hinders collisions. How $f_E(t)$ decreases exactly with increasing E_b, depends on the thermal energy taken by the system for different E_b and will be discussed in section 4.3.3. For $r < 1$, $f_E(t)$ shows a stronger decay the stronger the repulsion potential E_b has been chosen. A decay of $f_E(t)$ is the consequence of the decay in temperature due to dissipative collisions. Note that E_b becomes more important (relative to $mT_g(t)$) the cooler the system has become.

In order to show the decay of the collision rate for a dissipative system with $r = 0.85$, we performed a number of simulations with different E_b at fixed volume fraction $\nu = 0.076$. In the left panel of Fig. 4.7 we see $f_E(t)$ plotted versus time double-logarithmically. With increasing strength c_b, the collision frequency drops faster because stronger barriers E_b will result in fewer collisions. The right panel of Fig. 4.7 shows also a double logarithmic plot of $f_E(t)$ but against $mT_g(t)$. Here, the number of collisions per time decreases with decreasing temperature. Note that in repulsive dissipative systems E_b becomes more and more prominent the more the system has cooled down. This leads to an almost vertical drop of $f_E(t)$ for very low temperatures for certain values of the repulsion strengths as one can see in the right panel. The dashed lines correspond to the solutions of Eq. (4.17) and show generally a stronger decrease than the simulation results. The deviation originates from the many-body effect present in simulations, which is, however, not predicted by the two-particle theory expressed through Eq. (4.17). The many-body effect will be discussed in section 4.3.5.

---

[4] All systems discussed in this chapter have been equilibriated (with $r = 1$) such that their total kinetic energy remained constant with time. Thereafter, we activated dissipation and/or long-range forces and obtained the results discussed.

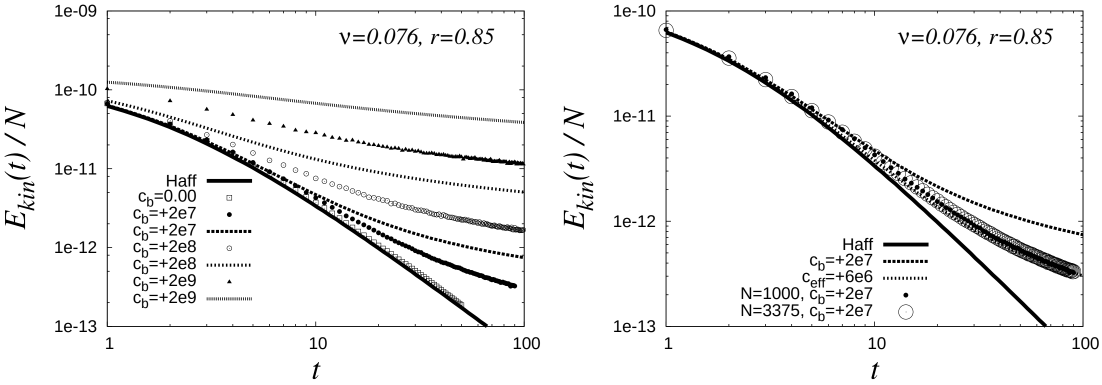

Figure 4.8: (Left) Kinetic energy per particle plotted over time for differently strong repulsive forces in comparison with theory. (Right) The simulation with $c_b = 2 \cdot 10^7$ is shown in comparison with theory (simulation data = symbols, theory = lines).

4.3.3 Kinetic Energy

In repulsive dissipative granular gases, the system cools down less strongly as if there would be no repulsive interactions because the repulsion hinders particles in colliding. The time behavior of the kinetic energy in such systems can be derived by means of the pseudo-Liouville operator as we have shown in appendix A.5. We obtained

$$\frac{\mathrm{d}E_{\mathrm{kin}}(t)}{\mathrm{d}t} = -f_E(t)\frac{N}{2}(1-r^2)mT_g(t) \quad , \tag{4.18}$$

where the only difference with Eq. (4.16) is the corrected collision frequency, $f_E(t)$. Eq. (4.18) is solved numerically and its solution is displayed for different repulsion strengths, c_b, in Fig. 4.8. Both the simulation data and the theoretical solutions of the kinetic energy per particle, $E_{\mathrm{kin}}(t)/N$, are plotted against time in a double logarithmic plot. Initially, the kinetic energy per particle decreases in time as it does also in dissipative systems without long-range repulsion forces. But the difference is that the decay becomes weaker the more the system cools down and it will not approach $\propto 1/t^2$ ($\rightarrow$ Eq. (4.14)) for large times. This is due to the fact that for low temperatures, E_b becomes relatively stronger compared with the temperature. The larger c_b the earlier the data deviate from *Haff*'s law, see data from bottom to top in the left panel. This corresponds to the results for the collision frequency in Fig. 4.7, where the stronger c_b has been chosen, the fewer collisions will occur and the less kinetic energy will be dissipated.

In the right panel of Fig. 4.8 the difference between theory and simulation is quantified by choosing c_b for solving Eq. (4.18) such that theory agrees roughly with data. For the density $\nu = 0.076$ and dissipation $r = 0.85$, we see that we have to choose $c_{\mathrm{eff}} = +0.6 \cdot 10^7$ for the two-particle energy barrier in order to obtain agreement with simulation with $c_b = +2 \cdot 10^7$. The two-particle potential is modified in the simulation such that it becomes a weaker *effective* potential. In all cases

$$E_{\mathrm{eff}} < E_b \tag{4.19}$$

was found. This is due to the influence of all the other bodies on each pair of particles. The many-body effect is discussed in section 4.3.5.

Long-time Behavior

If we run the simulations for sufficiently long times the systems would cool down until, due to the low temperatures, the particles cannot collide anymore. The total energy will show an asymptotic behavior when the actual thermal energy drops below the repulsive energy barrier. Most particles will move at relative velocities that are below the critical velocity and will not be able to collide and, hence, do not contribute to the dissipation of energy. Only the few particles populating the high-energy tail of the Maxwell-Boltzmann distribution in Fig. 4.1 are able to collide with others such that $E_{\mathrm{kin}}(t)$ would asymptotically approach a horizontal line in the left panel of Fig. 4.8. This would correspond to an asymptotic approach of $f_E(t)$ to a vertical line in the right panel of Fig. 4.7. However, the present results do not show the asymptotic behavior because the simulation time would have become too large in order to show a significant energy loss per unit time.

4.3.4 Dissipation Rate

The dissipation rate, $I(t)$, is defined as the amount of kinetic energy that is lost per unit time due to all dissipative collisions. The homogeneous cooling state of a granular gas shows a dissipation rate that decays like $\propto T_g(t)^{3/2}$. $I(t)$ is always negative which implies that there is a loss of kinetic energy and it is physically impossible to gain kinetic energy due to collisions. According to [43] and Eq. (4.18), we have

$$I(t) = \frac{\mathrm{d}E_{\mathrm{kin}}(t)}{\mathrm{d}t} = I^0(t)\,\exp\left(-\frac{E_b}{mT_g(t)}\right) \quad , \tag{4.20}$$

where $I^0(t) = -f_E^0(t)\frac{N}{2}(1-r^2)mT_g(t)$ is the dissipation rate for homogeneous particle systems without mutual long-range forces. The left panel of Fig. 4.9

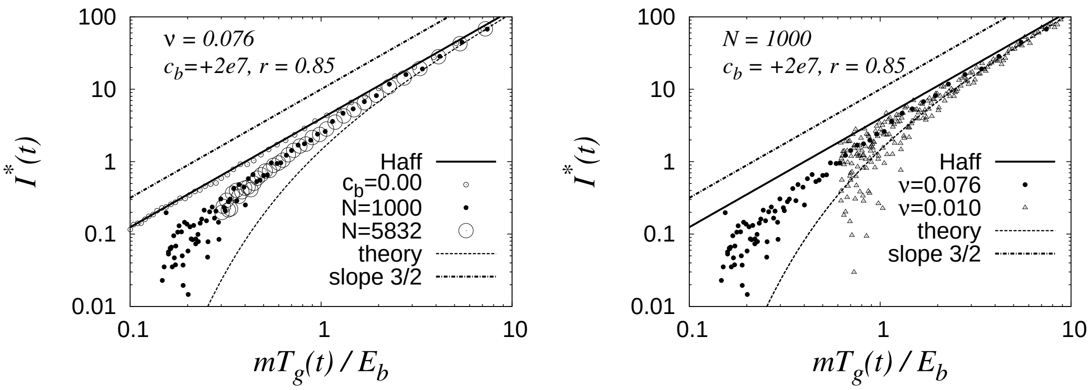

Figure 4.9: (Left) Dimensionless dissipation rate, $I^*(t)$, plotted against scaled temperature for two different particle numbers N (each with $\nu = 0.076$). Symbols are data, black line corresponds to *Haff*'s law, dashed line to theory and dash-dotted line indicates a slope of 3/2. (Right) Dimensionless (density-independent) dissipation rate for the two densities $\nu = 0.010$ and $\nu = 0.076$.

shows us the double logarithmic plot of the dimensionless dissipation rate,

$$I^*(t) = -\frac{I(t)}{Nna^2 g(2a) m^{-1/2} E_b^{3/2}} = \underbrace{8\sqrt{\pi}(1-r^2)\left(\frac{mT_g(t)}{E_b}\right)^{3/2}}_{I^{*0}(t)} \exp\left(- \frac{E_b}{mT_g(t)}\right) \quad ,$$

against the thermal temperature in units of the repulsive Coulomb barrier. $I^*(t)$ is not dependent on the number of particles and the density of the systems. Systems with different N and different ν show agreement for $c_b = 0$ and follow $I^{*0}(t)$. Note that $I(t)$ does not show agreement for different ν because denser systems will dissipate more energy per time unit than dilute systems. The data of a simulation with $N = 1000$ and one with $N = 5832$ are displayed in the left panel of Fig. 4.9 which agree nearly perfectly. This means, that the influence of many bodies on the collisional behavior does not change for different particle numbers at fixed volume fraction and, thus, any single particle is affected by only its nearest neighbors.

In the limit $E_b \to 0$, the dissipation rate of systems with repulsive long-range forces will approach the prediction by *Haff*, i.e., $I(t) \to I^0(t)$ and $I^*(t) \to I^{*0}(t)$, as it can be seen from Eq. (4.20). Or, generally, if $mT_g(t) \gg E_b$ the system will behave like a system without long-range forces and will cool down as $\propto T_g(t)^{3/2}$. For $mT_g(t) \ll E_b$, the long-range forces become very important and deviations from $I^0(t)$ and $I^{*0}(t)$ are strong.

Different Densities

For $c_b > 0$, systems with different ν will show differently strong deviations relative to $I^{*0}(t)$. In the right panel of Fig. 4.9, $I^*(t)$ is plotted against the thermal temperature in units of the potential barrier, $mT_g(t)/E_b$, in a double logarithmic plot. We see that the data set corresponding to $\nu = 0.010$ deviates earlier (stronger) from *Haff* (solid lines) than the one for $\nu = 0.076$ and is closer to the two-particle theory (dashed lines). This is as expected because two-particle theory represents the limit $\nu \to 0$ where we have $E_{\mathrm{eff}}/E_b \to 1$. In turn, we conclude that with increasing density the dissipation rate approaches that for the case without long-range potentials. This is equivalent to a decreasing effective potential which we try to understand in the following.

4.3.5 Many-Body and other Effects

In the preceding section, we observe that systems with increasing density show a cooling behavior that becomes more and more similar to that of systems without long-range forces, i.e., the effective repulsive energy barrier, E_{eff}, becomes weaker. We can explain this observation by the effect of many bodies on the colliding particle pairs. In the following, we present a one-dimensional model for the many-body effect that is consistent with the observations, but it is emphasized that the effect of the particle bulk may not be the only reason for the deviation between observation and theoretical prediction. Thereafter, we will attempt to quantify the effective energy barrier resulting from this effect.

A one-dimensional Model for the Effect of many Bodies

For the many-body effect, the example of a one-dimensional chain of repelling particles can be used: due to the larger inter-particle distances, neighboring particles push a pair of particles less strongly together, the lower the volume fraction. Thus, the many-body effect becomes weaker. Vice versa, dense granular gases with long-range repulsive forces behave nearly like *Haff*'s theory because particles will be pushed together more strongly by their close neighbors. Two cases are displayed in Fig. 4.10, where the (repulsion) potential energy in units of E_b is displayed as a function of the particle distance in units of the mean free path, l: (i) the case when two particles are far away from each other and the resulting potential minimum (solid lines) at $r = 1l$ is lower than for the case (ii) at $r = 0.5l$ when both particles are closer to each other. This situation is equivalent to a larger mean free path and lower density in case (i) and vice versa in case (ii). Let us consider a third particle that is located at the minimum in each case and can freely move. If this particle obtains kinetic energy such that it can

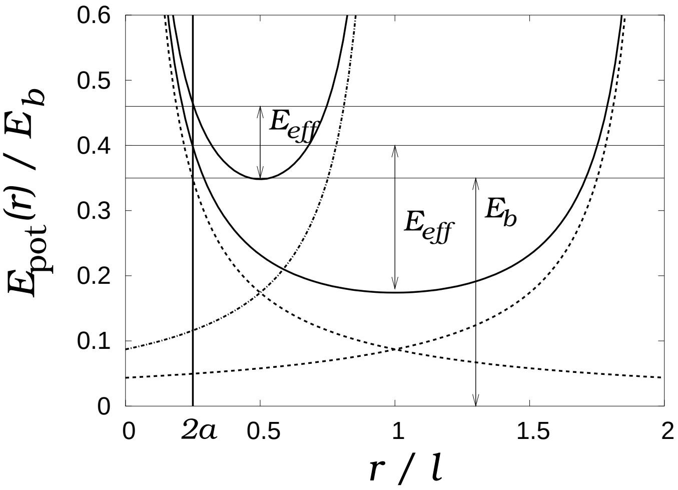

Figure 4.10: Illustration of the many-body effect. The potential between two particles in units of the Coulomb barrier, E_{pot}/E_b, is plotted against the distance in units of the mean free path, r/l. One particle is fixed and located at the origin, $r = 0$, the other one is located (i) at $r = 2l$ (low density) and (ii) at $1l$ (high density). Dashed lines denote the single particle potential for $r = 2l$, the dash-dotted line for $r = 1l$ and the solid lines denote the resulting two-particle potentials for both $r = 2l$ and $r = 1l$. A third test particle (not shown) is assumed to be located in the potential minima at $r = 1l$ (i) and $r = 0.5l$ (ii), respectively.

reach the collision distance at $r = 2a$ (solid vertical line), then it has to overcome a smaller effective potential, E_{eff}, in case (ii) than in case (i). The single particle potential lines are in both cases the same. That means, E_b does not change even if the mean free path and the density change. Conclusively, the ratio E_{eff}/E_b will decrease with increasing density and, thus, the effect of neighboring particles on the particle pair increases as well. This density dependency of E_{eff}/E_b is also estimated in [110], and since the maximum volume fraction for a 3D mono-disperse system of hard spheres is limited[5] we will thus get also a minimum effective potential between the particles for the highest possible densities. So, the dissipation rate, e.g., will only approach but never agree with the rate in systems without long-range forces.

---

[5] The highest possible density of a random close packing (rcp) of mono-disperse hard spheres is $\nu_{\mathrm{max}} \cong 0.64$ [124] whereas the highest possible packing of hard spheres at all is that of a face-centered cubic (fcc) or hexagonal cubic packing (hcp), i.e., $\nu_{\mathrm{max}} \cong 0.74$.

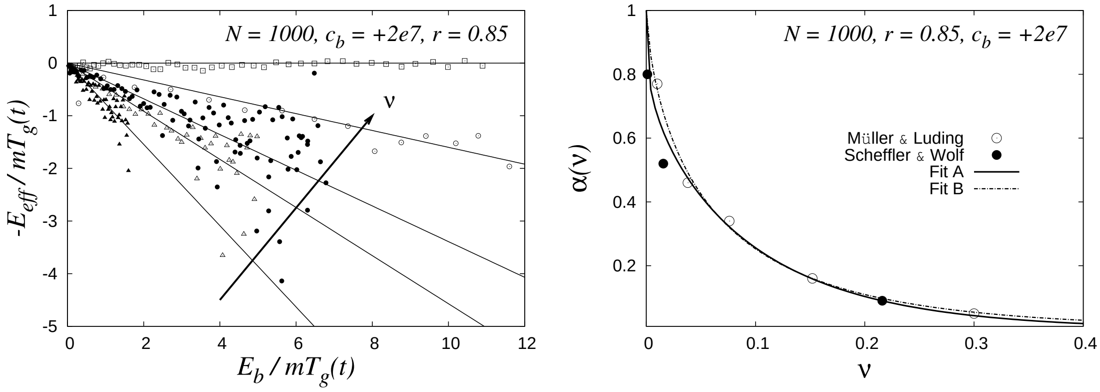

Figure 4.11: (Left) Arrhenius plot for $c_b = +2 \cdot 10^7$ and different densities. Lines are fits to the data, symbols represent data. From bottom to top: increasing density ($\nu = 0.010, 0.038, 0.076$ and 0.152) showing decreasing slopes. Time evolves to the right. The horizontal line corresponds to a system with $c_b = 0$. The arrow also indicates increasing influence of the many-body effect. (Right) The ratio $\alpha(\nu) = E_{\text{eff}}/E_b$ corresponds to the slopes of the left panel and is plotted against the volume fraction ν. “Fit A” includes all data, “Fit B” excludes the data of Scheffler & Wolf [111]. The fit is done by Eq. (4.22), the fit parameters are listed in table 4.1.

Fit 1 (Linear Fits from Dissipative Simulations)

Now, in order to quantify how much E_{eff} is reduced as compared to E_b, a so-called Arrhenius plot is set up, similar to [110,111], see the left panel of Fig. 4.11. Here, we have plotted $\ln\big(I(t)/I^0(t)\big) = -E_{\text{eff}}/\big(mT_g(t)\big)$ against $E_b/\big(mT_g(t)\big)$. From simulations we obtain $I(t)$ via Eq. (4.20), $I^0(t)$ via Eq. (4.16) and the respective $T_g(t)$. We fit the data for the densities $\nu = 0.010, 0.038, 0.076$ and 0.152 with a linear function (solid lines), assuming E_{eff} to be linearly dependent on E_b. The slopes of the fitting lines will quantify the deviation between data and theory. Since for dissipative systems an Arrhenius plot shows strongly scattered values[6], we only roughly realize a linear dependence between E_{eff} and E_b. So, we will set $E_{\text{eff}}/\big(mT_g(t)\big) = \alpha(\nu)\ E_b/\big(mT_g(t)\big)$, i.e., for the correction factor,

$$\exp\left(- \frac{E_{\text{eff}}}{mT_g(t)} \right) = \exp\left(- \alpha(\nu)\ \frac{E_b}{mT_g(t)} \right) \quad . \tag{4.21}$$

Then, E_{eff} is a function of E_b with a slope $0 < \alpha(\nu) < 1$. So, α quantifies the density-dependent fraction of E_b which is shared by E_{eff}. In the right panel of

---

[6] We have averaged $\ln\big(I(t)/I^0(t)\big)$ linear in time. So, for larger times, i.e., larger values of $E_b/\big(mT_g(t)\big)$, statistics will decrease because less collisions contribute to the dissipation rate.

	a	b	c
Fit A $^{(*)}$	8.00	1.00	0.25
Fit B $^{(**)}$	0.00	6.65	0.68

$^{(*)}$ including Scheffler values
$^{(**)}$ excluding Scheffler values

Table 4.1: Parameters for the fit function in Eq. (4.22) in the right panel of Fig. 4.11. Fit function A includes the values found by Scheffler & Wolf [110, 111], fit function B does not consider them.

Fig. 4.11 a linear-linear plot shows the deviation (between the case including long range forces and the case without) expressed by the ratio, $\alpha(\nu) = E_{\text{eff}}/E_b$, against the density ν. An empirical function

$$\alpha(\nu) = \exp\Big(- a\nu - b\nu^c \Big) \tag{4.22}$$

has been chosen, where a, b and c are fit parameters. α decays with ν, where the starting point is $\alpha(\nu = 0) = 1$. The shape of the fit function did not appear as a power law and a simple exponential did not work well either. The figure shows fits to all data points including the values found in [111] ("Fit A") and to our data points only ("Fit B", open circles), where the first term is neglected ($a = 0$). This leaves two fit parameters b and c, and thus represents a stretched exponential. The corresponding parameters for both fits are listed in Tab. 4.1. Unfortunately, the density-dependence of α can be fit by two completely different exponentials and, thus, we cannot really determine the shape of the fit function. Anyway, from the fit functions it follows, that for a repulsive granular gas, e.g., with density $\nu = 0.076$, the effective many-body potential is only about 30 % of the two-body potential[7], whereas the effective potential of a granular gas with lower density $\nu = 0.010$ is already about 70 % of the two-body potential. So, the many-body effect increases with density and disappears (i.e., $\alpha \to 1$) for $\nu \to 0$. No data are available for $\nu > 0.3$ and the quality of the Arrhenius plot fits does not allow for a more quantitative conclusion anyway.

Fit 2 (Non-linear Fits from Elastic Simulations - Part I)

Due to the strongly scattered values in the Arrhenius plot, we fail to extract a more subtle density dependency of $\alpha(\nu)$. We therefore look for another way to extract $E_{\text{eff}}/\big(mT_g(t)\big)$ from the simulation that we can plot as a function of $E_b/\big(mT_g(t)\big)$: we perform a series of "elastic" simulations with different initial

---

[7] A crosscheck by adjusting c_{eff} to c_b in the right panel of Fig. 4.8 gives $-E_{\text{eff}}/E_b = -c_{\text{eff}}/c_b \approx -6 \cdot 10^6/2 \cdot 10^7 = -0.3$ and is consistent with the results of the Arrhenius plot.

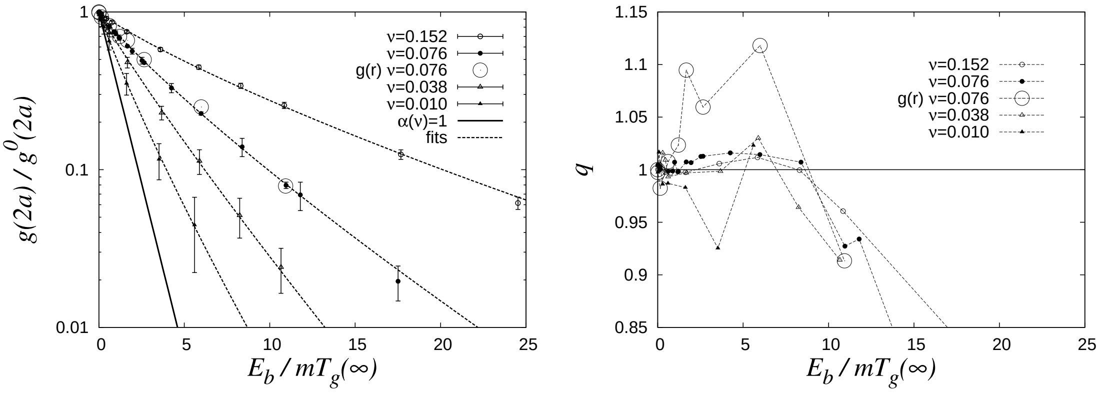

Figure 4.12: (Left) Small symbols correspond to data obtained by computing the ratio of collision frequencies, $f_E(t)/f_E^0(t)$, large open circles correspond to data obtained by the extrapolation method applied to $g(r_{ij})$. Black lines are best fits according to Eq. (4.24) (the corresponding fit-parameters are listed in Tab. 4.2, indicated by $^{(2)}$). Errorbars denote the standard deviation. (Right) The quality factor of the fits of the left panel.

temperature but for a fixed density. After reaching an equilibriated state, each simulation provides a single pair of $E_{\text{eff}}/\big(mT_g(t)\big)$ and $E_b/\big(mT_g(t)\big)$. Carrying out many simulations for a given ν provides the same information as the Arrhenius plot from one single cooling simulation, but without bad statistics. The data extraction from the elastic simulations is as follows:

$$\frac{g(2a)}{g^0(2a)} \overset{!}{=} \frac{f_E(t)}{f_E^0(t)} = \exp\left(- \frac{E_{\text{eff}}}{mT_g(t)} \right) , \tag{4.23}$$

i.e., we can use Fig. 4.6 and take the $g(2a)$ for different E_b in units of $g^0(2a)$. More details on this data analysis are presented in appendix C. Alternatively, we extract the collision frequency, $f_E(t)$, for different E_b in units of $f_E^0(t)$. The superscript “0” denotes the respective quantities without long-range forces. We plot the results in the left panel of Fig. 4.12 which is a log-linear plot of $g(2a)/g^0(2a)$ as a function[8] of $E_b/\big(mT_g(\infty)\big)$. We realize that for the density $\nu = 0.076$ both extraction methods provide the same results (emphasized by the exclamation mark atop the first equal sign in Eq. (4.23)). The extraction from Fig. 4.6 is additionally indicated by “$g(r)$” in Fig. 4.12 (large open circles). The extraction of the results from $f_E(t)/f_E^0(t)$ is carried out for all densities (small symbols). So, we can conclude that the Boltzmann correction factor of Eq. (4.23) does in particular correct the pair correlation function at contact and hence the dynamical

---

[8] Elastic simulations with a certain initial temperature, $T_g(0)$, will reach soon thermal equilibrium with constant temperature, $T_g(\infty) \neq T_g(0)$, where $T_g(\infty)$ depends on the initial conditions E_b and $T_g(0)$. In thermal equilibrium the systems exhibit a Maxwell-Boltzmann velocity distribution as shown in Fig. 4.1.

ν	$\alpha(\nu)$ $^{(1)}$	$\alpha(\nu)$ $^{(2)}$	$\beta(\nu)$ $^{(2)}$	$\gamma(\nu)$ $^{(2)}$	$\alpha(\nu)$ $^{(3)}$	$\delta(\nu)$ $^{(4)}$	$\epsilon(\nu)$ $^{(4)}$
0.152	0.16	1	0.811	1.033	0.14	0.187	0.0085
0.076	0.34	1	0.677	1.057	0.28	0.336	0.0201
0.038	0.46	1	0.535	1.088	0.43	0.500	0.0331
0.010	0.77	1	0.340	1.150	0.66	0.736	0.0514

$^{(1)}$ see left panel of Fig. 4.11, linear fit with Eq. (4.21)
$^{(2)}$ see left panel of Fig. 4.12, non-linear fit with Eq. (4.24)
$^{(3)}$ see left panel of Fig. 4.12, linear fit with Eq. (4.21)
$^{(4)}$ see left panel of Fig. 4.12, linear fit with Eqs. (4.25) and (4.26)

Table 4.2: Upper part: fit parameters of different fit functions for different densities. Lower part: fit parameters for $\alpha(\nu)$ and $\beta(\nu)$, see Eq. (4.26).

observables such as $f_E(t)$, $E_{\text{kin}}(t)$ and $I(t)$. Additionally, the left panel of Fig. 4.12 shows also the limit $\nu \to 0$ which is represented by the solid line where we assume the validity of the two-particle theory, i.e., $E_{\text{eff}} = E_b$.

But let us now focus on whether the assumption of a linear dependency between E_{eff} and E_b, as Eq. (4.21) expresses, is valid. A closer look at the curves in Fig. 4.12 gives the impression of a non-linear dependency. Apparently, higher densities show stronger deviations from linearity and therefore we will extend the correction factor of Eq. (4.21) such that

$$\exp\left(-\frac{E_{\text{eff}}}{mT_g(t)}\right) = \exp\left(-\alpha(\nu)\,\frac{E_b}{mT_g(t)}\right)\exp\left(\beta(\nu)\,\left(\frac{E_b}{mT_g(t)}\right)^{\gamma(\nu)}\right) \quad . \tag{4.24}$$

In this extension, we can set $\alpha(\nu) = 1$ because then we have all density dependencies in the non-linear correction term, and the exponential with $\alpha(\nu) = 1$ can be still identified with the correction for the $\nu \to 0$ limit theory prediction. In this case, we have two more fit parameters than in Eq. (4.21), whose variation leads to the fits in the left panel of Fig. 4.12 (dashed lines). The parameters are shown in Tab. 4.2, indicated by $^{(2)}$. The quality of this fit is shown in the right panel by the quality factor, q, as a function of $E_b/\big(mT_g(\infty)\big)$. As we can observe, the quality is quite well in the range $E_b/\big(mT_g(\infty)\big) < 10$, i.e., $q \approx 1$, but deviates stronger for larger values of E_b. Although not being fitted and thus with worse quality, the values, $g(2a)/g^0(2a)$, obtained from Fig. 4.6 are also displayed in the quality plot (large open circles). Note, that for $\alpha = \gamma = 1$, the fit by Eq. (4.24) agrees with the linear fit by Eq. (4.21).

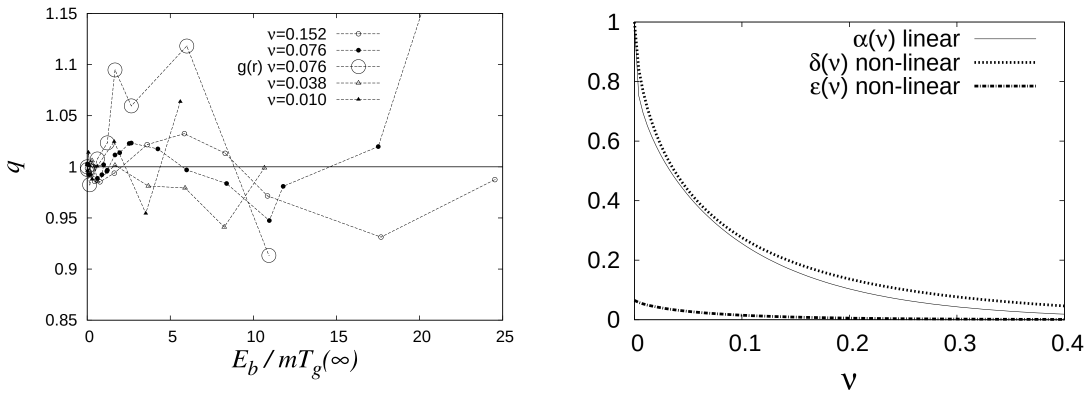

Figure 4.13: (Left) Quality factor of the fit function expressed by Eqs. (4.25) and (4.26). The respective fit parameters are listed in Tab. 4.2. (Right) For the “linear” case, only $\alpha(\nu)$ is plotted and we use Eq. (4.21) and the parameters of Fit 1 in Tab. 4.1. For the “non-linear” case, both $\alpha(\nu)$ and $\beta(\nu)$ are plotted, see Eqs. (4.25), (4.26) and the respective parameters in the last line of Tab. 4.2.

Fit 3 (Linear Fits from Elastic Simulations)

For the sake of completeness, we show in the table for different densities also linear fits to the (non-linear) data of the left panel of Fig. 4.12, indicated by $^{(3)}$. Both Fit 3 and Fit 1 are linear fits in the range $E_b/\big(mT_g(\infty)\big) < 12$ and agree quite well within the error margin of the strongly scattered values in the Arrhenius plot.

Fit 4 (Non-linear Fits from Elastic Simulations - Part II)

The final goal is to find a correction factor that fits the non-linear E_b-dependency of E_{eff} for all (in particular, larger) values of $E_b/\big(mT_g(\infty)\big)$.
A new more promising correction factor will then be Eq. (4.24) (where we have found $\alpha = 1$ and $\gamma \approx 1$ for small $E_b/(mT_g(\infty))$)[9] multiplied by a factor that accounts for the deviations for larger $E_b/\big(mT_g(\infty)\big)$:

$$\exp\left(- \frac{E_{\text{eff}}}{mT_g(t)} \right) = \exp\left(- \delta(\nu)\, \frac{E_b}{mT_g(t)} \right) \left(1 + \epsilon(\nu) \left(\frac{E_b}{mT_g(t)} \right)^2 \right) \quad , \qquad (4.25)$$

where $\delta(\nu)$ and $\epsilon(\nu)$ are new fit parameters. The term $1 + \epsilon\big(E_b/(mT_g(t))\big)^2$ can be regarded as a correction of the right-hand-side of Eq. (4.21), i.e., $\delta(\nu) \approx \alpha(\nu)$,

---

[9] For $\alpha = 1$ and $\gamma \approx 1$, see Tab. 4.2, Eq. (4.24) leads to $\exp(-x)\exp(-\beta x) = \exp(-(1-\beta)x) = \exp(-\delta x)$, where $\delta = 1 - \beta$ and $x = E_b/\big(mT_g(\infty)\big)$.

improving the fit for larger values of $E_b/(mT_g(t))$. In total, the right-hand-side of Eq. (4.25) identifies with a Taylor series expansion of the exponential $\exp(\alpha(\nu)E_b/(mT_g(t)))$ truncated at the second order term in $E_b/\big(mT_g(\infty)\big)$. The fit parameters can be fit themselves with the exponentials

$$\begin{aligned} \delta(\nu) &= a_0 \exp\Big(-b_0\nu^{c_0}\Big) \\ \epsilon(\nu) &= a_1 \exp\Big(-b_1\nu^{c_1}\Big) \quad . \end{aligned} \tag{4.26}$$

where $a_0 = 1.00,\ a_1 = 0.065,\ b_0 = 5.468,\ b_1 = 9.002,\ c_0 = 0.628$ and $c_1 = 0.790$ are the fit parameters for the density functions.
Using Eqs. (4.25) and (4.26), a best fit provides the fit parameters $\delta(\nu)$ and $\epsilon(\nu)$ listed in Tab. 4.2 with the indication $^{(4)}$ and the quality factor for the fit is shown in the left panel of Fig. 4.13. As compared to the quality factor in the right panel of Fig. 4.12, the quality of the "new" fit including the known functions for $\delta(\nu)$ and $\epsilon(\nu)$ is better for larger $E_b/\big(mT_g(\infty)\big)$.
To summarize, the right panel displays the analytical functions $\delta(\nu)$ (dotted line) and $\epsilon(\nu)$ (dash-dotted line) of Eq. (4.26) we found ($\gamma(\nu) = 2$ is not shown). For comparison, $\alpha(\nu)$ (thin solid line) from Eq. (4.22) (Arrhenius plot) is also shown (where E_{eff} is supposed to be a linear function of E_b).
So, the evaluation of elastic simulations with different repulsion intensities lead us to the conclusion that the deviations between the theory and simulation data lead to a complex dependency between the effective and the theoretical two-particle Coulomb barrier. This dependency is more complex than concluded in [111] and in section 4.3.4.
In the next section we use the fit function (4.25) to solve Eq. (4.18) numerically and to obtain a better prediction of the decaying kinetic energy in a repulsive granular gas.

4.3.6 Improved Time Evolution of Dynamical Observables

In the last subsection we observed that E_{eff} does not depend on E_b linearly as Eq. (4.21) implies but rather non-linearly, see Eq. (4.25). That implies that the deviations between theory and simulation are more complex than originally assumed. We will now use the non-linear relation between E_{eff} and E_b, see Eqs. (4.25) and (4.26) and the respective parameters in Tab. 4.2, and insert it into the equations (4.17) and (4.18) for the collision frequency and kinetic energy, respectively. We assume that the time evolution of $f_E(t)$ and $E_{\text{kin}}(t)$ will be now correctly predicted.
The left panel of Fig. 4.14 shows the collision frequency and is the same as the right panel of Fig. 4.7 but additionally includes the solution of Eq. (4.17) with the non-linear extension of E_{eff} of Eq. (4.25) (solid lines). The predictions agree with

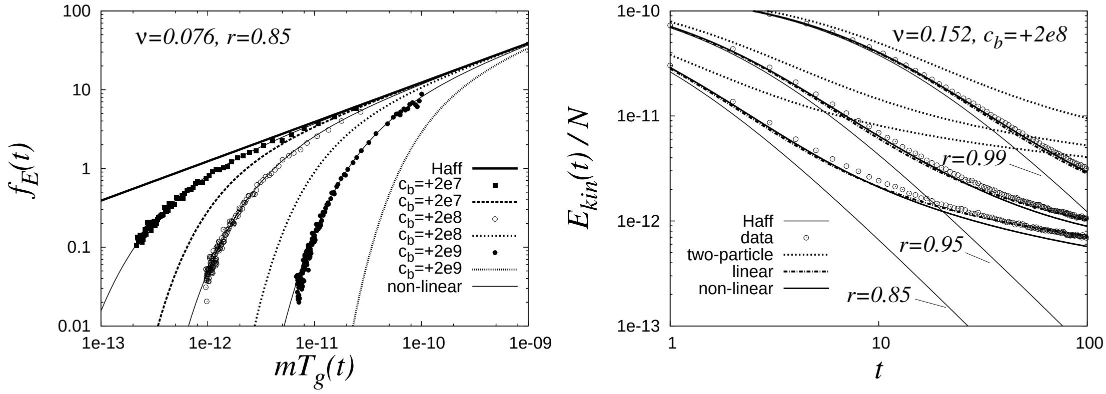

Figure 4.14: (Left) Decay of the collision frequency, $f_E(t)$, with thermal temperature, $mT_g(t)$, of a system with fixed $\nu = 0.076$ and $r = 0.85$ for different repulsion strengths, c_b. (Right) Decay of the kinetic energy per particle, E_{kin}/N, with time, t, of a system with fixed $\nu = 0.152$ and $c_b = +2 \cdot 10^8$ for different dissipation, r.

the data. On the other hand, the right panel shows $E_{\text{kin}}(t)/N$ with time likewise in a double logarithmic plot for three systems, each with different dissipation. Besides the solutions of the dilute limit predictive theory (dashed lines) that show strong deviation from data (symbols), it is shown the solutions with the non-linear correction (thick solid lines), see Eq. (4.25), and, as a comparison, the solutions with the linear correction (dash-dotted lines), see Eq. (4.21). The "new" predictions are closer to the data but still do not exactly agree.

Due to the fact that the solutions are based on elastic simulations where no dissipation between two colliding particles is active, we assume that dissipative effects are responsible for the deviation we observe[10]. As we can see in the figure, these effects are stronger the more dissipative the system becomes. These dissipative effects appear to be cumulative, because deviations become larger with time.

Anyway, the introduction of a density-dependent non-linear relation between E_{eff} and E_b improves the prediction of the time behavior of repulsive many-body systems drastically and might be a promising starting point for further theoretical investigation.

---

[10] The detailed investigation of E_{eff} in elastic systems led to a correction factor that does not account for dissipative effects such as the decrease of relative velocity after a collision. Applying the correction factor on dissipative particle systems will therefore not result in total agreement.

4.3.7 Summary for Repulsive Systems

Repulsive forces hinder particles from colliding. That is why dissipative granular gases with long-range repulsive forces show a reduced collision frequency, a less strong decay of the total kinetic energy with time and therefore a reduced dissipation rate as compared to systems without long range forces.

The two-particle theory for repulsive long-range forces we developed by means of the *pseudo-Liouville* operator formalism is a theory for the dilute limit, $\nu \to 0$. The pair distribution function at contact without long-range forces, $g^0(2a)$, see Eq. (4.8), becomes unity and the dissipation rate is corrected by a Boltzmann factor, $\exp\big(-E_b/(mT_g(t))\big)$. Here, E_b is the repulsive energy barrier that must be overcome by two approaching particles in order to have a collision. The theoretical results were already found phenomenologically in Ref. [110,111] and confirmed by our simulations for low density and weak dissipation.

If we deal with finite densities, E_b will be decreased by the presence of many nearby particles, resulting in an effective energy barrier, E_{eff}, and the density-dependence of $g^0(2a)$ becomes important. This results in a decreased pair distribution function at contact, $g(2a) = g^0(2a)\,\exp\big(-E_{\text{eff}}/(mT_g(t))\big)$, that corrects all those dynamical observables that contain $g(2a)$.

Finally, we empirically determined the density-dependence of E_{eff} by simulations and found that E_{eff} is non-linear dependent on E_b in the range $E_b/\big(mT_g(t)\big) < 25$ and for $\nu \leq 0.152$. We determined a non-linear analytical relation for the effective energy barrier as a function of density and interaction strength and used it successfully for an improved theoretical prediction of the dissipation rate, irrespective of density, dissipation and interaction strength.

4.4 Attractive Long-Range Interactions

In contrast to repulsive forces, attractive long-range forces are expected to support cluster formation in the system as it is already observed in dissipative systems without long-range forces. It is to be expected that in the presence of attractive forces, a dissipative system will evolve into an inhomogeneous state. So, the validity of the attractive theory introduced in this chapter is limited to the initial phase of the evolution of such systems, as long as the conditions for a homogeneous cooling state are fulfilled.

4.4.1 Pair Distribution Function

The pair distribution function is a measure for how the pair distances are distributed within an N-body system. Particle systems with exclusively mechanical

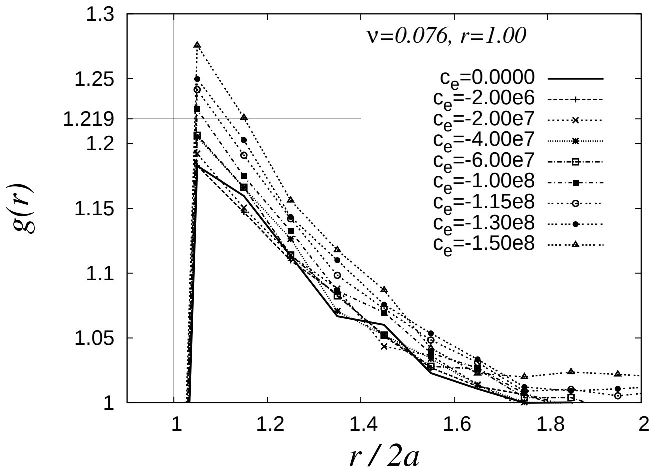

Figure 4.15: Pair distribution function, $g(r_{ij})$, plotted against the pair distance, $r_{ij}/2a$, for different attractive escape potentials, denoted by the c_e. The data are time-averaged in the homogeneous regime. Note that $g(r)$ is plotted here from $g(r) = 1$.

interactions will show a distribution of pair distances that has its maximum at $r_{ij} = 2a$, as we saw in Fig. 4.6 for the case $c_b = 0$. The same figure shows also how this distribution changes if we activate a mutual repulsive $1/r$ long-range potential between the particles. Then, the number of pair distances at $r_{ij} = 2a$ decreases if E_b becomes stronger because the probability for finding a particle at this distance drops due to the repulsion.

For attracrive $1/r$ long-range potentials, the pair distribution function at contact is expected to show the opposite trend. The probability to find a neighbor particle at $r_{ij} = 2a$ will increase if E_e becomes stronger. This is shown in Fig. 4.15, where $g(r_{ij})$ is plotted against the separation length between two particles, r_{ij}, scaled with the particle diameter, $2a$, for different attraction strengths, c_e. Stronger attractive forces lead to larger $g(r_{ij})$, as we can see. Systems with weak attraction forces are shown in order to guarantee a homogeneous particle distribution during the whole simulation time. As for the case of repulsive long-range interactions, also here we average over many time snapshots in order to obtain the $g(r_{ij})$ results with good statistics. Too strong attraction will lead to large-scale inhomogeneities (not shown here), for which the pair distribution function does not approach unity for large pair distances, indicating higher particle densities and large-scale correlations. The investigation of these effects in elastic particle systems is not considered in this thesis.

The value of $g(r_{ij})$ at $r_{ij} = 2a$ without long-range attractive interactions is analytically given by Eq. (4.8) and the point of intersection between the horizontal line at $g(2a) \approx 1.219$ and the vertical line at $r_{ij} = 2a = 0.001$ represents its

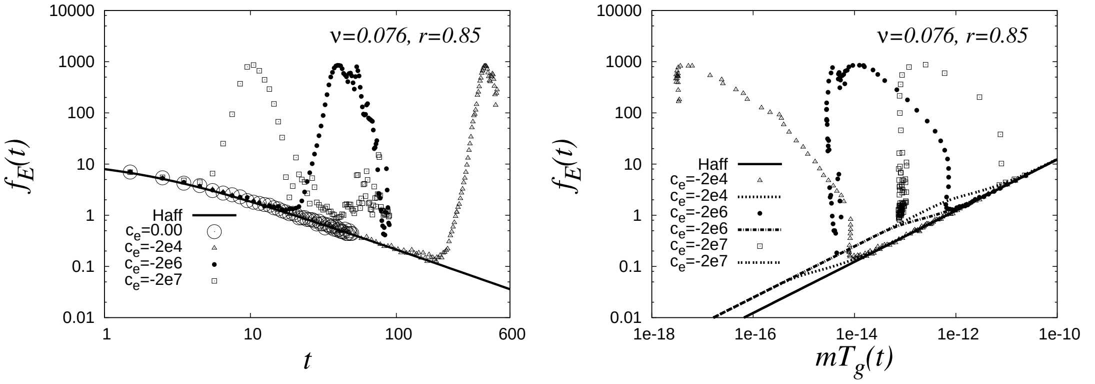

Figure 4.16: Collision frequency, $f_E(t)$, of a dissipative system with $N = 1000$ particles, $r = 0.85$ and $\nu = 0.076$ for differently strong attraction forces, c_e, plotted against time, t, (left) and the actual thermal energy, $mT_g(t)$ (right). Symbols correspond to simulation data, the solid line to *Haff*'s theory, Eq. (4.15), and the dashed lines to the corresponding theory, according to Eq. (4.27).

nominal value. As for the repulsive case displayed in the left panel of Fig. 4.6, the data point indicating the maximum of $g(r_{ij})$ does not reach the nominal value because it is shifted slightly to the right. For more details on the data analysis we refer to appendix C. We will see there that the maximum of $g(2a)$ for $c_e = 0$ is indeed given by Eq. (4.8).

4.4.2 Collision Frequency

In contrast to repulsive dissipative systems, the pseudo-Liouville operator formalism (as shown in appendix A.4.3) will lead to an increasing collision frequency for $c_e < 0$:

$$f_E(t) = f_E^0(t) \left[2 - \exp\left(- \frac{E_e}{mT_g(t)} \right) \right] \quad , \tag{4.27}$$

where $E_e := |c_e G m^2|/(2a)$ denotes the corresponding two-particle *escape* energy barrier at contact and is discussed in section 2.2. $f_E^0(t)$ corresponds to *Haff*'s collision frequency for systems without long-range forces. We performed a number of simulations for different $|c_e|$, with fixed volume fraction $\nu = 0.076$, and normal restitution $r = 0.85$. In Fig. 4.16, $f_E(t)$ is plotted against time in a double logarithmic plot. All the simulations have in common that in the beginning $f_E(t)$ drops according to *Haff*'s law. Then, a steep increase follows until a maximum collision frequency is reached, whereafter $f_E(t)$ drops rapidly. The larger $|c_e|$ the earlier the increase sets in because higher escape energies E_e result in more

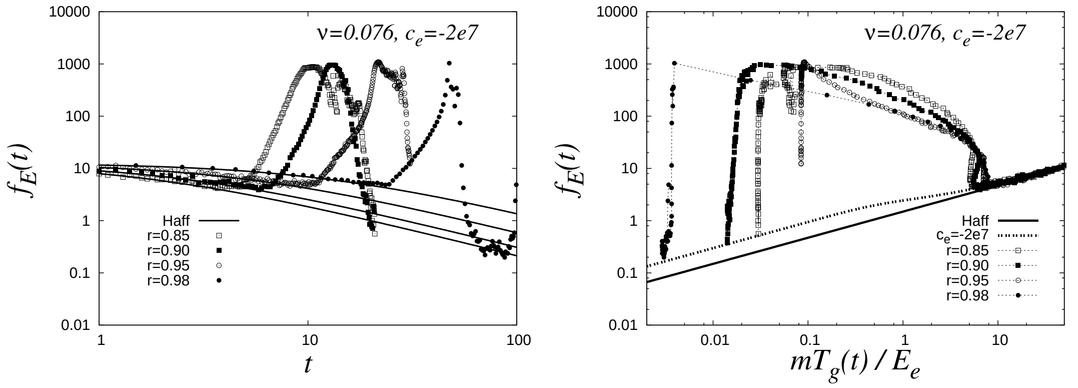

Figure 4.17: Collision frequency, $f_E(t)$, for different dissipation plotted against time, t (left) and scaled thermal energy, $mT_g(t)/E_e$ (right) for $N = 1000$. Symbols are data, solid lines are the corresponding *Haff* results, the dashed line corresponds to the two-particle theory.

collisions. In the beginning of the simulation, at high temperatures, the correction factor, $\big[2-\exp\big(-E_e/(mT_g(t))\big)\big]$, is close to unity and we have $f_E(t) \approx f_E^0(t)$. In this stage, the particles in the system are still nearly homogeneously distributed and all simulations reveal the homogeneous state in *Haff*'s sense.
In the right panel of Fig. 4.16 we have plotted $f_E(t)$ against the thermal energy, $mT_g(t)$. For different c_e, the initial increase of $f_E(t)$ relative to *Haff* (thick solid line) is predicted well by the two-particle theory (dashed lines), see Eq. (4.27).

Differently Dissipative Attractive Systems

Now, we vary the coefficient of restitution, r, and keep c_e (and ν) fixed. Fig. 4.17 is a double logarithmic plot of the collision frequency against time and shows, that for higher dissipation, $f_E(t)$ starts to increase at earlier times. For larger times, $f_E(t)$ decays stronger for higher dissipation. The right panel shows the collision frequency plotted against the scaled thermal energy, $mT_g(t)/E_e$. Here, we also have shown Eq. (4.27) (dashed lines) and see that theory again predicts pretty well the critical temperature where the increase of the collision frequency (i.e., deviation from *Haff*) sets in. It appears that in all simulations the system cools down to a certain temperature (almost independent of r) at which the increase of $f_E(t)$ starts. For strong dissipation, the system reaches the critical temperature earlier in time than for weak dissipation (data not shown). If we zoom in the right panel of Fig. 4.17 around the critical thermal energy, where $f_E(t)$ starts to increase strongly, we realize that the data follow the two-particle theory (dashed line) immediately before the divergence of the collision rate sets in (see Fig. 4.18). So, the homogeneous two-particle theory correctly predicts an increased collision

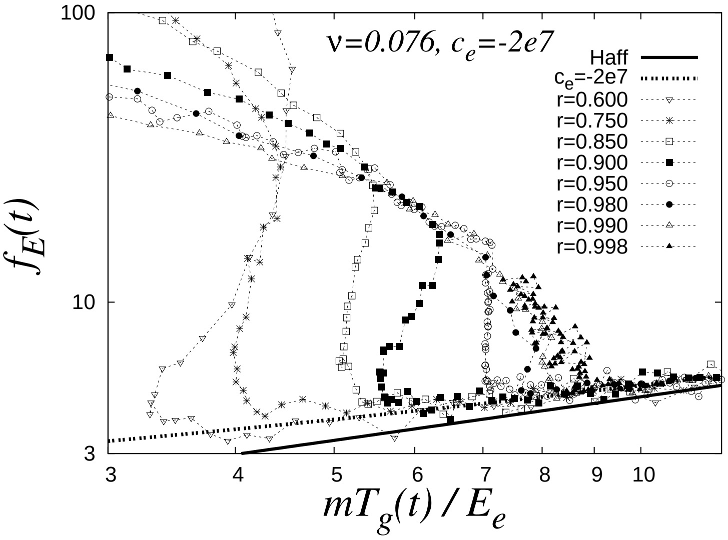

Figure 4.18: A zoom in the right panel of Fig. 4.17 around the critical temperature. Some more dissipative simulation results are added. The rapid increase of $f_E(t)$, indicating the transition from the homogeneous cooling state to the inhomogeneous regime, is shifted systematically to lower values of $mT_g(t)/E_e$ for stronger dissipation r. Time evolves to the left.

rate as compared with *Haff*, just before strong inhomogeneities are formed and the collision rate grows rapidly. Interestingly, the maximum collision frequency does not appear to depend on dissipation strength, an almost constant $f_E^{\max}$ is reached[11].

Dissipation and Critical Temperature

Fig. 4.18 shows a systematic shift of the critical temperature towards lower values for stronger dissipation. To interpret this observation, let us assume an equilibriated elastic system with actual thermal energy, referenced to the escape energy barrier, $mT_g(t)/E_e$. If we choose a low initial temperature such that $mT_g(0)/E_e$ is smaller than mT_g^{crit}/E_e, we will immediately observe clustering. If we adjust $mT_g(0)/E_e > mT_g^{\text{crit}}/E_e$, we will never observe clustering. If we consider dissipative particles in the latter case, $T_g(t)$ starts at $T_g(0) > T_g^{\text{crit}}$ and decays with

---

[11] A maximum collision frequency, $f_E^{\max} \approx 1000$, indicates a maximum density where each particle experiences 1000 binary collisions per unit time. During the theoretical collision time, $t_c = 0.001$, every particle would experience $t_c f_E^{\max} \approx 1$ collision and cannot collide more frequently, explaining $f_E^{\max}$. For $N = 3375$, the same maximum density is reached because it is also $t_c f_E^{\max} \approx 1$ (not shown). $f_E^{\max} \approx 1/t_c$ depends on the material parameters such like the stiffness of the collision, the particle's radius, density, but not on dissipation r.

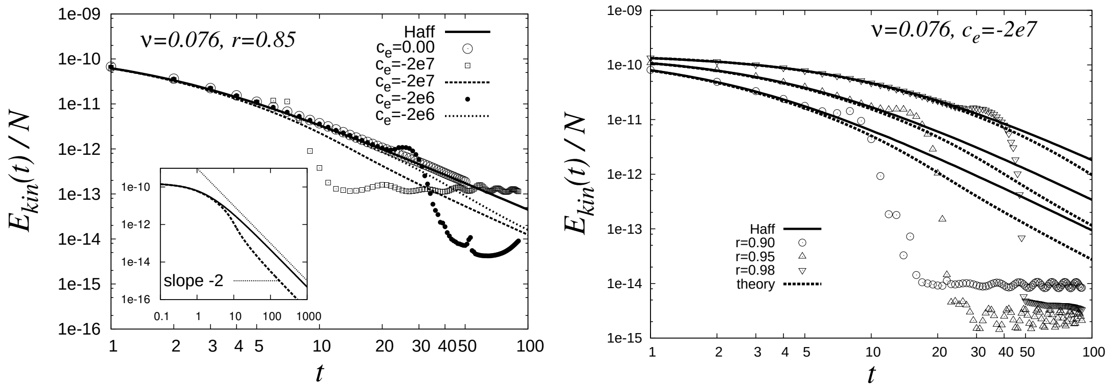

Figure 4.19: Kinetic energy per particle plotted versus time: different values of $|c_e|$ for $r = 0.85$ (left) and one value of $|c_e|$ for different dissipation $r = 0.90, 0.95, 0.98$ (right). The inset in the left panel shows the long-time behavior of both Eq. (4.14) and the solution of Eq. (4.28), as solid and dashed lines, respectively.

time. At some time, due to the dissipative collisions, $T_g(t)$ falls below $T_g^{\rm crit}$ and cluster growth starts.
The amount of dissipated kinetic energy of a binary collision is quantified by the dissipation strength. Considering a number of collisions in the system per unit time, a strongly dissipative gas loses more energy during a time period than a weakly dissipative gas, resulting in a lower temperature in the same time. This means that the transition to the inhomogeneous regime take place at lower (critical) temperatures for stronger dissipation.

4.4.3 Kinetic energy

In appendix A.5.3, the total kinetic energy in the system is described by the ordinary differential equation

$$\frac{\mathrm{d}E_{\rm kin}(t)}{\mathrm{d}t} = -f_E(t)\frac{N}{2}(1-r^2)mT_g(t) \quad , \tag{4.28}$$

which we will solve numerically. The solution of Eq. (4.28) is displayed for different parameters c_e in Fig. 4.19 and compared to the results of the simulations. Here, in the left panel, the kinetic energy per particle, $E_{\rm kin}(t)/N$, is plotted against time in a log-log-diagram for $r = 0.85$ and $\nu = 0.076$. In the beginning of the simulation we see again that the energy drops as *Haff* predicts until the system has evolved into the inhomogeneous regime which is indicated by the remarkable energy hump. The strong decay of the energy after the hump during $t = 7...10$ corresponds to the strong increase of the collision frequency in Fig. 4.16

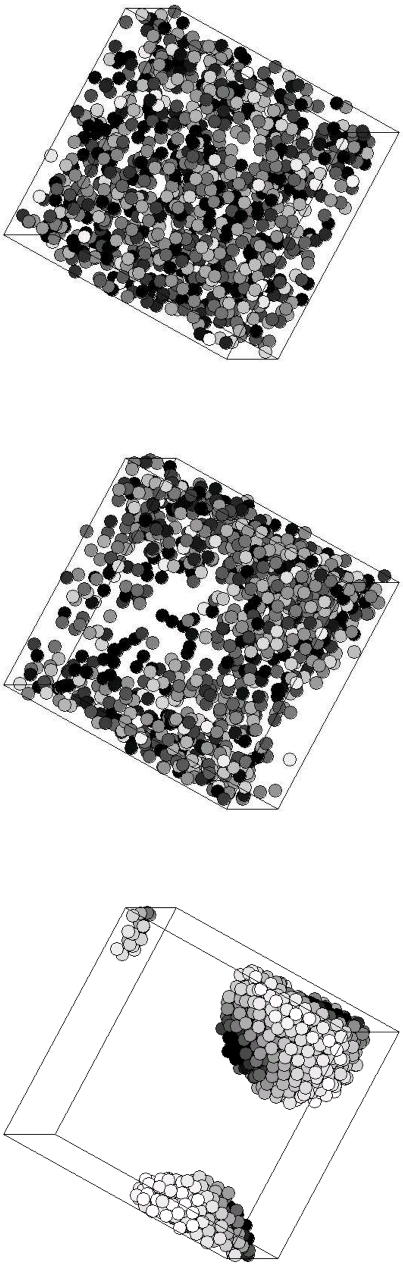

Figure 4.20: The three regimes of an attractive dissipative system with $N = 1000$, $\nu = 0.076$, $a = 0.0005$, $r = 0.90$ and $c_e = -2 \cdot 10^7$. Black particles have low, bright particles have high velocities. From top to the bottom: (*homogeneous regime*) Homogeneous cooling state and the two-particle theory applies; (*inhomogeneous regime*) Clustering; particle pairs come closer which results in the "hump" in the kinetic energy; (*agglomerate regime*) All particles are together forming a single freely spinning agglomerate. The effect of periodic boundaries is visible here.

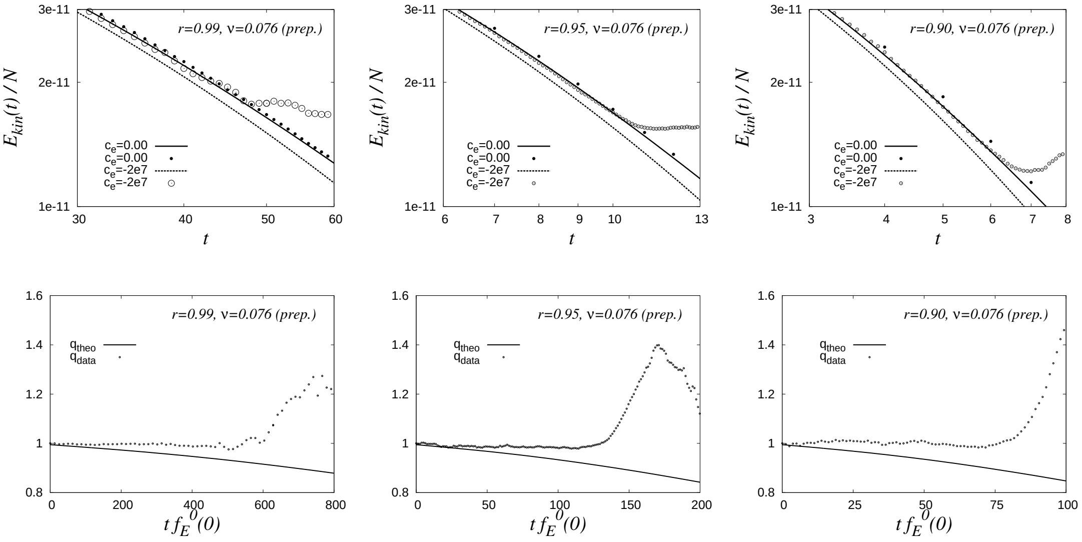

Figure 4.21: (Top panels) Kinetic energy per particle, $E_{\mathrm{kin}}(t)/N$, plotted against time, t, for the homogeneous regime for different dissipation. Black lines are *Haff*, dashed lines correspond to the two-particle theory. (Bottom panels) Quality factors, q_{data} and q_{theo}, are shown versus the number of dissipative collisions per particle, $t f_E^0(0)$, for the corresponding top panel data. “(*prep.*)” means that we have prepared the initial random configuration with the same c_e as we use for the simulation.

for $c_e = -2 \cdot 10^7$. Generally, three regimes are shown, as we can see also for simulations with different dissipation for a fixed attractive potential in the right panel of Fig. 4.19: first, kinetic energy corresponds to *Haff*’s theory (homogeneous regime), second, kinetic energy increases and reaches a maximum whereafter it drops (inhomogeneous regime) and third, average kinetic energy remains constant (agglomerate regime) on a very low energetic level, due to agglomerate rotation. Fig. 4.20 displays a typical snapshot of each regime for a system with $N = 1000$. As we can see, the two-particle theory predicts an ever decreasing kinetic energy over all times. The deviation from *Haff* reveals a stronger decrease than *Haff* and starts always roughly at the time when the hump is formed. For larger times, both run parallel to each other with a slope of -2, see the inset of the left panel of Fig. 4.19. The hump and the agglomerate formation cannot be predicted by the pseudo-Liouville operator theory because they occur in the strongly inhomogeneous regimes.

Focussing on the Homogeneous Regime

The construction of the pseudo-Liouville operator in appendix A.2 assumes a homogeneous distribution of the particles. That is why the two-particle theory, expressed by, e.g., Eq. (4.28), is only valid for homogeneous particle systems. In the following, we therefore consider the early homogeneous regime and will check the agreement between theory and simulation.

In the upper panels of Fig. 4.21 we have plotted the energy evolution of the homogeneous regime *before* the hump has formed. We see that the simulation is less dissipative than the two-particle theory predicts, i.e., the data always lie above the two-particle theory. From this we conclude, that the effective attractive many-body potential is weaker than predicted for two particles:

$$|E_{\text{eff}}| < |E_e| \quad . \tag{4.29}$$

The same inequality was found for the effective repulsive many-body potential, expressed by Eq. (4.19). But, while a weaker effective repulsive many-body potential leads to more collisions and thus to a stronger cooling behavior of the system, a weaker effective attractive many-body potential leads to fewer collisions and thus to a reduced rate of cooling.

The lower panels of Fig. 4.21 show how the quality factors, q_{theo} and q_{data}, evolve with the number of dissipative collisions per particle, $tf_E^0(0)$. q_{theo} and q_{data} are defined as the ratios between the kinetic energy of the two-particle theory and *Haff*'s law and between the kinetic energy of the simulation and *Haff*'s law, respectively. $tf_E^0(0)$ gives us roughly the number of collisions a particle has in average at time t if we count from the beginning of the simulation and the collision rate would remain unchanged. q_{theo} decays because the kinetic energy predicted by the two-particle theory decays relative to the *Haff* case. Remarkably, q_{data} is approximately unity. This means that the kinetic energy of the attractive simulation is predicted by *Haff*'s law and is not, as theory predicts, cooling down stronger due to the attraction.

Under which conditions can theory predict the evolution of the simulation? We expect better predictions if the long-range potential is less prominent, either due to lower density, smaller intensity of c_e, or in case of weaker dissipation. In the following, we will therefore have a look at systems with lower densities at fixed $c_e = -2 \cdot 10^7$, for which the influence of the mutual attractive interactions, i.e., of the many-body effect, should be less important.

Lower Densities at fixed c_e

For systems with given $c_e = -2 \cdot 10^7$ and $r = 0.95$ but different densities $\nu = 0.010$ and 0.076, the number of dissipative collisions until the inhomogeneous regime

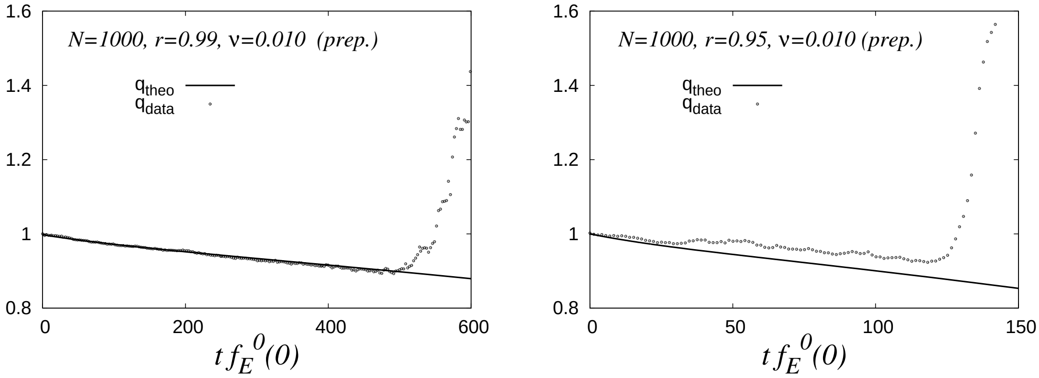

Figure 4.22: Same as the lower panels of Fig. 4.21. Quality factors are shown for the homogeneous regimes for lower volume fractions.

is reached is comparable as we can see from the Figs. 4.21 and 4.22. For both densities we find $tf_E^0(0) \approx 120$. This leads us to the conclusion that systems with different densities must undergo a certain number of dissipative collisions in order to reach the threshold temperature, which indicates the starting point of the inhomogeneous regime. This means that attractive dissipative systems have to lose a certain amount of kinetic energy in order to become inhomogeneous. This corresponds to a threshold thermal energy, whose existence we implicitly assumed in the previous sections.

Let us have a look at q_{theo} and q_{data} where now the influence of the mutual long-range potential is less prominent due to the lower densities. If we compare the quality factors for the simulations with $r = 0.95$ and different density, $\nu = 0.076$ and 0.010 in the lower panels of Fig. 4.21 and in Fig. 4.22, we observe what we expected: a better agreement between q_{theo} and q_{data} for lower densities. The lower density of $\nu = 0.010$ makes at least q_{data} running parallel to q_{theo} which means that the data follow the prediction but do not agree. If we additionally consider weak dissipation, say $r = 0.99$, as displayed in the left panel of Fig. 4.22, we observe a quite good agreement between data and theory. This result gives us the certainty that the pseudo-Liouville operator formalism in appendix A is a good Ansatz for the theoretical treatment of $1/r$ long-range *attractive* potentials as long as we deal with a dilute (weak many-body effect!) homogeneous distribution of weakly dissipative particles. Further discussion on this can be found in appendix A.6.

In Fig. 4.23 we have plotted the dimensionless collision frequency, $f_E^*(t)$, versus the scaled thermal energy, $mT_g(t)/E_e$ (left panel) for different densities. The right panel zooms into the left panel and displays the region around the critical thermal energy. The dimensionless quantity, $f_E^*(t)$, is independent of the density and, thus, we can easily compare it with results of simulations even for different densities. We made $f_E(t)$ dimensionless such as we did for the dimensionless

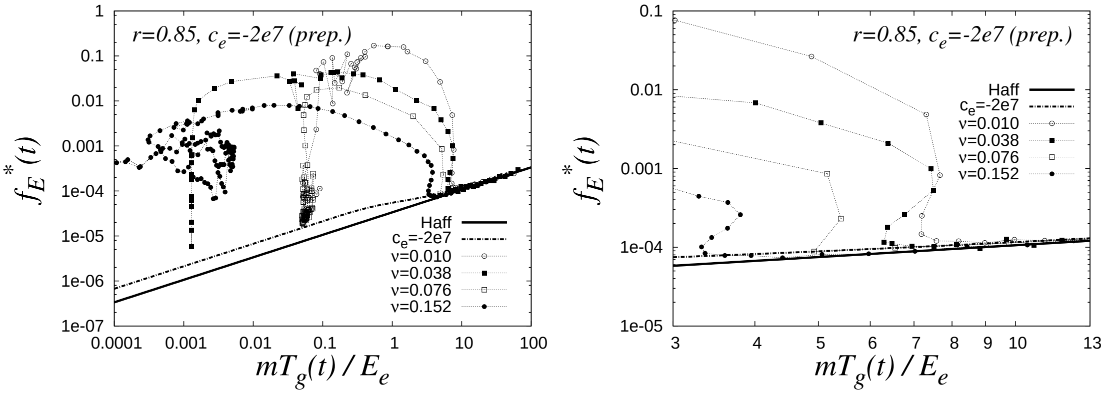

Figure 4.23: (Left) Dimensionless collision frequency, $f_E^*(t)$, plotted against scaled thermal energy for different densities. (Right) A zoom into the left panel around the critical thermal energy. Black lines correspond to *Haff*, dash-dotted lines to two-particle theory and symbols are data.

dissipation rate, $I^*(t)$, in the left panel of Fig. 4.9. Now, we can compare the apparent critical thermal energies of simulations with different density and observe in the right panel of Fig. 4.23 a systematic shift of the critical temperature towards lower values for higher densities. This observation is similar to that in the right panel of Fig. 4.18 where stronger dissipation leads to lower critical thermal energies. In order to give an interpretation for this observation, we tie up to the interpretation of the results in Fig. 4.18: during a given time, stronger dissipation leads to a lower critical temperature at which cluster growth sets in as compared to the case of weak dissipation.
Exactly here we start our interpretation for the shift of the critical temperature towards lower values due to higher densities. If we fix the dissipation and increase the density ν, the mean free path will decrease and the collision frequency will increase. That is, the amount of dissipated energy per unit time increases as well. In this sense, an increase of ν is equivalent to an increase of r (Fig. 4.18), and both effects will lead to a shift of the onset of inhomogeneities to a lower value of $mT_g(t)/E_e$.

4.4.4 Many-Body and other Effects

The remarkable fact that the energy decay of dense attractive dissipative granular gases agrees with the energy decay of the same systems without long-range forces – as long as the systems are in the homogeneous cooling state – can be explained by the effect of many bodies on a colliding pair of particles. A significant change of the parameters ν, r and c_e does not affect this observation. Only for low densities, little dissipation and weak attraction, the energy decay becomes

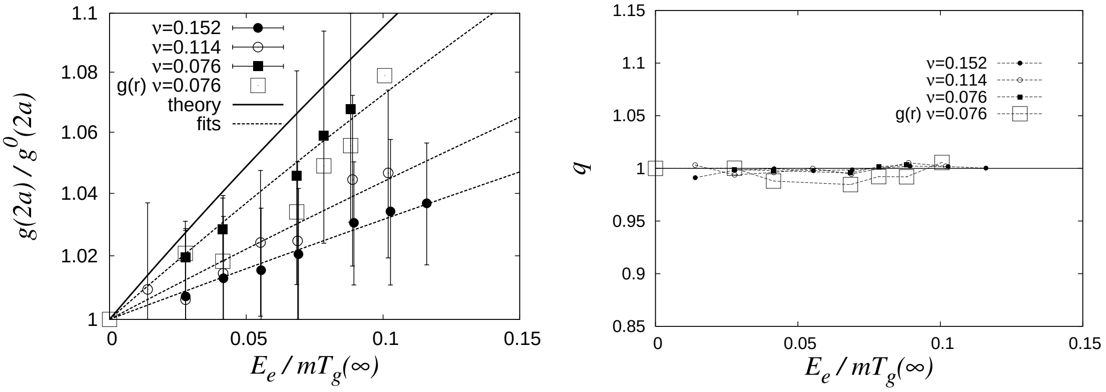

Figure 4.24: (Left) Small symbols correspond to data obtained by computing $f_E(t)/f_E^0(t)$ from the simulations, large open squares correspond to data obtained by extrapolation of $g(r)$. Dashed lines are best fits (the corresponding fit-parameters are listed in Tab. 4.3). The black line represents the two-particle theory. Errorbars denote an error margin of once the standard deviation. (Right) The quality factor, q, of the fits of the left panel.

stronger and approaches the prediction of the two-particle theory, as shown in the left panel of Fig. 4.22.

As already done in section 4.3.5 for repulsive systems, we now focus on elastic simulations in order to exclude dissipative effects. We extract the correction factor for attractive forces, $\left[2-\exp\left(E_{\text{eff}}/(mT_g(t))\right)\right]$, from the scaled collision frequency, $f_E(t)/f_E^0(t)$, and plot it as a function of the order parameter, $E_e/\left(mT_g(\infty)\right)$, as shown in the left panel of Fig. 4.24 for three different densities (small symbols). The panel additionally shows the results extracted from $g(2a)/g^0(2a)$ in Fig. 4.15 for the density $\nu = 0.076$ (large open squares). Although not showing perfect agreement between the data of both extraction methods for $\nu = 0.076$ (compare small solid with large open squares), we set for the attractive case – according to Eq. (4.23):

$$\frac{g(2a)}{g^0(2a)} \overset{!}{=} \frac{f_E(t)}{f_E^0(t)} = 2 - \exp\left(-\frac{E_{\text{eff}}}{mT_g(t)}\right) \quad . \tag{4.30}$$

Due to the fact that we consider only small values of E_e (in order to guarantee a homogeneous system), we are limited to small values of the coupling parameter, i.e., we can write the correction factor as

$$\begin{aligned} \frac{g(2a)}{g^0(2a)} = 2 - \exp\left(-\frac{E_{\text{eff}}}{mT_g(t)}\right) \quad &= \quad 2 - \exp\left(-\alpha(\nu)\,\frac{E_e}{mT_g(t)}\right) \\ &\overset{E_e \ll mT_g(t)}{\approx} \quad 1 + \alpha(\nu)\,\frac{E_e}{mT_g(t)} \end{aligned} \tag{4.31}$$

ν	0.152	0.114	0.076	0.038	0.010
$\alpha_b(\nu)$ $^{(*)}$	0.21	–	0.35	0.48	0.74
$\alpha_e(\nu)$ $^{(**)}$	0.32	0.45	0.75	–	≈ 1

$^{(*)}$ see Fig. 4.12 (left), linear fit with Eq. (4.21) for $E_b/\big(mT_g(\infty)\big) = 0...1$

$^{(**)}$ see Fig. 4.24 (left), linear fit with Eq. (4.31) for $E_e/\big(mT_g(\infty)\big) = 0...0.15$

Table 4.3: The correction factor for both the repulsive, $\alpha_b(\nu)$, and the attractive case, $\alpha_e(\nu)$, listed for different densities, ν. The fits are done in the limit $E_{b/e} \ll mT_g(\infty)$.

and realize that E_{eff} is linearly dependent on E_e for small E_e. $\alpha(\nu)$ is the density-dependent proportionality constant that corresponds to the positive slopes in the left panel of Fig. 4.24. The black line corresponds to the two-particle solution, $\nu \to 0$, for which $\alpha(\nu) \to 1$. The dashed lines are fits to the data for different densities.

The right panel of Fig. 4.24 shows the quality factor, q, of the fits which is the ratio of the data points and their best fit. The fit quality for the data set represented by the large open squares (where data are extracted from $g(2a)/g^0(2a)$) is worst in comparison to that for the other data sets, because for the computation of q, we use the fit to the solid squares (for which the data are extracted from $f_E(t)/f_E^0(t)$). Generally, the fits for the attractive case are qualitatively better (i.e., the quality factor is closer to unity) than for the repulsive case, as we can see from the left panel of Fig. 4.13. This is not surprising, because we are here limited to a smaller fit range, i.e., $E_e/\big(mT_g(\infty)\big) < 0.15$.

Excursion: Comparison with the Repulsive Case for $E_b \ll mT_g(\infty)$

For small order parameters, i.e., for $E_{b/e} \ll mT_g(\infty)$, E_{eff} depends linearly on $E_{b/e}$ for both the repulsive and the attractive case. The correction factor then simplifies to

$$1 \pm \alpha_{b/e}(\nu)\,\frac{E_{b/e}}{mT_g(t)}\quad ,$$

where the positive sign denotes the attractive and the negative sign the repulsive case. Note that $|E_b| = |E_e|$. The proportionality constants $\alpha_{b/e}(\nu)$ of the linear regime are listed in Tab. 4.3. If we compare the linear fits for the case $E_{b/e} \ll mT_g(\infty)$ we see that $\alpha_b(\nu) < \alpha_e(\nu)$ for a given ν. For the low density limit $\nu \to 0$, we obtain $\alpha_{b/e}(\nu) \to 1$, wich is equivalent to a vanishing many-body effect and a maximum correction of $g(2a)$ (i.e., a maximum deviation from $g(2a)/g^0(2a) = 1$).

4.4.5 Improved Time Evolution of Dynamical Observables

For solving Eq. (4.28) with the correction factor in Eq. (4.31), we are – in contrast to the repulsive case in section 4.3.6 – limited to the case $E_e \ll mT_g(t)$ (because of maintaining the homogeneous state). In this limit, E_{eff} is linearly dependent on E_e and different densities provide different values of the proportionality constant, $\alpha(\nu)$. Fig. 4.25 shows the order parameter, $mT_g(t)/E_e$, as a function of time, t, for a given attraction strength, $c_e = -2 \cdot 10^7$. The dashed lines denote the solution of Eq. (4.28) assuming the linear dependency between E_{eff} and E_e. The solid lines correspond to *Haff*'s law without attraction. Open circles correspond to the respective attractive simulation in the homogeneous regime which finally shows the transition to the inhomogeneous regime indicated by the strong increase of the order parameter. In the insets of the panels, we see that data (open circles) mostly deviate from theory (dashed lines). When we investigate strongly dissipative systems, theory does not provide correct results even if we consider the many-body effect by using Eq. (4.31) with $\alpha(\nu) = 0.75$. We observe that too strong dissipation or too high densities surprisingly lead to a cooling behavior that can be predicted very well by *Haff*'s theory (see the upper left panel of Fig. 4.25, where $r = 0.95$ and $\nu = 0.076$). On the other hand, if we decrease the dissipation and hence the dissipative effects, the agreement between theory and data improves. Dissipative effects can also be diminished by decreasing the density which leads to fewer collisions per unit time. If we deal with sufficiently weak dissipation and very dilute systems we will observe nearly perfect agreement between theory and simulation (see the lower right panel of Fig. 4.25, where $r = 0.99$ and $\nu = 0.010$).

Due to the fact that we are able to extract the $\alpha(\nu)$ for different ν by fitting the results for only small inverse order parameters, see the range $E_e/\big(mT_g(\infty)\big) \approx 0...0.15$ in the left panel of Fig. 4.24, we assume to have an agreement between theory and data for the range $mT_g(t)/E_e \gtrsim 7$ in the panels of Fig. 4.25, irrespective of ν and r. This is what we do not see and, so, we conclude that the many-body effect is not only responsible for the deviations, i.e., dissipative effects also have to be considered – such as in the repulsive case.

4.4.6 Cluster Regime

The inelasticity of particle collisions is responsible for the clustering phenomenon which is reported in many articles [34,43,75,81,84]. Associated with the transition from the homogeneous cooling state to the inhomogeneous regime and finally to cluster formation in a dissipative granular gas is a drastical change of the velocity field of the granular medium. Initial vortices can grow and are accompanied by density inhomogeneities [10]. Growing density inhomogeneities are quantitatively described by small spatial sinoidal density perturbations. Dissipation must exceed

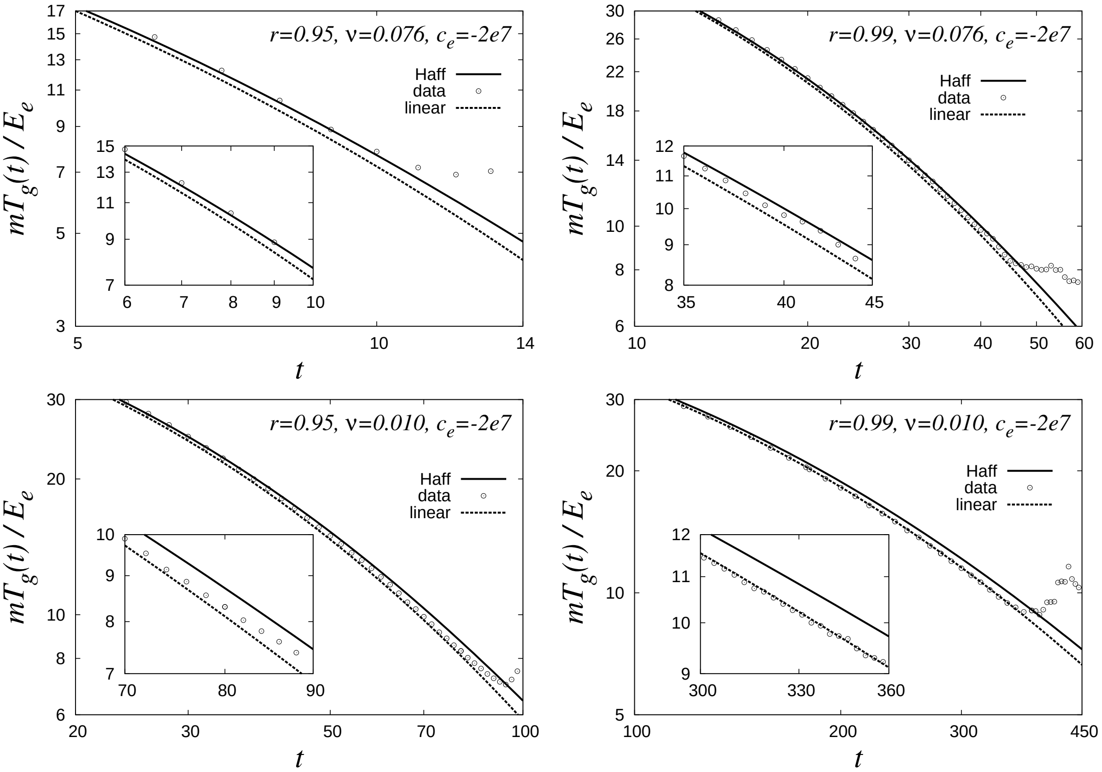

Figure 4.25: The order parameter, $mT_g(t)/E_e$, plotted as a function of time, t, for the attraction $c_e = -2 \cdot 10^7$. Solid lines are *Haff*'s prediction, dashed lines are the solution of Eq. (4.28) using the linear correction of Eq. (4.31) in the limit $E_e \ll mT_g(t)$. (Left) The parameters $r = 0.95$, $\nu = 0.076$ and $\alpha(\nu) = 0.75$ are used. (Right) The parameters $r = 0.99$, $\nu = 0.010$ and $\alpha(\nu) = 1$ are used. The insets show a zoom into the plots just before the initial increase of kinetic energy ($\hat{=}$ inhomogeneous regime) sets in.

a critical value, r_{cl}, in order to allow for the growth of density perturbations with a wave length of the order of the system's size L [81, 85]. The agitation of perturbations with smaller wave lenghts requires stronger dissipation, i.e., $r < r_{\mathrm{cl}}$, whereas no clustering at all is observed if dissipation is weaker than the critical magnitude. Whether density perturbation modes become unstable, depends on the degree of inelasticity, r, the system size, L, and the number of particles, N, in the system. Note that L and N enter the volume fraction, ν, and the

ν	L	$L/(2a)$	l_{opt}	r_{cl}	r_{sh}
0.010	0.037	37	0.374	–	–
0.038	0.024	24	0.912	–	–
0.076	0.019	19	1.446	–	0.70
0.152	0.015	15	2.296	0.48	0.89
0.300	0.012	12	3.612	0.83	0.95

Table 4.4: We use $N = 1000$ and $a = 0.0005$. The critical coefficient of restitution for cluster instability, r_{cl}, and for shear instability, r_{sh}, are listed for different densities, ν, and system sizes, L, for systems without long-range attractive forces. l_{opt} is the optical length which is a measure for the density of the system.

dimensionless optical length[12], $l_{\mathrm{opt}} = \nu \frac{L}{2a}$. It was found [84] that

$$r_{\mathrm{cl}} = \sqrt{1 - \frac{25\pi^3}{192 l_{\mathrm{opt}}^2}} \quad .$$

For the instability of the gas against shear modes, it is

$$r_{\mathrm{sh}} = \sqrt{1 - \frac{5\pi^3}{144 l_{\mathrm{opt}}^2}} \quad ,$$

where $r_{\mathrm{sh}} > r_{\mathrm{cl}}$, as it can be seen in Tab. 4.4 for the systems we simulated. To summarize, one obtains for sufficiently weak dissipation, $r > r_{\mathrm{sh}}$, the homogeneous cooling state, whereas for sufficiently strong dissipation, $r < r_{\mathrm{cl}}$, cluster formation occurs. The domain $r_{\mathrm{sh}} > r > r_{\mathrm{cl}}$ supports shear fluxes in the system while the density remains about homogeneous. According to the table, the systems with $\nu \leq 0.076$ are too small in order to allow for growing perturbations even if we would apply $r \to 0$.

If we now additionally consider $E_e > 0$, all the facts stated above are supported by the presence of attractive forces. That means in particular, the critical coefficients of restitution, r_{cl} and r_{sh}, are shifted to higher values, and perturbations with wave lengths of the order of L can occur even for less dissipative particles than calculated. This is, e.g., why we observe clustering in our attractive simulations ($c_e = -2 \cdot 10^7$) with $L = 0.015$ ($\nu = 0.152$) already for dissipation $r = 0.85 > r_{\mathrm{cl}}$ (see the right panel of Fig. 4.23), although for $c_e = 0$ we would have to choose $r < 0.48$ in order to observe cluster growth.

---

[12] The optical length, l_{opt}, is the fraction of the path of a straight line through the simulation volume in units of the particles' diameter, $2a$, that runs through particles. Hence, it is a measure for the system's density.

4.4.7 Summary for Attractive Systems

Simulating dissipative particle systems with mutual long-range attractive forces always show three distinguishable regimes both in energy and collision frequency plots: a homogeneous regime, which can be predicted by *Haff*'s law in most cases, an inhomogeneous regime in which both kinetic energy and the collision frequency increase strongly and reach a maximum and, finally, the agglomerate regime, in which these quantities drop to a minimum, since particles form an agglomerate that is spinning inside the simulation space.
The two-particle theory for attractive long-range forces we developed by means of the *pseudo-Liouville* operator formalism is a theory for the dilute limit, $\nu \to 0$, where the pair distribution function at contact, see Eq. (4.8), becomes unity and the correction factor is determined as $2 - \exp\big(-E_e/(mT_g(t))\big)$. Here, E_e is the attractive escape energy barrier the relative velocity of two separating particles has to fall below in order to have a collision. The resulting prediction of the time evolution of the total kinetic energy for very dilute systems ($\nu \approx 0.01$) was confirmed by the present simulations.
As soon as we deal with finite densities, the density-dependence of $g(2a)$ becomes important and the two-particle escape energy barrier, E_e, will become an effective barrier, E_{eff}, which is reduced as compared to E_e. This gives an increased pair distribution function at contact, $g(2a) = g^0(2a)\ \big[2 - \exp\big(-E_{\text{eff}}/(mT_g(t))\big)\big]$, for which the density-dependence of E_{eff} was empirically determined by simulations. We found that E_{eff} is linearly dependent on the density for $\nu \leq 0.152$ in the range $E_e/\big(mT_g(t)\big) < 0.15$, in which the onset of cluster growth can be excluded. In contrast to the repulsive case, however, we were not able to improve the prediction of the dissipation rate by applying the empirical findings. Instead, *Haff*'s prediction interestingly applies for finite densities and strong inelasticity. This leads us to the conclusion that not only volume exclusion effects but also other (dissipative) effects play an important role if we investigate inelastic systems with finite density.

4.5 Summary

The cooling behavior of a homogeneously distributed system of hard spheres that interact via short-range forces can be predicted by the so-called *pseudo-Liouville* operator formalism. This formalism was extended for both mutual repulsive and attractive $1/r$ long-range potentials. The resulting modified cooling behavior was compared with the results obtained from the simulation of soft sphere systems.
For the repulsive case in the dilute limit, the modified theory leads to a Boltzmann factor that corrects the pair distribution function at contact, resulting in

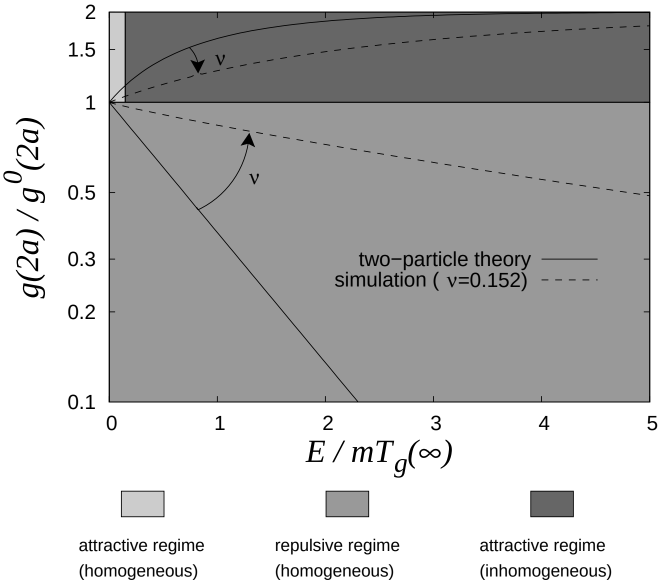

Figure 4.26: The correction factor is plotted against $E_{b/e}/\big(mT_g(\infty)\big)$, and corrects the pair distribution function at contact in the presence of long-range forces. Solid lines denote the two-particle theory in the dilute limit, dashed lines the results for a finite density. Note, that for the dark shaded area the correction factor cannot be determined due to the growth of inhomogeneities.

a correction of the dissipation rate

$$I(t) = I^0(t)\, \exp\left(- \frac{E_b}{mT_g(t)} \right) \quad .$$

As compared to the case without long-range forces, the dissipation rate is decreased. For the attractive case, theory provides a different correction term, leading to the corrected dissipation rate

$$I(t) = I^0(t) \left[2 - \exp\left(- \frac{E_e}{mT_g(t)} \right) \right] \quad ,$$

which is increased as compared to the case without long-range forces. For the dilute limit, for which the pair distribution function at contact, $g^0(2a)$, is unity, we confirmed the result by simulations for both the repulsive and attractive case. In the limit of vanishing long-range forces, theory provides *Haff*'s law [43], as expected, where $I(t) = I^0(t)$ and $I^0(t)$ is the dissipation rate of a granular system without long-range repulsive forces.

Increasing the density ν, $g^0(2a)$ will become different from unity and the correction factors become density dependent, due to an effective energy barrier, E_{eff}. E_{eff} is reduced for both the repulsive and attractive case as compared to systems without long-range forces. This results in a modified pair distribution function which is decreased in the repulsive and increased in the attractive case as compared to the case without long-range forces. The dashed lines in Fig. 4.26 represent $g(2a)$ in units of $g^0(2a)$. With increasing density, the cooling behavior becomes more and more similar to that of systems without long-range forces (i.e., the dashed lines approach the horizontal line at $g(2a)/g^0(2a) = 1$).

Finally, we investigated empirically how the correction factor changes for systems with different densities. In the repulsive case, we found a density-dependent effective repulsive energy barrier that is non-linearly dependent on E_b, which we successfully used in order to improve the prediction of the dissipation rate.

In the attractive case, we found the density-dependent effective escape energy barrier to be linearly dependent on E_e. Using this empirical finding, however, it was not possible to improve the prediction of the cooling behavior, instead, the cooling rate surprisingly behaves similar to the case without long-range attraction. That leads us to the conclusion that density effects are not the only reason for the deviation, but also effects due to dissipation might play a role.

5 Ring-Shaped Particle Systems

Disk-like structures are very common in the universe and are represented by, e.g., galaxies, accretion disks and planetary rings. In general, disks and rings around central gravitational bodies are a natural consequence of dissipation in rotating systems. A spherical cloud of debris rotating around a central body settles into a flat circular ring system because of the dissipative nature of the macroscopic (granular) particles and of the conservation of total angular momentum. Central bodies such as the planets of the solar system are oblate which results in the conservation of the axial component of angular momentum only, which leads every spherical cloud evolving to a flat ring that orbits around the planet in its equatorial plane.

Such ring systems are differentially orbiting according to the Keplerian laws: ring material closer to the central body is moving faster than that farther away. Viscous shear stresses are the consequence, converting systematic particle motion (on ellipsoidal Keplerian paths) into random motion which leads to a persistently increasing granular temperature of the ring. As a consequence, the ring system spreads radially and vertically. Likewise, collisions between the ring particles redistribute angular momentum and lead to a radial mass flow towards the central body and simultaneously to a radial transport of angular momentum towards outer regions, see Ref. [100].

Many structures are observed in the ring systems of the giant planets in the solar system. The most popular example, Saturn's rings, exhibits a wealth of structures in both radial and azimuthal direction that result from physically completely different processes. The most important process is the inelastic collision between ring particles. The removal of kinetic energy due to collisions can keep the planetary ring narrow and counteracts the heating process due to viscous shearing [112]. Dissipative collisions are mainly responsible for the unique wealth of structures. While stable cluster formation is observed in freely evolving granular gases due to the inelastic nature of inter-particle collisions [34, 75, 81, 82, 85], one observes transient clustering in granular ring systems in a permanent tidal field with Keplerian shear, as observed in Refs. [115, 118]. The influence of satellites (small moonlets embedded in the ring or separated from it) on the ring dynamics is important as well. Saturn's moons exert forces on the ring material, shepherding the particles in the ring, even clearing regions, whereby gap formation and gravitational wakes are a consequence, see Refs. [106, 116, 117]. An extensive review on planetary rings, e.g., is given in Refs. [31, 35, 107, 121].

In the following section, we investigate the time evolution of a complete dilute ring-shaped N-body system by Molecular Dynamics methods. The dynamics is governed by dissipative particle-particle collisions and we will add mutual long-range attractive interactions [77] later on in order to study the influence of dissipative contact forces and long-ranged attraction forces on the viscous behavior of such particle systems. First of all, we focus on general aspects that are important for the understanding of disk-shaped particle systems.

5.1 General Aspects

In the following, we will explain the basic aspects that are important for the understanding of the motion of particles in a central gravitational potential.

5.1.1 Keplerian Motion

The presence of a central gravitational potential can deflect or even capture bodies that approach from infinity, see Fig. 2.1 (c). For the trajectory of a particle i that moves in a central potential, *Newton*'s equations of motion provide the general equation of a conic section in polar coordinates, r_{ic} and ϕ,

$$r_{\mathrm{ic}}(\phi) = \frac{p}{1+\varepsilon_{\mathrm{ecc}}\cos(\phi)} \quad ,$$

where the *numerical eccentricity*, $\varepsilon_{\mathrm{ecc}}$, determines the type of the section. Here, we define r_{ic} to be the closest distance between m_i and M_c for $\phi = 0$, and the largest for $\phi = \pi$. Then, $r_{\mathrm{ic}}(\phi = \pi/2) = L_i^2/(GM_c m) = p$, where $L_i = m_i|\boldsymbol{r}_{\mathbf{ic}} \times \boldsymbol{v}_\phi|$ is the orbital angular momentum of the particle. Particle trajectories with $\varepsilon_{\mathrm{ecc}} = 0$ describe a perfectly circular path, whereas those with $\varepsilon_{\mathrm{ecc}} = 1$ describe a parabola. In the case $0 < \varepsilon_{\mathrm{ecc}} < 1$, the path can either be described by an ellipse (see Fig. 5.1 (left), where $\langle E_{\mathrm{tot}}\rangle < 0$) or by a hyperbola (see Fig. 2.1 (b), where $\langle E_{\mathrm{tot}}\rangle > 0$). The central body is located in one of the two focal points of the ellipse (**1st Keplerian law**). As long as the orbital angular momentum is constant in time, the motion of the particle is such that a line joining the particle and the central body sweeps out equal areas in equal time intervals. This means, that particles close to the central body move faster than particles farther away (**2nd Keplerian law**). Balancing the centrifugal and gravitational force, $m_i v_\phi^2/r_{\mathrm{ic}} = GM_c m_i/r_{\mathrm{ic}}^2$, one obtains the Keplerian velocity of a particle in azimuthal direction:

$$v_\phi = \left(\frac{GM_c}{r_{\mathrm{ic}}}\right)^{\frac{1}{2}} \quad . \tag{5.1}$$

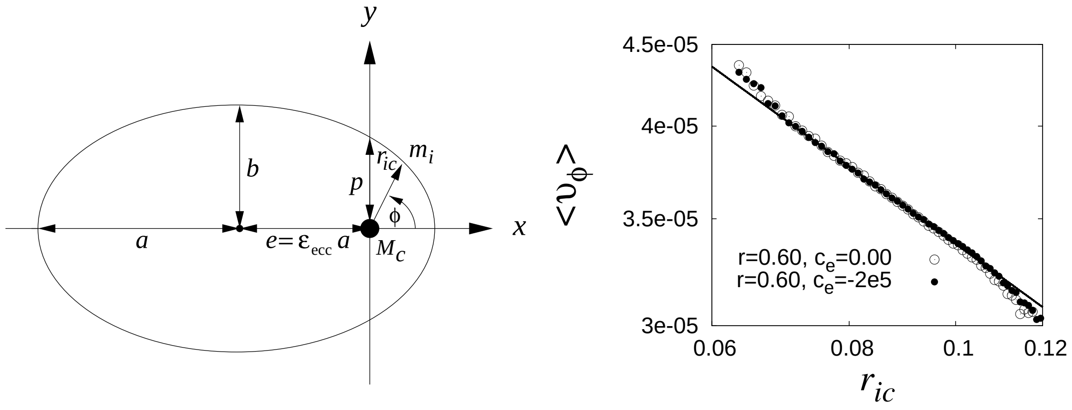

Figure 5.1: (Left) Illustration of a typical Keplerian trajectory of a single particle with mass m_i moving in a central potential with mass M_c. a and b denote the semi-major and minor axes, respectively, e the eccentricity and $\varepsilon_{\mathrm{ecc}}$ the *numerical* eccentricity. (Right) Double logarithmic plot of the Keplerian motion in azimuthal direction as a function of radial distance for a non-gavitating system (large open circles) and a gravitating system (small solid circles), each with $r = 0.60$. The solid line corresponds to Eq. (5.1).

Assuming circular paths, i.e., $r_{\mathrm{ic}} \approx a$, one can set for the orbital period, $T = 2\pi a/v_\phi$, and find that $T^2/a^3 \approx 4\pi^2/(GM_c)$ is constant for all particles moving around M_c, irrespective of their mass (**3$^{\mathrm{rd}}$ Keplerian law**). The approximation sign is because we implicitly assume a spatially fixed M_c, i.e., $M_c \gg m_i$.

The right panel of Fig. 5.1 shows the double logarithmic plot of the mean azimuthal velocity, $\langle v_\phi \rangle$, as a function of the radial distance, r_{ic}. The straight solid line represents Eq. (5.1) and symbols are data. Solid circles represent a gravitating ring system with $r = 0.60$, open circles correspond to the same system without attraction. Deviations from Eq. (5.1) can be seen for $r_{\mathrm{ic}} < 0.07$ and $r_{\mathrm{ic}} > 0.11$, for which too few particles contribute to the computation of the mean azimuthal velocity and statistics becomes unrelieable.

5.1.2 Granular Temperature

In section 4.1.1 we defined a granular temperature for homogeneous N-body systems, for which the particles have a fluctuating energy component only and do not have a mean velocity component. In contrast, a granular annular flow will indeed show a movement of the particle bulk into a special direction which is the azimuthal direction. This is due to the Keplerian motion of the particles. So, for the granular temperature, we use

$$T_g(t) = \frac{1}{3}\Big(\big\langle \boldsymbol{v}^2(t) \big\rangle - \big\langle \boldsymbol{v}(t) \big\rangle^2 \Big) \tag{5.2}$$

instead of Eq. (4.3). The ring-shaped geometry of the system requires a specific treatment of the squared mean in Eq. (5.2). Plausibility considerations lead us to

$$\big\langle \boldsymbol{v}(t) \big\rangle^2 \to \big\langle |\boldsymbol{v}(t)| \big\rangle^2 \quad ,$$

where we calculate the magnitude of the overall velocity vector before we calculate its mean, see Ref. [86]. This procedure makes sure that velocity components of different sign[1] will not cancel each other and, so, all particles' velocities will contribute to the granular temperature.

Finally, we remark that the velocity distribution of the particles within ring systems are far from the Maxwellian distribution – not only because of the dissipative character of particle collisions but also due to the shear forces that are permanently acting on the particles.

5.1.3 Virial Theorem

Multiplying Newton's equations of motion of a many-body system with the velocity vector of a particle i gives

$$\sum_i m_i \ddot{\boldsymbol{r}}_i \cdot \dot{\boldsymbol{r}}_i = \sum_i \left(\boldsymbol{F}_i^{\text{con}} + \boldsymbol{F}_i^{\text{diss}} \right) \cdot \dot{\boldsymbol{r}}_i \quad ,$$

where we split up the total force acting on the particle i into the conservative (due to the central mass M_c) and dissipative contributions. With the left-hand-side as the total kinetic energy, E_{kin}, and $\sum_i \boldsymbol{F}_i^{\text{con}} \cdot \dot{\boldsymbol{r}}_i = -\sum_i (\nabla_i E_{\text{pot}}) \cdot \dot{\boldsymbol{r}}_i = -\mathrm{d}E_{\text{pot}}/\mathrm{d}t$, we can write

$$\frac{\mathrm{d}}{\mathrm{d}t}\left(\underbrace{\frac{1}{2}\sum_i m_i \boldsymbol{v}_i^2}_{E_{\text{kin}}} \underbrace{-GM_c \sum_i \frac{m_i}{|\boldsymbol{r}_{\text{ic}}|} + c_e G \sum_{i,j} \frac{m_i m_j}{|\boldsymbol{r}_{ij}|}}_{E_{\text{pot}}} \right) = \sum_i \boldsymbol{F}_i^{\text{diss}} \cdot \dot{\boldsymbol{r}}_i \quad . \tag{5.3}$$

In the case of elastic systems the right-hand-side of Eq. (5.3) will be zero and the total energy, $E_{\text{tot}} = E_{\text{kin}} + E_{\text{pot}}$, will be conserved. For the case of inelastic collisions, i.e., $\boldsymbol{F}_i^{\text{diss}} = -\sum_{i,j} \gamma\big(\boldsymbol{v}_{ij}(t) \cdot \boldsymbol{n}_{ij}(t) \big) \boldsymbol{n}_{ij}(t)$, E_{tot} decreases in time. In a central potential, the time derivative of the sum of the total kinetic energy and

---

[1] The overall velocities of two particles whose positions are point symmetric in relation to the central potential will cancel each other more or less because their velocity vectors are identical in magnitude but directed oppositely.

the total potential energy will equal the dissipative force times the velocity of the particle. The *Virial theorem* states that for particles in a central gravitational field such as expressed by Eq. (2.1), the time average of the total negative potential energy is twice the time average of the kinetic energy of all particles:

$$-\langle E_{\text{pot}} \rangle_t \;=\; 2\langle E_{\text{kin}} \rangle_t \quad . \tag{5.4}$$

In astrophysics, it is common to use this relationship between kinetic and potential energy in order to determine the mass, M_c, of the central body or, in case of globular star clusters, the effective mass of the cluster, assuming no mutual attraction forces between the stars. Then, from Eq. (5.4) results

$$M_c = \left\langle \sum_{i=1}^{N} m_i \boldsymbol{v}_i^2 \right\rangle_t \; / \; \left\langle G \sum_{i=1}^{N} \frac{m_i}{|\boldsymbol{r}_{\text{ic}}|} \right\rangle_t \quad ,$$

where the $\boldsymbol{v}_i$, r_i and m_i are observable quantities.

5.1.4 Optical Depth

The optical depth, τ, is defined as the ratio of the total surface area of particles to the area of the ring they reside in. For a mono-disperse particle size distribution of ΔN particles with radius a in a ring of width ΔA, τ reads

$$\tau := \frac{\Delta N \pi a^2}{\Delta A} = \frac{\pi a^2}{m}\rho^* \quad , \tag{5.5}$$

where $\rho^* = \Delta N m / \Delta A$ is the two-dimensional mass density (surface density) of the ring and does not depend on the ring's vertical height. This holds as long as we deal with vertically thin ring systems. Note, that the optical depth can exceed unity.

The optical depth is dimensionless and its importance stems from the fact that most physical quantities (such as impact frequency and kinematic viscosity) can be expressed as a function of τ only.

5.1.5 Kinematic Viscosity

Generally, the kinematic viscosity is dependent on the density, Eq. (5.5). In the case of a freely evolving gas, for which the volume force is zero, the kinematic viscosity increases with temperature and is referenced to the density, i.e., $\nu^* = T_g(t)/\tau$. As soon as we deal with gases moving in a central gravitational field, the density-dependent kinematic viscosity reads

$$\nu^*(R,t) = 0.46\, \frac{3T_g(t)}{\Omega(R)} \frac{\tau}{1+\tau^2} \quad ,$$

where $\Omega = \Omega(R) = 2\pi/T_{\text{Kep}}$ is the Keplerian frequency. On the other hand, for low densities, the kinematic viscosity is found to be

$$\nu^*(R,t) = k_\nu \frac{3T_g(t)}{\Omega(R)}\tau \quad , \tag{5.6}$$

which is confirmed both theoretically in Refs. [18,36] and by simulations, e.g., in Refs. [42,130], where $k_\nu \approx 0.15$ is a constant. In the simulations, the kinematic viscosity is supposed to obey Eq. (5.6) because we deal with dilute ring systems ($\tau < 0.3$).

5.2 The Model System

Before we investigate complete ring shaped particle systems, we will introduce the simulation method we developed. We will extend the Molecular Dynamics simulation method, as introduced in section 3.1, by the volume force of a central body. Long-range attractive interaction forces between all ring particles and all others are computed according to the hierarchical linked cell algorighm with non-periodical boundary conditions, as described in section 3.6. The HLC method is applied on ring-shaped particle systems in Ref. [87].

5.2.1 Forces

For solving *Newton*'s equations of motion for each particle, the algorihm computes the new positions of the particles by means of *Verlet*'s integration scheme described in chapter 3.1. For doing this, the integrator needs to know the currently acting forces on any particle. In the following, we summarize the forces that can act on the particles in our model.

(i) Short-Range Forces

short-range forces are activated only if particles are in mechanical contact. A mechanical contact between two particles in our simulations occurs as soon as both particles overlap, i.e., when the absolute value of the distance vector between the particles becomes smaller than the sum of their radii. The overlap is quantified by $\delta(t)$. Then, the force on particle i is computed by

$$\boldsymbol{F}_i(t) = k\delta(t)\boldsymbol{n}_{ij}(t) - \gamma\big(\ \boldsymbol{v}_{ij}(t)\cdot\boldsymbol{n}_{ij}(t)\ \big)\boldsymbol{n}_{ij}(t) \quad ,$$

whereas for the other particle j, the force is calculated via $\boldsymbol{F}_j = -\boldsymbol{F}_i$. k and γ are material parameters, determining the strength of the repulsive and that of the dissipative force, respectively. The second term in the equation is the dissipative force that reduces the repulsion force, resulting in a loss of kinetic energy after the collision. For more details on the short-range forces considered, we refer to section 3.1.1.

(ii) Long-Range Forces

The computation of long-range forces on a particle i is carried out in several steps: the immediate vicinity of particle i contains $M_{\text{ico}} - 1$ particles within the inner cut-off sphere (see section 3.6.2), where M_{ico} is the typical number of neighboring particles. The force between each of the $M_{\text{ico}} - 1$ particles and particle i is calculated separately.

The next steps consist of the calculation of the force between i and the pseudo particles of any hierarchy applied. Due to the special geometry of thin ring systems, we make the hierarchical structure in z-direction composing only of one linked cell (lower panel of Fig. 5.2), while arranging $3^{H_{\max}}$ linked cells in x and y-direction (upper panel). So, in contrast to the homogeneous particle systems of chapter 4, we have a reduced number of $3^{H_{\max}} \times 3^{H_{\max}} \times 1$ basic cells for the linked cell neighborhood search and $(3\times3\times1)-1 = 8$ pseudo particles in each hierarchy that act on i. So, the total long-range force contribution for particle i reads

$$\boldsymbol{F}_i(t) = \sum_{j=1}^{M_{\text{ico}}-1} \boldsymbol{F}_{ij}(t) + \sum_{h=1}^{H_{\max}} \sum_{\alpha=1}^{8} \left(\boldsymbol{F}_{i\alpha}^{(M)(h)}(t) + \boldsymbol{F}_{i\alpha}^{(Q)(h)}(t) \right) ,$$

where $\boldsymbol{F}_{ij}$ is given in section 2.1.1 and $\boldsymbol{F}_{i\alpha}^{(M)}, \boldsymbol{F}_{i\alpha}^{(Q)}$ are given in section 2.3. The maximum hierarchy $H_{\max}$ is chosen such that each linked cell contains not too many particles. Otherwise, a large number of particles per cell will make the HLC algorithm running inefficiently, because in each linked cell every particle is checked with all others in the same cell. Typically, we use $H_{\max} = 4$ which provides 81 linked cells in x and y-direction, leading to an optimal average number of less than 10 particles per cell. The geometrical properties of the HLC structure in arbitrary dimension d is summarized in section 3.6.3.

(iii) Volume Force

The volume force of the central gravitational potential keeps the particles in Keplerian orbits, where the centrifugal force balances the attractive volume force. The central potential is assumed to be fixed in the geometrical center of the simulation volume and acts on each particle. The volume force is only dependent on the distance vector, $\boldsymbol{r}_{ic}$, between the particle i and the central potential, and

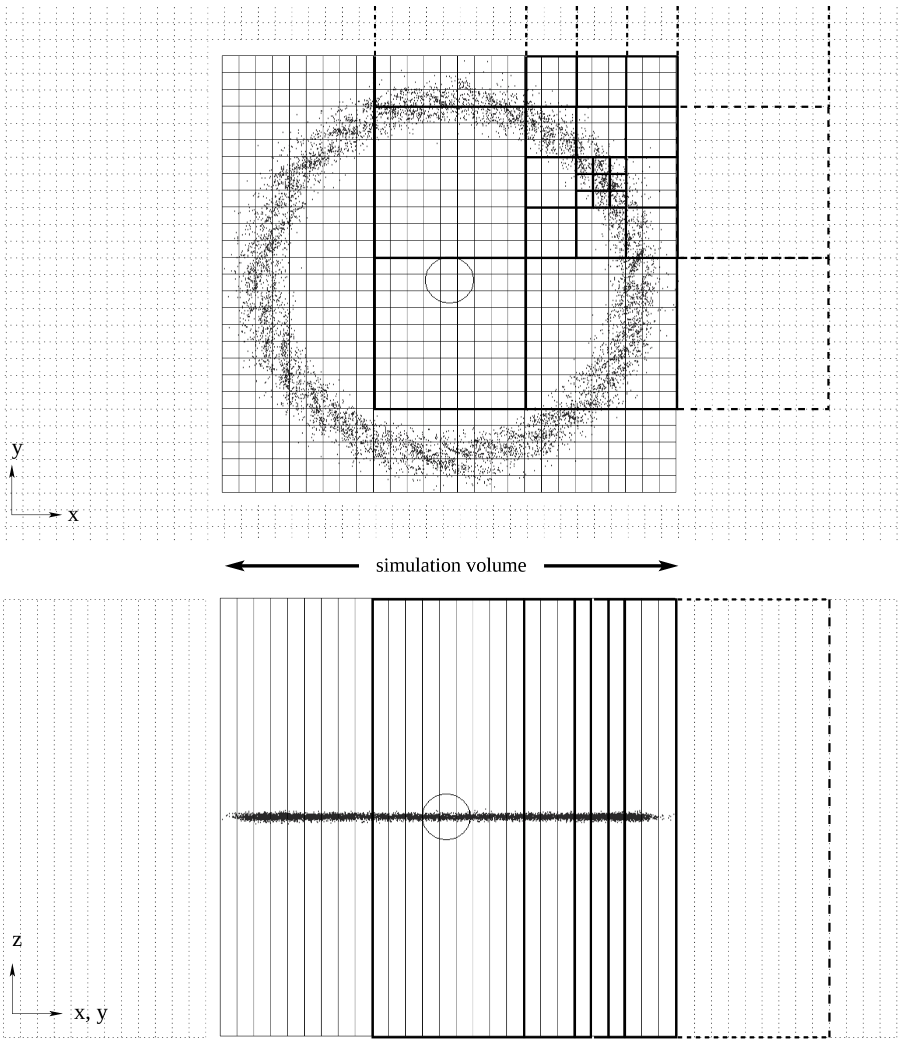

Figure 5.2: The HLC algorithm for ring-shaped particle systems with $H_{\mathrm{max}} = 3$. Thin solid lines show the linked cell structure of the simulation volume, thick solid lines show the HLC structure. Dashed lines show the HLC structure outside the simulation volume in case of non-periodical boundaries. (Top) The HLC structure in plane view. (Bottom) The HLC structure in side view.

reads

$$\boldsymbol{F}_i(t) = -GM_c m_i \frac{\boldsymbol{n}_{ic}(t)}{r_{ic}^2(t)} \quad .$$

The volume force depends on the mass of the central potential, M_c, and on the mass of the particle i, m_i. The unit vector, $\boldsymbol{n}_{ic}(t) = (\boldsymbol{r}_i(t) - \boldsymbol{r}_c)/|\boldsymbol{r}_i(t) - \boldsymbol{r}_c|$, points towards i and G is the gravitational constant introduced in section 2.1.1.

5.2.2 Adjusting the Time Step

Long-range interactions can be considered as collisions without mechanical contact. Transferring the idea of the spring model (cf. section 3.1.1) to long-range interactions[2], we can set for the theoretical collision time

$$t_c = \frac{\pi}{\omega_0} = \frac{\pi}{\sqrt{K/m_{\text{red}}}} \quad , \tag{5.7}$$

where K is the spring constant containing the information about the nature of the long-range interaction potential we focus on. $m_{\text{red}} = m_i m_j/(m_i + m_j)$ is the reduced mass for the case that we distinguish between ring particles and the central body. Such as in the case of mechanical contacts, where K is equivalent to the spring constant, k, that can be obtained by the second spatial derivative of the short-ranged spring potential,

$$K = \frac{\mathrm{d}^2}{\mathrm{d}r_{ij}^2}\left(\frac{1}{2}k\big(2a - r_{ij}\big)^2\right) = k \quad ,$$

long-range interactions provide a spring constant, that can be computed by the second spatial derivative of the long-ranged gravitational potential. This gives

$$K = \frac{\mathrm{d}^2}{\mathrm{d}r_{ij}^2}\left(-\frac{c_e G m_i m_j}{r_{ij}}\right) = -\frac{2c_e G m_i m_j}{r_{ij}^3} \quad . \tag{5.8}$$

Inserting this K in Eq. (5.7) gives the collision time

$$t_c = \frac{\pi}{\sqrt{-2c_e G(m_i + m_j)/r_{ij}^3}} \overset{!}{=} z\Delta t \quad , \tag{5.9}$$

for the long-range interaction potential. Here, the theoretical collision time increases with distance, r_{ij}, between particle i and particle j. The rule that a mechanical contact should be well resolved for the MD integrator, i.e., the collision time of a head-on collision with spring constant k should take at least $z =$ 50...100 time steps, applies to the case of long-range forces as well. Taking $z = 100$ and m_i, m_j as the particle's or central body's mass, we obtain the required time step from Eq. (5.9) that increases with $r_{ij}^{3/2}$. Note, that for interactions with the central body, we set $c_e = -1$ in Eq. (5.8). Using the closest possible distance, i.e., at physical contact between two particles, we obtain the minimum time step one has to take for the simulation.

Fig. 5.3 shows the time step, Δt, of Eq. (5.9) as a function of the inter-particle

---

[2] We leave out the damping term of the spring model because long-range interactions do not dissipate kinetic energy.

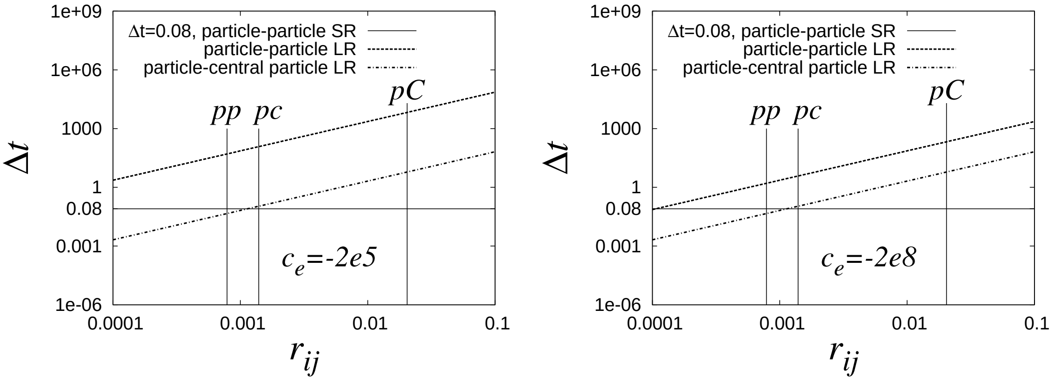

Figure 5.3: The simulation time step, Δt (in CPU-seconds), is plotted double-logarithmically as a function of the inter-particle distance, r_{ij} (in arbitrary units). Vertical lines indicate the closest distances (i.e., at contact) between two ring particles ("pp") and between a ring particle and central particle with small ("pc") and large radius ("pC"). The inclined lines denote the required time step predicted by Eq. (5.9) for interactions between two ring particles (dashed lines) and between a ring particle and the central particle (dash-dotted lines). The horizontal lines denote the time step $\Delta t = 0.08$, that we use in the simulations together with $k = 4.55 \cdot 10^{-17}$. (Left) Using $c_e = -2 \cdot 10^5$. (Right) Using $c_e = -2 \cdot 10^8$.

distance, r_{ij}, in a logarithmic plot for the cases $c_e = -2 \cdot 10^5$ (left) and $c_e = -2 \cdot 10^8$ (right panel). The upper inclined lines give the minimum time step for a long-range interaction between two ring particles and are shifted vertically depending on the choice of c_e (compare the left with the right panel), whereas the lower ones are valid for the long-range interactions between a ring particle and the central body.

For the simulations, we have chosen $\Delta t = 0.08$ (horizontal line), resulting from Eq. (5.9) with a ring particle's mass, $m_i = m_j = 5.899 \cdot 10^{-16}$, and a closest possible approach of $r_{ij} = 2a = 7.86 \cdot 10^{-4}$ (vertical line, indicated by "pp"). For closest encounters of ring particles to the central body, the required minimum time step is $\Delta t = 0.11$ ("pc", contact at $r_{ij} = a + a_c = 1.393 \cdot 10^{-3}$) and $\Delta t = 6.06$ ("pC", contact at $r_{ij} = 2.0393 \cdot 10^{-2}$) for a central particle's radius of $a_c = 0.001$ and $a_c = 0.02$, respectively. This guarantees a proper simulation run as long as the ring particles are farther from the central body than $r_{ij} = r_{ic} = 1.393 \cdot 10^{-3}$.

To verify these considerations, we run simulations with the spring constant, $k = 4.55 \cdot 10^{-17}$, self-gravitation strength, $c_e = -2 \cdot 10^8$, and time step, $\Delta t = 0.08$, but different radius of the central body, $a_c = 0.001$ and 0.02. Hence, we allow for different close encounters between the ring particles and the central mass. In Fig. 5.4 we see the total kinetic energy of the system referenced to the initial value

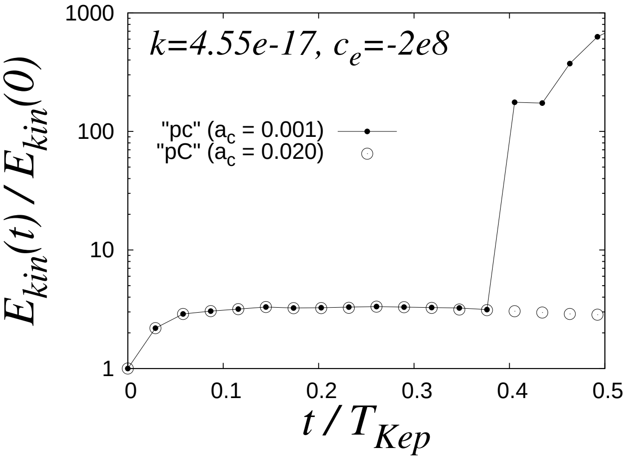

Figure 5.4: The total kinetic energy referenced to the initial energy, $E_{kin}(t)/E_{kin}(0)$, plotted against time in units of the Keplerian period, t/T_{Kep}. The simulation with a central body's radius $a_c = 0.001$ (small solid circles) runs improperly, while the one with $a_c = 0.020$ (open circles) runs properly.

as a function of time in a semi-logarithmic plot. The choice of a large radius of the central body ("pC") provides a proper run of the simulation, whereas a small radius ("pc") shows a rapid gain of kinetic energy (at $t \approx 0.38\ T_{\mathrm{Kep}}$), which indicates an improper run. A too small radius allows for a too close encounter, where the particle will be influenced by strong gravity and its trajectory will be strongly curved. If the time step is chosen too large for this interaction, the MD integrator cannot resolve the trajectory properly and, hence, solves the equations of motion inaccurately. This results in a rapid gain of kinetic energy as shown in the figure. So, the time step has to be adjusted carefully, not only with respect to the stiffness of mechanical contacts, but also with respect to the nature of the implemented long-range potential.

5.2.3 HLC versus PP

Adjusting the time step correctly to the spring stiffness and, according to the previous section, also to the strength of the gravitational potential, we will compare now the results obtained by the Hierarchical Linked Cell method with those of reference simulations. The reference simulations use – such as in chapter 4 – the PP method (cf. section 3.2) and hence are highly accurate but very expensive in computational time.

We set up a vertically thin disk with $N = 4728$ particles at an initial granular temperature, let it evolve in time and extract its actual time-dependent thermal

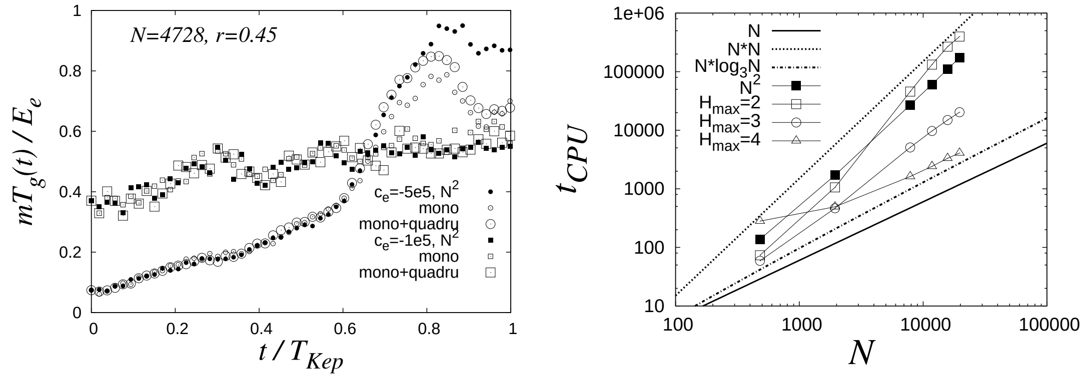

Figure 5.5: (Left) The actual thermal energy in units of the escape energy barrier is plotted against the time in orbital periods. Open symbols corresp-sond to the results of the HLC code, solid symbols to the results of the pair-wise summation method. (Right) The central processor unit time, t_{CPU} (in CPU-seconds), for the MD simulation of ring-shaped particle systems including long-range attraction forces is plotted logarithmically as a function of the particle number, N. Lines correspond to expected values, symbols to simulation results.

energy. If we plot the total thermal energy, $mT_g(t)$, of the disk in units of the escape potential, E_e (see section 2.2), as a function of time we will see an increasing function, see the left panel of Fig. 5.5. The energy shows different offsets (due to the different reference, E_e) and is evolving for two different attraction strengths. In the case $c_e = -1 \cdot 10^5$, the simulation results obtained by the different simulation methods agree very well over the whole time range displayed. For the case $c_e = -5 \cdot 10^5$, however, the results diverge. This seems to be the consequence of applying a larger attraction strength. Comparing this with the findings for attraction forces in homogeneous systems, see section 3.7.2, we expect better agreement for all times if we adjust $mT_g(t = 0)/E_e > 1$.

The additional computation of quadrupole moments for the force contributions at each hierarchy level slightly improves the results (large open circles) as compared to the usage of monopole terms only (small open circles). Nevertheless, we obtain better agreement between the results of the HLC and the direct summation code, the lower the attraction forces are chosen, and if we consider quadrupole terms in addition to the monopole force computation.

5.2.4 Computational Time

As mentioned in section 3.6.7, a linked cell should contain no more than 10 particles, otherwise the linked cell neighborhood search and hence the hierarchical linked cell algorithm will become computationally very expensive. In the right panel of Fig. 5.5 we plot the computing time of the CPU, t_{CPU}, as a function of the number of particles, N, of the ring-shaped particle system in a double-logarithmic plot. For low hierarchies, $H_{\max} = 2$ and $H_{\max} = 3$, the CPU time increases with N as $\mathcal{O}(N^2)$, because of the increasing number of particles per linked cell. A larger maximum hierarchy level $H_{\max}$ is expected to result in a reduced time effort. Indeed, for $H_{\max} = 4$, we observed an increase of the computational time expense with N as $\mathcal{O}(N\log N)$. However, the same efficiency as we observed for homogeneous systems (see Fig. 3.9) is surprising, because here we deal with completely inhomogeneous systems, where many linked cells remain empty during the simulation, see Fig. 5.2.

For a given small number of particles, e.g., $N \approx 500$, one can clearly see that the computational time jumps to large values for $H_{\max} = 4$ as compared to lower maximum hierarchies. Increasing $H_{\max}$ gives less particles within the inner cut-off sphere to be computed pair-wise but leads to an increased computational time expense for small N. This can be explained by the increased time for administrating and constructing the more complex HLC structure. On the other hand, for large particle numbers, the force computation time becomes more prominent as compared to the administration time. So, higher hierarchies are more efficient for larger particle numbers, so that the HLC algorithm behaves as order $\mathcal{O}(N\log N)$.

5.3 The Deliquescing Particle Ring

Ring-shaped particle systems that encircle central gravitational potentials in a plane are differentially moving. According to the second Keplerian law, parts of the ring closer to the central potential move faster than those that are radially farther away from the center. This results in shear forces between the particles, i.e., inner particles will be decelerated, outer particles will be accelerated. Due to collisions, particle velocity components will become disordered, resulting in random motion set up onto the azimuthal Keplerian overall motion. This unsystematic motion contributes to the granular temperature in the system and results finally in a radially and vertically dispersing ring system. These systems are far from being in thermodynamical equilibrium. They are persistently heating up, resulting in an increasing kinetic energy and temperature.

To understand how those dilute ring-shaped particle systems evolve in time, it is important to quantify the kinematic viscosity[3], ν, which is the only material parameter that we will try to understand better in the following.

---

[3] We will use here the Greek character, ν, for the kinematic viscosity and do not run risk to mistake it with the volume fraction of the preceding chapter. The volume fraction only makes sense as long as we deal with homogeneous particle systems which is not the case here.

5.3.1 The Hydrodynamic Equations in 2D

In this section we will discuss the approximate hydrodynamic momentum balance equations for a viscous annular flow of material encircling a central body in a thin layer. The underlying thin-disk approximation, see Refs. [78,100,119], states that the mean vertical height must be much smaller than the radial extension of the disk. If so, all physical quantities can be integrated over the vertical height which reduces the problem to a 2D problem. We keep in mind, that the mass flow is still imbedded in three dimensions, and so, the volume force is still proportional to R^{-2}.

The approximate momentum balance equation is found if we assume that

- all physical quantities are constant over the height of the disk, so, the z-component of the quantities entering the hydrodynamic equations vanish
- the radial mass flow is negligible as compared to the azimuthal mass flow, i.e., $\langle v_R \rangle \ll \langle v_\phi \rangle$
- there is no resulting mean mass flow in vertical direction, i.e., $\langle v_z \rangle \approx 0$, because we assume the same mass flow in positive as in negative vertical direction
- the system is an axi-symmetric system, i.e., the derivative with respect to the azimuthal component vanishes
- the volume viscosity is negligible as compared to the shear viscosity because we do not assume a significant volume change of the ring
- the pressure gradient is negligible as compared to the viscous terms [100].

These assumptions lead us to a simplified set of hydrodynamic equations in polar coordinates, i.e., the equation of continuity reads

$$\frac{\partial \rho^*}{\partial t} + \frac{1}{R}\frac{\partial(\rho^* R v_R)}{\partial R} = 0 \tag{5.10}$$

and we obtain for the R and ϕ components of the Navier-Stokes equations

$$\begin{aligned} \frac{\partial v_R}{\partial t} &+ v_R \frac{\partial v_R}{\partial R} - \frac{v_\phi^2}{R} = -\frac{G M_c}{R^2} \\ &+ \frac{1}{\rho^*}\frac{2}{R}\left(\frac{\partial}{\partial R}\left[\nu^* \rho^* \left(\frac{2}{3}\frac{\partial(R v_R)}{\partial R} - v_R\right)\right] + \frac{\nu^* \rho^*}{R}\left(\frac{1}{3}\frac{\partial(R v_R)}{\partial R} - v_R\right)\right) \ , \end{aligned} \tag{5.11}$$

$$\frac{\partial v_\phi}{\partial t} + v_R \frac{\partial v_\phi}{\partial R} + \frac{v_R v_\phi}{R} = \frac{1}{\rho^*}\frac{1}{R^2}\frac{\partial}{\partial R}\left[R^3 \nu^* \rho^* \frac{\partial}{\partial R}\left(\frac{v_\phi}{R}\right)\right] \ . \tag{5.12}$$

Eqs. (5.11) and (5.12) can be simplified further. The two dimensional kinematic viscosity, ν^*, is responsible for the radial momentum transport due to interparticle collisions. As a consequence, the radial and vertical spreading of the ring depends on ν^*. Since $\langle v_R \rangle \ll \langle v_\phi \rangle$, in Eq. (5.11) all terms containing ν^* and v_R can be neglected as compared to the contribution of the volume force, $-GM_c/R^2$, and we obtain the azimuthal (Keplerian) velocity $v_\phi = (GM_c/R)^{1/2}$. In contrast, in Eq. (5.12) we still have to consider a non-vanishing kinematic viscosity. Inserting the expression for the Keplerian velocity in Eq. (5.12), we obtain the radial velocity

$$v_R = -\frac{3}{\rho^* R^{\frac{1}{2}}} \frac{\partial}{\partial R} \left(\nu^* R^{\frac{1}{2}} \rho^* \right) \quad . \tag{5.13}$$

In contrast to the azimuthal velocity, v_R vanishes if ν^* is assumed to be zero since there is no radial spreading when there is no friction. Inserting the radial velocity of Eq. (5.13) in the equation of continuity, Eq. (5.10), gives

$$\frac{\partial \rho^*(R,t)}{\partial t} = \frac{3}{R} \frac{\partial}{\partial R} \left[R^{\frac{1}{2}} \frac{\partial}{\partial R} \Big(\nu^*(R,\rho^*) R^{\frac{1}{2}} \rho^*(R,t) \Big) \right] \quad , \tag{5.14}$$

where we have written the dependencies of the variables on R and t explicitly. In the following, we will make the equation dimensionless. As a first step, we switch from ρ^* and R to the dimensionless quantities $\tau(R,t)$, see Eq. (5.5), and $s = R/R_0$, respectively. Here is $s_0 = 1$ at the density maximum. Eq. (5.14) then becomes

$$\frac{\partial \tau(s,t)}{\partial t} = \frac{3}{R_0^2 s} \frac{\partial}{\partial s} \left[s^{\frac{1}{2}} \frac{\partial}{\partial s} \Big(\nu^*(s,\tau) s^{\frac{1}{2}} \tau(s,t) \Big) \right] \quad .$$

Now, let us make $\nu^*(s,\tau)$ and the time, t, dimensionless. For this, we have to discuss the Ansatz for the integrated kinematic viscosity. According to Ref. [42] and Eq. (5.6), we use the Ansatz

$$\nu^*(s,\tau) = k_\nu \frac{3T_g(t)}{\Omega(R_0)} \; s^{\frac{3}{2}} \tau(s,t) \quad ,$$

where $3T_g(t)$ is the time-dependent total velocity dispersion at the center s_0 of the ring, see Eq. (5.2), $k_\nu \approx 0.15$ a constant [36,130], and $\Omega(s) = \Omega(R_0) s^{-3/2}$ the Keplerian orbital frequency in the dimensionless radial coordinate, s. Let us put s and τ in arbitrary powers and obtain a more general form for ν^*. Then, we have

$$\nu^*(s,\tau) = \nu_0 s^\alpha \tau(s,t)^\beta \quad , \tag{5.15}$$

where $\nu_0 = 3k_\nu T_g(t)/\Omega(R_0)$. Inserting this Ansatz in the PDE, we obtain

$$\frac{\partial \tau(s,t)}{\partial t} = \frac{3}{R_0^2 s} \frac{\partial}{\partial s} \left[s^{\frac{1}{2}} \frac{\partial}{\partial s} \Big(\nu_0 s^{\alpha+\frac{1}{2}} \tau(s,t)^{\beta+1} \Big) \right] \quad .$$

Finally, using the time transformation $t = \theta R_0^2/(12\nu_0)$, we will make the PDE entirely dimensionless

$$\frac{\partial \tau(s,\theta)}{\partial \theta} = \frac{1}{4s}\frac{\partial}{\partial s}\left[s^{\frac{1}{2}} \frac{\partial}{\partial s}\left(s^{\alpha+\frac{1}{2}} \tau(s,\theta)^{\beta+1} \right) \right] \quad , \tag{5.16}$$

where θ is termed the *viscous time.* Note, that θ is not linear with t, because of the time-dependence of ν_0.

Furthermore, we can transform Eq. (5.16) into an equation that takes the shape of the diffusion equation. With the substitution

$$u(s,\theta) = s^{\alpha+\frac{1}{2}} \tau^{\beta+1} \tag{5.17}$$

and its derivative with respect to τ,

$$\frac{\partial u}{\partial \tau} = (\beta+1) s^{\alpha+\frac{1}{2}} \tau^{\beta} = (\beta+1) s^{\alpha+\frac{1}{2}} \left(\frac{u}{s^{\alpha+\frac{1}{2}}} \right)^{\frac{\beta}{\beta+1}} \quad ,$$

we can eliminate τ in Eq. (5.16) by setting

$$\frac{\partial u}{\partial \theta} = \frac{\partial u}{\partial \tau}\frac{\partial \tau}{\partial \theta} = \frac{1}{4}(\beta+1) u^{\beta/(\beta+1)} s^{(\alpha-\beta-\frac{1}{2})/(\beta+1)} \frac{\partial}{\partial s}\left[s^{\frac{1}{2}} \frac{\partial u}{\partial s} \right] \quad . \tag{5.18}$$

Now, we eliminate s by setting $s = x^2$ with $\partial s/\partial x = 2x$ and $\partial x/\partial s = 1/(2x)$, and can write

$$\frac{\partial}{\partial s}\left[s^{\frac{1}{2}} \frac{\partial u}{\partial s} \right] = \frac{\partial x}{\partial s}\frac{\partial}{\partial x}\left(x \frac{\partial x}{\partial s}\frac{\partial u}{\partial x} \right) = \frac{1}{4x}\frac{\partial^2 u}{\partial x^2} \quad .$$

Using this result in Eq. (5.18), leads to a Diffusion equation

$$\frac{\partial u}{\partial \theta} = \underbrace{\frac{1}{16}(\beta+1)\frac{u^{\beta/(\beta+1)}}{x^{(3\beta-2\alpha+2)/(\beta+1)}}}_{D(x,u;\alpha,\beta)} \frac{\partial^2 u}{\partial x^2} \tag{5.19}$$

with the variable diffusion constant, $D(x,u;\alpha,\beta)$, that depends on the new radial coordinate, x, and implicitly (via u) on the viscous time, θ. α, β are constant parameters. For $\alpha = 1$ and $\beta = 0$, we obtain the constant diffusion coefficient $D = 1/16 = \text{const.}$, representing the usual equation of diffusion. For $\alpha = 0$ and $\beta = 0$, the solution of Eq. (5.19) is given, for example, in Ref. [100]. A more general solution has been shown in Ref. [78]. In the following, we will discuss Eq. (5.19) for different α and β.

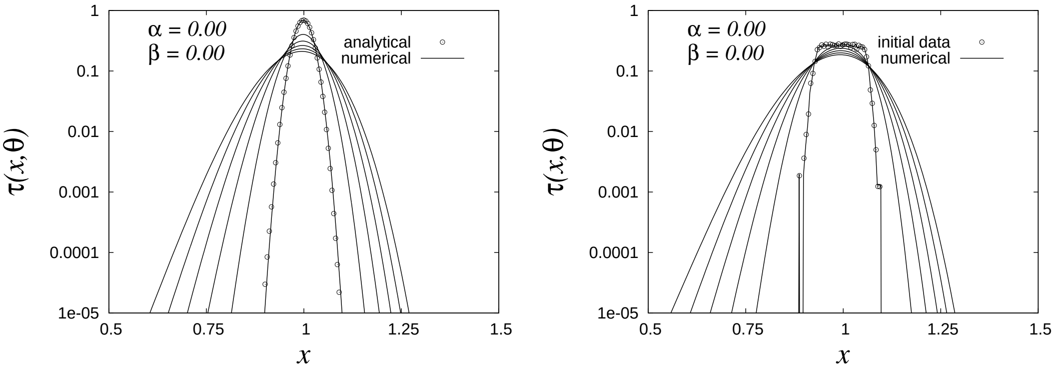

Figure 5.6: The optical depth, τ, as it follows from the numerical solution of Eq. (5.19), plotted as a function of x (lines) for $\alpha = \beta = 0$ in a semi-logarithmical plot for the viscous times $\theta = 0.000$, 0.007, 0.014, 0.021, 0.028 and 0.035. (Left) The initial condition is an analytical Gaussian (symbols). (Right) The initial condition is a typical initial MD data set (symbols).

5.3.2 Density-independent Kinematic Viscosity

In this case, we set $\beta = 0$ and the Ansatz Eq. (5.15) is not dependent on τ, i.e., in the new coordinate x we have

$$\nu^*(x) = \nu_0 x^{2\alpha} \qquad \text{and} \qquad u(x,\theta) = x^{2\alpha+1}\tau(x,\theta) \ \ ,$$

and the diffusion constant in Eq. (5.19) turns into $D = (1/16)x^{2\alpha-2}$. The PDE can then be solved analytically by separating of variables [78,100,119].
Fig. 5.6 shows the resulting optical depth in the new coordinates x, θ as a function of x in a semi-logarithmical plot. In the left panel lines correspond to the numerical solution of Eq. (5.19) for $\alpha = \beta = 0$, symbols to the analytical initial Gaussian function we used. As long as $\beta = 0$, we will always find an analytical solution for τ. The right panel shows the numerical solution for $\alpha = 0$, $\beta = 0$, that evolves from a typical initial data set used as input for our MD simulations.

5.3.3 Radius and Density dependent Kinematic Viscosity

Now, we set $\alpha \neq 0$, $\beta \neq 0$ and hence assume that the viscosity being dependent on both the radial coordinate and the density. First, we set $\alpha = 3/2$ and $\beta = 1$, as proposed in Ref. [42]. This gives

$$\nu^*(x,\tau) = \nu_0 x^3 \tau(x,\theta) \qquad \text{and} \qquad u(x,\theta) = x^4 \tau(x,\theta)^2 \ \ ,$$

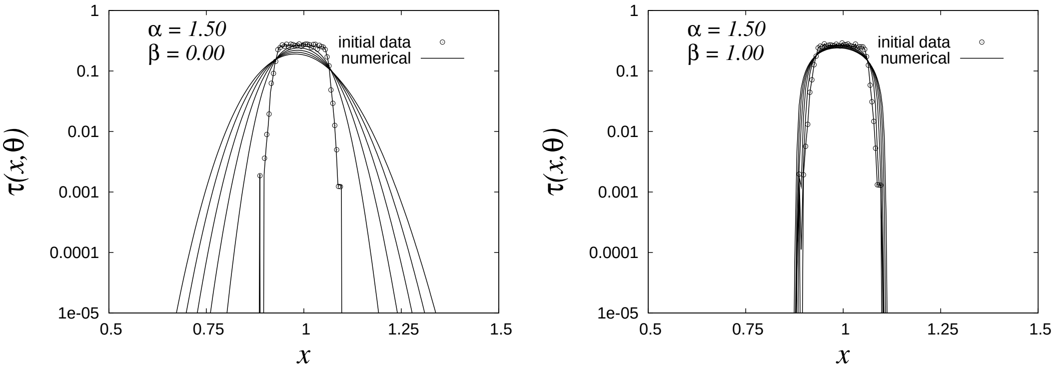

Figure 5.7: The optical depth, τ, plotted as function of x in a semi-logarithmical plot for $\alpha = 1.5, \beta = 0.0$ (left) and $\alpha = 1.5, \beta = 1.0$ (right) and evolves from the same initial MD data set as shown in Fig. 5.6. The curves correspond to the viscous times $\theta = 0.000$, 0.007, 0.014, 0.021, 0.028 and 0.035.

and the diffusion constant in Eq. (5.19) turns into $D = (1/8)u^{1/2}x^{-1}$. We will solve the resulting PDE numerically and obtain results for τ as a function of x, which is shown semi-logarithmically in the right panel of Fig. 5.7. Obviously, the ring is predicted not to deliquesce that strong as it is shown in the left panel for the case $\alpha = 1.5$ and $\beta = 0$.

5.3.4 Moments of the Distribution

A good test for the quality of the numerical solution of Eq. (5.19) is to compute the moments of the radial distribution of the optical depth and see them evolve in time. The total mass of the ring can be obtained by using polar coordinates R, φ:

$$Nm = \int_0^\infty \int_0^{2\pi} \rho^*(R,t)\; R\; \mathrm{d}\varphi\; \mathrm{d}R \overset{(5.5)}{=} \frac{m}{\pi a^2} \int_0^\infty \int_0^{2\pi} \tau(R,t)\; R\; \mathrm{d}\varphi\; \mathrm{d}R \quad . \tag{5.20}$$

Evaluating the integral over the azimuthal angle, φ, the normalized probability distribution function in the radial coordinate, R, reads $f(R,t) = 2R\tau(R,t)/(Na^2)$ and gives the probability to find a particle in the interval $[R, R + \mathrm{d}R]$. The i'th moment of an arbitrary distribution is defined as $\mu^{(i)} = \int_0^\infty R^i f(R,t)\; \mathrm{d}R$. The most general form of the i'th moment in the coordinates R and t reads

$$\mu^{(i)} = \frac{2}{Na^2} \int_0^\infty R^{i+1} \tau(R,t) \quad , \tag{5.21}$$

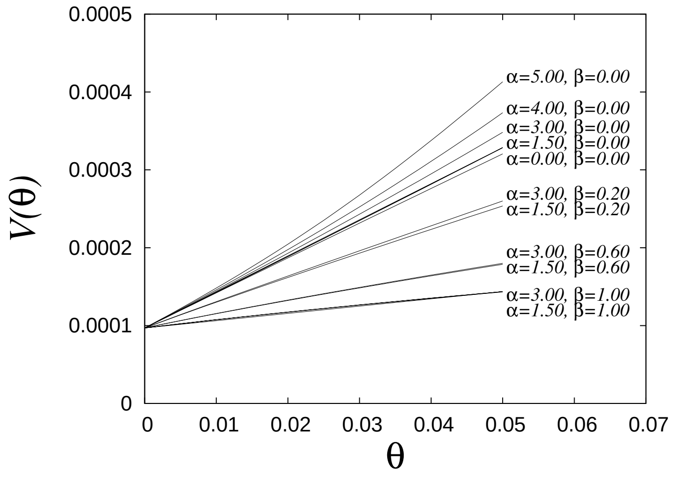

Figure 5.8: The variance, $V(\theta)$, of the radial distribution of $\tau(R)$, see Eq. (5.24), plotted as a function of the viscous time, θ, for different parameters, α and β. Solid lines correspond to the numerical solution.

where R_0 is the radial center of the ring where τ has its maximum. The zeroth ($i = 0$) moment of any distribution gives unity. The first ($i = 1$) moment gives here the radial center of mass, R_0. Expressing the moments in the new coordinates, x and θ, by using the transformations, $R = R_0 x^2$ and $t = \theta R_0^2/(12\nu_0)$, gives

$$\mu^{(i)}(\theta) = \frac{4R_0^{2+i}}{Na^2} \int\limits_0^\infty \tau(x,\theta)\ x^{2i+3}\ \mathrm{d}x \quad . \tag{5.22}$$

Using the substitution $u(x,\theta) = x^{2\alpha+1}\tau^{\beta+1}(x,\theta)$, we obtain the i'th moment

$$\mu^{(i)}_{\alpha,\beta}(\theta) = \frac{4R_0^{2+i}}{Na^2} \int\limits_0^\infty x^{(2i+2i\beta+3\beta-2\alpha+2)/(\beta+1)}\ u(x,\theta)^{1/(\beta+1)}\ \mathrm{d}x \quad , \tag{5.23}$$

depending on the parameters α and β. The time evolution of the variance of the normalized distribution used in Eqs. (5.22) and (5.23), i.e.,

$$V_{\alpha,\beta}(\theta) = \mu^{(2)}_{\alpha,\beta}(\theta) - \left(\mu^{(1)}_{\alpha,\beta}(\theta)\right)^2 \quad , \tag{5.24}$$

is plotted against θ in Fig. 5.8 for different parameter sets α, β. The variance is a measure for the width of the ring with its center at $\mu^{(1)} \approx R_0$, and will be later the reference measure for comparing simulation results with theory. We see that, as long as $\beta = 0$, the variance of the distribution of τ increases significantly with the viscous time for different α. As soon as we choose $\beta \neq 0$, the slope drops to smaller

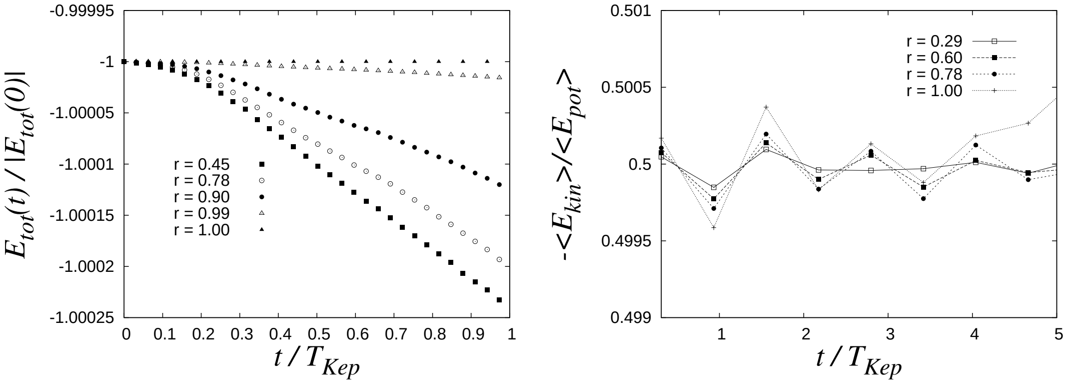

Figure 5.9: (Left) The total energy of differently dissipative rings as a function of orbital periods. (Right) According to the Virial theorem Eq. (5.4), the ratio, $-\langle E_{\rm kin}\rangle_t/\langle E_{\rm pot}\rangle_t$, is plotted over the number of orbital periods.

values and the variance will be entirely determined by β. For increasing β, the slope will become significantly smaller, independent of the choice of α. It seems, that for $\beta \neq 0$, the density-dependence of ν^* (determined by β) characterizes the spreading of the ring stronger than the dependence on R (determined by α).

5.4 Non-gravitating Ring Systems

In this subsection we investigate complete ring systems by means of MD simulations as introduced in section 5.2 with different dissipation strength and without self-gravity.

Total Energy and the Virial Theorem

According to the Kepler laws, the particles' trajectories are ellipsoidal with $0 < \varepsilon_{\rm ecc} < 1$ in Eq. (5.1), leading to a negative total energy of the particle system. The left panel of Fig. 5.9 shows the total energy, referenced to its absolute magnitude, as a function of orbital periods. As expected, the energy is negative and decays to larger negative values for stronger dissipative ring systems. This holds only for particles that are bound in a central (gravitational) field. The Virial theorem is also valid for particles moving on closed paths in a central gravitational field. Then, Eq. (5.4) holds. In the right panel of Fig. 5.9, the ratio, $-\langle E_{\rm kin}\rangle_t/\langle E_{\rm pot}\rangle_t = 0.5$, is plotted against time. The Keplerian period, $T_{\rm Kep}$, is mirrored by the oscillating data, showing a larger amplitude for $r = 1.00$ (strong heating) than for $r = 0.29$ (weak heating). The peaks do not coincide with integer numbers

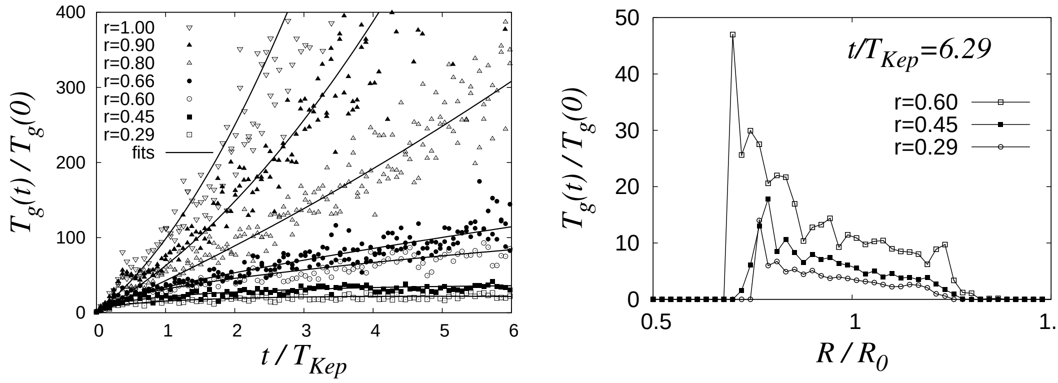

Figure 5.10: The granular temperature in units of the initial value, $T_g(t)/T_g(0)$, is plotted as a function of orbital periods, t/T_{Kep} (left), and as a function of the scaled radial coordinate, R/R_0, for the time $t/T_{\mathrm{Kep}} = 6.3$ (right), for different dissipation r. Solid lines correspond to fit functions, according Eq. (5.26).

of t/T_{Kep} because not all values from the data set are plotted due to the time average. We see that the ratio indeed oscillates around the mean value of 0.5, also for differently dissipative particle systems. However, as discussed in section 5.1, in the presence of dissipative particle collisions, Eq. (5.4) does not hold. Still, the Virial theorem seems to be valid since in dilute systems dissipative particle collisions are so rare that they do not considerably affect the energy content of the system. According to the left panel, only 0.025 % of the total energy has been removed after one orbital period for the case $r = 0.45$. Thus, Eq. (5.4) is approximately valid.

Temperature

Due to Keplerian shear, viscous heating does occur and the ring permanently heats up, counteracting the collisional cooling process, see Ref. [112]. As we can see from the left panel of Fig. 5.10, the granular temperature, referenced to its initial value, taken at the center R_0 of the ring rises stronger in time with decreasing dissipation. The fact that for low dissipation heating can overcome cooling processes results in both a radially and vertically deliquescing particle ring. In contrast, strongly dissipative disks remain narrow and deliquesce less than elastic rings because the vlocity dispersion scales with the vertical height [35]. For a specific dissipation, there will be a (constant) density for which the viscous energy gain balances the collisional energy loss. Too high dissipation would lead the disk evolving to a quasi monolayer, whereas a too low dissipation would lead the disk evolving to a spherical cloud [18]. In the figure, we see that the temperature for strongly dissipative rings ($r = 0.29, 0.45$) increases less strong with time, reaching almost a horizontal line, whereas weakly dissipative rings ($r \geq 0.60$) show a permanently increasing temperature, indicating a spreading ring system. In the right panel of Fig. 5.10, the referenced temperature is plotted as a function of the scaled radial coordinate, R/R_0, for differently dissipative particle systems for a given time $t = 6.2\ T_{\mathrm{Kep}}$. One can clearly see, that the temperature decreases with larger radial coordinate, such as the temperature does at the center, $R/R_0 = 1$, for decreasing r.

Kinematic Viscosity

We will now apply the theoretical results of section 5.3 to a deliquescing particle ring. We solve the partial differential equation, Eq. (5.19), numerically for the optical depth, $\tau(R,t)$, in the radial coordinate and time. For the solution, we consider the kinematic viscosity to be differently dependent on the radial coordinate R and optical depth τ by adjusting the parameters α and β, see Eq. (5.15). As a result, we obtain solutions for τ depending on α and β, see the figures 5.6 and 5.7. We extract the optical depth from differently dissipative simulations and compare it with the numerical results in order to obtain information about the kinematic viscosity in our particle systems.

For comparison we use the time evolution of the variance of τ, as expressed by Eq. (5.24). The variance of the numerical solutions is computed for all viscous times, θ, whereas V obtained from the simulations is calculated for all real times in units of the orbital period, t/T_{Kep}. In order to compare the variances, we have to transform the real time into the viscous time via

$$\theta = \frac{12\nu_0}{R_0^2}\, t = \frac{72\pi k_\nu T_g(t)}{R_0^2 \Omega(R_0)^2} \left(\frac{t}{T_{\mathrm{Kep}}}\right) \quad , \tag{5.25}$$

where we have used $\nu_0 = 3k_\nu T_g(t)/\Omega(R_0)$ and $\Omega(R_0) = 2\pi/T_{\mathrm{Kep}}$. Note, that ν_0 is dependent on time via $T_g(t)$. The real time dependency of θ cancels in Eq. (5.19) since we solve it for θ. Whereas for the time transformation in Eq. (5.25) we need to know the exact dependence, so, we use

$$\frac{T_g(t)}{T_g(0)} = a_0\left(\frac{t}{T_{\mathrm{Kep}}}\right) + a_1\left(\frac{t}{T_{\mathrm{Kep}}}\right)^P \tag{5.26}$$

for fitting the temperature in the left panel of Fig. 5.10 (see the solid lines). Here, we set $P = 2$ for the simulations with $r = 1.00$, 0.90 and 0.80 and $P = 0.5$ for $r = 0.66$, 0.60, 0.45 and 0.29. A best fit provides the dimensionless fit parameters, a_0 and a_1, and we can insert Eq. (5.26) into Eq. (5.25), obtaining finally the time transformation.

In the left panel of Fig. 5.11, the variances obtained by the numerical solutions

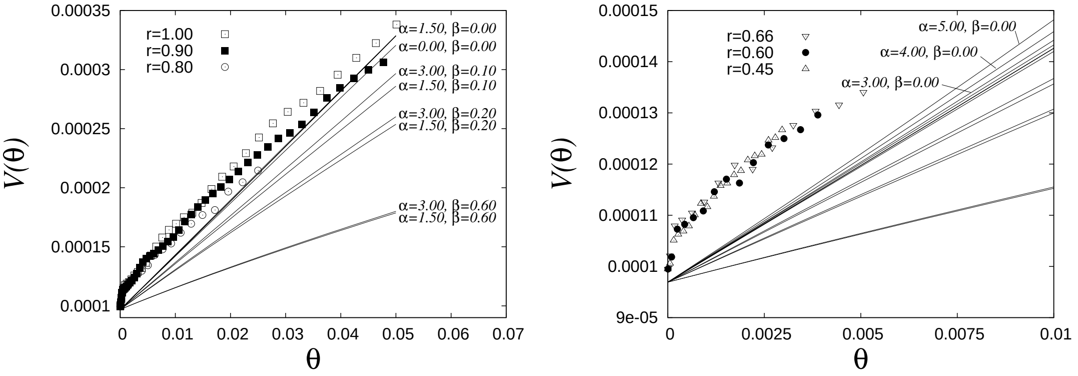

Figure 5.11: (Left) The variance, $V(\theta)$, of the radial distribution of $\tau(x,\theta)$, see Eq. (5.24), plotted as a function of the viscous time, θ, for different parameters, α and β. Solid lines correspond to the numerical solution, symbols to data of different dissipation. (Right) The same as left but with simulation results of stronger dissipation.

are plotted as a function of θ for different models for ν^*, i.e., for different parameter sets α, β given in the panel. In addition, the variances obtained from differently dissipative ($r = 1.00, 0.90, 0.80$) simulations are plotted, after being time-transformed. The data sets increase for short viscous times stronger (for $\theta < 0.002$), and for large viscous times weaker (for $\theta > 0.02$) than theory predicts. For intermediate viscous times the slopes can be regarded as increasing linearly, such as the theoretical results. The same we observe for stronger dissipative simulations ($r = 0.66, 0.60, 0.45$) in the right panel. Due to the case that stronger dissipation leads to a weaker increase of temperature, see the left panel in Fig. 5.10, the viscous time-scale becomes shorter for stronger dissipation as compared to the case of weaker dissipation. In the right panel, we plotted the cases $\alpha = 5.00, 4.00, 3.00$ and $\beta = 0$ in addition to the theoretical results of the left panel. To summarize, for intermediate viscous times, simulation results show a linear increase of the variances such as the theoretical predictions. However, no data set of α, β leads to a correct prediction of the dynamical behavior of the particle ring.

5.5 Gravitating Ring Systems

In this section, we will investigate self-gravitating ring systems by computer simulations using the Hierarchical Linked Cell algorithm introduced in section 5.2. The ring particles will experience their mutual gravitational potential in addition to the central potential.

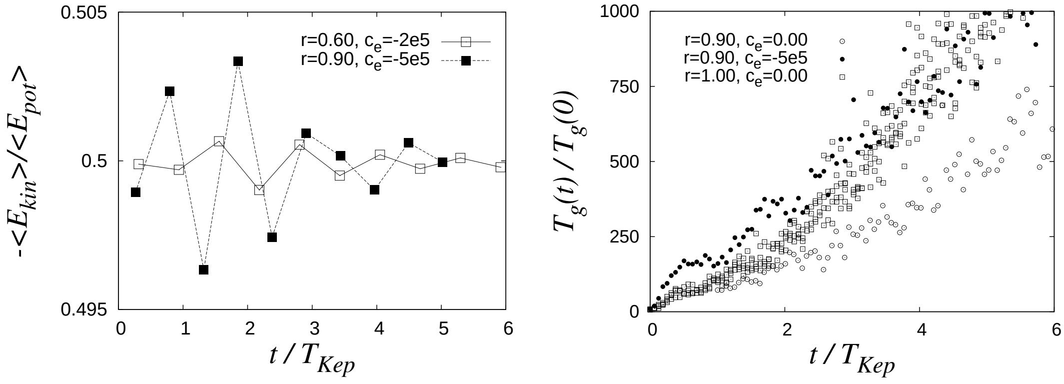

Figure 5.12: (Left) Eq. (5.4) is plotted against the time in Keplerian periods for two differently attractive and dissipative systems. (Right) The granular temperature in units of the initial value, $T_g(t)/T_g(0)$, is plotted as a function of orbital periods, t/T_{Kep}, for a gravitating and non-gravitating system, both with $r = 0.90$. For comparison, the result of a non-dissipative system without attraction forces is added.

Virial Theorem and Temperature

In section 5.1.3 we found that the Virial theorem is approximately valid for our systems, even if we deal with dissipative systems. Now, is it valid for self-gravitating systems as well? Particles in self-gravitating systems influence each other while orbiting around the central body. Both the mutual attraction and the volume force scale with $s = 3$ in Eq. (2.3). We assume, that the Virial theorem is still valid since the condition that the particles must interact with a $1/r$ long-range potential is fulfilled. The left panel of Fig. 5.12 shows the ratio $-\langle E_{\mathrm{kin}}\rangle_t/\langle E_{\mathrm{pot}}\rangle_t$ as a function of time in units of the Keplerian orbital period, T_{Kep}. We see, besides oscillatoric effects that mirror the periodicity of the orbiting ring, that the ratio keeps the value 0.5 predicted by Eq. (5.4) over the whole simulation time. This means that the combination of the volume force with the mutual long-range attraction force obeys the Virial theorem as well.

In the right panel of Fig. 5.12, we plot the temperature taken at the ring center and referenced to its initial value as a function of time in units of T_{Kep}. We see (for $r = 0.90$), that in presence of attraction forces the temperature increases stronger than for the case $E_e = 0$. For comparison, it is also shown the temperature increase of a non-gravitating system but with $r = 1.00$. Anyway, a system with $r = 1.00$ is supposed to heat up stronger than a system with $r = 0.90$. The additional attraction makes the system with lower dissipation heating up with the same rate as the elastic system – at least for the simulation time showed. Particles that influence each other via attraction forces, convert potential energy into kinetic energy if they come closer to each other. In combination with contact

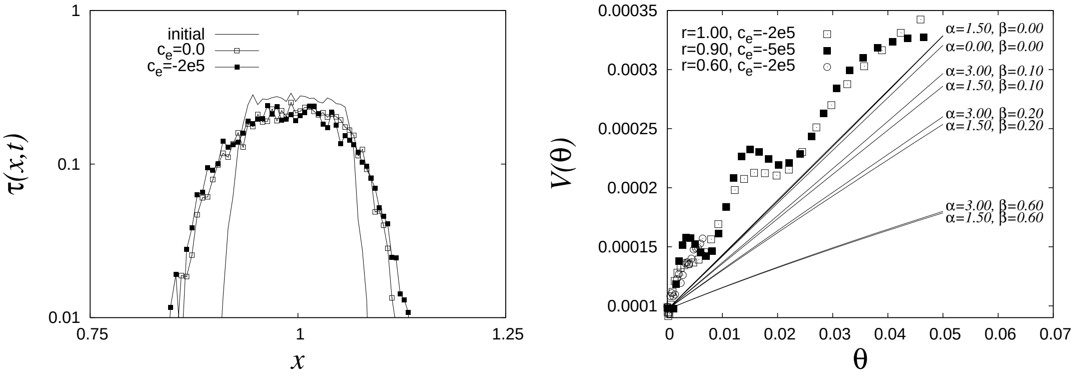

Figure 5.13: The optical depth, τ, is plotted as a function of the scaled radial coordinate, $x = \sqrt{R/R_0}$ for a non-gravitating (open squares) and a gravitating ring (solid squares), both with dissipation $r = 0.60$ at $t = 2.9\ T_{\mathrm{Kep}}$. The line without symbols corresponds to the initial MD configuration.

collisions, this gives rise for an increase of the disordered motion of the particles, resulting in an increase of the granular temperature.

Kinematic Viscosity

Due to the fact that gravitating ring systems heat up stronger than non gravitating rings, Fig. 5.12 (left) for $r = 0.90$, they consequentially deliquesce faster in time. This can be seen in the left panel of Fig. 5.13, where we show the radial profile of the optical depth over the radial coordinate, x, which we introduced in section 5.3.1. The profile develops from an initial configuration with initial optical depth of about $\tau_0 = 0.3$ (line without symbols), to a deliquesced profile after almost three Keplerian orbital periods, where it becomes broader. If we consider only dissipation, here $r = 0.90$, the profile (open squares) shows a smaller width than the profile of a gravitating ring (solid squares) with $r = 0.90$ and $c_e = -2 \cdot 10^5$ at $t = 2.9\ T_{\mathrm{Kep}}$. Generally, for a given time, gravitating rings show larger variances of the distribution of τ than non-gravitating rings. In the right panel of Fig. 5.13, the variances from different dissipative self-gravitating rings are shown. Strong self-gravity in combination with low dissipation results in an oscillating variance, which does not fit to any parameter set α, β. So, we cannot make a proper ansatz of the kinematic viscosity, expressed by Eq. (5.15).

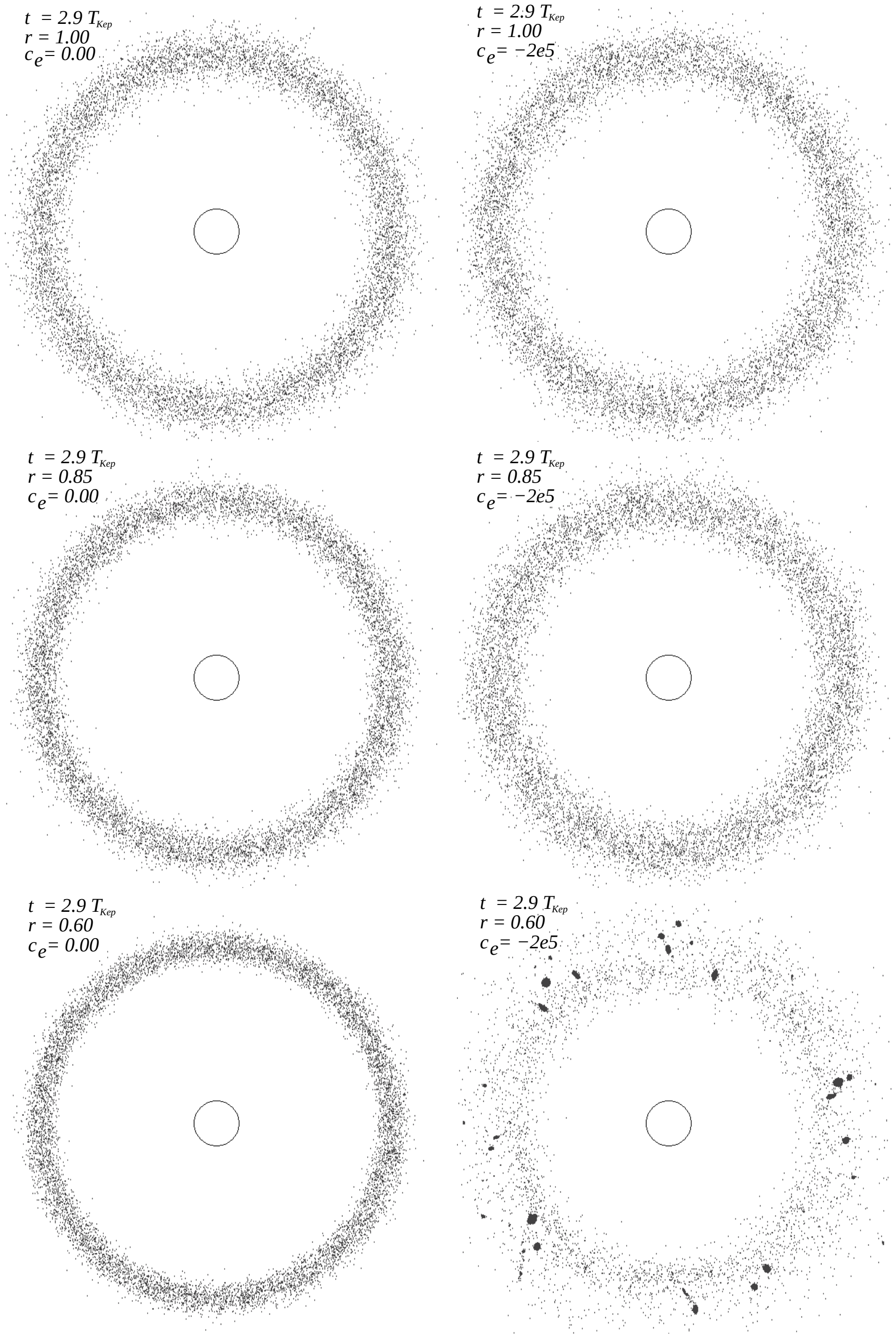

Figure 5.14: Simulation results at $t = 2.9\ T_{\mathrm{Kep}}$: for $r = 1.00$, 0.85 and 0.60. (Left) Systems without attractive long-range forces. (Right) Systems with attractive long range forces, $c_e = -2 \cdot 10^5$.

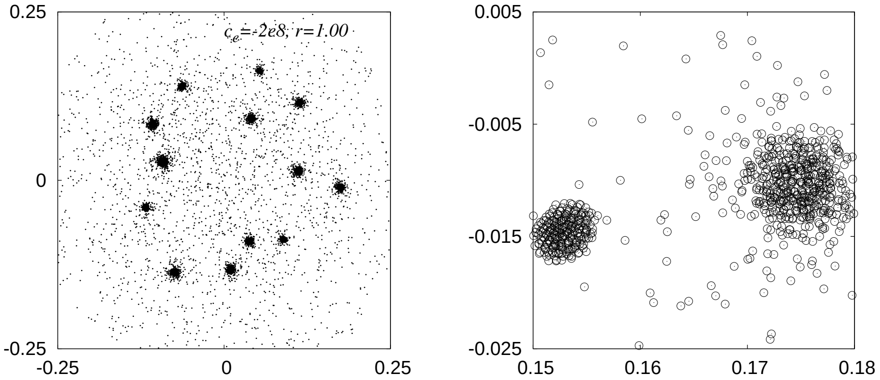

Figure 5.15: (Left) An elastic simulation with strong attraction forces. (Right) Two clusters of two different simulations ($r = 0.60, c_e = -2 \cdot 10^5$ and $r = 1.00, c_e = -2 \cdot 10^8$) shown in the same plot. The cluster on the left has formed under inelastic conditions, whereas the cluster on the right has formed under elastic conditions. The particle size displayed is in scale to the cluster size.

Clustering

Dissipation and attraction strength enhance clustering in particle rings whereas the permanent shear rate is counteracting the formation of lumps and “moonlets”. Fig. 5.14 shows typical ring-shaped particle systems without self-gravity (left) and with self-gravity (right) at $t = 2.9\ T_{\text{Kep}}$. The dissipation strength increases from top to the bottom panels. For dissipation $r = 0.85$ there is still no clustering shown whereas for $r = 0.60$ cluster formation has already sets in. This confirms our assumption that dissipation enhances the clustering process.

On the other hand, elastic systems ($r = 1.00$) under permanent shear can also show clustering if attraction is tuned sufficiently strong. The left panel of Fig. 5.15 shows a ring system where the attraction force has been chosen such high that clustering set in. However, the nature of the clusters is different for the elastic case as compared to the inelastic case. Since in the latter case particles tend to stay together after a collision due to the removal of kinetic energy, in the elastic case, particles bounce against each other, not losing kinetic energy. This different behavior results in a different surface structure of the clusters. While in the inelastic case, clusters exhibit a well-defined surface, in the elastic case, the cluster's surface is not well-defined due to the non-decreasing relative velocities of the particles.

The right panel shows two particle clusters obtained from two different simulations. In the panel, the cluster on the left has formed under gravity and dissipative conditions ($c_e = -2 \cdot 10^5, r = 0.60$), whereas the cluster on the right has formed under (strong) gravity and elastic conditions ($c_e = -2 \cdot 10^8, r = 1.00$). One can clearly see the "rough" surface of the elastic cluster.

5.6 Summary

In this chapter we investigated complete ring-shaped elastic and dissipative particle systems with and without self-gravity. We focused on the time evolution, where the particle systems deliquesce due to permanent viscous shear determined by the two dimensional kinematic viscosity. We developed a partial differential equation for the optical depth, assuming different ansatzes for the kinematic viscosity. We compared the variance of the solutions for the optical depth with those of the simulations. We found that both theory and simulations show an increasing variance with time and, moreover, theory predicts the behavior of the rings better for intermediate viscous times than for short and long times. However, we were not able to find parameter sets for α and β, leading to different models for the kinematic viscosity, that describe the dynamical behavior of the rings properly for all times: theory predicts a linear increase of the variance, whereas simulations show a non-linear increase, even an oscillatoric increase of the variance in the case of gravitating rings.
Moreover, we showed that for a given attraction strength, dissipation must be strong enough in order to obtain clustering processes that can compete with the present shear rate. On the other hand, we showed that even for completely elastic particle systems, the attraction strength must be adjusted sufficiently high in order to support clustering.

6 Summary

In this thesis, on purpose, we focussed on the most challenging, longest ranging potentials. We analyzed granular media of low densities obeying $1/r$ long-range interaction potentials between the granules. Such systems are termed granular gases and differ in their behavior from ordinary gases by dissipative interactions, i.e., they do not conserve energy. Due to the dissipation, a unique wealth of structures can occur, enhanced or hampered by long-range interactions.

Numerics

For the analysis of such systems, we developed a soft sphere Molecular Dynamics (MD) method in three dimensions, taking properly into account the interplay between dissipative contacts and long-range interaction forces. Due to the infinite range of the $1/r$ potential, we would have to consider the interaction of all particles with all others, resulting in a computational time effort that scales like $\mathcal{O}(N^2)$, where N is the particle number. We were able to bypass the pair-wise treatment by exploiting the linked cell structure we use for the neighborhood search such that particles in cells are considered as pseudo particles and grouped together in a hierarchical way. This hierarchical set-up based on linked cells is new to our knowledge. The combination with a multipole expansion of the mass distribution inside the pseudo particles gives a reduced number of interaction partners. The implementation of this Hierarchical Linked Cell (HLC) algorithm including periodic or wall boundary conditions shows a scaling behavior as $\mathcal{O}(N \log N)$, as confirmed by various simulations. We found that the results of the HLC algorithm agree with those of the direct summation code as long as the temperature is higher or about the same as the repulsion/attraction energy barrier.

Dilute Homogeneous Granular Systems

The second part of the thesis was devoted to the investigation of the cooling behavior of dissipative granular gases in presence of mutual long-range repulsive and attractive forces. In order to obtain reference results, we exclusively treated the particles pair-wise, limiting us to small particle numbers in the simulations. In order to understand the cooling behavior, we applied the *pseudo Liouville* operator theory. Although dealing with soft spheres under the influence of mutual long-range forces, we observed good agreement between theory and simulations in the limit of low densities and weak dissipation. In the case of repulsive long-range forces, the dissipation rate is reduced, taking into account the repulsive energy barrier the relative velocity of two approaching particles must exceed in order to collide. In the case of attractive forces, the dissipation rate is increased due to an escape energy barrier the relative velocity of two separating particles must overcome in order to not experience a collision. Both qualitative effects vanish if we consider the case of vanishing long-range force intensity or density. Our repulsive theory confirms earlier heuristic results [111], while the attractive theory is new to our knowledge.

Even though, the theory works in the dilute limit, for finite densities, the dissipation rate observed from simulations changes with increasing density and allows us to empirically provide a predictive analytical correction factor dependent on the density. We performed various elastic simulations with different repulsive and attractive strengths for densities in the range $0.010 \leq \nu \leq 0.152$. The correction is non-linear dependent on density in the repulsive case and linear dependent in the attractive case, at least for the stable homogeneous cooling state examined. We used the empirical findings for the solution of the equations for the energy evolution with time and obtained an improved prediction, in good quantitative agreement with simulations. Small deviations remain and are supposed to be a consequence of dissipation because they increase with dissipation strength. In the attractive case, the improvement was less successful. Surprisingly, for moderate densities and dissipation strengths, the attractive systems show the same dissipation rate as systems without attraction forces.

Dilute Ring-Shaped Granular Systems

The third part of the thesis contains the investigation of self-gravitating ring-shaped particle systems. We applied the HLC code and tested it for such strongly inhomogeneous systems. It works well and, such as for homogeneous systems, the computational time expense scales as $\mathcal{O}(N\log N)$. We found that for sufficiently strong attraction forces, elastic systems show clustering even though a permanent shear rate and shear heating are present. Strong dissipation also leads to inhomogeneous rings, formation of clusters, and “planetesimals”.

Moreover, we developed and numerically solved an approximate Navier-Stokes hydrodynamic set of equations for the projected density with different Ansatzes for the kinematic viscosity and compared the solutions with our simulation results. The agreement is good only for intermediate times, whereas for short times, besides initial equilibration effects, the rings spread faster and for later times the rings spread slower than predicted by theory.

Samenvatting

In dit proefschrift wordt het gedrag geanalyseerd van lage concentraties granulaire materialen met $1/r$ grote-reikwijdte interactie potentialen tussen de deeltjes. Zulke systemen worden granulaire gassen genoemd. Ze verschillen in hun gedrag van gewone gassen door de dissipatieve interacties, die dus niet voldoen aan behoud van energie. Door de dissipatie ontstaat een breed scala van structuren, versterkt of verzwakt door de interacties met grote reikwijdte.

Numerieke Aspecten

Voor de analyse van zulke systemen is een driedimensionale "soft sphere" Moleculaire Dynamica (MD) methode ontwikkeld, die op de correcte wijze dissipatieve contacten en interactiekrachten met grote reikwijdte combineert. I.v.m. de oneindige reikwijdte van de $1/r$ potentiaal, zouden we de interactie van alle deeltjes met alle andere deeltjes moeten beschouwen, wat resulteert in een rekentijd die schaalt als $\mathcal{O}(N^2)$, waarbij N het aantal deeltjes is. We waren in staat de paarsgewijze behandeling te vermijden door gebruik te maken van de "linked cell" structuur, die gebruikt wordt voor het zoeken van naburige deeltjes, op een dusdanige manier dat deeltjes in een cel beschouwd worden als pseudo-deeltjes die gegroepeerd worden in een hiërarchische wijze. Deze hiërarchische opzet, gebaseerd op de "linked cells", is nieuw voor zover ons bekend. De combinatie een multipool expansie van de massaverdeling binnen de pseudo-deeltjes geeft een reductie van het aantal partners dat een interactie vertoont. De implementatie van dit "Hierarchische Linked Cell" (HLC) algoritme, inclusief periodieke en vaste-wand randvoorwaarden, is succesvol verricht. Het schalingsgedrag, als $\mathcal{O}(N \log N)$, is bevestigd door vele simulaties. De resultaten van het HLC-algoritme komen good overeen met die van een directe-som algoritme als de temperatuur hoger of van dezelfde ordegrootte is als de afstotings-/attractie-energiebarrière.

Lage-Concentratie, Homogene Granulaire Systemen

Het tweede deel van dit proefschrift betreft het onderzoek naar het afkoelingsgedrag van dissipatieve granulaire gassen in de aanwezigheid van elkaar onderling aantrekkende of afstotende krachten met grote reikwijdte. Om de meest nauwkeurige resultaten te verkrijgen, worden alle deeltjes paarsgewijs beschouwd, wat ons beperkt tot kleine aantallen deeltjes in de simulaties. Om het afkoelingsgedrag te begrijpen is de *pseudo Liouville* operator theorie gebruikt. Hoewel zachte deeltjes met interactie met grote reikwijdte beschouwd worden, is er een goede overeenkomst tussen theorie en simulaties in de limietgevallen van lage concentraties en zwakke dissipatie. In het geval van afstotende krachten met grote reikwijdte, is de dissipatiesnelheid verlaagd, gelet op het feit dat de relatieve snelheid van twee deeltjes een afstotende energiebarrière moet overschrijden, opdat deze deeltjes botsen. In het geval van aantrekkende krachten is de dissipatiesnelheid hoger, gezien de ontsnappingsenergie-barrière waaronder de relatieve snelheid moet liggen voordat de deeltjes botsen. Beide effecten verdwijnen als de sterkte van de interactie met grote reikwijdte verdwijnt of als de deeltjesconcentratie naar nul gaat. De correctiefactor bij afstotende krachten is al eerder, op een heuristische wijze beschreven [111]. De resultaten bij aantrekkende krachten zijn nieuw, voor zover ons bekend.

Voor eindige concentraties neemt de dissipatiesnelheid af (in vergelijking met het geval zonder krachten met grote reikwijdte) bij afstotende krachten, terwijl deze toeneemt in het geval van aantrekkende krachten. Daarom is onderzocht hoe de dissipatiesnelheid varieert met toenemende concentratie. Er is een empirische, analytische correctiefactor geformuleerd, die afhangt van de concentratie. Vele elastische simulaties zijn uitgevoerd met verschillende sterktes van de afstotende en aantrekkende interacties voor concentraties $0.010 \leq \nu \leq 0.152$. De correctiefactor hangt op een niet-lineaire wijze af van de concentratie bij afstotende krachten en op een lineaire wijze bij aantrekkende krachten. De empirische bevindingen zijn gebruikt bij de oplossing van de vergelijkingen voor de dissipatiesnelheid, wat een verbeterde voorspelling oplevert. Kleine afwijkingen bleven bestaan, welke mogelijk een gevolg zijn van dissipatie. In het geval van aantrekkende krachten was de verbetering niet succesvol, maar verrassenderwijze bleek dat voor niet te lage concentraties en dissipatie, de aantrekkende systemen dezelfde dissipatiesnelheid hebben als systemen zonder aantrekkende krachten.

Lage-Concentratie, Ringvormige Granulaire Systemen

Het derde deel van het proefschrift betreft onderzoek naar zelf-graviterende ringvormige deeltjessystemen. De HLC-code is getest en toegepast op de sterk heterogene systemen. De code werkt goed en de rekentijd schaalt als $\mathcal{O}(N\log N)$, net als voor homogene systemen. Voor voldoende grote aantrekkende krachten blijken elastische systemen ook te kunnen clusteren, ondanks de aanwezigheid van permanente afschuivingsnelheid en -opwarming. Sterke dissipatie leidt tot heterogene ringen, de vorming van clusters en “planetesimals”.

Bovendien zijn er benaderende Navier-Stokes, hydrodynamische vergelijkingen voor de concentraties opgesteld en numeriek opgelost, met verschillende aannames voor de kinematische viscositeit. De oplossingen zijn vergeleken met de resultaten van de simulaties. De overeenkomst is alleen goed voor middelmatige tijden. Voor kortere tijden spreiden de ringen sneller (afgezien van initiële evenwichtseffecten); voor langere tijden spreiden de ringen langzamer dan voorspeld door de theorie.

7 Concluding Remarks and Outlook

Dilute Homogeneous Granular Systems

- We found that attractive dissipative systems show clustering for a given attraction strength when dissipation is strong enough and/or density is sufficiently high. In astrophysics, the question is important, under which circumstances a homogeneous cloud of particles will be instable against its own gravity and collapses in order to form "planetesimals". More precisely, what is the minimum mass (which is connected to the self-attraction strength) of the cloud in order to collapse. It is worth to estimate the minimum mass of the particle systems we investigated as a function of dissipation and attraction strength.

- Dissipative homogeneous granular gases show cluster growth for a given dissipation strength, if the system's size and/or the density are large enough. Vice versa, for a given system size and density, there is a critical dissipation strength, which discriminates between the homogeneous cooling state and the instable regime. The presence of long range repulsive and attractive forces will hamper and enhance cluster formation, respectively. That is, in particular, the critical dissipation strength will be decreased due to repulsion and increased due to attraction forces. By using the correction factors for the energy dissipation rate we empirically found, a hydrodynamic

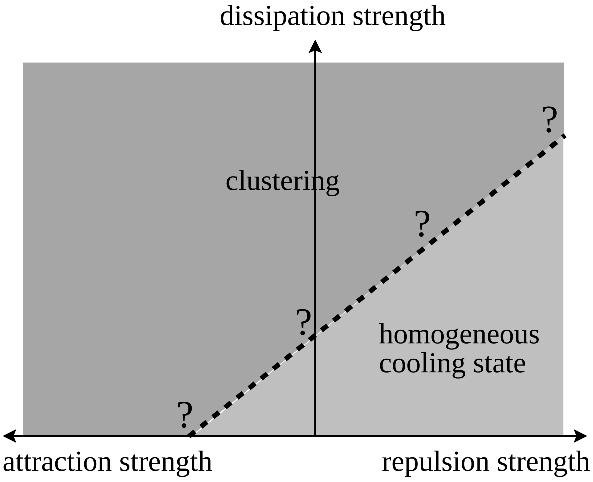

stability analysis of the homogeneous cooling state will give the critical dissipation as a function of the strength of the long-range force. This leads to a “phase diagram” in the parameter space of dissipation and force strength. Note, that there also exists a regime with attraction and dissipation that remains homogeneous. Furthermore, we can prove the shape of the function with simulations by systematically varying the parameters dissipation and force strength.

Ring-Shaped Granular Systems

- We were simulating complete ring shaped particle systems evolving in time. Besides the fact that both dissipation and self-gravitation strongly influence the dynamical behavior of the ring systems, we observed initial oscillatoric equilibration effects as well. So, it is recommendable, from the technical point of view, to spend effort on finding initially equilibriated ring systems for the MD procedure, in order to obtain results that are free from such effects. In order to achieve this, one has to take into account that the center of mass must be exactly located at the center of the central body.

- For low dissipation, the particle systems spread in both radial and vertical direction. Thus, the optical depth is changing radially and with time, as does the granular temperature. In contrast, in the approximate two-dimensional Navier-Stokes hydrodynamic set of equations used, a granular temperature is assumed that is constant in radial direction and changes with time. As a representative temperature, we used the granular temperature measured at the ring center, i.e., for a constant radius. For further investigation, it will be useful to determine the exact radial dependence of the temperature that enters the equations for the kinematic viscosity. For example, the temperature can be empirically determined as a function of the radial coordinate by simulations.

- In presence of mutual attraction forces between the ring particles, we found that the time evolution of the temperature differs stronger from the one we obtained by non-gravitating systems the lower the dissipation has been chosen. This results in a different dynamical behavior of the ring which we did not account for when solving the hydrodynamic equations. So, it is recommendable to extend the hydrodynamic equations by a self-gravity term.

A Some Kinetic Theory

Although we treat particles in our MD simulations as dissipative soft spheres with a smooth interacting potential, we will apply in this appended chapter the concept of the *pseudo-Liouville* operator to describe both repulsive and attractive mutual long-range potentials between mono-disperse particles with radius a theoretically. The pseudo-Liouville operator was derived for elastic, discontinuous hard core potentials. In order to apply it for inelastic hard sphere potentials [28] it was extended by both normal [126] and tangential restitution [56, 76].

A.1 The Liouville Operator

From *Hamiltonian* mechanics we know that the Hamilton function $\mathcal{H}$ ("Hamiltonian") determines the time evolution of a mechanical observable, $A(\{\boldsymbol{q}(t), \boldsymbol{p}(t)\})$, via the so-called *Poisson* bracket, $\{A, \mathcal{H}\}$, i.e.,

$$\frac{\mathrm{d}A}{\mathrm{d}t} = \sum_{j=1}^{N} \Big(\frac{\partial A}{\partial \boldsymbol{q}_j} \frac{\mathrm{d}\boldsymbol{q}_j}{\mathrm{d}t} + \frac{\partial A}{\partial \boldsymbol{p}_j} \frac{\mathrm{d}\boldsymbol{p}_j}{\mathrm{d}t} \Big) = \sum_{j=1}^{N} \Big(\frac{\partial \mathcal{H}}{\partial \boldsymbol{p}_j} \frac{\partial A}{\partial \boldsymbol{q}_j} - \frac{\partial \mathcal{H}}{\partial \boldsymbol{q}_j} \frac{\partial A}{\partial \boldsymbol{p}_j} \Big) =: \{A, \mathcal{H}\} \ . \quad (A.1)$$

The sets $\{\boldsymbol{q}_j\}$ and $\{\boldsymbol{p}_j\}$ are called *generalized variables* and are completely independent from each other. It is $\mathrm{d}\boldsymbol{q}_j/\mathrm{d}t = \partial\mathcal{H}/\partial\boldsymbol{p}_j$ and $\mathrm{d}\boldsymbol{p}_j/\mathrm{d}t = -\partial\mathcal{H}/\boldsymbol{q}_j$, which are referred to as the *Hamiltonian equations* of motion. The Hamiltonian corresponds to the total energy of the system (in case of constraints that are not explicitly dependent on time we have energy conservation, i.e., $\mathrm{d}\mathcal{H}/\mathrm{d}t = 0$),

$$\mathcal{H} = \sum_{j=1}^{N} \frac{\boldsymbol{p}_j^2}{2m_j} + \sum_{j=1}^{N-1} \sum_{k=j+1}^{N} \varphi(|\boldsymbol{q}_{jk}|) \ ,$$

where the first term corresponds to the kinetic energy and the second term to the potential energy for pair-interactions. For time dependent constraints such as (tangential or normal) dissipative collisions, $\mathcal{H}$ is not a conserved quantity anymore so that Eq. (A.1) becomes invalid. The *Liouville* operator $\mathcal{L}$ is then defined by the relation

$$\begin{aligned} i\mathcal{L}A := \{A, \mathcal{H}\} &= \sum_{j=1}^{N} \frac{\boldsymbol{p}_j}{m_j} \frac{\partial}{\partial \boldsymbol{q}_j} A - \sum_{j=1}^{N-1} \sum_{k=j+1}^{N} \frac{\partial \varphi}{\partial \boldsymbol{q}_{jk}} \Big(\frac{\partial}{\partial \boldsymbol{p}_j} - \frac{\partial}{\partial \boldsymbol{p}_k} \Big) A \\ &= i\mathcal{L}^{\text{free}} A + i\mathcal{L}^{\text{coll}} A \ , \qquad (A.2) \end{aligned}$$

where $i = \sqrt{-1}$ is the imaginary unit, and we can split it up into a free-streaming $\mathcal{L}^{\text{free}}$ (corresponding to the translation of freely moving particles) and a collisional component $\mathcal{L}^{\text{coll}}$ (corresponding to interacting particle pairs). The latter is defined for continuously differentiable (smooth) potentials. With Eqs. (A.1) and (A.2), the time evolution of the mechanical observable is then the solution of the differential equation $(\mathrm{d}/\mathrm{d}t)A(\{\boldsymbol{q}(t), \boldsymbol{p}(t)\}) = i\mathcal{L}A(\{\boldsymbol{q}(t), \boldsymbol{p}(t)\})$, i.e.,

$$A(\{\boldsymbol{q}(t), \boldsymbol{p}(t)\}) = \exp(i\mathcal{L}t)A(0) \quad . \tag{A.3}$$

In the next section, we will focus on how $\mathcal{L} = \mathcal{L}(\{\boldsymbol{q}(t), \boldsymbol{p}(t)\})$ looks like in order to get an expression for A. Specific examples for A and an exact derivation for $(\mathrm{d}/\mathrm{d}t)A$ will be shown later.

A.2 The pseudo-Liouville Operator

For a granular system with spheres interacting via hard sphere potentials, see Eq. (4.6), we cannot apply derivatives as occurring in Eq. (A.2) because they are not defined for a discontinuous hard sphere potential. On the other hand, due to dissipation, the Hamiltonian is not a conserved quantity anymore and we have to rewrite the interaction term, $\mathcal{L}^{\text{coll}}$, in Eq. (A.2), according to [13, 28, 76] and references therein:

$$\mathcal{L}^{\text{coll}} = \sum_{j=1}^{N-1} \sum_{k=j+1}^{N} |\boldsymbol{v}_{jk} \cdot \hat{\boldsymbol{r}}_{jk}| \Theta(-\boldsymbol{v}_{jk} \cdot \hat{\boldsymbol{r}}_{jk}) \delta(|\boldsymbol{r}_{jk}| - 2a) \Big(b_{jk}^{+} - 1 \Big) \quad , \tag{A.4}$$

which takes the discontinuous hard core potential properly into account. This new operator, together with the unchanged part, $\mathcal{L}^{\text{free}}$, preserves the formal structure of Eq. (A.2),

$$i\mathcal{L}A := \sum_{j=1}^{N} \boldsymbol{v}_j \frac{\partial}{\partial \boldsymbol{r}_j} A + \sum_{j=1}^{N-1} \sum_{k=j+1}^{N} |\boldsymbol{v}_{jk} \cdot \hat{\boldsymbol{r}}_{jk}| \Theta(-\boldsymbol{v}_{jk} \cdot \hat{\boldsymbol{r}}_{jk}) \delta(|\boldsymbol{r}_{jk}| - 2a) \Big(b_{jk}^{+} - 1 \Big) A \quad , \tag{A.5}$$

and $\mathcal{L}$ can therefore be referred to as a *pseudo*-Liouville operator. Here, we used the particles' positions and velocities as generalized variables. $\mathcal{L}^{\text{coll}}$ selects only those particle pairs that will collide:

- $|\boldsymbol{v}_{jk} \cdot \hat{\boldsymbol{r}}_{jk}|$ is the normal component of relative velocity and increases the number of collisions per time unit the larger it is
- $\delta(|\boldsymbol{r}_{jk}| - 2a)$ makes sure, that particle j will collide with particle k at distance $2a$. The contact point is somewhere at the surface of particles j and k. So, the condition that the collision parameter $|\boldsymbol{b}|$ must be smaller than the diameter of a particle, $2a$, for having a collision is automatically fulfilled

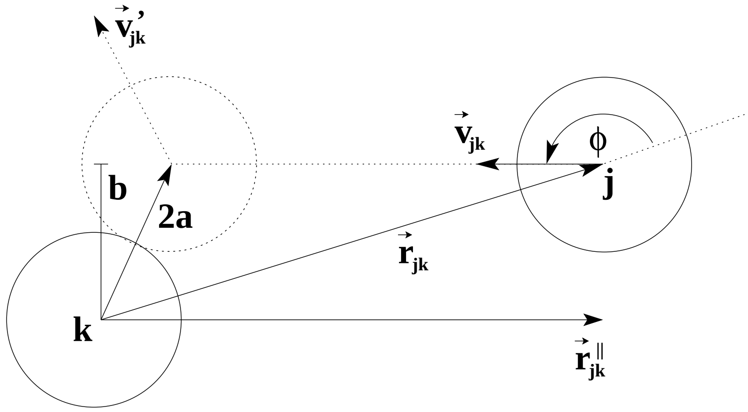

Figure A.1: Two particles j and k, each with radius a, are about to collide.

- $\Theta(-\boldsymbol{v}_{jk} \cdot \hat{\boldsymbol{r}}_{jk})$ does not vanish (is unity) if $\boldsymbol{v}_{jk} \cdot \hat{\boldsymbol{r}}_{jk} = v_{jk}\cos(\phi) < 0$ for $\pi/2 < \phi < 3\pi/2$, i.e., if the normal velocity leads to an approach of the particles, see Fig. A.1
- the collision operator $(b_{jk}^{+} - 1)$ acts on $A(\{\boldsymbol{q}(t), \boldsymbol{p}(t)\})$ and gives its change due to a collision and replaces instantaneously the generalized variables just before the collision, $\{\boldsymbol{q}(t), \boldsymbol{p}(t)\}$, by those just after, $\{\boldsymbol{q}'(t), \boldsymbol{p}'(t)\}$.

A.3 Ensemble Averages

If we know the N-particle phase space distribution function, $\rho(\Gamma; t)$, at a certain time t (e.g., $t = 0$) we will be able to determine the dynamical observable $A(\Gamma; t)$ for every time thereafter. Here, Γ denotes the sets $\{\boldsymbol{r}\}, \{\boldsymbol{v}\}$. For a homogeneous and Maxwellian N-body system [76], $\rho(\Gamma; t)$ is determined in three dimensions by

$$\rho(\Gamma; t) = \Big(\frac{1}{2\pi T_g(t)}\Big)^{3N/2} \exp\Big(-\sum_{l=1}^{N} \frac{\boldsymbol{v}_l^2}{2T_g(t)}\Big) \frac{W(\{\boldsymbol{r}\})}{\int \prod_{l=1}^{N} \mathrm{d}\boldsymbol{r}_l \; W(\{\boldsymbol{r}\})} \tag{A.6}$$

with $T_g(t)$ as the granular temperature and

$$W(\{\boldsymbol{r}\}) = \exp\left(-\frac{1}{T_g(t)} \sum_{j=1}^{N-1} \sum_{k=j+1}^{N} \varphi(|\boldsymbol{r}_{jk}|)\right) = \prod_{j=1}^{N-1} \prod_{k=j+1}^{N} \Theta\big(|\boldsymbol{r}_{jk}| - 2a\big) \quad , \tag{A.7}$$

where the RHS is valid for hard spheres. Eqs. (A.6) and (A.7) give us the probability for finding the N-body system in a state with granular temperature $T_g(t)$

and energy $\sum_{j=1}^{N-1}\sum_{k=j+1}^{N}\varphi(|\boldsymbol{r}_{jk}|)$. For hard spheres, the exponential function corresponds to the Heaviside function due to the fact that one can never find a system with at least one pair of particles that overlap, i.e., that have a separation length of $|\boldsymbol{r}_{jk}| < 2a$ ("*excluded volume*").

Since we analyze a N-body system, we are interested in the ensemble average of A, i.e., $\langle A(t)\rangle$, in order to predict the time evolution of the observable by averaging over the phase space coordinates Γ:

$$\langle A\rangle(t) := \int \mathrm{d}\Gamma\ \rho(\Gamma;0)A(\Gamma;t) \quad . \tag{A.8}$$

According to Eq. (A.6), (A.7) and (A.8) we then obtain for the ensemble average at $T_g(t=0)$

$$\begin{aligned}\langle A\rangle &= \int \prod_{l=1}^{N} \mathrm{d}\boldsymbol{r}_l \mathrm{d}\boldsymbol{v}_l\ \rho(\{\boldsymbol{r},\boldsymbol{v}\};0)A(\{\boldsymbol{r},\boldsymbol{v}\}) \\ &= \Big(\frac{1}{2\pi T_g(t)}\Big)^{3N/2}\frac{1}{Z} \\ &\quad\times \int \prod_{l=1}^{N} \mathrm{d}\boldsymbol{r}_l \mathrm{d}\boldsymbol{v}_l \prod_{j=1}^{N-1}\prod_{k=j+1}^{N}\Theta\big(|\boldsymbol{r}_{jk}|-2a\big)A(\{\boldsymbol{r},\boldsymbol{v}\})\mathrm{exp}\Big(-\sum_{l=1}^{N}\frac{\boldsymbol{v}_l^2}{2T_g(t)}\Big)\end{aligned} \tag{A.9}$$

with

$$Z = \int \prod_{l=1}^{N} \mathrm{d}\boldsymbol{r}_l\ W(\{\boldsymbol{r}\}) = \int \prod_{l=1}^{N} \mathrm{d}\boldsymbol{r}_l \prod_{j=1}^{N-1}\prod_{k=j+1}^{N}\Theta\big(|\boldsymbol{r}_{jk}|-2a\big) = V^N \tag{A.10}$$

as the partition function that normalizes the probability and corresponds to the number of possible micro-states the system can take.

For convenience of nomenclature, we focus on a particular pair of particles $(1,2)$ by considering the particular positions $\boldsymbol{r}_j = \boldsymbol{R}_1$, $\boldsymbol{r}_k = \boldsymbol{R}_2$ and velocities $\boldsymbol{v}_j = \boldsymbol{v}_1$, $\boldsymbol{v}_k = \boldsymbol{v}_2$ and by multiplication and integration over the corresponding δ-functions. The spatial part of Eq. (A.9) can be rewritten as

$$\begin{aligned}&\int \prod_{l=1}^{N} \mathrm{d}\boldsymbol{r}_l \prod_{j=1}^{N-1}\prod_{k=j+1}^{N}\Theta\big(|\boldsymbol{r}_{jk}|-2a\big)A(\{\boldsymbol{r},\boldsymbol{v}\}) \quad \rightarrow \\ &\int \prod_{l=1}^{N} \mathrm{d}\boldsymbol{r}_l \mathrm{d}\boldsymbol{R}_1 \mathrm{d}\boldsymbol{R}_2\ \delta(\boldsymbol{r}_j-\boldsymbol{R}_1)\delta(\boldsymbol{r}_k-\boldsymbol{R}_2)\prod_{j=1}^{N-1}\prod_{k=j+1}^{N}\Theta\big(|\boldsymbol{r}_{jk}|-2a\big)A(\{\boldsymbol{r},\boldsymbol{v}\}) \\ &= N^2V^{N-2}\int \mathrm{d}\boldsymbol{R}_1\mathrm{d}\boldsymbol{R}_2\ g^0(\boldsymbol{R}_1,\boldsymbol{R}_2)A(\boldsymbol{R}_1,\boldsymbol{R}_2,\boldsymbol{v}_1,\boldsymbol{v}_2) \quad ,\end{aligned} \tag{A.11}$$

so that we can replace $\boldsymbol{r}_j$, $\boldsymbol{r}_k$, $\boldsymbol{v}_j$, $\boldsymbol{v}_k$ in $A(\{\boldsymbol{r},\boldsymbol{v}\})$ by $\boldsymbol{R}_1$, $\boldsymbol{R}_2$, $\boldsymbol{v}_1$, $\boldsymbol{v}_2$. $g^0(\boldsymbol{R}_1,\boldsymbol{R}_2)$ is the reduced two-particle distribution function or the *pair distribution function*.

The superscript “0” is introduced here in order to distinguish the pair distribution function later from that when long range forces are acting (no superscript). The $N-2$ identical integrations over Gaussians of the velocities in Eq. (A.10), i.e., $\mathrm{d}\boldsymbol{v}_3 ... \mathrm{d}\boldsymbol{v}_N$, can be carried out so that

$$\int \prod_{l=1}^{N} \mathrm{d}\boldsymbol{v}_l \, \exp\Big(- \sum_{l=1}^{N} \frac{\boldsymbol{v}_l^2}{2T_g(t)} \Big) = \Big(2\pi T_g(t) \Big)^{3(N-2)/2} \int \mathrm{d}\boldsymbol{v}_1 \mathrm{d}\boldsymbol{v}_2 \exp\Big(- \frac{\boldsymbol{v}_1^2 + \boldsymbol{v}_2^2}{2T_g(t)} \Big) \ . \tag{A.12}$$

Thus, altogether (Eqs. (A.10), (A.11) and (A.12)) one obtains for the dynamical variable

$$\begin{aligned} \langle A \rangle &= \frac{N^2}{V^2} \Big(\frac{1}{2\pi T_g(t)} \Big)^3 \\ &\times \int \mathrm{d}\boldsymbol{R}_1 \mathrm{d}\boldsymbol{R}_2 \mathrm{d}\boldsymbol{v}_1 \mathrm{d}\boldsymbol{v}_2 \; g^0(\boldsymbol{R}_1, \boldsymbol{R}_2) A(\boldsymbol{R}_1, \boldsymbol{R}_2, \boldsymbol{v}_1, \boldsymbol{v}_2) \exp\Big(- \frac{\boldsymbol{v}_1^2 + \boldsymbol{v}_2^2}{2T_g(t)} \Big) \end{aligned} \tag{A.13}$$

The pair distribution function, $g^0(\boldsymbol{R}_1, \boldsymbol{R}_2)$, gives the probability to find the particle j at $\boldsymbol{R}_1$ and k at $\boldsymbol{R}_2$, simultaneously. In the following, we only have to specify the dynamical variable $A(\boldsymbol{R}_1, \boldsymbol{R}_2, \boldsymbol{v}_1, \boldsymbol{v}_2)$.

A.4 Collision Frequency ...

Consider the collision frequency per particle and time unit as the dynamical observable and C the number of binary collisions in the whole system at time t so far,

$$\begin{aligned} f_E(t) &= \frac{2}{N} \frac{d}{\mathrm{d}t} \langle C \rangle (t) \overset{(A.3)}{=} \frac{2}{N} \langle i \mathcal{L}^{\mathrm{coll}} C \rangle (t) \\ &\overset{(A.13)}{=} \frac{2Ni}{V^2} \Big(\frac{1}{2\pi T_g(t)} \Big)^3 \int \mathrm{d}\boldsymbol{R}_1 \mathrm{d}\boldsymbol{R}_2 \mathrm{d}\boldsymbol{v}_1 \mathrm{d}\boldsymbol{v}_2 \; g^0(\boldsymbol{R}_1 - \boldsymbol{R}_2) \\ &\quad \times \mathcal{L}_{12}^{\mathrm{coll}} C \exp\Big(- \frac{\boldsymbol{v}_1^2 + \boldsymbol{v}_2^2}{2T_g(t)} \Big) \\ &\overset{(A.4)}{=} \frac{2Ni}{V^2} \Big(\frac{1}{2\pi T_g(t)} \Big)^3 \int \mathrm{d}\boldsymbol{R}_1 \mathrm{d}\boldsymbol{R}_2 \mathrm{d}\boldsymbol{v}_1 \mathrm{d}\boldsymbol{v}_2 \; g^0(\boldsymbol{R}_{12}) \exp\Big(- \frac{\boldsymbol{v}_1^2 + \boldsymbol{v}_2^2}{2T_g(t)} \Big) \\ &\quad \times |\boldsymbol{v}_{12} \cdot \hat{\boldsymbol{R}}_{12}| \Theta(-\boldsymbol{v}_{12} \cdot \hat{\boldsymbol{R}}_{12}) \delta(|\boldsymbol{R}_{12}| - 2a) \Big(b_{12}^{+} - 1 \Big) C \\ &= \frac{2Ni}{V^2} \Big(\frac{1}{2\pi T_g(t)} \Big)^3 \int \mathrm{d}\boldsymbol{R} \mathrm{d}\boldsymbol{r} \mathrm{d}\boldsymbol{V} \mathrm{d}\boldsymbol{v} \; g^0(\boldsymbol{r}) \exp\Big(- \frac{\boldsymbol{v}^2 + \boldsymbol{V}^2}{2T_g(t)} \Big) \\ &\quad \times |\sqrt{2}\boldsymbol{v} \cdot \hat{\boldsymbol{r}}| \Theta(-\sqrt{2}\boldsymbol{v} \cdot \hat{\boldsymbol{r}}) \delta(|\boldsymbol{r}| - 2a) \end{aligned} \tag{A.14}$$

where we set the substitutions $\boldsymbol{r} = \boldsymbol{r}_1 - \boldsymbol{r}_2$, $\hat{\boldsymbol{r}} = (\boldsymbol{r}_1 - \boldsymbol{r}_2)/|\boldsymbol{r}_1 - \boldsymbol{r}_2|$, $\boldsymbol{R} = \boldsymbol{r}_1 + \boldsymbol{r}_2$ and $\sqrt{2}\boldsymbol{v} = \boldsymbol{v}_1 - \boldsymbol{v}_2$, $\sqrt{2}\boldsymbol{V} = \boldsymbol{v}_1 + \boldsymbol{v}_2$. Free streaming does not change $C(t)$, thus it is $\langle i\mathcal{L}^{\text{free}}C\rangle(t) = 0$. The expression $(b_{12}^{+} - 1)C = \Delta C$ provides unity for each pair that collides, i.e., in total the integration provides the total number of collisions that occur in the system until time t. With $\int \mathrm{d}\boldsymbol{R} = V$, $n = N/V$ and integration over the velocity, $\int \mathrm{d}\boldsymbol{V}\ \exp(-\boldsymbol{V}^2/(2T_g(t))) = (2\pi T_g(t))^{3/2}$, we have

$$\begin{aligned} f_E(t) &= n\Big(\frac{1}{2\pi T_g(t)}\Big)^{3/2} \underbrace{\int\limits_0^{+\infty} \mathrm{d}r\ r^2 g^0(r)\delta(r-2a) \int\limits_0^{\pi} \mathrm{d}\vartheta\ \sin(\vartheta) \int\limits_0^{2\pi} \mathrm{d}\varphi}_{4a^2 g^0(2a)\ \times\ 2\ \times\ 2\pi} \\ &\quad \times \int\limits_{-\infty}^{+\infty} \mathrm{d}\boldsymbol{v}\ \exp\Big(-\frac{\boldsymbol{v}^2}{2T_g(t)}\Big)|\sqrt{2}\boldsymbol{v}\cdot\hat{\boldsymbol{r}}|\Theta(-\sqrt{2}\boldsymbol{v}\cdot\hat{\boldsymbol{r}}) \quad . \end{aligned} \tag{A.15}$$

In order to apply the theory for our problems of long range forces, we apply a new non-standard way of solving the integral. Instead of using spherical coordinates, we remain in the cartesian system such that the centre-to-centre-vector, $\hat{\boldsymbol{r}}$, defines one axis. We then will split up the relative velocity vector as $\boldsymbol{v}^2 = (\boldsymbol{v}\cdot\hat{\boldsymbol{r}})^2 + (\boldsymbol{v}\cdot\hat{\boldsymbol{s}})^2 + (\boldsymbol{v}\cdot\hat{\boldsymbol{t}})^2 = v_n^2 + v_s^2 + v_t^2$, where the unit vectors $\hat{\boldsymbol{r}}, \hat{\boldsymbol{s}}, \hat{\boldsymbol{t}}$ are perpendicular to each other, such that

$$\begin{aligned} f_E(t) &= 16n\pi a^2 g^0(2a)\Big(\frac{1}{2\pi T_g(t)}\Big)^{3/2} \int\limits_{-\infty}^{+\infty} \mathrm{d}v_n\ \exp\Big(-\frac{v_n^2}{2T_g(t)}\Big)|\sqrt{2}v_n|\Theta(-\sqrt{2}v_n) \\ &\quad \times \underbrace{\int\limits_{-\infty}^{+\infty} \mathrm{d}v_t\ \exp\Big(-\frac{v_t^2}{2T_g(t)}\Big)}_{\sqrt{2\pi T_g(t)}} \underbrace{\int\limits_{-\infty}^{+\infty} \mathrm{d}v_s\ \exp\Big(-\frac{v_s^2}{2T_g(t)}\Big)}_{\sqrt{2\pi T_g(t)}} \quad . \end{aligned} \tag{A.16}$$

A.4.1 ... in the Absence of Long Range Forces

In the absence of long range forces, integration over v_n leads to the classical *Haff* result

$$\begin{aligned} f_E^0(t) &= -16na^2\sqrt{\pi}g^0(2a)T_g(t)^{-1/2} \int\limits_{-\infty}^{0} \mathrm{d}v_n\ \exp\Big(-\frac{v_n^2}{2T_g(t)}\Big)v_n \\ &= 16na^2\sqrt{\pi}g^0(2a)T_g(t)^{1/2} \end{aligned} \tag{A.17}$$

because the Θ-function in Eq. (A.16) will only select from the interval $]-\infty, 0]$ and the negative sign in the first line comes if we neglect the absolute value bars of $|\sqrt{2}v_n|$ in the integrand.

A.4.2 ... in the Presence of Repulsive Long Range Forces

In the case of repulsive long range forces we have to specify the range of possible v_n. In order to have a collision, the initial normal relative velocity must exceed the repulsive potential barrier at contact: $v_n \leq -v_{n,b} = -\big(2c_b km/a\big)^{1/2}$ for monodisperse particles and the Θ-function has to select only velocities from the interval $]-\infty, -v_{n,b}]$. We obtain

$$\begin{aligned} f_E(t) &= 8\sqrt{2}na^2\sqrt{\pi}g^0(2a)T_g(t)^{-1/2} \\ &\quad\times \int\limits_{-\infty}^{+\infty} \mathrm{d}v_n \, \exp\Big(-\frac{v_n^2}{2T_g(t)}\Big)|\sqrt{2}v_n|\Theta\big(-\sqrt{2}(v_n+v_{n,b})\big) \\ &= -16na^2\sqrt{\pi}g^0(2a)T_g(t)^{-1/2} \underbrace{\int\limits_{-\infty}^{-v_{n,b}} \mathrm{d}v_n \; v_n \exp\Big(-\frac{v_n^2}{2T_g(t)}\Big)}_{-T_g(t)\exp\Big(-\frac{v_{n,b}^2}{2T_g(t)}\Big)} \\ &= f_E^0(t)\,\exp\Big(-\frac{v_{n,b}^2}{2T_g(t)}\Big) \end{aligned} \tag{A.18}$$

and see that the difference to the classical solution (A.17) is an exponential factor $\exp\big(-v_{n,b}^2/(2T_g(t))\big)$, where the critical velocity $v_{n,b}$ represents the strength of the repulsive potential at contact. For high granular temperatures or $T_g(t) \gg v_{n,b}^2$, the correction factor goes to unity and the repulsion cannot avoid particles from colliding anymore and the gas behaves like a classical granular gas without long range forces. For low temperatures, the exponential factor becomes important and has to be considered.

For small critical velocities, we can also expand the exponential factor in a Taylor's series about $v_{n,b} = 0$ and obtain for an expansion until the 4^{th} order in $v_{n,b}$

$$f_E(t) \approx f_E^0(t)\left(1 - \frac{1}{2}\frac{v_{n,b}^2}{T_g(t)} + \frac{1}{8}\frac{v_{n,b}^4}{T_g(t)^2}\right) \quad , \tag{A.19}$$

which gives best approximations at high temperatures. For low temperatures (at least for those $T_g(t)$ where long range forces become important) we need more polynoms than in Eq. (A.19) shown.

A.4.3 ... in the Presence of Attractive Long Range Forces

For attractive forces we have to extend the range of possible v_n. Not only approaching particles (which are specified by the velocity interval $]-\infty, 0]$) are about to collide but even those that move away from each other can collide. Therefore we have to extend the interval of velocities to $]-\infty, +v_{n,e}]$, where $v_{n,e}$ is the so-called "escape" velocity. v_n has to fall below this limit in order to support a collision, i.e., $v_n \leq +v_{n,e} = +\big(2|c_e|km/a\big)^{1/2}$ for mono-disperse particles. For a collision due to attractive forces, instead of Eq. (A.18) we obtain

$$\begin{aligned}
f_E(t) &= 8\sqrt{2}na^2\sqrt{\pi}g^0(2a)T_g(t)^{-1/2} \\
&\quad \times \int\limits_{-\infty}^{+\infty} \mathrm{d}v_n \, \exp\Big(-\frac{v_n^2}{2T_g(t)}\Big) \underbrace{|\sqrt{2}v_n|}_{\sqrt{2}v_n \mathrm{sgn}(v_n)} \Theta\big(-\sqrt{2}(v_n - v_{n,e})\big) \\
&= 16na^2\sqrt{\pi}g^0(2a)T_g(t)^{-1/2} \int\limits_{-\infty}^{+v_{n,e}} \mathrm{d}v_n \; v_n \mathrm{sgn}(v_n) \exp\Big(-\frac{v_n^2}{2T_g(t)}\Big) \\
&= 16na^2\sqrt{\pi}g^0(2a)T_g(t)^{-1/2} \\
&\quad \times \Bigg(\underbrace{\int\limits_{0}^{+v_{n,e}} \mathrm{d}v_n \; v_n \exp\Big(-\frac{v_n^2}{2T_g(t)}\Big)}_{T_g(t) - T_g(t)\exp\big(-\frac{v_{n,e}^2}{2T_g(t)}\big)} - \underbrace{\int\limits_{-\infty}^{0} \mathrm{d}v_n \; v_n \exp\Big(-\frac{v_n^2}{2T_g(t)}\Big)}_{-T_g(t)} \Bigg) \\
&= f_E^0(t) \left[2 - \exp\Big(-\frac{v_{n,e}^2}{2T_g(t)}\Big) \right] \qquad \text{(A.20)}
\end{aligned}$$

which exposes a different correction factor than Eq. (A.18). For high temperatures $T_g(t) \gg v_{n,e}^2$, again the exponential factor becomes unity and we obtain the classical result (A.17) for gases without long range forces. For low temperatures, the influence of the attractive potential becomes strong and the collision frequency increases up to twice the classical result.

For low escape velocities, we can do the same expansion as for the case of repulsion, see above, and obtain

$$f_E(t) \approx f_E^0(t) \left(1 + \frac{1}{2}\frac{v_{n,e}^2}{T_g(t)} - \frac{1}{8}\frac{v_{n,e}^4}{T_g(t)^2} \right) \;, \qquad \text{(A.21)}$$

which reveals similarity to Eq. (A.19) except for the sign from the second term in the brackets. The difference in sign gives rise to the fact that for attractive long range forces $f_E(t)$ increases and for repulsive long range forces it shows a decay comparing with the case where no long range forces act.

A.5 Kinetic Energy ...

Haff's law can be derived from the hydrodynamic energy balance equation [43, 93]. This equation balances the energy flux density through the surface of a volume element taken out from a cooling granular gas. There are many physical phenomena that determine the flux density: the transport of the kinetic energy per volume unit by the simple movement of the material results in a flux density, $w(t)\boldsymbol{u}$, where $w(t) = \frac{1}{2}\varrho u^2 + \frac{1}{2}\varrho\sigma_v^2$ is the kinetic energy density, $\boldsymbol{u}$ the overall velocity of the material and σ_v the fluctuating contribution that represents the granular temperature, according to Eq. (4.3). Then we have the flux density, $p\boldsymbol{u}$, which is generated by the pressure p perpendicular to the surface of the volume element by the surrounding elements. On the other hand, internal friction expressed by the macroscopic viscosity parameter η due to the movement of different parts of the fluid element relative to each other will produce heat which is carried with the velocity, $\boldsymbol{u}$. Moreover, driven by internal temperature gradients, heat can be transported from warmer to cooler regions within the volume element whose efficiency is determined by the thermal diffusivity, κ. The change of all these contributions to the energy density per time unit can be obtained by their spatial derivatives. Then the hydrodynamic energy density balance equation reads

$$\begin{aligned}\frac{\partial w(t)}{\partial t} = & -\frac{\partial}{\partial x_k}\underbrace{\Big(w(t)\left\langle v\right\rangle_k + p\left\langle v\right\rangle_k\delta_{ik}\Big)}_{\substack{\textit{energy density flux due}\\ \textit{to the movement of the}\\ \textit{fluid as a whole and the}\\ \textit{pressure onto the fluid}\\ \textit{element}}} + \frac{\partial}{\partial x_k}\underbrace{\left(\left\langle v\right\rangle_i\eta\Big(\frac{\partial\langle v\rangle_i}{\partial x_k} + \frac{\partial\langle v\rangle_k}{\partial x_i}\Big)\right)}_{\substack{\textit{energy density flux due}\\ \textit{to internal friction}}} \\ & + \frac{\partial}{\partial x_k}\underbrace{\left(\kappa\frac{\partial}{\partial x_k}\Big(\frac{1}{2}\varrho\sigma_v^2(t)\Big)\right)}_{\substack{\textit{energy density flux due}\\ \textit{to internal temperature}\\ \textit{gradients}}} + \underbrace{\gamma(t)}_{\substack{\textit{energy density dissipa-}\\ \textit{tion rate due to dissipa-}\\ \textit{tive particle-particle col-}\\ \textit{lisions}}} ,\end{aligned} \tag{A.22}$$

where $\gamma(t) < 0$ is the energy dissipation (cooling) rate due to dissipative collisions between the particles. According to Section 4.1.1, in Eq. (A.22) we have written for the overall velocity components, $u_k = \left\langle v\right\rangle_k$[1]. For a homogeneous system, we assume the same density of the volume element as for the whole system, i.e.,

---

[1] We have here used *Einstein*'s notation of vectors. In this notation we can avoid writing down vectors and use their components where repeated indices in a single term will be summed up, e.g., $\left\langle v\right\rangle_k\delta_{ik} = \sum_{k=1}^{3}\left\langle v\right\rangle_k\delta_{ik}$. δ_{ik} is the *Kronecker*'s symbol and vanishes if $i \neq k$.

$\varrho = Nm/V$, and it is $\partial/\partial x_k = 0$. We assume no macroscopic flow of particles, that is why we can set $w(t) = \frac{1}{2}\varrho\sigma_v^2 = \frac{1}{6}\varrho\left\langle v^2\right\rangle = \frac{1}{2}\frac{Nm}{V}T_g(t) = \frac{1}{3V}E_{\text{kin}}(t)$, according to Eqs. (4.2) to (4.3). With these assumptions we obtain from Eq. (A.22)

$$\frac{dw(t)}{dt} = \gamma(t) = \frac{1}{3V}\frac{dE_{\text{kin}}(t)}{dt} \quad . \tag{A.23}$$

Using $E_{\text{kin}}(t)$ as the dynamical observable as an ensemble average and considering $\langle i\mathcal{L}^{\text{free}}E_{\text{kin}}\rangle(t) = 0$ because free streaming particles do not change the energy, we will obtain

$$\begin{aligned}\frac{d}{\mathrm{d}t}\langle E_{\text{kin}}\rangle(t) &= \langle i\mathcal{L}^{\text{coll}}E_{\text{kin}}\rangle(t)\\ &\overset{(A.14)}{=} -\frac{N^2 i}{4V^2}m(1-r^2)\Big(\frac{1}{2\pi T_g(t)}\Big)^3\\ &\quad\times\int \mathrm{d}\boldsymbol{R}\mathrm{d}\boldsymbol{r}\mathrm{d}\boldsymbol{V}\mathrm{d}\boldsymbol{v}\; g(\boldsymbol{r})\exp\Big(-\frac{\boldsymbol{v}^2+\boldsymbol{V}^2}{2T_g(t)}\Big)\\ &\quad\times|\sqrt{2}\boldsymbol{v}\cdot\hat{\boldsymbol{r}}|\Theta(-\sqrt{2}\boldsymbol{v}\cdot\hat{\boldsymbol{r}})\delta(|\boldsymbol{r}|-2a)(b_{12}^{+}-1)E_{\text{kin}} \quad ,\end{aligned} \tag{A.24}$$

where the binary collision operator reduces the total kinetic energy by the amount

$$(b_{12}^{+}-1)E_{\text{kin}} = (b_{12}^{+}-1)\Big(\frac{1}{4}m\boldsymbol{v}_*^2\Big) = -\frac{1}{4}m(1-r^2)\Big((\boldsymbol{v}\cdot\hat{\boldsymbol{r}})^2 + v_{n,cr}^2\Big)$$

due to one binary collision for mono-disperse particles. $\boldsymbol{v}_*$ is here the modified relative velocity of both particles due to long range forces: the kinetic energy of both particles is reduced if the particles are decelerated relative to each other (approaching repulsive particles or separating attractive particles). The kinetic energy is increased if the particles are accelerated relative to each other (approaching attractive particles or separating repulsive particles, whereas the latter case will be rejected by the Θ-function anyway). $v_{n,cr}^2$ determines whether we have repulsive ($v_{n,cr}^2 = \text{sgn}(v_n)v_{n,b}^2$) or attractive ($v_{n,cr}^2 = \text{sgn}(-v_n)v_{n,e}^2$) forces. With the settings and integrations of the last section that led to Eq. (A.16), we analogously get

$$\begin{aligned}\frac{d}{\mathrm{d}t}\langle E_{\text{kin}}\rangle(t) &= -4\pi Nnm(1-r^2)a^2g^0(2a)\Big(\frac{1}{2\pi T_g(t)}\Big)^{1/2}\\ &\quad\times\int_{-\infty}^{+\infty}\mathrm{d}v_n\,\exp\Big(-\frac{v_n^2}{2T_g(t)}\Big)|\sqrt{2}v_n|\Theta(-\sqrt{2}v_n)\Big(v_n^2+v_{n,cr}^2\Big) \quad .\end{aligned} \tag{A.25}$$

A.5.1 ... in the Absence of Long Range Forces

In the absence of long range forces, this leads to the classical *Haff* result

$$\begin{aligned}\frac{d}{\mathrm{d}t}\langle E_{\mathrm{kin}}\rangle(t) &= -8\sqrt{\pi}Nnm(1-r^2)a^2g^0(2a)T_g(t)^{3/2} \\ &= -f_E^0(t)\frac{N}{2}(1-r^2)mT_g(t) \\ &=: I^0(t) \end{aligned} \tag{A.26}$$

because the Θ-function in Eq. (A.25) will only select from the interval $]-\infty, 0]$.

A.5.2 ... in the Presence of Repulsive Long Range Forces

With the Θ-function of Eq. (A.18) that selects the velocities of the interval $]-\infty, -v_{n,b}]$ which leads to a collision only in the case of respulsive potentials, Eq. (A.25) can be rewritten as

$$\begin{aligned} I(t) \equiv \frac{d}{\mathrm{d}t}\langle E_{\mathrm{kin}}\rangle(t) &= -4\pi Nnm(1-r^2)a^2g^0(2a)\Big(\frac{1}{2\pi T_g(t)}\Big)^{1/2} \\ &\quad \times \int_{-\infty}^{+\infty} \mathrm{d}v_n \, \exp\Big(-\frac{v_n^2}{2T_g(t)}\Big)|\sqrt{2}v_n| \\ &\quad \times \Theta\big(-\sqrt{2}(v_n+v_{n,b})\big)\Big(v_n^2+\mathrm{sgn}(v_n)v_{n,b}^2\Big) \\ &= 4\sqrt{\pi}Nnm(1-r^2)a^2g^0(2a)T_g(t)^{-1/2} \\ &\quad \underbrace{\times \int_{-\infty}^{-v_{n,b}} \mathrm{d}v_n \, \exp\Big(-\frac{v_n^2}{2T_g(t)}\Big)v_n\Big(v_n^2-v_{n,b}^2\Big)}_{-2T_g(t)^2\exp\Big(-\frac{v_{n,b}^2}{2T_g(t)}\Big)} \\ &= I^0(t)\,\exp\Big(-\frac{v_{n,b}^2}{2T_g(t)}\Big) \quad . \end{aligned} \tag{A.27}$$

This differential equation is only numerically solvable and the RHS of Eq. (A.27) represents the dissipation rate of a mono-dispersed granular gas of dissipative hard spheres in the presence of a repulsive long range potential.

A.5.3 ... in the Presence of Attractive Long Range Forces

With the Θ-function of Eq. (A.20) that selects the velocities of the interval $]-\infty, +v_{n,e}]$ which leads to a collision in the case of attractive potentials, Eq.

(A.25) can be rewritten as

$$\begin{aligned}
I(t) \equiv \frac{d}{\mathrm{d}t}\langle E_{\mathrm{kin}}\rangle(t) &= -4\pi Nnm(1-r^2)a^2 g^0(2a)\Big(\frac{1}{2\pi T_g(t)}\Big)^{1/2} \\
&\quad \times \int\limits_{-\infty}^{+\infty} \mathrm{d}v_n \, \exp\Big(-\frac{v_n^2}{2T_g(t)}\Big) \underbrace{|\sqrt{2}v_n|}_{\sqrt{2}v_n \mathrm{sgn}(v_n)} \\
&\quad \times\Theta\big(-\sqrt{2}(v_n - v_{n,e})\big)\Big(v_n^2 + \mathrm{sgn}(-v_n)v_{n,e}^2\Big) \\
&= -4\sqrt{\pi}Nnm(1-r^2)a^2 g^0(2a)T_g(t)^{-1/2} \\
&\quad \times \int\limits_{-\infty}^{+v_{n,e}} \mathrm{d}v_n \, \exp\Big(-\frac{v_n^2}{2T_g(t)}\Big)v_n \mathrm{sgn}(v_n)\Big(v_n^2 + \mathrm{sgn}(-v_n)v_{n,e}^2\Big) \\
&= -4\sqrt{\pi}Nnm(1-r^2)a^2 g^0(2a)T_g(t)^{-1/2} \\
&\quad \times \Bigg(\underbrace{\int\limits_{0}^{+v_{n,e}} \mathrm{d}v_n \, \exp\Big(-\frac{v_n^2}{2T_g(t)}\Big)v_n\Big(v_n^2 - v_{n,e}^2\Big)}_{2T_g(t)^2 - T_g(t)v_{n,e}^2 - 2T_g(t)^2\exp\Big(-\frac{v_{n,e}^2}{2T_g(t)}\Big)} \\
&\qquad \underbrace{- \int\limits_{-\infty}^{0} \mathrm{d}v_n \, \exp\Big(-\frac{v_n^2}{2T_g(t)}\Big)v_n\Big(v_n^2 + v_{n,e}^2\Big)\Bigg)}_{-2T_g(t)^2 - T_g(t)v_{n,e}^2} \\
&= I^0(t)\left[2 - \exp\Big(-\frac{v_{n,e}^2}{2T_g(t)}\Big)\right] \quad . \qquad \text{(A.28)}
\end{aligned}$$

This differential equation is only numerically solvable and the RHS of Eq. (A.28) represents the dissipation rate of a mono-dispersed granular gas of dissipative hard spheres in the presence of an attractive long range potential.

A.6 The Dilute Limit

The *pseudo-Liouville* operator formalism is a theory that considers binary particle collisions. Each pair of particle in a N-body system is checked for a collision. As soon as two arbitrary particles fulfil the conditions for a mechanical contact (see A.2), the formalism considers both particles to collide and to contribute to the change of the dynamical observables previously discussed. The formalism strictly considers binary collisions as interactions between hard spheres and would fail if multiple particle interactions take place.

In principle, the time of a binary collision is defined as the time span between the moment when the relative velocity starts to change due to the interaction force and the moment when it does not change anymore. This definition applies when both particles are separated by an infinite distance before and after the collision, *and* when during the collision time there are no more particles in the collision involved. Any deviation from these constraints makes the *pseudo-Liouville* operator concept useless in respect of its application to our systems.

So, we have to make a compromise when applying it to soft sphere particle systems including $1/r$ long range interaction potentials: we have to apply the formalism to systems in the dilute limit in order to obtain best agreement. In this ideal situation, particles are separated by infinite distances where even $1/r$ potentials are vanishing and long range multiple particle collisions do not occur. In this case, the *pseudo-Liouville* operator theory applies also to long range interacting soft spheres.

The results for the dynamical observables shown in the previous subsections contain the correction factor in the dilute limit by using the repulsive two particle energy barrier, E_b, and the attractive two particle escape energy barrier, E_e, respectively. Strictly spoken, they are inconsistent because they also contain the pair distribution function at contact, $g^0(2a)$, which considers finite densities. Nevertheless, in chapter 4 we have compared simulation results (where $\nu \neq 0$) with the theoretical results of this appendix (where $\nu \to 0$), always having in mind that the theoretical results partly account for non-vanishing densities via $g^0(2a)$.

A.7 More about the pseudo-Liouville Operator

Let us focus on the term $|\sqrt{2}v_n|$ within the pseudo-Liouville operator. As already remarked, its absolute value has influence on both the collision frequency and the loss of kinetic energy (due to collisions): the larger it is the faster the particle travels through the collision cylinder and the more often it can collide with a partner. However, the absolute value of the travel velocity of two approaching particles will, for example, be changed by long range forces such that it will be decelerated by a repulsive binary force or accelerated by an attractive binary force:

$$\begin{aligned} |\sqrt{2}v_n| \quad &\rightarrow \quad |\sqrt{2}(v_n + v_{n,b})| \qquad \text{with } v_n < 0 \text{ for repulsive particles} \\ |\sqrt{2}v_n| \quad &\rightarrow \quad |\sqrt{2}(v_n - v_{n,e})| \qquad \text{with } v_n < 0 \text{ or } v_n > 0 \text{ for attractive particles} \end{aligned}$$

Using this, we will get for the collision frequency in case of repulsive forces, according to Eq. (A.18),

$$\begin{aligned}
f_E(t) &= \ldots \\
&= -16na^2\sqrt{\pi}g^0(2a)T_g(t)^{-1/2} \int\limits_{-\infty}^{-v_{n,b}} \mathrm{d}v_n\ (v_n+v_{n,b})\exp\Big(-\frac{v_n^2}{2T_g(t)}\Big) \\
&= f_E^0(t)\ \Bigg[\exp\big(-A^2\big)+A\sqrt{\pi}\Big[\mathrm{erf}\big(A\big)-1\Big]\Bigg] \qquad \text{(A.29)}
\end{aligned}$$

and for the case of attractive forces, according to Eq. (A.20),

$$\begin{aligned}
f_E(t) &= \ldots \\
&= 16na^2\sqrt{\pi}g^0(2a)T_g(t)^{-1/2}\Bigg(\int\limits_{0}^{+v_{n,e}} \mathrm{d}v_n\ (v_n-v_{n,e})\exp\Big(-\frac{v_n^2}{2T_g(t)}\Big) \\
&\qquad -\int\limits_{-\infty}^{0} \mathrm{d}v_n\ (v_n-v_{n,e})\exp\Big(-\frac{v_n^2}{2T_g(t)}\Big)\Bigg) \\
&= f_E^0(t)\ \Bigg[2-\exp\big(-B^2\big)-B\sqrt{\pi}\Big[\mathrm{erf}\big(B\big)-1\Big]\Bigg]\ . \qquad \text{(A.30)}
\end{aligned}$$

Here, $\mathrm{erf}(\cdot)$ denotes the error function, $A^2 = v_{n,b}^2/\big(2T_g(t)\big)$, and $B^2 = v_{n,e}^2/\big(2T_g(t)\big)$. For $T_g(t) \to +\infty$ we have $A,\ B \to 0$ and $\mathrm{erf}(A),\ \mathrm{erf}(B) \to 0$. On the other hand, for $T_g(t) \to 0$ we have $A,\ B \to +\infty$ and $\mathrm{erf}(A),\ \mathrm{erf}(B) \to 1$. Thus, for both very low and very high temperatures, the modified and unmodified solution merge. Fig. A.2 displays the difference between the modification in $|\sqrt{2}v_n|$ and the unmodified solutions for $f_E(t)$ in the cases of repulsive and attractive long range forces for the case of intermediate temperatures. In this temperature regime, where the exponential correction factor becomes important, the modification $|\sqrt{2}v_n \pm \sqrt{2}v_{n,cr}|$ has much more influence. We see, that in the repulsive case (Fig. A.2, left) the modification gives a stronger repulsive potential than Eq. (A.18) predicts. This is reasonable, because the additional deceleration, $v_n + v_{n,b}$, of the particles in presence of repulsive forces leads to a stronger repulsive potential indeed. In the attractive case the modification likewise provides a stronger attractive potential which is also reasonable because of the additional acceleration, $v_n - v_{n,e}$, of particles. This results in an increase of $f_E(t)$ much earlier than the unmodified theory shows (Fig. A.2, right).

In contrast, note, that we saw in Chapter 4 that the simulation results show a weaker repulsive and attractive potential than the unmodified theory predicts (see inequalities (4.19) and (4.29)). The reason for this is the many-body effect mentioned there.

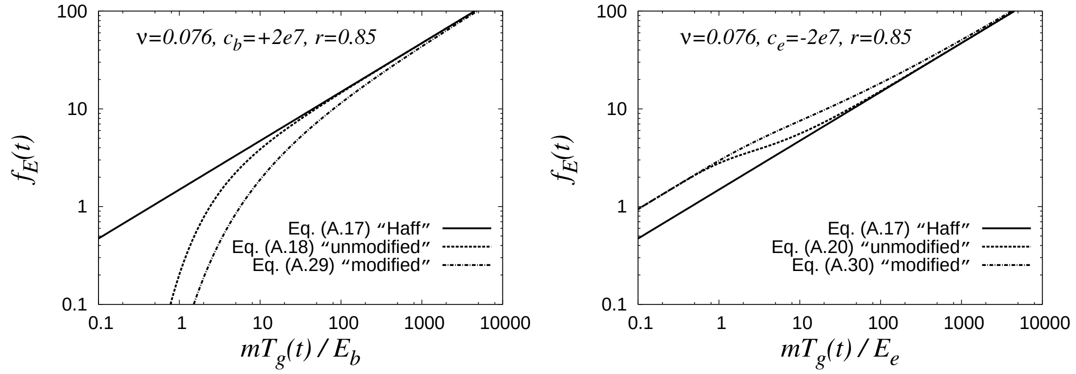

Figure A.2: Collision frequency, $f_E(t)$, plotted against scaled thermal energy for repulsive long range forces (left) and attractive long range forces (right), according to different equations.

A.8 Effective Particle Radius

Furthermore, but not relevant anymore for phenomena that are governed by particle-particle collisions with physical contacts, there have to be done some modifications in radius dependent quantities if we focus on phenomena that are affected by interactions over distances larger than $2a$. Diffusion, for example, depends not only on interactions via physical contact but also strongly on interactions via long range forces, i.e., it depends on changes of momentum due to any kind of interactions. Thus, the radius a becomes an effective radius, a_{eff}, where $a_{\text{eff}} > a$. Radius dependent quantities like the pair distribution function $g^0(2a)$ will be modified as well. $g^0(2a_{\text{eff}})$ will then take a larger (effective) excluded volume into account because particles will "see" each other now stronger than they would do if the interactions would take place via physical contacts only. However, examining this in more detail is far from the scope of this thesis.

B Multipole Expansion

In this Appendix we sketch briefly the derivation of Eq. (2.14) and of the corresponding potential ϕ_{ij}. According to Fig. 2.2, both the potential and the force of a distant particle ensemble α acting on the *poi* are:

$$\begin{aligned}
\phi_{i\alpha}\Big(\{r_{ij}\}\Big) &= -kc_i \sum_j^{n_\alpha} \frac{c_j}{|\boldsymbol{r}_{i\alpha} - \boldsymbol{r}_{j\alpha}|} \quad , \\
\boldsymbol{F}_{i\alpha}\Big(\{r_{ij}\}\Big) &= -kc_i \sum_j^{n_\alpha} c_j \frac{\boldsymbol{r}_{i\alpha} - \boldsymbol{r}_{j\alpha}}{|\boldsymbol{r}_{i\alpha} - \boldsymbol{r}_{j\alpha}|^3} \quad , \qquad \text{(B.1)}
\end{aligned}$$

where $\boldsymbol{r}_{i\alpha} = \boldsymbol{r}_i - \boldsymbol{R}^\alpha$, $\boldsymbol{r}_{j\alpha} = \boldsymbol{r}_j - \boldsymbol{R}^\alpha$ and we consider the case $|\boldsymbol{r}_{i\alpha}| \gg |\boldsymbol{r}_{j\alpha}|$ in the following. $\boldsymbol{R}^\alpha$ denotes the geometrical center of α, see Eq. (2.13), and n_α the number of single particles that make up α. With the equalities

$$\begin{aligned}
|\boldsymbol{r}_{i\alpha} - \boldsymbol{r}_{j\alpha}| &= (r_{i\alpha}^2 - 2\boldsymbol{r}_{i\alpha} \cdot \boldsymbol{r}_{j\alpha} + r_{j\alpha}^2)^{1/2} \quad , \qquad \text{and} \\
\frac{\boldsymbol{r}_{i\alpha} - \boldsymbol{r}_{j\alpha}}{|\boldsymbol{r}_{i\alpha} - \boldsymbol{r}_{j\alpha}|^3} &= -\boldsymbol{\nabla}_{i\alpha} \frac{1}{|\boldsymbol{r}_{i\alpha} - \boldsymbol{r}_{j\alpha}|}
\end{aligned}$$

for a conservative force, we can express Eq. (B.1) as function of the inverse distance

$$\begin{aligned}
\phi_{i\alpha} &= -kc_i \sum_j^{n_\alpha} \frac{c_j}{(r_{i\alpha}^2 - 2\boldsymbol{r}_{i\alpha} \cdot \boldsymbol{r}_{j\alpha} + r_{j\alpha}^2)^{1/2}} \\
\boldsymbol{F}_{i\alpha} &= kc_i \sum_j^{n_\alpha} c_j \boldsymbol{\nabla}_{i\alpha} \frac{1}{(r_{i\alpha}^2 - 2\boldsymbol{r}_{i\alpha} \cdot \boldsymbol{r}_{j\alpha} + r_{j\alpha}^2)^{1/2}} \quad , \qquad \text{(B.2)}
\end{aligned}$$

where $\boldsymbol{\nabla}_{i\alpha}$ denotes the derivative with respect to the three-dimensional distance vector $\boldsymbol{r}_{i\alpha}$ (this corresponds to a spatially fixed ensemble α and a virtual displacement of the *poi*). For large distances $|\boldsymbol{r}_{i\alpha}| \gg |\boldsymbol{r}_{j\alpha}|$, the inverse distance is approximated by

$$\begin{aligned}
\frac{1}{r_{ij}} = \frac{1}{(r_{i\alpha}^2 - 2\boldsymbol{r}_{i\alpha} \cdot \boldsymbol{r}_{j\alpha} + r_{j\alpha}^2)^{1/2}} &= \frac{1}{r_{i\alpha}} \left[1 + \left(\frac{r_{j\alpha}^2}{r_{i\alpha}^2} - 2\frac{\boldsymbol{r}_{i\alpha} \cdot \boldsymbol{r}_{j\alpha}}{r_{i\alpha}^2} \right) \right]^{-1/2} \\
&\approx \frac{1}{r_{i\alpha}} + \frac{\boldsymbol{r}_{i\alpha} \cdot \boldsymbol{r}_{j\alpha}}{r_{i\alpha}^3} + \frac{3(\boldsymbol{r}_{i\alpha} \cdot \boldsymbol{r}_{j\alpha})^2 - r_{i\alpha}^2 r_{j\alpha}^2}{2r_{i\alpha}^5}
\end{aligned}$$

in a Taylor series about the point zero. In the series we arranged the resulting terms regarding their order in $r_{j\alpha}/r_{i\alpha}$. Terms with 4th or higher order are neglected. Inserting the series into Eq. (B.2) and evaluating the gradient provides for the approximated force and the approximated potential

$$\begin{aligned}
\phi_{i\alpha} &\approx -kc_i \sum_j^{n_\alpha} c_j \Bigg(\underbrace{\frac{1}{r_{i\alpha}}}_{monopole} + \underbrace{\frac{\boldsymbol{r}_{i\alpha} \cdot \boldsymbol{r}_{j\alpha}}{r_{i\alpha}^3}}_{dipole} + \underbrace{\frac{3(\boldsymbol{r}_{i\alpha} \cdot \boldsymbol{r}_{j\alpha})^2 - r_{i\alpha}^2 r_{j\alpha}^2}{2r_{i\alpha}^5}}_{quadrupole} \Bigg) \\
\boldsymbol{F}_{i\alpha} &\approx -kc_i \sum_j^{n_\alpha} c_j \Bigg(\underbrace{\frac{\boldsymbol{r}_{i\alpha}}{r_{i\alpha}^3}}_{monopole} + \underbrace{\frac{3\boldsymbol{r}_{i\alpha}(\boldsymbol{r}_{i\alpha} \cdot \boldsymbol{r}_{j\alpha}) - \boldsymbol{r}_{j\alpha} r_{i\alpha}^2}{r_{i\alpha}^5}}_{dipole} \\
&\qquad + \underbrace{\frac{15\boldsymbol{r}_{i\alpha}(\boldsymbol{r}_{i\alpha} \cdot \boldsymbol{r}_{j\alpha})^2 - 6\boldsymbol{r}_{j\alpha}(\boldsymbol{r}_{i\alpha} \cdot \boldsymbol{r}_{j\alpha}) r_{i\alpha}^2 - 3\boldsymbol{r}_{i\alpha} r_{i\alpha}^2 r_{j\alpha}^2}{2r_{i\alpha}^7}}_{quadrupole} \Bigg) \quad .
\end{aligned} \tag{B.3}$$

This gives us the approximated expressions for the potential and the force on i generated by α at i's position, and, according to Eq. (2.2), we can switch between both equations by $\boldsymbol{F}_{i\alpha} = -\nabla_{i\alpha}\phi_{i\alpha}$. Eq. (B.3) is called the multipole expansion of the potential and the force, respectively, and corresponds to the first 3 terms in Eq. (2.12).

For each pseudo particle α we first have to identify and compute the elementary sums entering Eq. (B.3). This information we need for the computation of the vector $\boldsymbol{r}_{i\alpha}$ and of the n_α vectors $\boldsymbol{r}_{j\alpha}$.

So, the monopole contribution to the potential is

$$\phi_{i\alpha}^{(M)} = -kc_i \frac{1}{r_{i\alpha}} \sum_j^{n_\alpha} c_j \quad .$$

The dipole contribution to the potential

$$\begin{aligned}
\phi_{i\alpha}^{(D)} = -\frac{kc_i}{r_{i\alpha}^3} \sum_j^{n_\alpha} c_j (\boldsymbol{r}_{i\alpha} \cdot \boldsymbol{r}_{j\alpha}) = -\frac{kc_i}{r_{i\alpha}^3} \Big[&(x_i - R_x^\alpha) \underbrace{\sum_j^{n_\alpha} c_j (x_j - R_x^\alpha)}_{=\,0} \quad + \\
&(y_i - R_y^\alpha) \underbrace{\sum_j^{n_\alpha} c_j (y_j - R_y^\alpha)}_{=\,0} \quad + \\
&(z_i - R_z^\alpha) \underbrace{\sum_j^{n_\alpha} c_j (z_j - R_z^\alpha)}_{=\,0} \quad \Big] \quad = 0 \quad .
\end{aligned}$$

vanishes, because for $\boldsymbol{P}^\alpha = \boldsymbol{R}^\alpha$ we obtain $\sum c_j \boldsymbol{r}_j - \sum c_j \bigl(\frac{1}{\sum |c_j|} \sum |c_j| \boldsymbol{r}_j\bigr) = \boldsymbol{0}$ if we deal with equal masses (charges of the same sign). The quadrupole contribution to the potential is

$$\begin{aligned}
\phi_{i\alpha}^{(Q1)} = -\frac{3}{2}\frac{kc_i}{r_{i\alpha}^5}\sum_j^{n_\alpha} c_j(\boldsymbol{r}_{i\alpha}\cdot\boldsymbol{r}_{j\alpha})^2 = -\frac{3}{2}\frac{kc_i}{r_{i\alpha}^5}\Bigl[&(x_i - R_x^\alpha)^2 \sum_j^{n_\alpha} c_j (x_j - R_x^\alpha)^2 + \\
&(y_i - R_y^\alpha)^2 \sum_j^{n_\alpha} c_j (y_j - R_y^\alpha)^2 + \\
&(z_i - R_z^\alpha)^2 \sum_j^{n_\alpha} c_j (z_j - R_z^\alpha)^2 + \\
&2(x_i - R_x^\alpha)(y_i - R_y^\alpha) \sum_j^{n_\alpha} c_j (x_j - R_x^\alpha)(y_j - R_y^\alpha) + \\
&2(x_i - R_x^\alpha)(z_i - R_z^\alpha) \sum_j^{n_\alpha} c_j (x_j - R_x^\alpha)(z_j - R_z^\alpha) + \\
&2(y_i - R_y^\alpha)(z_i - R_z^\alpha) \sum_j^{n_\alpha} c_j (y_j - R_y^\alpha)(z_j - R_z^\alpha)\Bigr]
\end{aligned}$$

and

$$\begin{aligned}
\phi_{i\alpha}^{(Q2)} &= \frac{1}{2}\frac{kc_i}{r_{i\alpha}^3}\sum_j^{n_\alpha} c_j r_{j\alpha}^2 \\
&= \frac{1}{2}\frac{kc_i}{r_{i\alpha}^3}\Bigl(\sum_j^{n_\alpha} c_j (x_j^2 + y_j^2 + z_j^2) - 2\sum_j^{n_\alpha} c_j (x_j R_x^\alpha + y_j R_y^\alpha + z_j R_z^\alpha) \\
&\qquad + (R_x^{\alpha 2} + R_y^{\alpha 2} + R_z^{\alpha 2})\sum_j^{n_\alpha} c_j\Bigr) \quad .
\end{aligned}$$

For the force monopole term

$$\boldsymbol{F}_{i\alpha}^{(M)} = -kc_i \frac{\boldsymbol{r}_{i\alpha}}{r_{i\alpha}^3}\sum_j^{n_\alpha} c_j \quad .$$

For the force dipole terms

$$
\begin{aligned}
\boldsymbol{F}_{i\alpha}^{(D1)} &= -3kc_i\frac{\boldsymbol{r}_{i\alpha}}{r_{i\alpha}^5}\sum_j^{n_\alpha} c_j(\boldsymbol{r}_{i\alpha}\cdot\boldsymbol{r}_{j\alpha}) \\
&= -3kc_i\frac{\boldsymbol{r}_{i\alpha}}{r_{i\alpha}^5}\Big[(x_i-R_x^\alpha)\underbrace{\sum_j^{n_\alpha} c_j(x_j-R_x^\alpha)}_{=\,0}+(y_i-R_y^\alpha)\underbrace{\sum_j^{n_\alpha} c_j(y_j-R_y^\alpha)}_{=\,0} \\
&\qquad +(z_i-R_z^\alpha)\underbrace{\sum_j^{n_\alpha} c_j(z_j-R_z^\alpha)\Big]}_{=\,0} = \mathbf{0} \quad , \\
\boldsymbol{F}_{i\alpha}^{(D2)} &= kc_i\frac{1}{r_{i\alpha}^3}\sum_j^{n_\alpha} c_j\boldsymbol{r}_{j\alpha} = kc_i\frac{1}{r_{i\alpha}^3}\underbrace{\sum_j^{n_\alpha} c_j(\boldsymbol{r}_j-\boldsymbol{R}^\alpha)}_{=\,\mathbf{0}} = \mathbf{0} \quad .
\end{aligned}
$$

For the force quadrupole terms

$$
\begin{aligned}
\boldsymbol{F}_{i\alpha}^{(Q1)} &= -\frac{15}{2}kc_i\frac{\boldsymbol{r}_{i\alpha}}{r_{i\alpha}^7}\sum_j^{n_\alpha} c_j(\boldsymbol{r}_{i\alpha}\cdot\boldsymbol{r}_{j\alpha})^2 \\
&= -\frac{15}{2}kc_i\frac{\boldsymbol{r}_{i\alpha}}{r_{i\alpha}^7}\Bigg[(x_i-R_x^\alpha)^2\sum_j^{n_\alpha} c_j(x_j-R_x^\alpha)^2 \\
&\qquad +2(x_i-R_x^\alpha)(y_i-R_y^\alpha)\sum_j^{n_\alpha} c_j(x_j-R_x^\alpha)(y_j-R_y^\alpha) \\
&\qquad +(y_i-R_y^\alpha)^2\sum_j^{n_\alpha} c_j(y_j-R_y^\alpha)^2 \\
&\qquad +2(x_i-R_x^\alpha)(z_i-R_z^\alpha)\sum_j^{n_\alpha} c_j(x_j-R_x^\alpha)(z_j-R_z^\alpha) \\
&\qquad +(z_i-R_z^\alpha)^2\sum_j^{n_\alpha} c_j(z_j-R_z^\alpha)^2 \\
&\qquad +2(y_i-R_y^\alpha)(z_i-R_z^\alpha)\sum_j^{n_\alpha} c_j(y_j-R_y^\alpha)(z_j-R_z^\alpha)\Bigg] \quad ,
\end{aligned}
$$

$$
\begin{aligned}
\boldsymbol{F}_{i\alpha}^{(Q2)} &= 3kc_i\frac{1}{r_{i\alpha}^5}\sum_j^{n_\alpha} c_j\boldsymbol{r}_{j\alpha}(\boldsymbol{r}_{i\alpha}\cdot\boldsymbol{r}_{j\alpha}) \\
&= 3kc_i\frac{1}{r_{i\alpha}^5}\Bigg[(x_i - R_x^\alpha)\sum_j^{n_\alpha} c_j x_j(\boldsymbol{r}_j - \boldsymbol{R}^\alpha) + (R_x^{\alpha 2} - R_x^\alpha x_i)\underbrace{\sum_j^{n_\alpha} c_j(\boldsymbol{r}_j - \boldsymbol{R}^\alpha)}_{=\,\mathbf{0}} \\
&\qquad +(y_i - R_y^\alpha)\sum_j^{n_\alpha} c_j y_j(\boldsymbol{r}_j - \boldsymbol{R}^\alpha) + (R_y^{\alpha 2} - R_y^\alpha y_i)\underbrace{\sum_j^{n_\alpha} c_j(\boldsymbol{r}_j - \boldsymbol{R}^\alpha)}_{=\,\mathbf{0}} \\
&\qquad +(z_i - R_z^\alpha)\sum_j^{n_\alpha} c_j z_j(\boldsymbol{r}_j - \boldsymbol{R}^\alpha) + (R_z^{\alpha 2} - R_z^\alpha z_i)\underbrace{\sum_j^{n_\alpha} c_j(\boldsymbol{r}_j - \boldsymbol{R}^\alpha)}_{=\,\mathbf{0}}\Bigg] \quad ,
\end{aligned}
$$

and

$$
\begin{aligned}
\boldsymbol{F}_{i\alpha}^{(Q3)} &= \frac{3}{2}kc_i\frac{\boldsymbol{r}_{i\alpha}}{r_{i\alpha}^5}\sum_j^{n_\alpha} c_j r_{j\alpha}^2 \\
&= \frac{3}{2}kc_i\frac{\boldsymbol{r}_{i\alpha}}{r_{i\alpha}^5}\Bigg[\sum_j^{n_\alpha} c_j(x_j^2 + y_j^2 + z_j^2) - 2\sum_j^{n_\alpha} c_j(x_j R_x^\alpha + y_j R_y^\alpha + z_j R_z^\alpha) \\
&\qquad +(R_x^{\alpha 2} + R_y^{\alpha 2} + R_z^{\alpha 2})\sum_j^{n_\alpha} c_j\Bigg] \quad .
\end{aligned}
$$

To summarize, Tab. B.1 lists the elementary sums we need for the computation of each multipole moment.

	Elementary sums necessary for the multipole contributions
$\boldsymbol{R}^{\alpha}$	$\sum_j^{n_\alpha} \lvert c_j\rvert,\ \sum_j^{n_\alpha} \lvert c_j\rvert x_j,\ \sum_j^{n_\alpha} \lvert c_j\rvert y_j,\ \sum_j^{n_\alpha} \lvert c_j\rvert z_j$
$\phi_{i\alpha}^{(M)}$	$\sum_j^{n_\alpha} c_j$
$\phi_{i\alpha}^{(D)}$	$\sum_j^{n_\alpha} c_j,\ \sum_j^{n_\alpha} \lvert c_j\rvert,\ \sum_j^{n_\alpha} \lvert c_j\rvert x_j,\ \sum_j^{n_\alpha} \lvert c_j\rvert y_j,\ \sum_j^{n_\alpha} \lvert c_j\rvert z_j,\ \sum_j^{n_\alpha} c_j x_j,\ \sum_j^{n_\alpha} c_j y_j,\ \sum_j^{n_\alpha} c_j z_j$
$\phi_{i\alpha}^{(Q)}$	$\sum_j^{n_\alpha} c_j,\ \sum_j^{n_\alpha} \lvert c_j\rvert,\ \sum_j^{n_\alpha} \lvert c_j\rvert x_j,\ \sum_j^{n_\alpha} \lvert c_j\rvert y_j,\ \sum_j^{n_\alpha} \lvert c_j\rvert z_j,$ $\sum_j^{n_\alpha} c_j x_j,\ \sum_j^{n_\alpha} c_j y_j,\ \sum_j^{n_\alpha} c_j z_j,\ \sum_j^{n_\alpha} c_j x_j^2,\ \sum_j^{n_\alpha} c_j y_j^2,\ \sum_j^{n_\alpha} c_j z_j^2,\ \sum_j^{n_\alpha} c_j x_j y_j,\ \sum_j^{n_\alpha} c_j x_j z_j,\ \sum_j^{n_\alpha} c_j y_j z_j$
$\boldsymbol{F}_{i\alpha}^{(M)}$	$\sum_j^{n_\alpha} c_j,\ \sum_j^{n_\alpha} \lvert c_j\rvert,\ \sum_j^{n_\alpha} \lvert c_j\rvert x_j,\ \sum_j^{n_\alpha} \lvert c_j\rvert y_j,\ \sum_j^{n_\alpha} \lvert c_j\rvert z_j,$
$\boldsymbol{F}_{i\alpha}^{(D)}$	$\sum_j^{n_\alpha} \lvert c_j\rvert,\ \sum_j^{n_\alpha} \lvert c_j\rvert x_j,\ \sum_j^{n_\alpha} \lvert c_j\rvert y_j,\ \sum_j^{n_\alpha} \lvert c_j\rvert z_j,\ \sum_j^{n_\alpha} c_j x_j,\ \sum_j^{n_\alpha} c_j y_j,\ \sum_j^{n_\alpha} c_j z_j$
$\boldsymbol{F}_{i\alpha}^{(Q)}$	$\sum_j^{n_\alpha} c_j,\ \sum_j^{n_\alpha} \lvert c_j\rvert,\ \sum_j^{n_\alpha} \lvert c_j\rvert x_j,\ \sum_j^{n_\alpha} \lvert c_j\rvert y_j,\ \sum_j^{n_\alpha} \lvert c_j\rvert z_j,$ $\sum_j^{n_\alpha} c_j x_j,\ \sum_j^{n_\alpha} c_j y_j,\ \sum_j^{n_\alpha} c_j z_j,\ \sum_j^{n_\alpha} c_j x_j^2,\ \sum_j^{n_\alpha} c_j y_j^2,\ \sum_j^{n_\alpha} c_j z_j^2,\ \sum_j^{n_\alpha} c_j x_j y_j,\ \sum_j^{n_\alpha} c_j x_j z_j,\ \sum_j^{n_\alpha} c_j y_j z_j$

Table B.1: Elementary sums to be computed for the multipole contributions of both the potential and the force acting on the *poi* i by the particle ensemble α.

C Pair Distribution Function

Histograms of the pair distribution function show the normalized number of particles in the neighborhood of the reference particle in intervals of the distance, according to Eq. (4.11). We have shown the histograms for repulsive and attractive long range forces in Fig. 4.6 and 4.15, respectively. In these plots the maximum of $g(r_{ij})$ is not shown exactly at the distance $r_{ij} = 2a$ but slightly shifted to larger distances. This is, because we divide the distance space into bins of width Δr_{ij} (see the bars in the figure) such that the limits of a bin exactly coincides with $r_{ij} = 2a$. Due to the fact that the data points (solid circles) are located in the bin centers, no data point will be displayed at $r_{ij} = 2a$ and the maximum shown in the histograms is located at $2a + \frac{1}{2}\Delta r_{ij}$. Therefore, the maximum displayed is not equivalent with the value predicted by Eq. (4.11) in case of no long range interactions. For this reason, we will extrapolate the slope of $g(r_{ij})$ towards smaller r_{ij} by a straight line (dashed) until the line intersects with the vertical at $r_{ij} = 2a$,

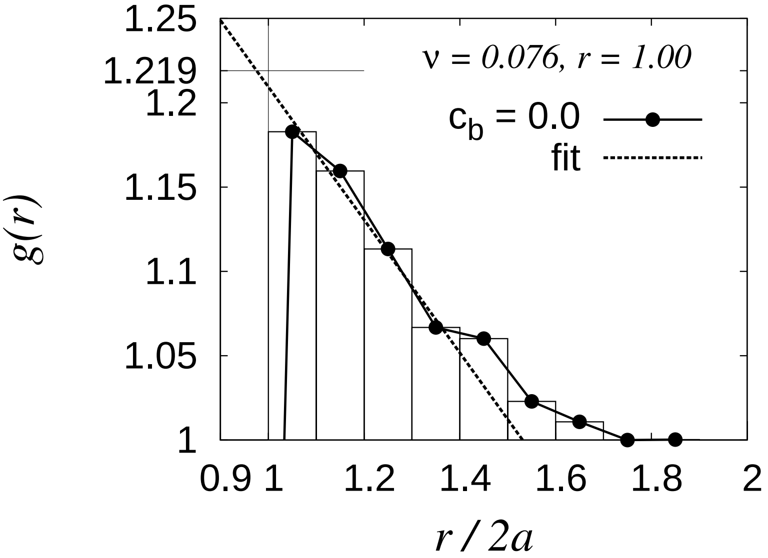

Figure C.1: A histogram of the pair distribution function, $g(r_{ij})$, plotted as a function of the particle pair distances, r_{ij}. Bars indicate the bin width, black circles are data points and the dashed line corresponds to the linear fit we use for the extrapolation.

assuming a linear increase of $g(r_{ij})$ towards the point $r_{ij} = 2a$. The extrapolation is shown in Fig. C.1 for the case without long range forces and for the density $\nu = 0.076$. Thus, Eq. (4.11) provides $g(2a = 0.001) = 1.219$, which corresponds to the horizontal line at $g(r_{ij}) = 1.219$. The extrapolation line is a linear fit on the data in the distance range $r_{ij}/2a \in [1 : 1.4]$, where the increase of $g(r_{ij})$ is steepest. However, the extrapolation still does not provide an intersection at the nominal value, but the intersection point is significantly increased as compared to the maximum of $g(r_{ij})$ shown.

Taking additionally into account the fact that, in case of soft spheres, an overlap of two colliding particles can occur, there is a small probability to find a neighbor particle also at a distance $r_{ij} < 2a$. This provides for non-vanishing values in the bin(s) to the left of $r_{ij} = 2a$. E.g., the line connecting the data points steeply decreases for $r_{ij} < 2a + \frac{1}{2}\Delta r_{ij}$ and indicates a non-vanishing contribution at $r_{ij} = 2a - \frac{1}{2}\Delta r_{ij}$. If we would deal with hard sphere systems, the probability to find neighbors at $r_{ij} < 2a$ will be zero. So, for our purposes, we have to add the small probability fraction to the bin at $2a + \frac{1}{2}\Delta r_{ij}$. This will lead to an increased peak probability and the peak would come once more closer to the predicted value $g^0(2a) = 1.219$.

In sections 4.3.5 and 4.4.4 we are interested in determining the ratio $g(2a)/g^0(2a)$ in order to obtain a correction factor for the dissipation rate due to the effective energy barrier. For this reason, we also extract values for $g(2a)/g^0(2a)$ from the figures 4.6 and 4.15, respectively. We will remark, that the extraction is carried out by the extrapolation method presented here.

References

[1] M. P. Allen and D. J. Tildesley. *Computer Simulation of Liquids.* Oxford University Press, Oxford, 1987.

[2] J. C. Almekinders and C. Jones. Multiple jet electrohydrodynamic spraying and applications. *J. Aerosol Sci.*, 30:969–971, 1999.

[3] J. S. Bagla. TreePM: A code for cosmological N-body simulations. *J. Astrophys. Astr.*, 23:185–196, 2002.

[4] J. Barnes. A modified tree code. don't laugh; it runs. *J. of Comp. Phys.*, 87:161–170, 1990.

[5] J. Barnes and L. Hernquist. Computer models of colliding galaxies. *Physics Today*, Mar.:54–61, 1993.

[6] J. Barnes and P. Hut. A hierarchical $O(N\log N)$ force calculation algorithm. *Nature*, 324:446–449, 1986.

[7] M. Baus and J.-P. Hansen. Statistical mechanics of simple coulomb systems. *Phys. Rep.*, 59(1):2–94, 1980.

[8] D. L. Blair and A. Kudrolli. Magnetized granular materials. In H. Hinrichsen and D. Wolf, editors, *The Physics of Granular Media.*, pages 281–296. Wiley-VCH, Weinheim, 2004.

[9] P. Bode and J. P. Ostriker. Tree particle-mesh: An adaptive, efficient, and parallel code of collisionless cosmological simulation. *Astrophys. J. Supplem. Series*, 145(1):1–13, 2003.

[10] J. J. Brey. Cluster instability in freely evolving granular gases. In D. Reguera, L. Bonilla, and J. R. (Eds.), editors, *Coherent Structures in Complex Systems.*, pages 392–407. Springer, Berlin Heidelberg, 2001.

[11] F. G. Bridges, A. Hatzes, and D. N. C. Lin. Structure, stability and evolution of saturn's rings. *Nature*, 309:333–, 1984.

[12] N. V. Brilliantov and T. Pöschel. Deviation from maxwell distribution in granular gases with constant restitution coefficient. *Phys. Rev. E*, 61:2809–, 2000.

[13] N. V. Brilliantov and T. Pöschel. *Kinetic Theory of Granular Gases.* Oxford University Press, Oxford, 2004.

[14] N. V. Brilliantov, F. Spahn, J.-M. Hertzsch, and T. Pöschel. A model for collisions in granular gases. *Phys. Rev. E*, 53:5382–, 1996.

[15] W. F. Busse and F. C. Starr. Change of a viscoelastic sphere to a torus by random impacts. *Am. J. Phys.*, 28:19–, 1960.

[16] N. F. Carnahan and K. E. Starling. Equation of state for nonattractive rigid spheres. *J. Chem. Phys.*, 51(2):635–636, 1969.

[17] Y. T. Cheng and D. E. Rodak. Is the lotus leaf superhydrophobic? *Appl. Phys. Lett.*, 86:144101, 2005.

[18] A. F. Cook and F. A. Franklin. Rediscussion of maxwell's adams prize essay on the stability of saturn's rings. *Astronomical Journal*, 69:173–200, 1964.

[19] J. W. Cooley and W. Tukey. An algorithm for the machine calculation of complex fourier series. *Math. Comput.*, 19:297–301, 1965.

[20] J. A. Cross. *Electrostatics: Principles, Problems and Applications.* Adam Hilger, Bristol, 1987.

[21] P. A. Cundall and O. Strack. A discrete numerical model for granular assemblies. *Géotechnique*, 29:47–65, 1979.

[22] S. M. Dammer, J. Werth, and H. Hinrichsen. Electrostatically charged granular matter. In H. Hinrichsen and D. Wolf, editors, *The Physics of Granular Media.*, pages 255–280. Wiley-VCH, Weinheim, 2004.

[23] C. A. de Coulomb. Théories des machines simples. *Academie des Sciences*, 10:166–, 1781.

[24] C. A. de Coulomb. *Mémoires sur l'Eléctricité et le Magnétisme.* Bachelier, Paris, 1785-1789.

[25] J. Duran. *Sands, Powders and Grains.* Springer-Verlag, New York, Inc., 2000.

[26] J. W. Eastwood, R. W. Hockney, and D. Lawrence. P3m3dp - the 3-dimensional periodic particle-particle-particle-mesh program. *Comp. Phys. Commun.*, 19:215–261, 1980.

[27] A. Einstein. Über die von der molekularkinetischen Theorie der Wärme geforderte Bewegung von in ruhenden Flüssigkeiten suspendierten Teilchen. *Ann. d. Physik und Chemie*, 17:549–560, 1905.

[28] M. H. Ernst, J. R. Dorfman, W. R. Hoegy, and J. M. J. van Leeuwen. Hard-sphere dynamics and binary-collision operators. *Physica*, 45(1):127–146, 1969.

[29] P. Eshuis, K. van der Weele, D. van der Meer, and D. Lohse. The granular leidenfrost effect: Experiment and theory of floating particle clusters. *Phys. Rev. E*, 95:258001, 2005.

[30] S. E. Esipov and T. Pöschel. The granular phase diagram. *J. Stat. Phys.*, 86(5/6):1385–1395, 1997.

[31] L. W. Esposito, J. N. Cuzzi, J. B. Holberg, E. A. Marouf, G. L. Tyler, and C. C. Porco. Saturn's rings, structure, dynamics and particle properties. In *Saturn*, pages 463–545. Univ. of Arizona Press, Tucson, AZ, 1984.

[32] P. W. Fowler, P. Lazzeretti, and W. Zanas. Anisotropic dispersion forces in methane mixtures. *Mol. Phys.*, 68(4):853–865, 1989.

[33] K. B. Geerse. *Application of Electrospray: from people to plants.* Ph.D. thesis, Technische Universiteit Delft, 2003.

[34] I. Goldhirsch and G. Zanetti. Clustering instability in dissipative gases. *Phys. Rev. Lett.*, 70(11):1619–1622, 1993.

[35] P. Goldreich. The dynamics of planetary rings. *Ann. Rev. Astron. Astrophys.*, 20:249–283, 1982.

[36] P. Goldreich and S. Tremaine. The velocity dispersion in saturn's rings. *Icarus*, 34:227–239, 1978.

[37] R. Greenberg and A. Brahic. *Planetary Rings.* Arizona University Press, Tucson, AZ, 1984.

[38] L. Greengard. *The Rapid Evaluation of Potential Fields in Particle Systems.* MIT Press, Cambridge, Massachusetts, 1988.

[39] L. Greengard. The numerical solution of the n-body problem. *Comp. in Phys.*, Mar./Apr.:142–152, 1990.

[40] L. Greengard and V. Rokhlin. A fast algorithm for particle simulations. *J. of Comp. Phys.*, 73:325–348, 1987.

[41] L. Grubmüller and P. Tavan. Multiple time step algorithms for molecular dynamics simulations of proteins: How good are they? *J. Comp. Chem.*, 19:1543–1552, 1998.

[42] J. Haenninen and H. Salo. Collisional simulations of satellite lindblad resonances. *Icarus*, 97:228–247, 1992.

[43] P. K. Haff. Grain flow as a fluid-mechanical phenomenon. *J. Fluid Mech.*, 134:401–430, 1983.

[44] J. M. Haile. *Molecular Dynamics Simulations - Elementary Methods.* John Wiley & Sons, Inc., New York, Chichester, Weinheim, Brisbane, Singapore, Toronto, 1997.

[45] J.-P. Hansen and I. R. McDonald. *Theory of Simple Liquids.* Academic Press Ltd., London, San Diego, 1990.

[46] D. Henderson. A simple equation of state for hard discs. *Molec. Phys.*, 30 (3):971–972, 1975.

[47] O. Herbst, R. Cafiero, A. Zippelius, H. J. Herrmann, and S. Luding. A driven two-dimensional granular gas with coulomb friction. *Phys. of Fluids*, 17(10):107102(1–16), 2005.

[48] O. Herbst, P. Müller, and A. Zippelius. Local heat flux and energy loss in a two-dimensional vibrated granular gas. *Phys. Rev. E*, 72(4):041303, 2005.

[49] L. Hernquist. Hierarchical N-body methods. *Comp. Phys. Commun.*, 48: 107–115, 1988.

[50] H. Hertz. Über die Berührung fester elastischer Körper. *J. f. d. reine u. angewandte Math.*, 92:156–171, 1882.

[51] G. M. Hidy and J. R. Brock. *The Dynamics of Aerocolloidal Systems.* Pergamon Press, Oxford, New York, Toronto, Sydney, Braunschweig, 1970. International Reviews in Aerosol Physics and Chemistry, Volume I.

[52] R. W. Hockney and J. W. Eastwood. *Computer Simulation Using Particles. Vol 1.* McGraw-Hill, New York, 1981.

[53] R. Hoffmann. *Modeling and Simulation of an Electrostatic Image Transfer.* (Ph.D. thesis) Shaker Verlag, Aachen, 2004.

[54] W. G. Hoover, editor. *Molecular Dynamics.* Springer, Berlin, 1986. Lecture Notes in Physics 258.

[55] P. Hut, J. Makino, and S. McMillan. Modelling the evolution of globular star clusters. *Nature*, 336(Nov.):31–35, 1988.

[56] M. Huthmann and A. Zippelius. Dynamics of inelastically colliding rough spheres: Relaxation of translational and rotational energy. *Phys. Rev. E*, 56(6):R6275–R6278, 1997.

[57] S. Ichimaru. Strongly coupled plasmas: high-density classical plasmas and degenerated electron liquids. *Rev. Mod. Phys.*, 54(4):1017–1059, 1982.

[58] J. N. Israelachvili. *Intermolecular and Surface Forces: with Applications to Colloidal and Biological Systems. (2^{nd} edition).* Elsevier, 1992.

[59] J. D. Jackson. *Classical Electrodynamics. (3^{rd} edition).* John Wiley & Sons, Inc., New York, Chichester, Weinheim, Brisbane, Singapore, Toronto, 1998.

[60] M. D. Joesten and L. J. Schaad. *Hydrogen Bonding.* Dekker, New York, 1974.

[61] J. E. Jones. On the determination of molecular fields. ii. from the equations of state of a gas. *Proc. R. Soc. London A*, 106:463–477, 1924.

[62] C. Kittel. *Introduction to Solid State Physics. (8^{th} edition).* John Wiley & Sons, Inc., New York, Chichester, Weinheim, Brisbane, Singapore, Toronto, 2005.

[63] W. Kleber and A. Lang. Triboelectrically charged powder coatings generated by running through holes and slits. *J. of Electrostatics*, 40&41: 237–240, 1997.

[64] C. W. J. Lemmens. *An Investigation, Implementation and Comparison of 3 important Particle Simulation Techniques: PP: Particle-Particle PM: Particle-Mesh TC: Tree-Code. Report 97-46.* Faculty of Technical Mathematics and Informatics, Delft, 1997.

[65] J. E. Lennard-Jones. Cohesion. *Proc. Phys. Soc.*, 43(240):461–482, 1931.

[66] D. Lohse, R. Bergmann, R. Mikkelsen, C. Zeilstra, D. van der Meer, M. Versluis, K. van der Weele, M. van der Hoef, and H. Kuipers. Impact on soft sand: Void collapse and jet formation. *Phys. Rev. Let.*, 93(19):198003, 2004.

[67] J. Lowell and A. C. Rose-Innes. Contact electrification. *Adv. in Phys.*, 29 (6):947–1023, 1980.

[68] S. Luding. Clustering instabilities, arching, and anomalous interaction probabilities as examples for cooperative phenomena in dry granular media. *T.A.S.K. Quarterly, Scientific Bulletin of Academic Computer Centre of the Technical University of Gdansk.*, 2(3):417–443, 1998.

[69] S. Luding. Collisions & contacts between two particles. In H. J. Herrmann, J.-P. Hovi, and S. Luding, editors, *Physics of dry granular media - NATO ASI Series E350*, page 285. Kluwer Academic Publishers, Dordrecht, 1998.

[70] S. Luding. Structure and cluster formation in granular media. *Pranama J. Phys.*, pages 1–10, 2004.

[71] S. Luding. Anisotropy in cohesive, frictional granular media. *J. Phys.: Condens. Matter*, 17:S2623–S2640, 2005.

[72] S. Luding. About contact force-laws for cohesive frictional materials in 2d and 3d. In P. Walzel, S. Linz, C. Krülle, and R. Grochowski, editors, *Behavior of Granular Media. Band 9: Schriftenreihe Mechanische Verfahrenstechnik. ISBN 3-8322-5524-9*, pages 137–147. Shaker Verlag, Aachen, 2006.

[73] S. Luding. Contact models for very loose granular materials. *IUTAM proceedings*, in press, 2006.

[74] S. Luding. Cohesive, frictional powders: contact models for tension. *Gran. Mat.*, accepted, 2007.

[75] S. Luding and H. J. Herrmann. Cluster growth in freely cooling granular media. *Chaos*, 9(3):673–681, 1999.

[76] S. Luding, M. Huthmann, S. McNamara, and A. Zippelius. Homogeneous cooling of rough, dissipative particles: Theory and simulations. *Phys. Rev. E*, 58:3416–3425, 1998.

[77] J. Lukkari and H. Salo. Numerical simulations of collisions in self-gravitating systems. *Earth, Moon and Planets*, 31:1–13, 1984.

[78] R. Lüst. Die Entwicklung einer um einen Zentralkörper rotierenden Gasmasse I. *Zeitschrift für Naturforschung*, 7a:87–98, 1951.

[79] A. D. McLachlan. Retarded dispersion forces between molecules. *Proc. R. Soc. Lond. Ser. A, Math. and Phys. Sci.*, 271(1346):387–401, 1963.

[80] A. D. McLachlan. Three-body dispersion forces. *Mol. Phys.*, 6(4):423–427, 1963.

[81] S. McNamara. Hydrodynamic modes of a uniform granular medium. *Phys. of Fluids A*, 5:3056–3070, 1993.

[82] S. McNamara and W. R. Young. Dynamics of a freely evolving, two-dimensional granular medium. *Phys. Rev. E*, 53:5089–5100, 1996.

[83] B. Meerson, T. Pöschel, P. Sasorov, and T. Schwager. Close-packed floating clusters: Granular hydrodynamics beyond the freezing point? *Phys. Rev. Lett.*, 024301, 2003.

[84] S. Miller. *Clusterbildung in Granularen Gasen. (in German).* Ph.D. thesis, Universität Stuttgart, 2003.

[85] S. Miller and S. Luding. Cluster growth in two- and three-dimensional granular gases. *Phys. Rev. E*, 69(3):031305 1–8, 2004.

[86] M.-K. Müller. *Untersuchung von Akkretionsscheiben mit Hilfe der Molekulardynamik. (in German).* Diploma thesis, Universität Stuttgart, 2001.

[87] M.-K. Müller and S. Luding. Long-range interactions in ring-shaped particle aggregates. In R. García-Rojo, H. Herrmann, and S. McNamara, editors, *Powders & Grains*, pages 1119–1122. Balkema, Leiden, 2005.

[88] M.-K. Müller, T. Winkels, J. M. K.B. Geerse, A. Schmidt-Ott, and S. Luding. Experiment and simulation of charged particle sprays. pages 1–4. PARTEC Nuremberg, 2004.

[89] B. Muth, M.-K. Müller, P. Eberhard, and S. Luding. Contacts between many bodies. In W. Kurnik, editor, *Machine Dynamics Problems*, pages 101–114. Warsaw, 2004.

[90] E. Németh. *Triboelektrische Aufladung von Kunststoffen. (in German).* Ph.D. thesis, Technische Universität Bergakademie Freiberg, 2003.

[91] I. Newton. *Philosophiæ Naturalis Principia Mathematica.* Londini: Jussu Societatis Regiæ, London, 1687.

[92] F. Niermöller. *Ladungsverteilung in Mineralgemischen und elektrostatische Sortierung nach Triboaufladung. (in German).* Ph.D. thesis, Technische Universität Clausthal, 1988.

[93] S. Ogawa. Multitemperature theory of granular materials. In S. C. Cowin and M. Satake, editors, *Proc. of US-Japan Symp. on Continuum Mechanics and Statistical Approaches to the Mechanics of Granular Media.*, pages 208–217. Gakujutsu Bunken, Fukyukai, 1978.

[94] J. S. Olafsen and J. S. Urbach. Clustering, order, and collapse in a driven granular monolayer. *Phys. Rev. Lett.*, 81:4369, 1998.

[95] J. A. G. Orza, R. Brito, T. P. C. van Noije, and M. H. Ernst. Patterns and long range correlations in idealized granular flows. *Int. J. of Mod. Phys. C*, 8(4):953–965, 1997.

[96] S. Pfalzner and P. Gibbon. *Many-Body Tree Methods in Physics.* Cambridge University Press, Cambridge, UK, 1996.

[97] T. Pöschel and S. Luding, editors. *Granular Gases.* Springer, Berlin, 2001. Lecture Notes in Physics 564.

[98] T. Pöschel and T. Schwager. *Computational Granular Dynamics.* Springer, Berlin, Heidelberg, New York, 2005.

[99] R. D. Present. *Kinetic Theory of Gases.* McGraw-Hill Book Comany, Inc., New York, Toronto, London, 1958.

[100] J. E. Pringle. Accretion discs in astrophysics. *Annual Review of Astronomy and Astrophysics*, 19:137–162, 1981.

[101] R. Ramírez, T. Pöschel, N. V. Brilliantov, and T. Schwager. Coefficient of restitution of colliding viscoelastic spheres. *Phys. Rev. E*, 60:4465–, 1999.

[102] D. C. Rapaport. *The Art of Molecular Dynamics Simulation.* Cambridge University Press, Cambridge, 1995.

[103] F. H. Ree and W. G. Hoover. Fifth and sixth virial coefficients for hard spheres and hard disks. *J. Chem. Phys.*, 40(4):939–950, 1964.

[104] P. Resibois. *Electrolyte Theory.* Harper and Row, New York, 1968.

[105] R. J. Sadus. *Molecular Simulation of Fluids - Theory, Algorithms and Object-Orientation.* Elsevier, Amsterdam, 1999.

[106] H. Salo. Gravitational wakes in saturn's rings. *Nature*, 359:619–621, 1992.

[107] H. Salo. Numerical simulations of the collisional dynamics of planetary rings. In *Granular Gases.* Springer, Berlin, Heidelberg, 2001.

[108] F. Sauter. *Theorie der Elektrizität. (21. Auflage).* Teubner Verlag, Stuttgart, 1973.

[109] J. Schäfer, S. Dippel, and D. E. Wolf. Force schemes in simulations of granular materials. *J. Phys. I*, 6:5–20, 1996.

[110] T. N. Scheffler. *Kollisionskühlung in elektrisch geladener granularer Materie. (in German).* Ph.D. thesis, Gerhard-Mercator-Universität Duisburg, 2000.

[111] T. N. Scheffler and D. E. Wolf. Collision rates in charged granular gases. *Gran. Mat.*, 4(3):103–113, 2002.

[112] J. Schmidt, H. Salo, O. Petzschmann, and F. Spahn. Vertical distribution of temperature and density in a planetary ring. *Astronomy and Astrophysics*, 345:646–652, 1999.

[113] K. E. Schmidt and M. A. Lee. Implementing the fast multipole method in three dimensions. *J. Stat. Phys.*, 63:1223–1235, 1991.

[114] T. Schwager and T. Pöschel. Coefficient of restitution of viscous particles and cooling rate of granular gases. *Phys. Rev. E*, 57:650–, 1998.

[115] F. Spahn. Planetary rings: Nonequilibrium systems in space. In *Stochastic Physics*. Springer, Heidelberg, 1997.

[116] F. Spahn, J.-M. Petit, and P. H. Bendjoya. The gravitational influence of satellite Pan on the radial distribution of ring-particles in the region of the Encke-division in Saturn's A ring. *Cel. Mech. and Dyn. Astr.*, 57:391–402, 1993.

[117] F. Spahn and J. Schmidt. Saturn's bared mini-moons. *Nature*, 440:614–615, 2006.

[118] F. Spahn, U. Schwarz, and J. Kurths. Clustering of granular assemblies with temperature dependent restitution under Keplerian differential rotation. *Phys. Rev. Let.*, 78(8):1596–1599, 1997.

[119] R. Speith and H. Riffert. The viscous gas ring as an astrophysical test problem for a viscous sph-code. *Journal of Computational and Applied Mathematics*, 109:231–242, 1999.

[120] V. Springel, S. D. M. White, A. Jenkins, C. S. Frenk, N. Yoshida, L. Gao, J. Navarro, R. Thacker, D. Croton, J. Helly, J. A. Peacock, S. Cole, P. Thomas, H. Couchman, A. Evrard, J. Colberg, and F. Pearce. Simulating the joint evolution of quasars, galaxies and their large-scale distribution. *Nature*, 435:629–636, 2005.

[121] G. R. Stewart, D. N. C. Lin, and P. Bodenheimer. Collision-induced transport processes in planetary rings. In *Planetary Rings*. The University of Arizona Press, Tucson, Arizona, USA, 1984.

[122] G. Sutmann and B. Steffen. A particle-particle particle-multigrid method for long-range interactions in molecular simulations. *Comp. Phys. Commun.*, 169(1-3):343–346, 2005.

[123] G. A. Tomlinson. A molecular theory of friction. *Phil. Mag.*, 7:905–939, 1929.

[124] S. Torquato, T. M. Truskett, and P. G. Debenedetti. Is random close packing of spheres well defined? *Phys. Rev. Lett.*, 10:2064, 2000.

[125] U. Trottenberg, C. W. Oosterlee, and A. Schüller. *Multigrid.* Academic Press, San Diego, 2001.

[126] T. P. C. van Noije, M. H. Ernst, and R. Brito. Ring kinetic theory for an idealized granular gas. *Physica A*, 251:266–283, 1998.

[127] L. Verlet. Computer "experiments" on classical fluids. I. Thermodynamical properties of Lennard-Jones molecules. *Phys. Rev.*, 159(1):98–103, 1967.

[128] O. R. Walton and R. L. Braun. Viscosity, granular-temperature, and stress calculations for shearing assemblies of inelastic, frictional disks. *Journal of Rheology*, 30(5):949–980, 1986.

[129] P. R. Wills and D. J. Winzor. van der Waals phase transition in protein solutions. *Acta Cryst.*, D61:832–836, 2005.

[130] J. Wisdom and S. Tremaine. Local simulations of planetary rings. *Astron. J.*, 95:925–940, 1988.

[131] D. E. Wolf, T. N. Scheffler, and J. Schäfer. Granular flow, collisional cooling and charged grains. *Physica A*, 274:171–181, 1999.

[132] G. H. Xu. A new parallel N-body gravity solver. *Astrophys. J. Supplem. Series*, 98(1):355–366, 1995.

[133] I. Yavneh. Why multigrid methods are so efficient. *Computing in Science & Engineering*, 8(6):12–22, 2006.

[134] K. Yoshikawa and T. Fukushige. PPPM and TreePM methods on GRAPE systems for cosmological N-body simulations. *Publications of the Astronomical Society of Japan*, 56(6):849–860, 2005.

Acknowledgements

I do not want to close this thesis without thanking all those who made this work possible.

Foremost, I want to express my gratitude to my promotor Prof. Dr. Stefan Luding who offered me the opportunity to join him in the Netherlands and pursue such an interesting research. I enjoyed great freedom during all stages of establishing this thesis. I benefited a lot from his vast experience in the field of granular media and their computational treatment and am greatly thankful for his tireless corrections of my thesis, publications and presentations. At this place I also want to thank him and his wife Gerlinde for the countless times they gave me accomodation and invited me for dinner. Unforgotten are the various astronomical observations we made during my stays at their home.

Likewise I am greatful to Prof. Dr. Hans Herrmann, Prof. Dr. Andreas Schmidt-Ott and Prof. Dr. Harry Hoeijmakers who gave me the opportunity to work on my thesis in their research groups at the Universities of Stuttgart, Delft and Twente.

I want to express special thanks to my former colleagues from Delft Tomek Trzeciak and Raghuraman Pitchumani for their help concerning Matlab issues. Special thanks also go to all my Delft colleagues who joined me over the years and diversified my life. I especially enjoy remembering the various “traditional” Dutch BBQs we had together. Moreover, I would like to express my appreciation for all the valuable hints regarding the organization of my defense given to me by my colleagues from Twente. In particular, I would like to mention our secretary Anjenet Mettivier-Meyer who never became tired in finishing organizational things for me. Furthermore, I am indebted to Dr. Niels Kruyt, who translated the summary of this thesis into Dutch.

I would like to thank Dr. Olaf Herbst for his proofreading of parts of the thesis and for his critical scientifical comments on it.

I want to acknowledge the financial support of the Deutsche Forschungsgesellschaft (DFG), of the TU Delft, of the Delft Centre for Computational Science and Engineering (DCSE) and of the faculty of Construerende Technische Wetenschappen (CTW) of the University of Twente.

Furthermore, I want to thank a lot of friends of mine who indirectly supported me during my Ph.D. project in the Netherlands: Bianca Weidemann, Karl-Heinz

Schmidt, Martin Karremann, Jürgen Falkner with whom I continued more or less frequently our tradition to visit the "Cannstatter Wasen" in Stuttgart after having moved to the Netherlands. I do not want to forget to thank Christian Peineke, Robert Andersson, Orion Mouraille, Antina Ghosh and Orencio Duran for the many hours we spent together with a lot of beers, dinners and Sneak Previews.

Finally, I would like to thank my family, especially my parents, for their enduring support in any imaginable way, and my beloved Sabrina for her tolerance, patience and careness during the "extended" final stage of my work.

Curriculum Vitæ

May 3, 1972 : born in *Mutlangen*, Germany

May 1992 : **Abitur**, *Wirtschaftsgymnasium Schwäbisch Gmünd*, Germany

1992 - 1993 : **Community Service**, *Schwäbisch Gmünd*, Germany
Care of severely disabled people

1993 - 2001 : **Studies of Physics**, *University of Stuttgart*, Germany
Diploma thesis: Untersuchung von Akkretionsscheiben mit Hilfe der Molekulardynamik (in German)

2001 - 2007 : **Ph.D. Research**, *University of Stuttgart*, Germany, *TU Delft* and *UTwente*, The Netherlands
Thesis title: Long-Range Interactions in Dilute Granular Systems

Feb. 8, 2008 : **public defense**, *UTwente*, The Netherlands

---

Conferences and Seminars

2001 **Granular Matter Symposium in Nijmegen**
Astrophysical Rings as an Example of Granular Media. Talk
2003 **Workshop: Cooperative Grains in Leiden**
Force Statistics in Dense Granular Packings. Talk
Traffic & Granular Flow in Delft
Modeling of Long Range Interactions Forces. Poster
2004 **Annular OSPT Meeting in Veldhoven**
Force Statistics in Dense Granular Packings. Poster
Partec 2004 in Nürnberg
Experiment and Simulation of Charged Particle Systems. Poster
2005 **Annular OSPT Meeting in Veldhoven**
Force Statistics on Surfaces of Confined Dense Granular Assemblies. Poster
Material Simulation Days in Mainz
Long Range Interactions in Ring Shaped Particle Aggregates. Poster
Powders & Grains in Stuttgart
Long Range Interactions in Ring-Shaped Particle Aggregates. Poster
Seminar IRI in Delft
Modeling of Long Range Interactions in Granular Media and their Applications. Talk
Seminar DCSE in Delft
Long Range Interactions in Granular Materials. Talk
DOW Chemicals in Terneuzen
Long Range Interactions in Granular Materials. Talk
2006 **Annular OSPT Meeting in Veldhoven**
Modeling of Long Range Interaction Forces in Discrete Many-Body Systems. Poster
Seminar ICP in Stuttgart
Long Range Forces in Granular Gases. Talk
2007 **Partec 2007 in Nürnberg**
Long Range Forces in Homogeneous Granular Gases. Poster
2008 **Seminar PoF in Twente**
Long Range Interactions in Dilute Granular Systems. Talk

Publications

B. Muth, **M.-K. Müller**, P. Eberhard and S. Luding:
Contacts between many bodies. Kurnik, W. (Ed.), Machine Dynamics Problems, Warzaw 2004, pp. 101-114

B. Muth, **M.-K. Müller**, P. Eberhard and S. Luding:
Collision Detection and Administration Methods for Many Particles with Different Sizes. DEM07 Proceedings CD

M.-K. Müller, T. Winkels, K. B. Geerse, J. C. M. Marijnissen, A. Schmidt-Ott, and S. Luding:
Experiment and Simulation of Charged Particle Sprays. PARTEC 2004, Nürnberg, Germany, pp. 1-4, CD Proceedings

J. C. M. Marijnissen, T. Ciach, **M.-K. Müller**, T. Winkels, K. B. Geerse, A. Schmidt-Ott, and S. Luding:
Experiment and Simulation of Electrospray Particle Flows for controlled release of drugs in: Traffic and Granular Flow '03
S. P. Hoogendoorn, S. Luding, P. H. L. Bovy,
M. Schreckenberg, D. E. Wolf (eds.)
Springer Verlag, Berlin, 2005, pp. 513-520

M.-K. Müller and S. Luding:
Long Range Interactions in Ring-Shaped Particle Aggregates. In: Powders & Grains 2005, Stuttgart, July 2005, R. Garcia-Rojo, H.J. Herrmann and S. McNamara (Eds.), Balkema, Leiden, Netherlands, pp. 1119-1122

M.-K. Müller and S. Luding:
Long Range Forces in Homogeneous Granular Gases. PARTEC 2007, Nürnberg, Germany, pp. 1-4, CD Proceedings

M.-K. Müller, T. Pöschel and S. Luding:
Force Statistics in Dense Granular Packings. In preparation

M.-K. Müller and S. Luding:
A Theoretical Approach for Long Range Forces in Homogeneous Dilute Granular Systems. In preparation

---